Modelling Interfacial Diffusion Processes for CZTS Thin Film Photovoltaics

Fatimah H Bahrani
Newcastle University
Newcastle upon Tyne, UK.

A thesis submitted for the degree of
Doctor of Philosophy
October, 2018

Dedicated to

My family.

Declaration

This thesis has not previously been submitted by the candidate for a degree in this or any other university.

Fatimah Bahrani

October, 2018

Acknowledgments

After expressing my gratitude to God, I would like to thank Dr Jonathan Goss for his invaluable assistance, support, understanding and guidance. I really appreciate the efforts you made throughout the duration of my studies. I am also highly indebted to Prof Patrick Briddon.

A special thanks goes to Oras Al-Ani for sharing her knowledge and experience. I would also like to thank my colleagues and friends in the ETM group who made my studies in Newcastle enjoyable.

Thanks to a special friend Zeenah Atwan for her endless support through the ups and downs of my PhD research studies. I am also extremely grateful to my wonderful friends Rounq Al-yahya and Maha Rahma for their love and support.

Most importantly, I would like to thank my parents, Mr Hameed Khaleel and Ms Adeebah Ali, sisters and brother for their unconditional inspiration and support.

Finally, I would like to acknowledge the financial support provided by the Higher Committee of Education Development, Iraq. Thanks also to Iraq cultural attaché, Basrah University and Iraqi Ministry of Higher Education and Scientific Research.

Abstract

Inexpensive and nontoxic Cu_2ZnSnS_4 (CZTS) based thin-film solar cells have features which make it well placed to replace silicon, binary (CdTe) and ternary Cu(In,Ga)S semiconductors in photovoltaic cells, and shows great promise for commercial photovoltaic applications.

As-grown CZTS shows p-type conductivity, most probably due to the shallow acceptor levels of the intrinsic defects, Cu_{Zn} and V_{Cu}. CZTS, which provides the function of an absorber layer, is complicated by the multiplicity of chemical elements, resulting in many possible primary native defects as well as secondary phases to consider, including vacancies, antisites and ZnS precipitates. Furthermore, CZTS is thermodynamically stable in only a relatively narrow range of the atomic chemical potentials, with practical, efficient devices obtained in relatively Cu-poor and Zn-rich conditions; it is under these growth conditions that ZnS is thought to constitute a significant competing secondary phase. Such secondary phases affect the performance of photovoltaic devices by reducing the volume of the absorber layer and decreasing the short circuit current. In addition to the absorber layer, CZTS-based PV devices require a buffer layer that provides the n-type portion of the junction. CdS has been commonly used as a partner in the heterojunction, but ZnS is a potential alternative buffer layer to replace CdS due to the toxicity of cadmium.

Density functional theory has been used to investigate the geometric and electronic properties of CZTS and its secondary phases. Under given growth conditions, the phase stability and the formation energy of the point defects, impurities and secondary phases are explained. It is found that Cu_{Zn} has the lowest formation energy compared to the other native defects under normal growth conditions, and V_{Cu} has a shallow accepter level.

Redistribution of native defects and impurities, as well as interdiffusion of elements at the heterojunction, is mediated by cation vacancies. In order to identify the most stable defects inside CZTS, and the influence of these defects on p-type conductivity, formation energies and diffusion barriers have been calculated. The Cu vacancy has the lowest diffusion barrier and formation energy compared with other native cation vacancies defects, and is therefore of importance for both doping and the intermixing of phases.

In CZTS/(ZnS or CdS) [100]-oriented heterojunctions with cubic ZnS or CdS there are two types of process, depending upon whether the vacancy originates in the CZTS or the other material. Due to the valence-band-offset between these materials charge transfer across the interface modifies the energetics of formation and motion of cation vacancies, due to the Coulombic attraction between valence band holes in the CZTS and an ionised acceptor in the buffer layer. Furthermore, it has been found that the larger lattice misfit between CZTS and CdS relative to at the CZTS-ZnS interface results in a significant an isotropy in the diffusion of cation vacancies in the CdS later.

In summary, through a combination of the simulation of thermodynamic and kinetic processes, it is possible to investigate quantitatively the role and potential impact of key defects involved in the doping and intermixing of heterostructure devices for CZTS-based thin-film PV.

Contents

Glossaries

Acronyms and abbreviations

BZ	Brillouin zone
CB	Conduction band
CBM	Conduction band minimum
CBO	Conduction band offset
CBS	Unoccupied electronic states
CL-NEB	Climbing image nudged elastic band
CZTS	Cu_2ZnSnS_4
DFT	Density functional theory
GGA	Generalised gradient approximation
HF	Hartree-Fock
k-point	A point in k-space
KS	Kohn-Sham
LDA	Local density approximation
MEP	Minimum energy path
MP	Monkhorst-Pack
PBE	Perdew, Burke and Ernzerhof
PV	Photovoltaic
ST	Stannite
VB	Valance band
VBM	Valance band maximum
VBO	Valence band offset
VBS	Occupied electronic states
WZ	Wurtzite
ZB	Zinc-blende

Glossaries

Glossary of mathematical notation

χ_S	Electron affinity
E^a	Activation energy
E_A	Accepter level
E^b	Binding energy
E_F	Fermi level
E^f	Formation energy
E^{for}	Forward migration barrier
η	Solar cell efficiency
FF	Fill factor
H_f	Formation enthalpy
hν	Photon energy
I	Solar cell output current
I_D	Diode current
I_L	light generated current
I_{mpp}	Maximum power point current
I_{SC}	Short circuit current
k	Wave vector
μ_e	Electron chemical potential
P_{in}	Input power
P_{max}	Maximum power
P_{out}	Output power
Φ_m	Metal work function
Φ_S	Semiconductor work function
R_S	Series resistance
V	Voltage across the output terminals
V_{OC}	Open circuit voltage
V_{mpp}	Maximum power point voltage

LIST OF FIGURES

LIST OF TABLES

Chapter 1

Introduction

1.1 Background

Most of the current global energy is produced from non-renewable, traditional sources of energy [1]. Carbon-based sources including burning coal, oil and gas, are among the most important sources of pollution. The greenhouse gas CO_2 is involved in global climate change, since the concentration of this gas is over 400 parts per million (ppm) today [2, 3], and the range for this gas was from 210-300 ppm for the 650,000 years before the industrial revolution [4, 5]. In addition, fossil fuels are a limited resource. Renewable energy sources such as wind, hydroelectricity and solar energy have become the most developed solutions to get clean energy, although one has to also factor in the manufacturing processes for these low-carbon energy generation methods [1, 6]. Due to the rapid increase in population [7], the consumption of energy worldwide is expected to grow from 16.2TW in 2007 to more than 30TW in 2050.

A significant source of renewable energy is solar energy. It is sustainable, abundantly available and environmental friendly [1]. Solar energy is converted into the main type's of heat and electricity by solar energy and photovoltaic, respectively [1]. Solar thermal energy collectors convert solar radiation into thermal energy through solar panels, absorb the incoming solar radiation and transport it to heat using a fluid, such as air, water or oil. A solar cell is basically a p-n junction diode of two semiconductor materials with different doping types and it converts sunlight energy into electricity through the photovoltaic effect. The first observed use of the photovoltaic effect was in 1839 by the French scientist Alexander-Edmond Becquerel [8, 9]. He found an electric current produced between two electrodes immersed in an electrolyte when one of these electrodes was illuminated with light [9, 10]. In 1941, Russell Ohl developed the first semiconductor p-n junction based on silicon crystal [11-14].

Although the extent of global solar radiation power on the earth is 125,000TW which is ten times greater than the world energy demand [15, 16], in practice, the actual power estimated to reach the surface of the earth is approximately 600TW. Therefore, if the conversion efficiency of a solar cell is 10%, the produced power would be about 60TW which is still nearly double the predicted energy consumption in 2050 [17-19]. More than $80 billion is being invested in the United States specifically to decrease the emission of greenhouse gases by 28% by 2020 [6]. In 2008, renewable energy approached 19% of the global energy consumed, which was a significant increase from 13% in 2003 [6]. The aim of the European Union (EU) is that, by 2020, renewable energy will contribute 20% of the total energy consumed [6]. The total capacity of solar cells installed globally has increased steeply, as shown in Fig. 1.1. The key strategies used to develop sustainable energy resources [20] are saving energy by reducing energy consumption, in addition to improving efficiency and using renewable energy to reduce greenhouse gas emission.

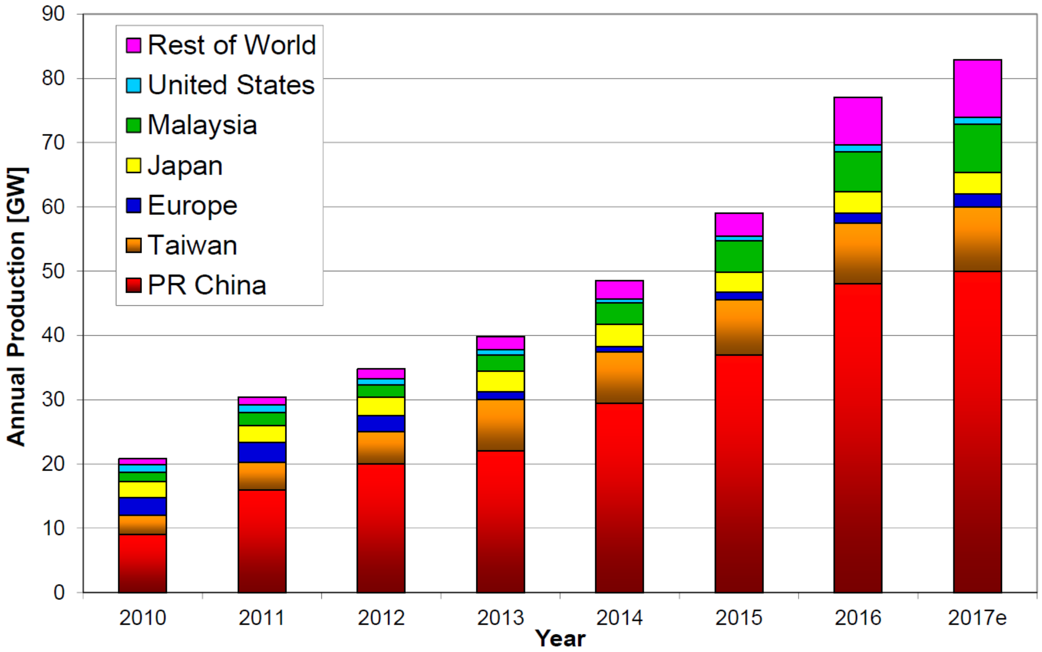

Figure 1. 1: The total solar cell capacity installed globally from 2010 to estimated figures for 2017; from top to bottom: China, Taiwan, Europe, Japan, Malaysia, United States and the rest of the world (graph adapted from Ref. [21]).

Today, one of the main issues photovoltaic (PV) technology faces is cost, and thus research has become focused on producing solar cells that are relatively low in cost and high in conversion efficiency [22]. Materials used in the composition of solar cells play a key role in determining both the cost and efficiency. Traditional solar cells are made from mono-crystalline silicon (c-Si). This has the advantage of being made up from an abundant, non-toxic material exhibiting long-term stability and relatively high efficiency [23]. However, it is expensive and has an indirect band gap (1.12eV at R.T.) which is not optimal for solar cell efficiency, because it causes a reduction in the absorption coefficient [24] and requires a thick layer. The optimum bandgap energy for a high efficiency solar cell [25] is in the range of 1.3-1.6 eV according to the Shockley-Queisser limit for the single pn-junction semiconductor in 1961 [26]. William Shockley and Hans-Joachim Queisser calculated the maximum theoretical conversion efficiency for a p-n junction as a function of the semiconductor band gap to collect power from the cell. The limit of this theory is based on the detailed balance principle for which photon flux into and out of a device is equal [27]. The incident sun spectrum is approximated as a black body emission with a surface temperature of 6000K [28]. The maximum limit for solar conversion efficiency is about 33.16% that occurs for the single pn-junction with a band gap of about 1.34eV [28]. The limit is only applied on solar cells with a single junction; solar cells with multiple junctions can exceed this limit.

Although crystalline silicon has excellent efficiency and long-term stability, it is costly. Therefore, to solve the economic issue, thin film solar cells are used as a better option to replace silicon for large-scale applications [29]. Thin film solar cells are employed as a second generation in manufacturing solar cells. Thin film technologies reduce the required material amount to create the active material for the solar cell, since thin film material commonly has a high absorption coefficient compared with crystalline materials. Thin film materials can be deposited on a low-cost layer including glass or plastic. The manufacturing process is faster, easier and cheaper than crystalline silicon [30]. Based on this technology, the solar cell is light, low cost and can be deposited on a large area.

Polycrystalline silicon PV is less expensive but, at the same time, less efficient, partly due to the crystallinity, but also due to higher levels of impurities that act as recombination centres for the electrons and holes [23]. Amorphous silicon (a-Si) is a non-crystalline silicon. It has a direct band gap with a high optical absorption coefficient for sunlight; therefore, only a thin layer is enough to produce a solar cell [31, 32]. It can be deposited on glass or plastic; therefore, it can be flexible [31]. However, it is less efficient than single- and polycrystalline solutions and has relatively high manufacturing costs [33] because of light-induced degradation due to impurities in a-Si such as nitrogen oxygen and hydrogen [34].

Organic photovoltaic materials (OPV) are suitable for some applications, particularly because they are characterised by a flexible thin film, and OPV has many advantages, such as low cost (material, processing), light, semitransparency and flexibility, but they have relatively low efficiency [35].

A competing class of materials used is made up of binary II-VI semiconductors, such as cadmium telluride (CdTe) thin films, and these kinds of solar cells have a low cost compared with single crystal silicon. CdTe has a direct band gap of about 1.44eV; it is suitable as an absorber material [36], as shown in Fig. 1.2. However, Cd is toxic and Te rare is and toxic. Although CdTe is considered cheaper than single crystal silicon, it remains relatively expensive [22, 37].

Subsequently, ternary I-III-VI_2 semiconductors such as copper indium gallium selenide $Cu(In,Ga)S_2$ (CIGS) are considered a viable alternative to CdTe. Such materials are non-toxic, but the cost of solar cells remains relatively high, because of the cost of In and Ga [38]. Chalcopyrite CIGS has stability in large area modules and that enhances the commercialisation of this cell [39]. CuInSe has low bandgap of about 1.2eV, whereas adding an amount of Ga to this compound improves the bandgap by making the bandgap bigger and close to the optimum bandgap value [36]. As the Ga increases, the bandgap will also increase, as shown in Fig. 1.2. Therefore, the CIGSe bandgap depends on controlling the ratio of In and Ga.

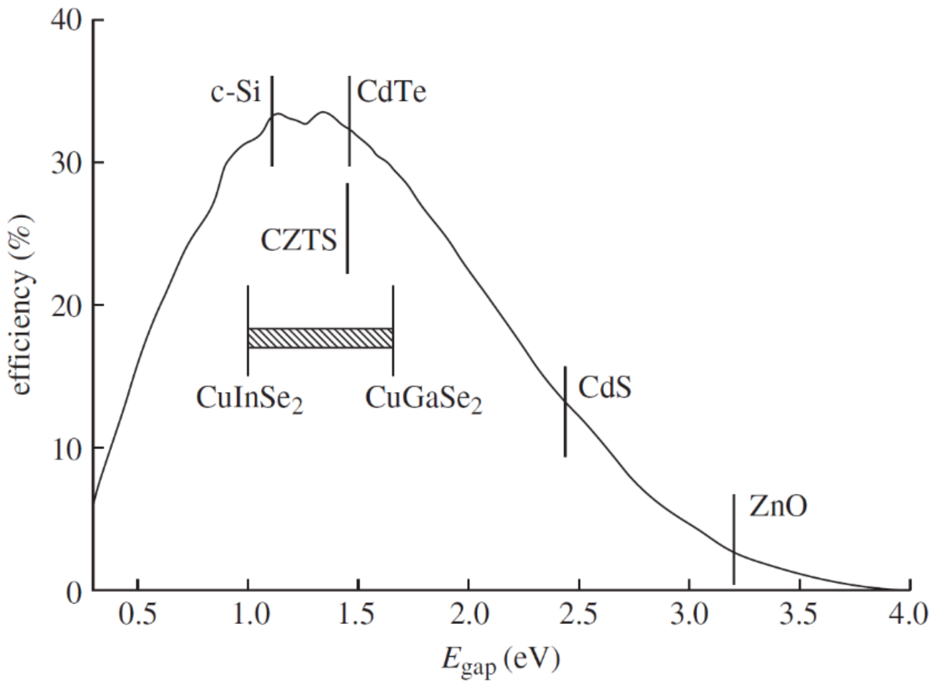

Figure 1. 2: Highest theoretical efficiency according to Shockley-Queisser limit for absorber (c-Si, CdTe, CIGS, CZTS) and window (CdS, ZnO) solar cells materials (graph taken from Ref. [36]).

Quaternary semiconductors of the I_2-II-IV-VI_4 family, including CZTS (Cu_2ZnSnS_4) and CZTSe [40], have features which make them well-placed to replace silicon, binary and ternary semiconductors in PV. In these cells, the costly indium is replaced by zinc. They are non-toxic, have a high absorption coefficient, and have direct band gaps of about 1.0 to1.5eV; therefore, the electron can transfer from the valence band to the conduction band without a change in momentum [39, 41]. They are low-cost (both in processing and materials) and are made up from earth-abundant elements, as shown in Fig. 1.3. According to Fig. 1.3, indium has the highest cost compared to other elements; in addition to gallium, telluride and selenium have a relatively low cost. Moreover, gallium, indium, telluride and selenium are rare elements compered to others, whereas sulphur, copper, zinc, tin and cadmium are cheaper than other elements and, at the same time, they are more abundant.

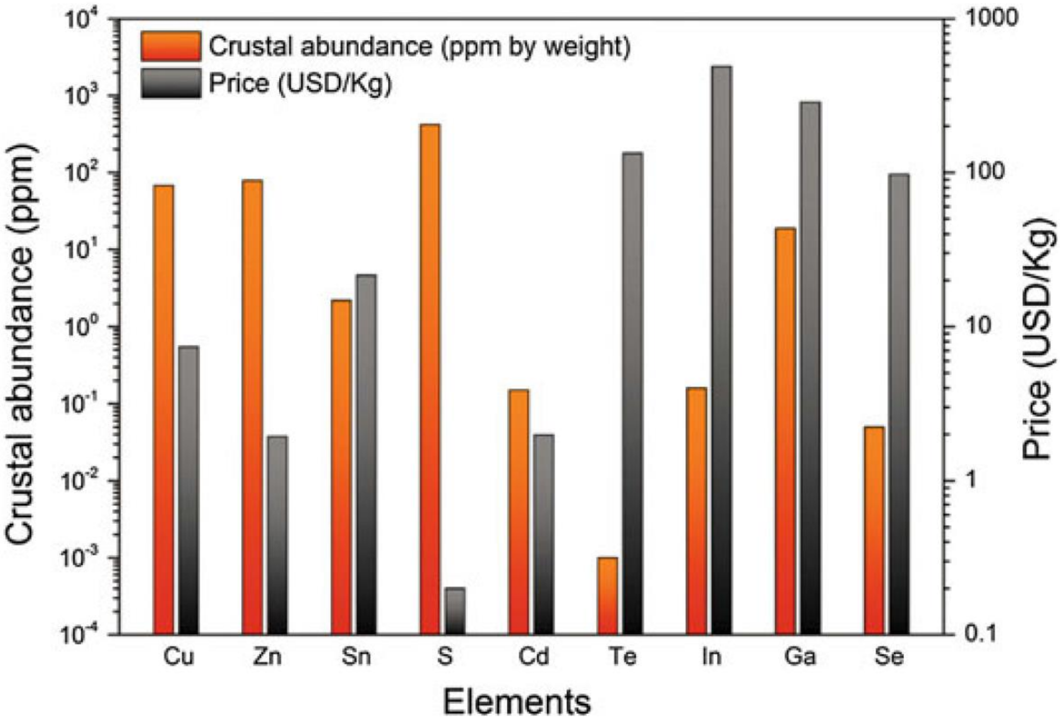

Figure 1.3: Relationship between price ($ per kg) and crustal abundance (ppm by weight) of elements (graph taken from Ref. [42] in 2016).

The experimental efficiency of the CZTSe at 12.6% is lower than that of the CdTe and CIGS which are 20.4% and 20.9%, respectively [43]. The conversion efficiency is based on the growth condition, crystalline quality, carrier concentration and the nature of the p-n junction [44].

1.2 Photovoltaic effect

Solar energy has significantly positive characteristics. For instance, it has a high capacity, has an effectively permanent source (the sun) and can be categorised as generating clean energy. At its most basic, a photovoltaic effect converts the sunlight directly into electricity energy and this is considered the basis of solar cell work [1, 45]. The terms photo and voltaic mean light and electricity, respectively. The conversion of light into electricity involves the generation of the charge carriers (e-h) by absorption of light, followed by separation of these charge carriers by an internal electric field, and finally the collection in an external circuit that represents a load [1].

1.2.1 Solar cell working principle

A solar cell is made up of junction of p-type (excess holes) and n-type (excess electrons) semiconductors of the same or different materials. The electrons near the interface diffuse from n-type into p-type and leave a positive charged ion in the n-side region and, similarly, the holes in the p-type region near the interface diffuse into n-type leaving a negative charged ion in the p-side region. The charged regions are called a space charge region (depletion region), since a net positive and negative charge density appear on the n- and p-type, respectively; therefore, the majority carriers are depleted [46]. An electric field is generated pointing from n- to p-type as a result of the charge densities on both sides of the interface. Due to the electric field, the electron (hole) drift current is generated in the opposite direction to the diffusion current of electrons (hole), respectively. The electric field increases as the electron and holes diffuse more until the electron and hole drift current becomes precisely equal and opposite to the electron and holes diffusion current. Therefore the junction is in equilibrium and the Fermi level is flat and constant through the junction when the external voltage is absent, as shown in Fig. 1.4. As a relevant example in CZTS thin film device, the absorber layer is CZTS and the n-type buffer layer might be CdS or ZnS.

However, when the light falls on the p-n junction [46], the photons with energy equal to or higher than the band gap of the semiconductor may be absorbed. The light absorption depends on the absorption coefficient and the film thickness [47]. Some valence electron become excited by these photons and create photo-generated electron-hole pairs which are separated by the electric field within the space charge region. The separated electrons and holes which are driven by the electric field are transferred to the conduction band (CB) of the n-type semiconductor and the valence band (VB) of the p-type semiconductor, respectively. The photocurrent is generated from the movement of these electrons and holes.

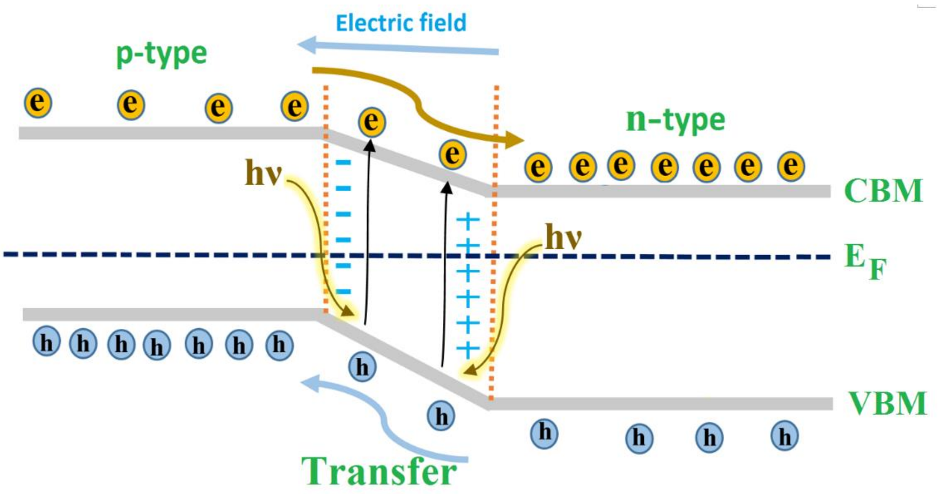

Figure 1.4: Schematic band structure for p-n junction solar cell. CBM and VBM: the conduction band minimum and valence band maximum, respectively. E_F: Fermi level and hν: energy per photon.

1.2.2 Basic thin film solar cell structure

A module of a basic thin film solar cell may consist of five layers: substrate, front contact, buffer layer, absorber layer and back contact, as shown in Fig. 1.5. Each layer [48] might have a different crystal structure, lattice constant, work function and carrier mobility. Therefore, these could produce stress, defects, interface states, surface recombination centres and inter-diffusion which will affect the efficiency and the life spans of the device.

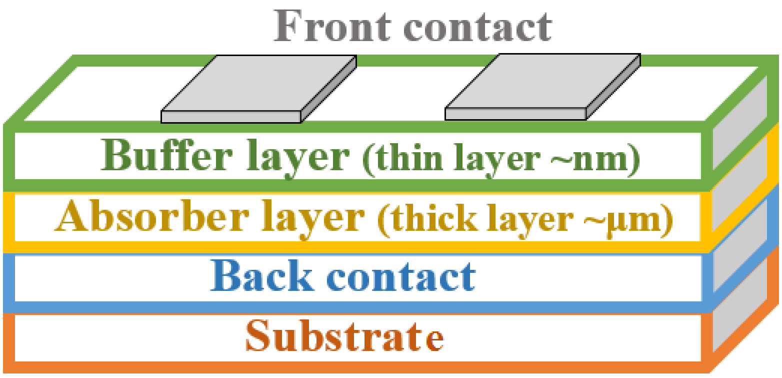

Figure 1.5: Schematic structure of basic solar cell

1.2.2.1 Substrate

The function of this layer is to provide mechanical support and carry the solar cell layers on it. The substrate in the solar cell is usually made up of glass such as soda-lime glass, metal as a conductor such as glass coated with Pt, and metal foil or plastic for flexibility, such as stainless steel or polymer, respectively. A conductive glass substrate is an excellent conductor; however, glass has shape limitations, fragility and is expensive [49]. Metal foil is flexible, inexpensive and lightweight with good electrical and thermal conductivities [49]. In addition, plastic substrate is flexible, low cost, light-weight and thinner; however, it is used only for applications requiring a low temperature because of its low heat resistance and the fact that it is difficult to handle because it bends [50-52].

1.2.2.2 Front contact

Transparent conducting oxide (TCO) is usually used as a front contact in solar cells, such as zinc oxide ZnO, indium tin oxide In_2O_3Sn (ITO) and fluorine-doped tin oxide SnO_2:F (FTO). TCO materials are transparent for most of the incident visible light. The TCO top layer is required to have high optical transparency; it should be a wide band gap semiconductor of more than 3eV. In addition, it should have low resistivity; the sheet resistivity should be less than $10\Omega/cm^2$ (specific area resistance).

1.2.2.3 Buffer layer

The main function of a buffer layer is to form a pn-junction with the absorber layer. In addition, the buffer layer should be able to allow the maximum amount of light to reach the junction and has less absorption and recombination loss with minimum resistance. In general, n-type material used as a buffer layer includes CdS, ZnS and In_2S_3. Doping density in the buffer layer should be more than that of the absorber layer to limit the depletion region at the absorber because the charge carriers are separated by its electric field [24]. The buffer layer is required to have a wide band gap for maximum transmission in the solar spectrum visible region. Furthermore, the lattice mismatch and the band offset alignment should be near to zero to reduce the dislocation and carrier traps at the junction.

1.2.2.4 Absorber layer

In this layer, the light absorption take place and the semiconductor absorber material should have a direct band gap (around 1.5eV) [24] since it has a high absorption coefficient. Thin film solar cell performance is based on the absorber layer, since absorbed light and the generated carriers occur in this layer. Therefore, this layer is the vital part of the solar cell. A p-type semiconductor is usually used as an absorber layer including Si, CdTe, CIGS and CZTS. The absorber layer is required to have [24] a direct band gap with a high absorption coefficient of more than $10^4 \mathrm{cm}^{-1}$.

1.2.2.5 Back contact

A metal contact is used as a back contact, such as Al, Ni, Au and Mo. The contact between the metal/semiconductor heterojunction depends on the work functions of the metal and electron affinity of the semiconductor. If the work function of the metal is greater than that of the semiconductor, the contact is ohmic when the semiconductor is p-type, as illustrated in Fig. 1.6, and is a Schottky contact when the semiconductor is n-type [53]. Due to the difference in the work function, a barrier arises between the metal and the semiconductor and that leads to the Schottky contact. The back contact is required to have a good electric contact (ohmic contact with the semiconductor), and it should have a good optical reflection since, when the light is not absorbed by absorber layer and reaches the back contact, it should be reflected back into the absorber.

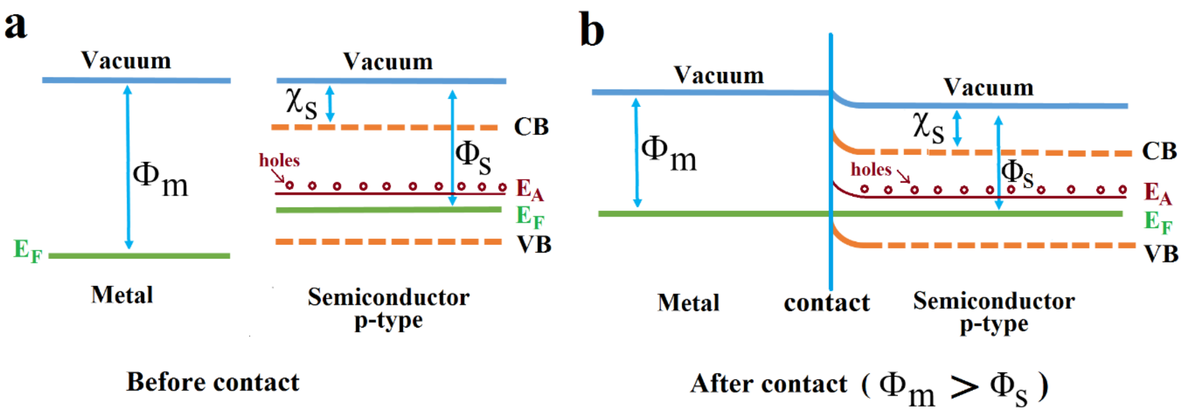

Figure 1.6: Band gap energy between metal and p-type semiconductor (a) before contact, (b) after contact when ($\Phi_m > \Phi_S$) ohmic contact. E_F: Fermi level, CB: conduction band and VB: valence band. Φ_m : metal work function, Φ_S : semiconductor work function and χ_S: electron affinity, E_A: accepter level.

1.2.3 Solar cell parameters

The key parameters for measuring solar cell performance, which depends on the current-voltage (*I*-*V*) characteristics, are shown in Fig. 1.7 below [54].

a. Series resistance R_S

This parameter represents the resistance that prevents the movement of carriers. In the illustrative equivalent circuit in Fig. 1.8, the series resistance is labeled R_S and it is a resistive term which reduces the current. In Fig 1.5, R_S is the resistance dominated by the relevant resistances in driving the current through the device; for example, there is intrinsic resistance of the buffer and absorber layer, and the electrical resistance of the material is ohmic resistance in addition to the fact that there is contact resistance in the buffer and absorber layers. All these types of resistance contribute to R_S. For the ideal solar cell, the series resistance is equal to zero (R_S=0). The following reasons could cause high R_S: (i) low conductivity of the buffer or absorber layer; (ii) non-ohmic contacts between the metal contacts and the semiconductor; and (iii) recombination processes of the carriers within the energy gap.

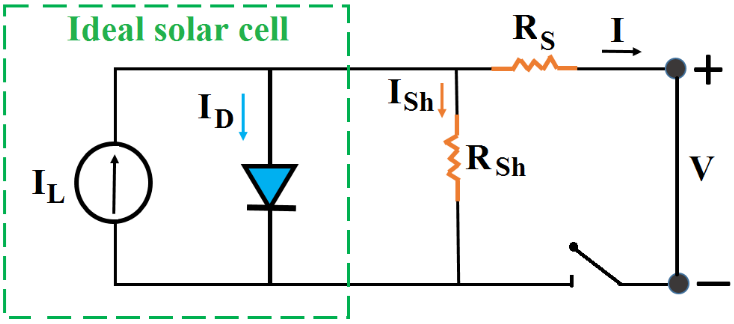

Figure 1. 7: Equivalent circuit of practical solar cell. I_L is the light generated current and I_D is the diode current. I_{Sh} and R_{Sh} are the shunt current and the shunt resistance, respectively and R_S is the series resistance. I is the solar cell output current and V is the voltage across the output terminals.

b. Shunt resistance R_{Sh}

The source of this resistance might be surface damage of the layers in addition to manufacturing defects, such as leakage current that results from low resistivity of certain parts, including the grain boundary and secondary phases. For the ideal solar cell, the shunt resistance is equal to infinity (R_{Sh}=∞). However, series resistance from ohmic loss and shunt resistance from leakage current are added to the actual solar cell (non-ideal solar cell) and they affect solar cell performance. In the illustrative equivalent circuit, Fig. 1.7, the shunt resistance is labeled R_{Sh}.

c. Short circuit current I_{SC}

I_{SC} is the current passing through the junction under lighting when there is no load. The quantity is affected by a change in series resistance in the device. For an ideal solar cell, the light generated current I_{L} inside the solar cell and I_{SC} are identical. Therefore, I_{SC} is the maximum current in the solar cell. I_{SC} is based on the solar cell area; therefore, it is common to use short circuit current density (J_{SC} in mA/cm^2) instead of the I_{SC}. In addition, I_{SC} depends directly upon the incident light intensity and, when there is high series resistance (>10Ω/cm^2) in the solar cell, I_{SC} become less than the light generated current.

d. Open circuit voltage V_{OC}

V_{OC} is the voltage across the junction under lighting when the switch in Fig. 1.7 is open. V_{OC} is the potential difference between the top and bottom contact when the device is not loaded and is under illumination. V_{OC} depends mainly upon the saturation current of the solar cell, which is based on recombination in the solar cell. Therefore, V_{OC} is a measure of the recombination in the device. This amount is not affected by the change of series resistance since at V_{OC} there is no flow of current, but it is sensitive to the changing shunt resistance in the device. V_{OC} increases with increases in the band gap, whereas I_{SC} decreases as the bandgap increases.

e. Fill factor FF

FF is defined as the ratio of the maximum power ($P_{\mathrm{max}} = I_{\mathrm{mpp}} V_{\mathrm{mpp}}$) generated by the solar cell to the product of V_{OC} and I_{SC}, as in Eq. 1.1 [55]. In ideal solar cells, the value of the FF is equal to one, where I_{mpp} and V_{mpp} are maximum power point current and maximum power point voltage, respectively.

$$\mathrm{FF} = \frac{I_{\mathrm{mpp}} V_{\mathrm{mpp}}}{I_{\mathrm{SC}} V_{\mathrm{OC}}} \qquad 1.1$$

Graphically, the fill factor is a measure of the *I-V* solar cell characterises, as shown in Fig. 1.8, where area A refers to the secureness of the *I-V* for the working solar cell and area B refers to the secureness of the *I-V* for the ideal solar cell; the ratio between them represents the FF.

$$\mathrm{FF} = \frac{\text{area A}}{\text{area B}} \qquad 1.2$$

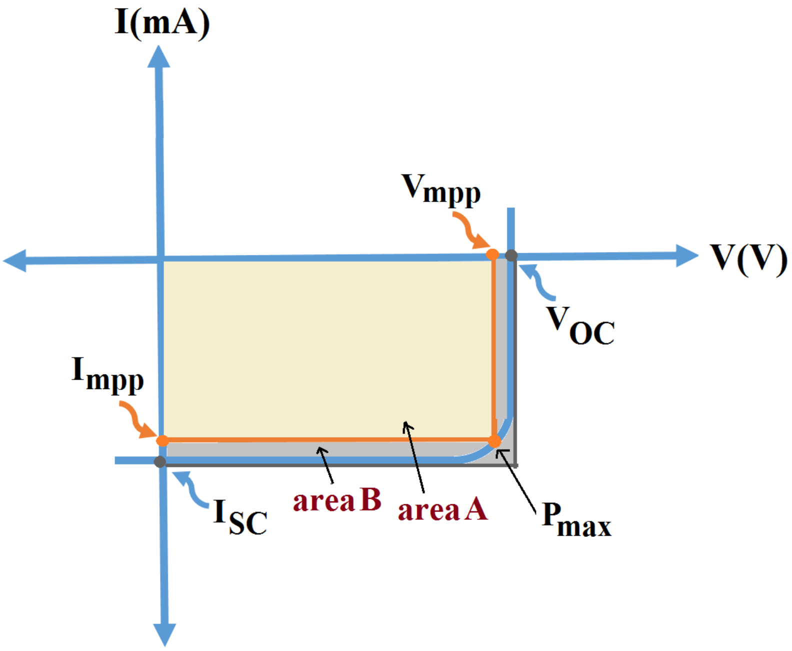

Figure 1. 8: I-V solar cell characteristics. I_{mpp} and V_{mpp} are maximum power point current and maximum power point voltage, respectively and P_{max} is the maximum power. V_{OC} is the open circuit voltage and the short circuit current is I_{SC}.

f. Efficiency η

The efficiency of the solar cell is defined as the ratio of the output power (P_{out}) generated by the solar cell to input power from the sun (sunlight), as in Eq. 1.4 [4].

$$\eta = \frac{P_{\text{out}}}{P_{\text{in}}} \qquad 1.4$$

This parameter is usually used for comparing the performance of one solar cell with another. The efficiency mainly depends upon the incident sunlight and the temperature of the solar cell. The performance of the solar cell usually decreases as the temperature increases because the internal carrier recombination rates are increased, due to increased carrier concentrations [56]. In addition, the life time is another critical source which affects efficiency. The life time is the average time spent by minority carriers in the excited state after an electron hole is generated by light before they recombine. The life time in the semiconductor materials depends on the recombination rate which is controlled by the concentration of minority carriers and crystal quality including secondary phases. The recombination rate will be zero when there is no excess for the minority carrier. Therefore, when the life time of the minority carriers is long, the solar cell generally will be more efficient.

Moreover, predicting efficiency changes over time plays an important role in the growth of the solar cell industry. Therefore, knowing the degradation rate of the solar cell is important for determining the power delivery over time [57]. A high degradation rate leads to the production of less power. The common reasons for degradation are light intensity, humidity and temperature [58]. In general, efficiency is based on temperature dependence, transmission, reflected loss, resistance loss and recombination due to traps.

Although some materials have a higher efficiency than others, there are other essential factors that should be taken into consideration including large-area, low cost and toxicity, which are important for commercial photovoltaic devices. Therefore, compromises between these factors and performance should be taken into account for the solar cell to be commercialised.

In addition to these essential parameters which affect the solar cell efficiency, when the solar cell is a hetero-structure, the band offset has a role to play as explained in the next section.

1.3 Band offset alignment

The band offset at the hetero-interface describes the difference in the energy band gap across the interface. The absolute magnitude of mismatch of the conduction band minimum (valence band maximum) of the two materials is called the conduction band offset (CBO) and the valence band offset (VBO), respectively [59]. The different physical and chemical properties of interfacial layers often cause unfavourable band alignment and interfacial states that lead to a high carrier recombination and eventually result in lower device efficiency [59]. In a hetero-structure, the electrical properties of the junction strongly depend on the energy band alignment at the interface of the two different semiconducting materials [60]. However, the band offset alignment commonly forms between the buffer layer or secondary phase and the absorber layer. This band alignment depends on whether the band gap of the buffer layer or the secondary phase is greater or smaller than that of the absorber layer. In general, the alignment of the conduction and valence bands of two semiconductors is classified into three types [61]. The optimum solar cell performance usually requires no potential barrier at the junction, but in the heterojunction solar cell, commonly, there is a band offset at the interface. There is a wide variety in potential band offset, but there are specific operational reasons why particular types of band offset are more desirable for solar cells than others and this is reviewed in this section.

1.3.1 The straddled alignment band offset

The band offset energy of the straddled is referred to as type one band alignment. In general, for type one heterojunctions, the CBM and the VBM of the narrow band gap semiconductor are located within the band gap of the wide band gap semiconductor.

In this case, the band gap of the buffer layer is bigger than that of the absorber layer. The CBM of the p-type absorber layer lies below that of the buffer layer and the VBM of the absorber layer is located higher than the buffer layer; both the CBM and VBM are located outside the band gap of the absorber layer [59], as shown in Fig. 1.9 (a). Therefore, the CBO is positive and it is often referred to as spike-like band offset alignment. The spike-like alignment acts as the barrier against photo-generated electrons in the heterojunction [59, 62], and a large potential barrier could prevent the flow of electrons from the absorber to buffer layer and this leads to high carrier losses [59].

The variation in solar cell parameters is a function of the CBO [62]. It is found that a maximum barrier of the CBO of the buffer layer which does not significantly affect the cell efficiency is a little positive in the range of (0-0.4) eV. The position of the buffer layer CBM prefer to be slightly higher than that of the absorber layer in the range of (0- 0.4) eV [62, 63]. When the spike in the CBO is about 0.4eV, the photo-generated electrons can cross over this relatively small barrier; therefore, the *J*sc and FF are nearly constant [62]. When the spike becomes over 0.4eV, it acts as a considerable barrier for electrons [60, 62]. The large electron barrier at the hetero-interface against photo-generated electrons leads to decreases in the *J*sc and the FF [62]. The photo-generated electrons flowing from the absorber towards the buffer layer are blocked by the large barrier. However, V_{OC} is approximately stable and this is due to the fact that the barrier against injected electrons causing recombination between majority carriers at the interface has not been formed [62]. The band offset become a barrier for both the minority and majority carriers in the absorber layer [64]. Then, the buffer layer simply reduces the conductivity but does not enhance the carrier recombination rate in the absorber layer [64]. For example, the CBO of the ZnS secondary phase inside CZTS is about 1.3eV [65]; therefore, such a large spike will create a high resistance barrier to carrier flows. Thus, the ZnS phase may hinder the flow of photo-excited carriers (electrons), reducing the photo current, impeding the flow of majority carriers (holes), and increasing the series resistance [64].

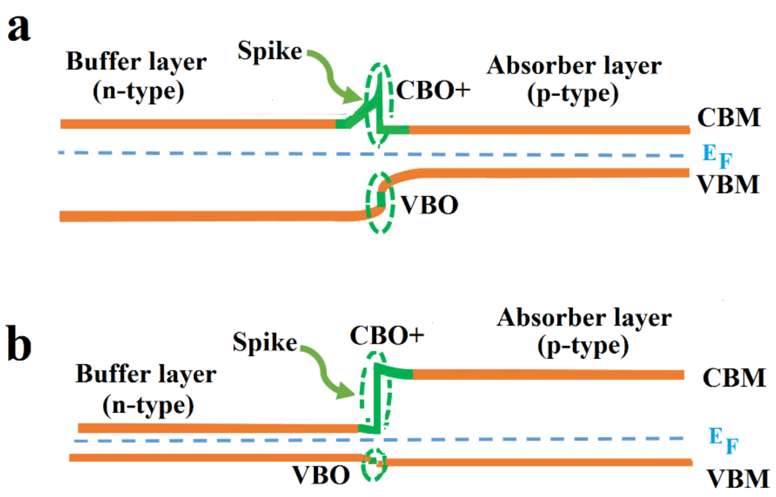

Figure 1. 9: Schematic electronic structure for heterojunction band offset types of straddled band lineups between p-type semiconductor (absorber layer) and n-type semiconductor (buffer layer). CBM: conduction band minimum, VBM: valence band maximum, VBO: valence band offset, CBO: conduction band offset and E_F; Fermi level: (a) the band gap of the buffer layer is bigger than that of the absorber layer, (b) the band gap of the buffer layer is smaller than that of absorber layer.

On the other hand, if the band gap of the buffer layer (or the secondary phase) is smaller than that of the absorber layer [64], as shown in Fig. 1.9 (b). The buffer layer or the secondary phase will act as a sink for both the minority and majority carriers and support the carrier recombination [64]. Thus the carrier separation is not easy, and the carrier collection efficiency of the cell would be reduced. Carriers will be trapped within the smaller band gap semiconductor [66]. Therefore, if the small band gap material is the buffer layer (or secondary phase), then carrier separation and collection efficiencies will be reduced.

1.3.2 The staggered band offset alignment

The band offset energy of the staggered is referred to as type two band alignment. In the staggered type two heterojunctions, either the CBM or the VBM of one semiconductor is lying outside the band gap of the other semiconductor [67]. In this case, the CBM of the p-type absorber layer lies higher than the buffer layer and the VBM of the absorber layer is located higher than the buffer layer [59], as shown in Fig. 1.10. Therefore, the CBO is negative and it is often referred to as cliff-like band offset alignment. This cliff acts as the barrier against injected electrons [62]. Due to this barrier, the electron transport gets easier from the absorber to the buffer layer, the trap states is dominant and recombination between majority carriers via defects at the interface occurs [59].

CBO affects the variation of solar cell parameters. V_{OC} and FF decrease with increases in the cliff in the CBO value of more than 0eV due to the recombination between carriers via defects at the interface [62]. However, the barrier against photo-generated electrons is not formed and J_{sc} is nearly constant [62].

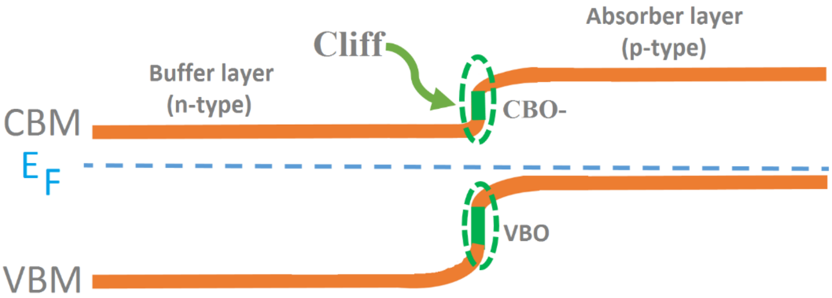

Figure 1. 10: Schematic electronic structure for heterojunction band offset types of staggered band lineups between p-type semiconductor (absorber layer) and n-type semiconductor (buffer layer). CBM: conduction band minimum, VBM: the valence band maximum, VBO: valence band offset, CBO: conduction band offset and E_F: Fermi level.

It has been concluded that the ideal CBO for solar cells is a moderately positive where CBO is between (0-0.4)eV [62, 63], since this prevents losses in open circuit voltage due to a reduction of buffer/absorber interface recombination. Furthermore, this small spike has no negative influence on electron transport and excellent performance can be obtained. Therefore, the slightly positive band offset (spike-like) is important for high device performance.

1.3.3 The broken gap band offset alignment

The band offset energy of the broken gap is also called type two band alignment. The broken gap alignment forms when the line-up of the staggered band is carried to its extreme [61]. In this case, the conduction band minimum of one semiconductor lies below the valence band maximum of the other semiconductor [67], as shown in Fig. 1.11. The electrons and holes are spatially separated at the interface and localised on both sides of the interface; therefore, both of them could be conducting and the electrons and holes coexist in the structure [68]. That leads to the creation of carrier tunnel transitions across the interface. This type of band alignment produces a large band offset [67]. For instance, in an n-type

InAs/ p-type GaSb heterojunction, the VBM of GaSb lines above the CBM of the InAs, and the valence band offset is 0.57eV where the band gap of InAS and GaSb are 0.42 and 0.81eV, respectively [69].

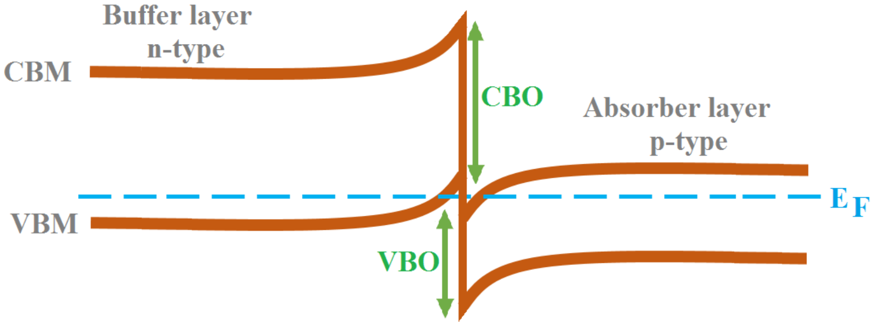

Figure 1. 11: Schematic electronic structure for heterojunction band offset types of broken gap lineups between p-type semiconductor (absorber layer) and n-type semiconductor (buffer layer). CBM: conduction band minimum, VBM: the valence band maximum, VBO: valence band offset, CBO: conduction band offset and E_F: Fermi level.

1.4 CZTS based solar cells

Copper zinc tin sulfide (CZTS), is considered a promising thin film photovoltaic (PV), since it is non-toxic, low-cost, and made up from Earth-abundant elements [70, 71]. CZTS has a direct band gap of about 1.5 eV [72, 73] which is close to the optimum band gap for photovoltaic applications, as shown in Fig. 1.2. The first report identifying the photovoltaic effect of CZTS was by Ito and Nakazawa in 1988 and they studied the electrical and optical properties of CZTS [44, 74, 75]. The first CZTS-based solar cell was reported by Katagiri in 1997 and the conversion efficiency of the device was 0.66% [76-78]; this had increased to 2.63% by 2001 [72]. CZTS is a promising candidate for commercial solar cells [79-81]. As-grown CZTS shows p-type conductivity, most probably due to the shallow acceptor levels of the intrinsic defects, Cu_{Zn} and V_{Cu} [22, 82]. This quaternary semiconductor is favourable for photovoltaic devices since it has a high optical absorption coefficient over $10^4 cm^{-1}$ in the visible wavelength region [83], although a recently reported efficiency of 8.5% remains inefficient compared to other materials such as CIGS with reported efficiencies of over 20% [84]. The theoretical power conversion efficiency is 32% for CZTS solar cells [26, 85, 86]. The huge gap in the conversion efficiency between the experimental data and theoretical predictions might be mainly attributed to a low open circuit voltage [87] and a possible reason of this is disorder among the Cu and Zn cations in the crystal structure.

In addition to this, the stoichiometric lack, bulk complicated nature, surface defects and difficulty in preparing single phase CZTS without secondary phases [88] are all significant.

CZTS is thermodynamically stable in a relatively narrow region of atomic chemical potentials [40, 82], and secondary phases such as ZnS, Cu_2SnS_3 and Cu_2S might become significant contaminants under some growth conditions. However, efficient devices are obtained for Cu-poor/Zn-rich compositions [89, 90], where intrinsic defects (Cu_{Zn} and V_{Cu}) are responsible for the p-type conductivity [89, 90].

Many approaches have been implemented to fabricate the CZTS-based thin film, including chemical path deposition [91], electrodeposition [92], spin-coating [93], co-sputtering [94], spray pyrolysis [95], and thermal evaporation [96].

Recently, research into the properties of CZTS and related compounds has grown dramatically, as shown in Figure 1.12, although the period between the first design of the quaternary semiconductors and their application has been long, since these materials are complicated because of the multiplicity of elements [40]**.**

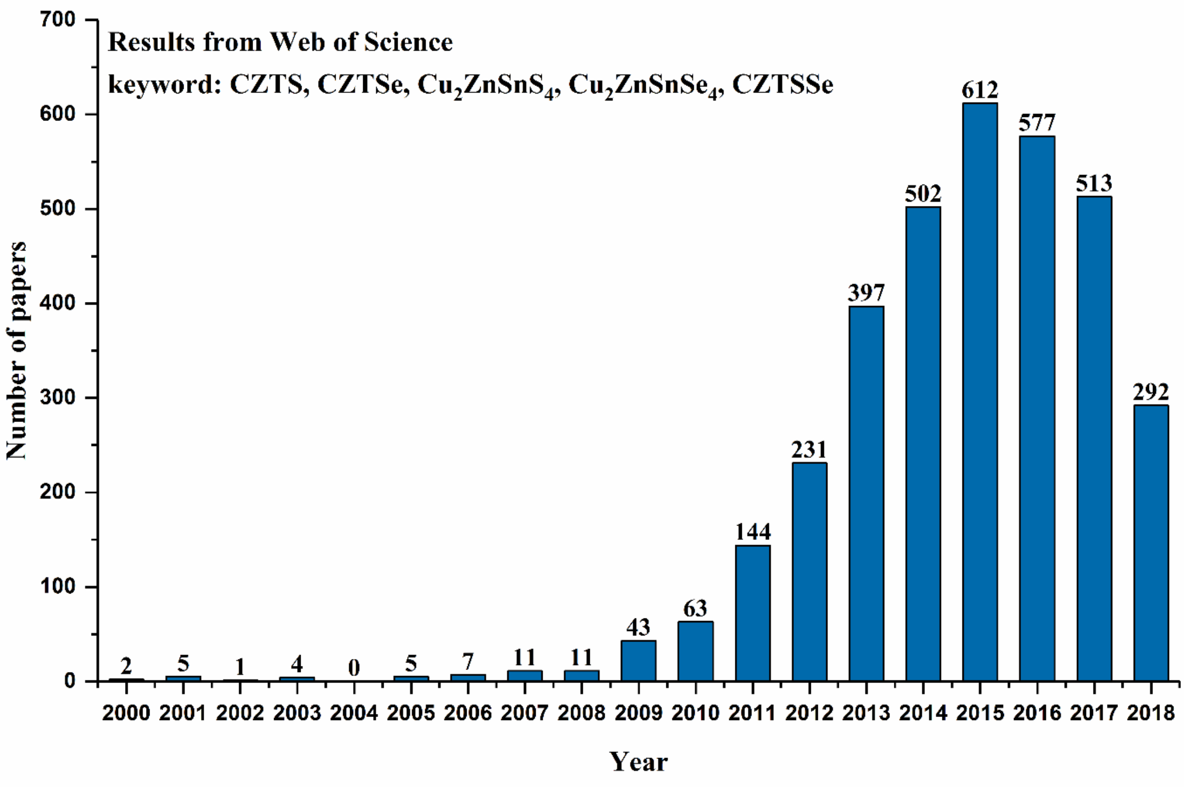

Figure 1. 12: Number of research papers regarding CZTS and related materials during the period from 2000 to 11 July 2018.

1.5 Crystalline structure of CZTS compound

It is agreed that binary II-VI chalcogenide compounds mainly have two crystal structures: zinc-blende (ZB) and wurtzite (WZ). Ternary I-III-VI_2 compounds including chalcopyrite and a CuAu-like structure [97-99] can be taken as derived from a binary zinc-blende by replacing Group II of the binary structure with Groups I and III, whilst the derivation phases of wurtzite binary are wurtzite-chalcopyrite and a wurtzite-CuAu-like structure, as shown in Fig. 1.13.

To obtain the quaternary structure, Group III in both ternary chalcopyrite and CuAu-like structures is replaced by Group II and IV pairs, respectively. The replacement in chalcopyrite provides a tetragonal kesterite crystal structure, whereas the substitution in CuAu-like structures provides a tetragonal stannite crystal structure. The replacement in wurtzite–chalcopyrite and wurtzite- CuAu-like structures provides a monoclinic wurtzite-kesterite crystal structure and pseudo-orthorhombic wurtzite-stannite crystal structure [97-99].

The formation energy for a kesterite structure is smaller than for a stannite structure and these require less formation energy than other structures, whereas the formation energy for a wurtzite-stannite structure is smaller than for a wurtzite-kesterite structure [98]. For the derivation phases of binary zinc-blende [99], the chalcopyrite and kesterite structures represent the stable phase, while the CuAu-like and stannite structures are the metastable phases. The most stable phase of the CZTS is a kesterite structure [98].

Part of the problem is that CZTS in principle may occur in many crystal structures, such as the well-ordered stannite and kesterite phases, which are considered to be more thermodynamically stable than others [43]. The difference in energy between the kesterite and stannite phases is about 2.8 meV/atom [100, 101]. According to this small energy difference, there is partial disorder of the Cu/Zn sub-lattice and it is not stable. The band gap of kesterite is approximately 100 meV larger than that of the stannite; thus, devices comprised of mixed phases would be affected by electronic fluctuations. If the mixed phases are common, a band offset might be formed due to small differences in the band gap between the mixed phases kesterite and stannite. These mixed phases lead to an accumulation of the charge and this could be a source of resistance. Materials, in practice, may be also disordered, with particular issues arising in the Cu and Zn sites [102]. Defects such as missing copper atoms (copper vacancies) are thought to be responsible for the as-grown p-type conduction.

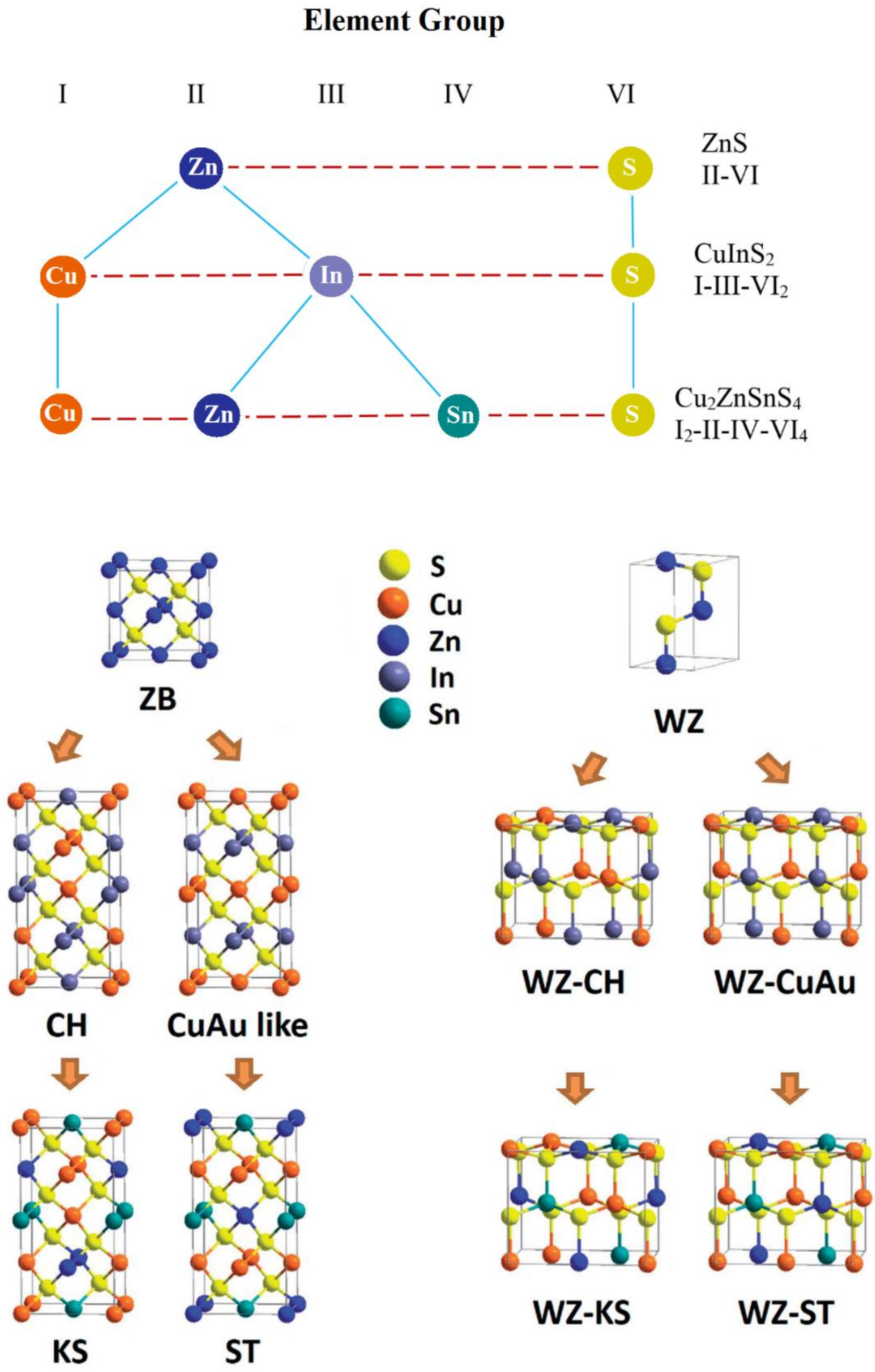

Figure 1. 13: Schematic diagram of the crystal structure of binary ZnS, kesterite (KS), stannite (ST), chalcopyrite and CuAu-Like structural derivation of zinc-blend (ZB), as compared with wurtzite-kesterite (WZ-KS), wurtzite-stannite (WZ-ST), wurtzite-chalcopyrite (WZ-CH) and wurtzite- CuAu-Like (WZ-CuAu) structural derivation of ZnS wurtzite (WZ), (graph adapted from Ref. [99]).

1.6 Key defects in CZTS-based materials

In the kesterite crystal structure [40], the intrinsic lattice defects (vacancies, self-interstitials and antisites) play a significant role in determining the structural, electronic, electrical and optical properties for the absorber layer in a PV module. A high population of intrinsic defects which possess donor and acceptor properties will lead to significant changes in the concentration of carriers, and this will clearly influence electrical conductivity. For CZTS, there are many possible primary native defects to consider, but they may be grouped as follows [40].

a. Vacancies – this means a missing atom, which depending on the atom may be written as V_{Cu}, V_{Zn}, V_{Sn} or V_S.
b. Antisites – these are where one chemical species replaces another, with the key examples being metal atom interchange, i.e. Cu_{Zn}, Zn_{Cu}, Cu_{Sn}, Sn_{Cu}, Zn_{Sn} and Sn_{Zn} where the subscript gives the atom site in the crystal. Antisites involving the group-VI sites are energetically less favourable [40].
c. Interstitials – these are additional atoms which may be located in the space between host atoms, or may be more intimately chemically associated with the crystal (such as split interstitial structures), and are denoted Cu_i, Zn_i, Sn_i and S_i.
d. Native-defect clusters [40] – although there is a huge variety of possible combinations of native defects, some have been identified as more significant than others, including the V_{Cu}+Zn_{Cu}, $2Cu_{Zn}$+Sn_{Zn} and Zn_{Sn}+$2Zn_{Cu}$.
e. Where antisites precipitate, secondary phases may form which include a series of binary and ternary composites, chiefly being ZnS, SnS, SnS_2, CuS, Cu_2S and Cu_2SnS_3.
f. Extended defects including grain boundaries dislocations and stacking faults.

Amongst the defects [40], V_{Cu} and Cu_{Zn} acceptor defects are thought to be responsible for p-type doping; V_{Cu} has the shallower acceptor level and Cu_{Zn} has the lowest formation energy, with Cu_{Sn} considered a key centre for carrier recombination. Although kesterite is typically p-type as-grown, other deep donors such as Sn_{Cu}, Sn_{Zn}, Zn_i and V_S will also influence the performance of a CZTS-based solar cell, since these defects will also act as centres of electron-hole recombination [40]. It is worth noting that the high efficiency of the CZTS occurs under Cu poor and Zn rich conditions, $Cu/(Zn+Sn) \approx 0.8$, so non-stoichiometric materials are key to the understanding and optimisation of CZTS and related materials for PV applications [40].

1.7 Other key efficiency factors

Although material quality and defects are the main focus of this thesis, there are other factors that have a significant impact upon the operation of a PV system, which are listed here for CZTS-based devices.

1.7.1 Back contact/CZTS interface

A commonly used back contact metal is molybdenum (Mo) with CZTS(e) being the absorber layer, but this contact is not an ohmic contact [103-105]. The work function and the electron affinity of the Mo and the CZTS are about 5eV and 4.5eV, respectively [106, 107].The interface between these two materials is thought to be relatively unstable, with the formation of secondary phases, such as $MoS(e)_2$, $Cu_2S(e)$, ZnS(e), SnS(e), and because voids are found at the interface [105, 108]. The non-ohmic contact leads to high series resistance between the Mo contact and the CZTS layer, with a consequent reduction in the current density and FF [103-105].

To improve the efficiency [104], alternative back contact materials might be employed which prevents undesirable interaction (such as intermixing) between the CZTS and electrode as shown in Fig. 1.14. Suggested materials include titanium nitride (TiN), titanium diboride (TiB_2) and zinc oxide (ZnO), with the back contact layer introduced between the absorber and electrode as shown in Figure 1.14. For example, there is an efficiency increase from 1.13% to 4.3% when a 10nm layer of ZnO is used, chiefly because of the reduction in R_s from 19.7 $\Omega\mathrm{cm}^2$ to 15.1 $\Omega\mathrm{cm}^2$ and increase in the shunt resistance from 152 $\Omega\mathrm{cm}^2$ to 1630 $\Omega\mathrm{cm}^2$ [109]. 70nm of TiB_2 may be effective because it reduces the R_s, but is more efficient from 22.0 $\Omega\mathrm{cm}^2$ to 10.9 $\Omega\mathrm{cm}^2$, with efficiency increasing from 3.06% to 4.20% [110]. Alternative back contact Au is used instead of Mo and the efficiency increases from 1.05% to 1.95% whereas the R_s reduces from 10 $\Omega\mathrm{cm}^2$ to 2.5 $\Omega\mathrm{cm}^2$ [111].

For a CZTSe cell, the efficiency increases from 2.5% to 6.0% when a 10nm layer of ZnO is used, chiefly because of the reduction in R_s from $2-3\ \Omega cm^2$ to 0.5 $\Omega\mathrm{cm}^2$ [104]. 100nm of TiN may be effective because it reduces the barrier height between Mo and CZTS from

135±8 meV to 15±3 meV, again reducing R_s, but more modestly from 1.3 Ωcm^2 to 0.9 Ωcm^2, with a small efficiency increase from 7.5% to 8.8% [105].

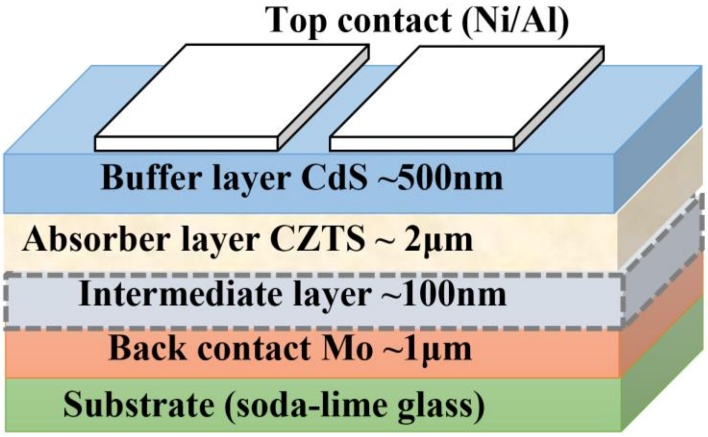

Figure 1. 14: Schematic structure of typical CZTS solar cell

1.7.2 Buffer layer/ CZTS interface

CdS is currently generally [112, 113] used as a buffer layer in this kind of cell (such as is illustrated in Figure 1.14). ZnS is also used as an alternative buffer layer to replace CdS [114] due to the toxicity of cadmium. ZnS has a good lattice-match with CZTS(e) [112].

Assuming CdS or ZnS are in zinc-blende phases grown on the tetragonal kesterite phase of CZTS ($a = 5.448$Å) [115], the lattice misfit in (001)-planar between CZTS and the ZnS ($a = 5.418$) is small, at about 0.5%, while the lattice mismatch is much larger at 7% between CdS ($a = 5.879$Å) [65].

Turning to the electronic structure [116, 117], the key parameters arising from the difference in band-gaps are the valence band offset (VBO) and conduction band offset (CBO) at the interface between the buffer layer and CZTS(e). Table 1.1 shows the band offset between the CZTS absorber layer and the buffer layer ZnS or CdS; the differences in these results are based on the orientation and growth conditions. These alignments have a dramatic impact on the charge transport across the heterojunction interface. In this case, the value of CBO is small and positive and the open circuit voltage is high. When the CBO spike is small enough, electrons can transfer from CZTSe to the buffer layer, and recombination in the interface is reduced [117]. The best performance for a solar cell occurs [116] when (0.0 eV $\leq \Delta Ec \leq$ 0.4 eV). The CBO and VBO in the CdS/CZTSe are approximately equal to 0.34 eV and 0.93eV, respectively. The band offset with spike-like has more effieciency than that of cliff-like [118] because of reducing recompenation [119].

Table 1. 1 : Illustration of the band offset alignment between the CZTS absorber layer and different buffer layers, CdS and ZnS. All the numbers are in eV.

Interface	CBO	VBO	Nature of band alignment	Ref.
CZTS/CdS	0.26	0.74	Cliff-like	[120]
CZTS/CdS	0.13	0.98	Cliff-like	[121]
CZTS/CdS	0.18	0.57	Spike-like	[65]
CZTS/ZnS	1.36	0.92	Spike-like	[65]
CZTS/ZnS	0.86	-	Spike-like	[89]

1.8 Thesis objectives

Electronic, electrical, thermodynamic and structural properties of materials, interfaces and defects have been studied using computational methods, primarily using first-principle density functional theory (DFT) [122], which represents an essentially quantum-mechanical treatment of the electronic part of the materials systems [22].

1.8.1 Modelling CZTS (Chapter 4)

a. Bulk CZTS

The key crystal system will be modelled, and random stoichiometric arrangements (where the Cu:Zn:Sn ratio is fixed but their locations are random, and Zn-rich phases have been guided by experimental observation. The analysis in each case will specifically include:

- The electronic structure via band structures and electronic densities of states
- The lattice constants and other geometrical factors such as bond lengths and angles

In all cases, the data generated will be compared with available experimental and theoretical data from the literature.

b. Native defects of CZTS

Defects critical for electrical properties will be analysed and calculated properties will be compared with the literature. Key properties include:

- Electronic structure: to calculate the band structure of defects to identify the introduction of gap states
- Electrical level (donor and accepter): this differs from the electronic structure as it involves a change of charge state, and is essentially a thermodynamic property

- Formation energy: this amounts to an estimate of the low temperature free energy of formation of the defects, allowing, in absolute terms, the identification of the dominant defects under different growth conditions
- Kinetics: calculation of the activation energies for migration, including the antisites, substitutions and vacancies

1.8.2 Modelling ZnS and CdS (Chapter 5 and 7)

a. Bulk cubic and strained ZnS and CdS

Buffer layers ZnS and CdS will be modelled. Strained ZnS and CdS have been modelled to build an epitaxial interface between the buffer and the absorber layer. The analysis includes:

- Lattice constants, bond lengths and angles
- The strain in ZnS and CdS

b. Native defects of bulk cubic and strained ZnS and CdS

Antisites, substitutions and vacancy defects in buffer layers ZnS and CdS will be modelled. The analysis will include:

- Formation energy
- Kinetics

1.8.5 Modelling semiconductor hetero-structure interfaces, particularly CdS/CZTS and ZnS/CZTS (Chapter 6 and 8)

- Initially ideal interfaces have been modelled, with particular reference to the band-structure to extract band-offsets, interfacial strain and gap state formation.
- Intermixing between the materials will then be examined to determine the impact upon the ideal interface properties.

Chapter 2

Theoretical Background and the AIMPRO Package

2.1 Introduction

In order to fully describe the quantum mechanical system consisting of a set of nuclei and electron, such calculations are impossible to perform precisely when the number of particles in the system increases; it becomes a many body problem. *Ab initio* techniques have been used to solve this very complicated issue accurately. The ultimate role of an *ab initio* method is to find a solution to the many body quantum mechanical wave equation commonly known as the Schrödinger equation. Solving the Schrödinger equation for some cases, such as for a harmonic oscillator and hydrogen atom, is relatively easy. However, solving it for a system wherein a number of electrons and nuclei are interacting with each other is not possible due to the lack of an analytic solution and, therefore, many approximations have been made.

This chapter discusses the information regarding the methods that have been used for solving the Hamiltonian of the Schrödinger equation for a complex system. Born-Oppenheimer approximation has been used for simplification of the Schrödinger equation. Density Functional Theory (DFT) which is used in this thesis and Hartree-Fock (HF) theory have been used to solve the many body problems. In addition, there is a brief explanation of the important approximations implemented in the AIMPRO code. The AIMPRO code enables the application of DFT to solve problems in solid, liquid and gas systems.

2.2 Many Body Problem

Quantum mechanics as a methodology has been used to provide an accurate description of a system. The wave function and operators of any given system delivers all the information to provide an accurate description of the system. The use of the Schrödinger equation is the fundamental task in describing the behaviour of systems of interacting nuclei and electrons.

The many body time independent Schrödinger equation for a system of interacting electrons and nuclei in three dimensions could be expressed as:

$$\hat{H}\,\Psi_i(r) = E_i\Psi_i(r) \tag{2.1}$$

where $\hat{H}$ is the Hamiltonian operator and Ψ_i is the wave function and E_i is the total energy of the system in the i^{th} state.

The many body electronic Hamiltonian formula usually contains kinetic and potential energy terms and can be expressed as:

$$\hat{H} = \hat{T}_e + \hat{T}_N + \hat{V}_{e-N} + \hat{V}_{e-e} + V_{N-N} \tag{2.2}$$

where $\hat{T}_e$, $\hat{T}_N$ refer to the kinetic energy of electrons and nuclei, respectively, $\hat{V}_{e-e}$, $\hat{V}_{N-N}$ represent the repulsive Coulomb potentials of electron-electron and nuclear-nuclear interactions, respectively, and $\hat{V}_{e-N}$ is the attractive Coulomb potential of electron-nuclear interaction. In atomic units, e, ħ, m_{e} and $4\pi\epsilon_0$ are assumed to be one. Then, 1atomic unit of energy is equivalent to 27.212eV, and 1atomic unit of length is equivalent to a Bohr radius (0.529Å). The Hamiltonian operator for a system consisting of electrons and nuclei in atomic units is:

$$\hat{H} = \overbrace{-\sum_{i=1}^{N}\frac{1}{2}\nabla_i^2}^{\text{term 1}} \underbrace{-\sum_{A=1}^{M}\frac{1}{2M_{\mathrm{A}}}\nabla_{\mathrm{A}}^2}_{\text{term 2}} \overbrace{-\sum_{i=1}^{N}\sum_{A=1}^{M}\frac{Z_{\mathrm{A}}}{|r_i - R_{\mathrm{A}}|}}^{\text{term 3}} + \underbrace{\sum_{i=1}^{N}\sum_{j>i}^{N}\frac{1}{|r_i - r_j|}}_{\text{term 4}} + \overbrace{\sum_{A=1}^{N}\sum_{B>A}^{M}\frac{Z_{\mathrm{A}}Z_{\mathrm{B}}}{|R_{\mathrm{A}} - R_{\mathrm{B}}|}}^{\text{term 5}} \tag{2.3}$$

where M_{A} is the mass of nucleus A, Z_{A} is the charge of nucleus A. r and R refer to the electron and nuclear positions respectively, r_i is the coordinate of electron i and R_{A} is the coordinate of nucleus A.

The first term in Eq. 2.3 represents the kinetic energies of electrons, the second term represents the kinetic energies of nuclei, the third term represents the Coulomb attraction electrostatic potential of electron-nuclear, and the fourth term represents the Coulombic potentials of electron-electron interaction, and the last term contains the Coulombic potentials of nuclear- nuclear interaction.

This Hamiltonian seems rather complicated, and indeed it is impossible to solve the Schrödinger equation for this Hamiltonian directly. The direct numerical solution of the Schrödinger equation for a system with interacting particles of electrons and nuclei is a complex issue. In general, there is no known analytical solution to this problem; therefore, a set of important approximations must be used to obtain a solution as present in the next sections.

2.3 Born-Oppenheimer Approximation

Due to the large nuclei mass compared to the electron mass (where the proton or neutron mass is around 1836 times larger than that of the electron), the nuclei motion are much slower than that of electrons. The Born and Oppenheimer approximation [123] assumed that the nuclei are stationary objects whilst the electrons are moving in a field of fixed nuclei. According to this approximation, the nuclear-nuclear term could be considered as a constant and the nuclear kinetic term could be eliminated from Eq. 2.3. The Born-Oppenheimer approximation decouples the total wave function motion of nuclear and electron in the many body system.

$$\Psi_{\text{total}} = \Psi_{\text{electronic}}\Psi_{\text{nuclear}} \tag{2.4}$$

The electronic Hamiltonian ($\widehat{H}_{\text{electronic}}$) for a system with fixed atomic positions is written as:

$$\widehat{H}_{\text{electronic}} = -\sum_{i=1}^{N}\frac{1}{2}\,\nabla_i^2 - \sum_{i=1}^{N}\ \sum_{A=1}^{M}\frac{Z_A}{|r_{iA}|} - \sum_{i=1}^{N}\ \sum_{j>i}^{N}\frac{1}{|r_{ij}|} \tag{2.5}$$

$$\widehat{H}_{\text{electronic}} = \widehat{T}_e + \widehat{V}_{e-N} + \widehat{V}_{e-e} \tag{2.6}$$

Although this approximation involves simplified Schrödinger equations and reduces the time cost needed for calculation, the wave function still cannot be solved exactly for a large system. Further approximations need to be made.

2.4 Solving the Many Body Wave Function Problem

Electron motion has been explained by quantum mechanics theory. HF (wave function approach) and DFT (electron density approach) are established methods to solve many body problem, and provide details to characterise the electronic and atomic structure. It is important to clarify some general quantum mechanical concepts including correlation and exchange that are used to describe electron-electron interaction.

Correlation interaction means that when a given electron moves, its electrostatic potential will affect the positions of other electrons. Each electron position is correlated to the all other electrons' positions. In HF theory, this effect is entirely missing.

Exchange interaction is associated with the Pauli principle, reflecting the antisymmetry of the wave function with respect to the exchange of two electrons, such that if two electrons are exchanged, the wave function will change the sign.

2.4.1 Hartree-Fock Approximation

The HF method is a method to determine the ground state wave function [124]. This method replaces the many body wave function with a simpler wave function. In this approximation, the electronic wave function should obey the Pauli exclusion principle to be anti-symmetrical with respect to the exchange of any two electron coordinates. This has been achieved in the HF approximation by forming the many electron wave function as a Slater determinant of single-electron wave functions. This approach produces a set of one electron equation which could be easily solved.

$$\Psi_i(r_1, \dots\dots\dots, r_n) = (n!)^{-1/2} \begin{bmatrix} \Psi_1(r_1) & \Psi_1(r_2) & \dots. & \Psi_1(r_n) \\ \Psi_2(r_1) & \Psi_2(r_2) & \dots. & \Psi_2(r_n) \\ . & . & . & . \\ . & . & . & . \\ \Psi_n(r_1) & \Psi_n(r_2) & \dots. & \Psi_n(r_n) \end{bmatrix} \tag{2.7}$$

Despite the fact that HF approximation gives reasonable results for atoms and many molecules, in a solid state these calculations are complicated and although this approximation is included in the exchange interaction, it does not include the correlation effect. The main issue of this method is that the energy difference between the occupied and empty states are generally overestimated, and even an incorrect ground state is obtained. The correction of this method by using the configuration interaction to include the correlation effect is computationally demanding since it needs to calculate simultaneously a number of many body states; therefore, the alternative method of DFT is used to get better results.

2.4.2 Density Functional Theory

DFT is a quantum mechanical method used in physics and chemistry to describe the ground state properties of many body systems and used to study a variety of materials such as atoms, molecules and solids. This approach describes the properties of an interacting system of electrons and nuclei in terms of the electronic electron density instead of many body wave functions as in HF theory. This concept has been proved by Hohenberg- Kohn (HK) theorems and applied using Kohn-Sham (KS) equations. DFT is extremely successful in examining features of the surfaces and interfaces in a material, and it gives a dramatic reduction in computing time.

2.4.2.1 Hohenberg-Kohn Theorems

HK theorems [125] provided the formal basis of DFT in 1964, and two fundamental theorems are used to find the exact ground state energy. This theory depends on the electron density as a basic variable instead of the many electron wave functions.

The first theorem attempts to solve the wave equation and it is supposed that there is one-to-one correspondence between the ground state electron charge density $n(r)$ and the external potential $V_{\text{ext}}(r)$; therefore, the energy is uniquely defined by the density. This means that, for two systems with the same $n(r)$, they will have the same $V_{\text{ext}}(r)$ unless they differ by a trivial additive constant.

$$V_{\text{ext}}(r) \leftrightarrow n(r) \tag{2.8}$$

To prove this theorem, it is assumed that, if there are two wave functions, Ψ_1 and $\Psi_{2,}$ at the same charge density, but arising from different external potentials, V_1 and V_2 , the total energy for the two system can be written as:

$$E_1 = \langle \Psi_1 | \widehat{H}_1 | \Psi_1 \rangle,\ E_2 = \langle \Psi_2 | \widehat{H}_2 | \Psi_2 \rangle \tag{2.9}$$

The Hamiltonian for two systems are:

$$\widehat{H}_1 = T + U + \mathrm{V}_1,\ \ \widehat{H}_2 = T + U + \mathrm{V}_2 \tag{2.10}$$

Where T and U are the kinetic and electron interaction energy, in the Hamiltonian Eq. 2.10, the only thing that will change is the external potentials.

Therefore

$$\hat{H}_1 = \hat{H}_2 + (\mathrm{V}_1 - \mathrm{V}_2) \tag{2.11}$$

By applying the variational principle yields:

$$E_1 = \langle \Psi_2 | \hat{H}_1 | \Psi_2 \rangle, \; E_2 = \langle \Psi_1 | \hat{H}_2 | \Psi_1 \rangle \tag{2.12}$$

The inequalities can be written as:

$$E_1 \leq \langle \Psi_2 | \hat{H}_2 + \mathrm{V}_1 - \mathrm{V}_2 | \Psi_2 \rangle$$

$$E_1 < E_2 + \langle \Psi_2 | V_1 - V_2 | \Psi_2 \rangle \text{ and } E_2 < E_1 + \langle \Psi_1 | V_2 - V_1 | \Psi_1 \rangle \tag{2.13}$$

This leads to:

$$E_1 + E_2 < E_2 + E_1 \tag{2.14}$$

This result is logically impossible, since it is assumed that the two systems have the same density; therefore, it should have the same energy. Thus, the previous statement cannot be true.

The second theorem supposed that the correct ground state density is the one that minimises total electronic energy of the system, when the input density is the true ground state density. This means that, when the electronic density is equal to the ground state density $n(r) = n_0(r)$, it will give the lowest energy (ground state energy) of the system.

$$E[n] = T[n] + V_{e-e}[n] + V_{e-N}[n] \tag{2.15}$$

where $T[n]$ and $V_{e-e}[n]$ can be indicated as universally valid $F[n]$, while $V_{e-N}[n]$ depends on the actual system.

$$E[n(r)] = F[n(r)] + V_{\text{ext}}[n(r)] \tag{2.16}$$

The energy functional $E[r]$ always remains larger than that of the ground state $E_0[r]$. $F[n]$ represents as a universal functional since it does not depend explicitly on the external potential, but depends on the electronic density. $F[n]$ depends on the electron-electron interaction and electron kinetic energy. $V_{\text{ext}}(r)$ represents the effects of the electron-nucleus interactions in addition to the interaction of electrons with other external fields. Hohenberg and Kohn failed to give a sufficiently exact formula for electron-electron effects. The exact ground state density $E_0[r]$ or $F[n]$ remains unknown. KS made progress to resolve this problem.

2.4.2.2 Kohn-Sham Equations

Kohn and Sham theorems [126] proposed that the actual system of interacting electrons is replaced with an auxiliary system of non-interacting electrons that has an electronic charge density exactly the same as that of the actual interacting system; therefore, the total energy of a system is expressed as a functional of the charge density as written:

$$E_{\text{total}}[n] = T[n] + E_{\text{ext}}[n] + E_{\text{e-e}}[n] + E_{\text{xc}}[n] \tag{2.17}$$

where $E_{\text{ext}}[n]$ is the energy of an external potential acting on the system, and $E_{\text{e-e}}[n]$ represent the electron-electron interaction, T[n] is the kinetic energy functional. $E_{\text{xc}}[n]$ represents the exchange-correlation energy. For systems of interacting electrons, the issues to resolve the $E_{\text{e-e}}[n]$ and $T[n]$ forms are solved. This system is solved iteratively until reaching self-consistency (Section 1.6). Although the KS approach accounts for the exact ground state density of a system consisting of non-interacting electrons, the exchange-correlation energy functional is still an unknown term.

2.4.2.3 Exchange-Correlation Functional

In order to describe the exchange-correlation functional E_{xc} in DFT, several approximations have been supposed. The simplest approximation is the local density approximation (LDA); the idea behind this approximation is that for a system with a given local density, the exact E_{xc} density will be replaced with that of a homogeneous electron gas that has the same electron density at each point in space. The E_{xc} in LDA is a function of the electron density at that same point; therefore, this approximation is assumed to be local. This treats the inhomogeneous electron as locally uniform. The exchange-correlation functional for an inhomogeneous system is defined within the LDA as:

$$E_{\text{xc}}[n] = \int n(r)\varepsilon_{\text{xc}}(n)dr \tag{2.18}$$

Here $\varepsilon_{\mathrm{xc}}(n)$ is the exchange-correlation energy per electron in a homogeneous electron gas with density $n(r)$. Despite the fact that the DFT method in LDA is successful for a large variety of problems, giving reasonable descriptions of inhomogeneous systems particularly when the charge density varies slowly, the description of many interesting systems requires improvements mainly for surfaces. LDA approximation [127] can be extended by taking into account not only the magnitude of the electron charge density at a certain point, but also its gradient which is useful for a system when the density undergoes spatial changes, producing an alternative method to LDA known as generalised gradient approximation (GGA) [128]. Therefore, GGA gives more accuracy in term of the E_{xc}. The gradient of the exchange-correlation energy of density $\varepsilon_{\mathrm{xc}}(n, \nabla_n)$ at each point in the system is taken into account; therefore, the $E_{\mathrm{xc}}[n]$ functional is expressed as:

$$E_{\mathrm{xc}}[n] = \int n(r)\varepsilon_{\mathrm{xc}}(n, \nabla_n)dr \tag{2.19}$$

The GGA has achieved greater accuracy compared to LDA, and generally produces better total energy, binding energies, bond lengths and angles. However, GGA generally produces slightly larger lattice constant and smaller bulk moduli than LDA. In general, both LDA and GGA methods give a bandgap underestimation result. In this thesis, the GGA method is used which was developed by Perdew, Burke and Ernzerhof (PBE), as implemented in the AIMPRO code.

2.5 Supercell Approach

A unit cell consists of a number of primitive cells that represent the smallest cell in the crystal used to simulate an infinite and periodic system of bulk materials. The supercell is a repeating non-primitive unit cell used usually to model defects, interfaces and surfaces. In this thesis, one of the applications is the treatment of defects in bulk crystalline materials. For instance, if there is a supercell containing 64 atoms of $(Cu_2ZnSnS_4)_8$ composition and one Cu atom is removed from the composition, the effective Cu vacancy concentration is 1.56% of the supercell atoms and represents 3.12% of the [Cu]. In supercell preparation, when a defect is placed inside the unit cell, the main point should consider that this defect is also repeated throughout the three dimensions of the distance (a_0), which is the supercell length, to avoid the interaction between defect-defect and to ensure sufficient separation between them. When there is a defect inside the unit cell, this defect will arrange periodically and that means repeating the defect throughout the three dimensions. The defect will interact with its images (the repeated defect) in other unit cells when the number of atoms is not large enough to give sufficient separation between the defect and repeated image so that defect-defect interaction will be created. Large supercells should be used to avoid interaction, which arise from the periodic boundary condition by repeating the supercell infinity in all directions to form continuous crystals, although this will increase the computing cost by orders of magnitude. Therefore, the balance between the computing cost and model size should be achieved by choosing an approximate structure.

2.6 Self-Consistency Cycle

Knowing the charge density is necessary to determine the potential for solving KS equations to achieve an accurate minimum energy calculation of the system. It is extremely complex to find the wave function of the system directly; therefore, an iterative procedure is utilised to construct the effective potential and this procedure is known as a self-consistency cycle as shown in Fig. 2.1. In this approach, achieving minimum total energy is done by redistributing the charge around the system, and this means that the assumptions made at the beginning of the cycle are consistent with the results.

In the Schrödinger equation (Section 2.2), the operator and the wave function depend on the solution, and the solution is unknown. The processes to generate the effective potential begin with an initial guess of the charge density either from the density of the neutral atoms or the output of a previous calculation. This initial charge density used to solve the KS equation, and from the solution of the KS equation can generate a new charge density. Depending on this initial solution, the operator will have another value. If the output generated charge density is consistent with the input charge density, this means that there is self-consistency, so the end point of the loop has been reached. Conversely, if the output and input charge density are not the same, both of the input and output charge density will combine, and this combined result will be used as an input for the next cycle to find a new charge density. Self-consistency in AIMPRO calculations reaches a convergence point when the difference between the input and the output energy is less than 10^{-5} atomic units.

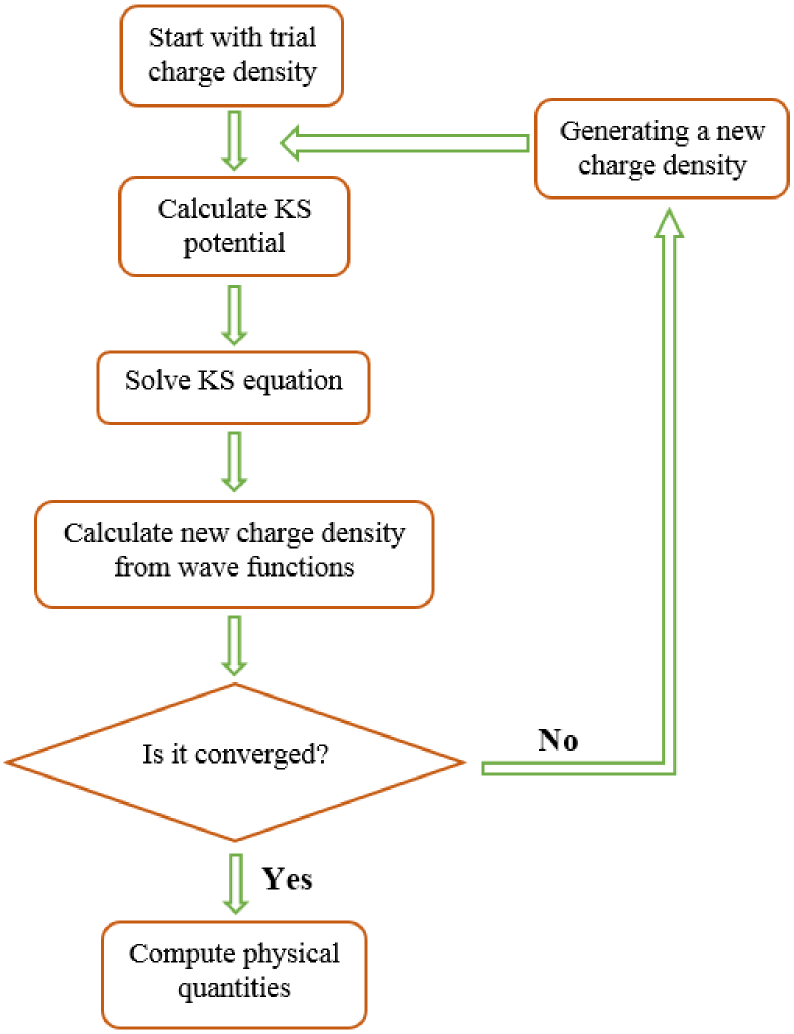

Figure 2. 1: The schematic flow chart showing the self-consistency cycle

2.7 The AIMPRO Software Package

AIMPRO is a quantum mechanical code [129]. This code uses DFT to successfully simulate various types of materials, such as metals, insulators and semiconductors [130], and generally gives good results when compared with experimental results. AIMPRO has been used to perform the calculations for the results presented in this thesis. Details regarding the important elements of the AIMPRO package have been described in this chapter.

2.7.1 Brillouin Zone Sampling

The total energy in a periodic system involves the integration over *k*-point over the Brillouin zone (BZ) which is required to calculate the structural and electronic properties of the system.

For a periodic structure, rather than taking integrals on unlimited points in real space, by taking advantage of Bloch theorem, integrals are taken on a finite first Brillouin zone that is defined as a primitive unit cell in reciprocal space. The BZ is sampled by the Monkhorst-Pack scheme (MP) [131, 132]. With the MP sampling as used by AIMPRO, the integrals are made on limited numbers of points in the first Brillouin zone. The finite number of points is called the *k*-point mesh.

The MP mesh of *k*-point is defined by three integers *I*, *J* and *K* that define a grid in a reciprocal space as follows:

$$\vec{k}(i,j,k) = \frac{2i-I-1}{2I}\,\overrightarrow{a_1} + \frac{2j-J-1}{2J}\,\overrightarrow{a_2} + \frac{2k-K-1}{2K}\,\overrightarrow{a_3} \tag{2.20}$$

where

$$i = 1, 2, 3..., I, \qquad j = 1, 2, 3..., J, \qquad k = 1, 2, 3...,K \tag{2.21}$$

$\overrightarrow{a_1}$, $\overrightarrow{a_2}$ and $\overrightarrow{a_3}$ are unit vectors of reciprocal space. Each one of the three integers *I*, *J* and *K* is more than or equal to 1, and when *I*, *J* and *K* are equal, the sampling scheme is labelled as MP-I^3.

In the band structure, a path in the reciprocal space is defined by adopting special *k*-points in the BZ, and the path is also known as high-symmetry points, which are chosen by following the symmetry of the unit cell (Fig. 2.2). The BZ centre is always labelled as Γ point.

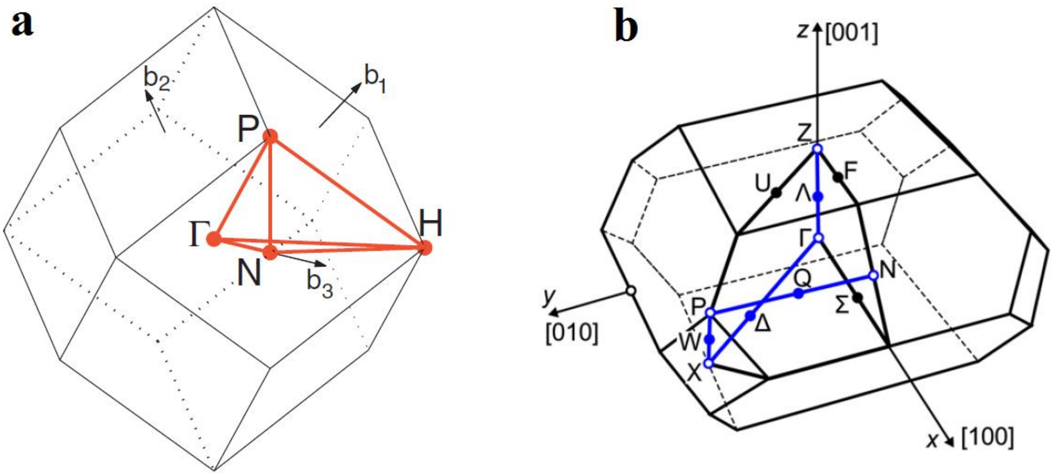

Figure 2. 2: First Brillouin zone of (a) body-centred cubic lattice [133], (b) body-centred tetragonal lattice [134], where *Γ*, *Z*, *U*, *P*, *X*, *N*, *H* and *F* are high-symmetry points in the BZ.

The more *k*-points defined in the MP mesh the more accurate it is, but it will be computational demanding. Therefore, the balance between accuracy and time should be taken into account to choose the number of points for the mesh. For bulk CZTS supercell with 64 atoms, the difference between MP-2^3 and MP-4^3 is 1.2 meV, as shown in Fig. 2.3; therefore, MP-2^3 was chosen to be sufficient to converge the total energy and used for calculations in this thesis.

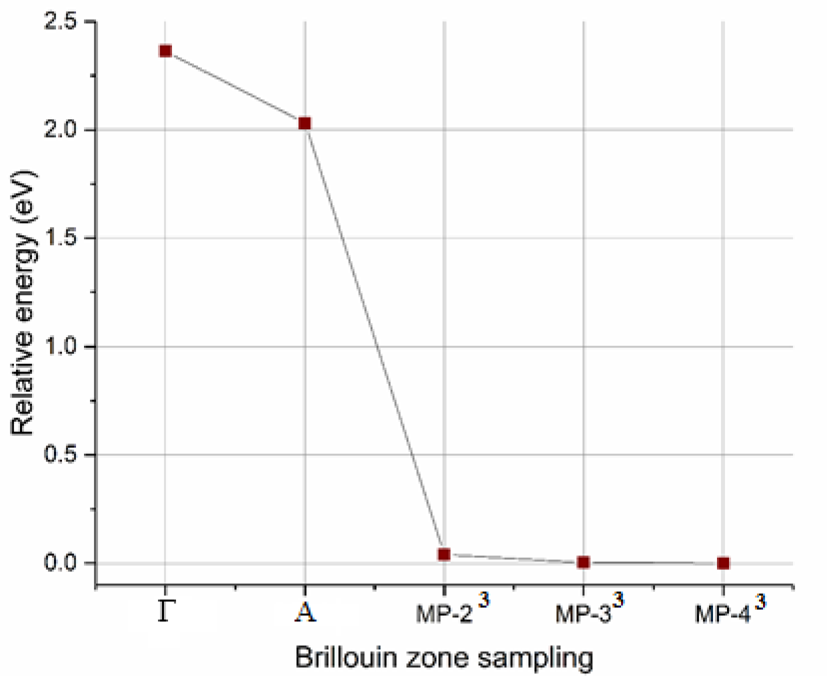

Figure 2. 3: Effect of Brillouin zone sampling on the bulk CZTS supercell with 64 atoms. The relative energies have been calculated with respect to MP-4^3 as a reference energy for the supercell (Eqs. 2.15, 2.16). The labels Γ and A are consisted with conventional labelling of Brillouin zone [133].

2.7.2 Basis Set Functions

One of the most important features of DFT modelling is the selection of suitable basis set functions that are used to present electron states and charge densities. For electronic structure calculations, the Cartesian Gaussian function is a common type of basis set function. Gaussian basis sets have several advantages; for example, only a small number of functions per atom are required, thereby reducing the cost and time of the calculations. In addition, this basis set is localised and rapidly decays from the centre of the atomic site. AIMPRO uses Gaussian basis sets to reduce the computation time of the DFT calculation.

For example, in this thesis, the basis sets used to represent Cu, Zn, Sn, and S for bulk CZTS are CZTS-“*dddd*”, which consist of 40 functions per atom. The four letters “*dddd*” following the material indicate the number of exponents (the width of the function), where each letter "*d*" represents exponents of *s*, *p* and *d* orbitals which have 10 functions, and include the orbital angular momentum l=2. In this case, the first exponent "*s*" is the smallest and they increase in size to the final one "*d*". For Cd, the basis set is CdS-"*dddd*".

For a modelling system, the big basis sets have more accuracy but there is a greater computational cost. Therefore, the balance between accuracy and computational cost should be made in selecting the best basis set that can cover the needs for orbitals. For example, Sn has different basis sets, such as CZTS-"*dddd*", CZTS-"*ddpp*", SnH4-"*dddd*", SnH4-"*pddd*", alphaSn-"*dddd*" and alphaSn-"*ddpp*" which have 40, 28, 40, 34, 40 and 22 numbers of basis functions per atom, respectively. In each case for an Sn basis set, the exponents are preceded by a specific system, and this mean that these exponents are chosen to be optimal for that specific system. Fig. 2.4 illustrates the relationship between the number of basis functions per atom and the time for the different sampling including Γ and MP-2^3.

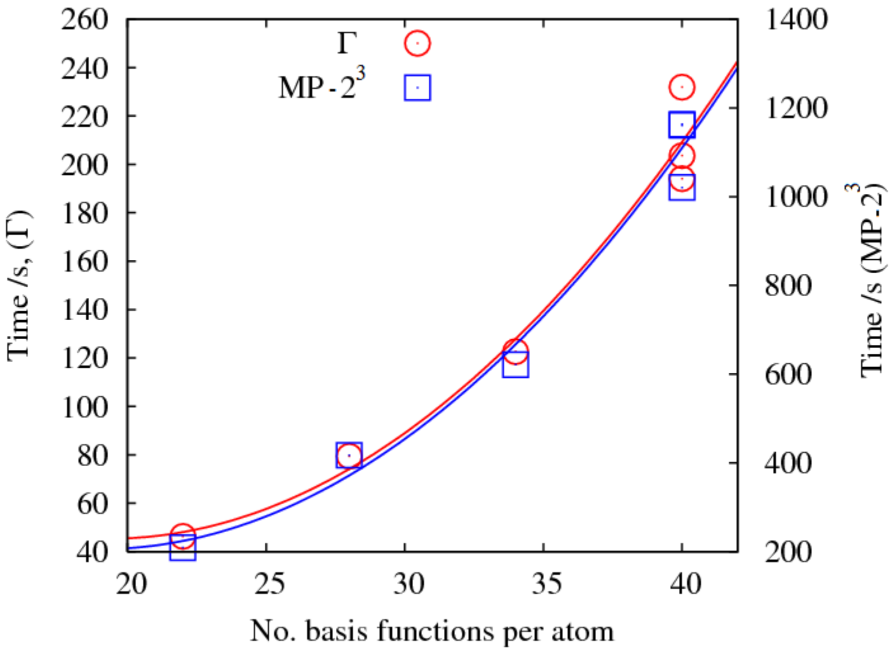

Figure 2. 4: Computed time as a function of the different basis functions for Γ and MP-2^3

A plane wave basis is used to make a Fourier expansion of the charge density [135]. For CZTS structure, the total energy of the structure has been converged at the cut-off energy (E_{cut}) for the plane wave basis to 250Ha and it represents the default value. This value of E_{cut} was sufficient to converge the energies to about 10meV, as shown in Fig. 2.5, and used for all of the calculations in this thesis. E_{cut} must be large enough to cover a sufficient number of plane-waves for accurate calculations [136]. For ZnS, E_{cut} is 250Ha and for CdS E_{cut} is 100Ha.

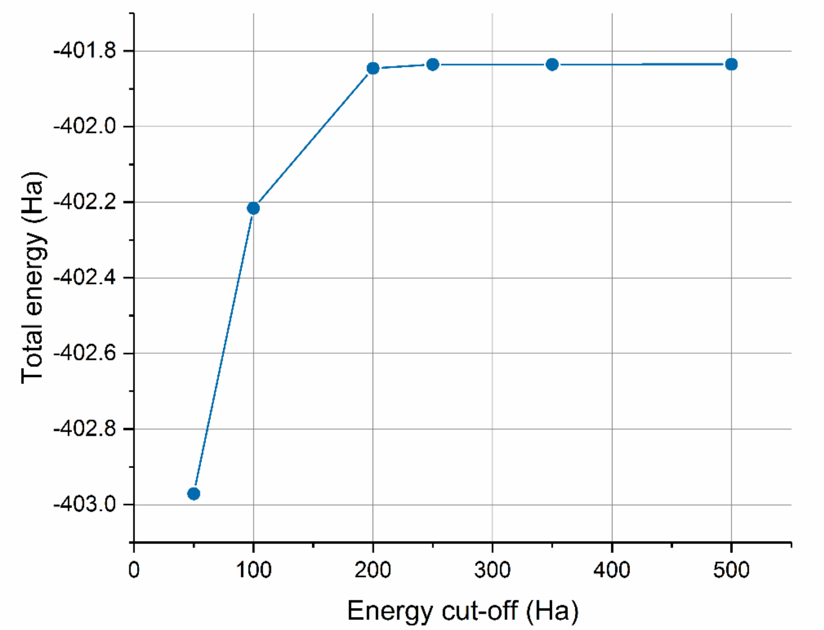

Figure 2. 5: Illustration of the convergence in the total energy of CZTS as a function of the plane wave energy cut-off

2.7.3 Pseudopotential Approximation

In the atom, electrons can be divided into core and valence. For instance, the electronic structure of Cu is $1s^12s^22p^63s^23p^63d^{10}4s^1$. In this case, the core electrons may be chosen to be $1s^12s^22p^63s^23p^6$, and the valence electrons are $3d^{10}4s^1$. The core electrons are tightly bonded, and do not participate in chemical bonding. The oscillation of the core electrons wave function is rapid, and force the valence band states to also oscillate rapidly near the nucleus to be orthogonal. The wave function of the valence electrons should fit with that of the core electrons and this is very expensive computationally; therefore, an effective approach should be used to eliminate the core electrons from the calculations.

A pseudopotential [137] is an approximation used to replace the complicated effects of the core electrons and the nuclear Coulomb potential with an effective potential. This leads to a solution for the KS equation by using an effective potential term rather than the Coulomb potential term for core electrons. Two main constraints must be applied in constructing the pseudopotential. Firstly, the true atomic potential and the pseudopotential should be identical outside the core. Secondly, the true wave function and the pseudo wave function should be the same outside the core region (Fig. 2.6).

The important benefits of pseudopotential approximation are that it excludes explicit calculation of core electrons. Firstly, fewer basis set functions are required since the number of electron states needed for calculations is smaller; thus, the computing cost is lower.

Secondly, the total energy is not dominated by the core electrons, so the error rate calculations are reduced.

For the DFT results presented in this thesis, the pseudopotential approximation implemented in AIMPRO is derived from the work of Harwigsen, Goedecker, and Hutter (HGH) [138], which produced pseudopotentials for all elements. In this thesis, elements are modules using norm-conserving pseudopotentials, with $3d^{10}4s^1$, $3d^{10}4s^2$, $5s^25p^2$, $3s^23p^4$ and $4d^{10}5s^2$ valence sets for Cu, Zn, Sn, S and Cd, respectively.

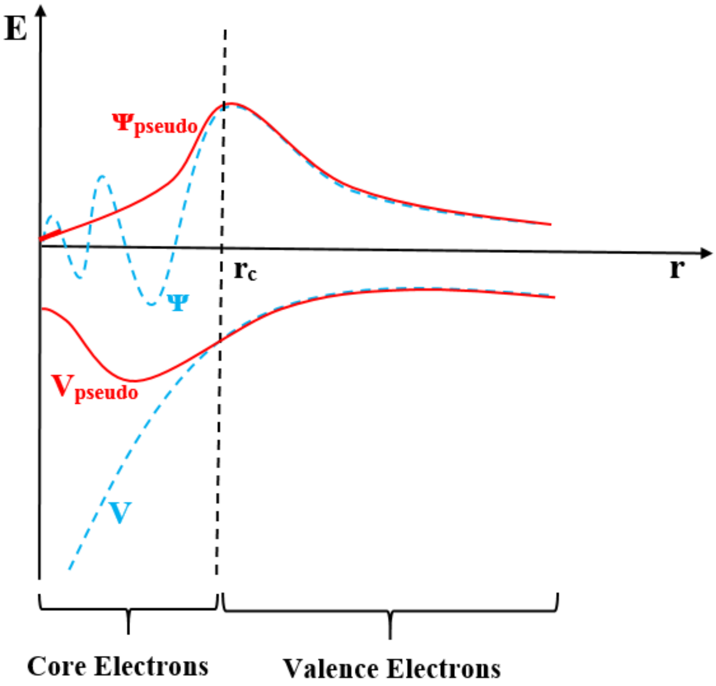

Figure 2. 6: Schematic diagrams illustrating the comparison of a real wave function and Columbic potential (dashed blue line) with one in the pseudo wave function and pseudopotential (solid red line). The real and pseudo wave function and potentials match above a certain cut-off radius rc. The cut-off radius rc indicates the defined region at which point the real and pseudo wave function and their potentials must match.

2.8 Summary

In this chapter, fundamental methods used in AIMPRO code have been described, and the theoretical principals behind this code including a many body Schrödinger equation and approximations that are employed to simplify the complexity of this equation are explained. For a quantum mechanical system consisting of a set of nuclei and electrons, DFT method implemented in AIMPRO is used to solve the Schrödinger equation. The ground state properties of a system are determined by the DFT method that uses the charge density as a basic variable rather than solving the many body equation for all electrons.

Chapter 3

The AIMPRO Calculation of Energetics

3.1 Introduction

Despite the fact that a significant number of experimental techniques are employed to observe the properties of materials such as defects in crystalline solids, modelling techniques could be used to analyse many of the complex problems that faced experimental investigations. Density functional theory (DFT), as implemented in AIMPRO, is a successful method that has the capability to calculate a wide range of experimental observables. This chapter presents an outline of the method that could be used to estimate experiment observables including electrical structure, formation energy, electrical levels and diffusion barrier.

3.2 Structural Optimisation

One of most important computational tasks is to find the stable structure of a system. The optimisation process means all the atoms are allowed to move until the energy is reduced and the force on all atoms reaches below the threshold value which is numerically indistinguishable from zero. In the AIMPRO code, the conjugate gradient algorithm [139-141] is used to select the direction that is adopted to minimise the energy by displacing the atoms in a direction in which the energy is reduced.

The total energy obtained for an equilibrium structure might be the local minimum instead of the global minimum energy based on the starting structure. For example, CZTS have two structures, kesterite and stannite, depending on the order of the Cu and Zn atoms. Kesterite structure is the ground state energy and represents the global energy, whereas the stannite structure has higher energy than kesterite and represents the local minimum energy.

The structure that has the minimum energy is defined as the ground state structure. Structures are optimised until the difference in energy between the sequence iterations is below 10^{-5} Ha, and forces are below 10^{-3} atomic units.

3.3 Lattice Constants

The lattice constant is a fundamental property of the material. In the crystal structure, the unit cell dimensions are defined by the lattice vectors. Theoretically, the calculated lattice constant values are found by optimising the atoms' positions within the unit cell for a number of lattice constants. The resulting energies for an isotropic problem can be fitted to the Birch-Murnaghan equation of state [142], Eq. 3.1, and the value that has the lowest energy represents the lattice constant, as shown in Fig 3.1. The equilibrium lattice constants are estimated from the fit.

$$E(\mathrm{V}) = E_0 + \frac{B_0\mathrm{V}}{B_0'}\left[\frac{\left(\frac{\mathrm{V}_0}{\mathrm{V}}\right)^{B_0'}}{B_0'-1} + 1\right] - \frac{B_0\mathrm{V}_0}{B_0'-1} \qquad (3.1)$$

where E and V refer to the total energy and volume, respectively. E_0 and V_0 are the equilibrium energy and volume. The bulk modulus is B_0 and the first derivative of the bulk modulus with pressure is B_0'.

In LDA calculations, the lattice constant is generally underestimated, whereas the lattice constant in GGA is slightly overestimated. In both cases, the lattice constants have acceptable agreement with experiment.

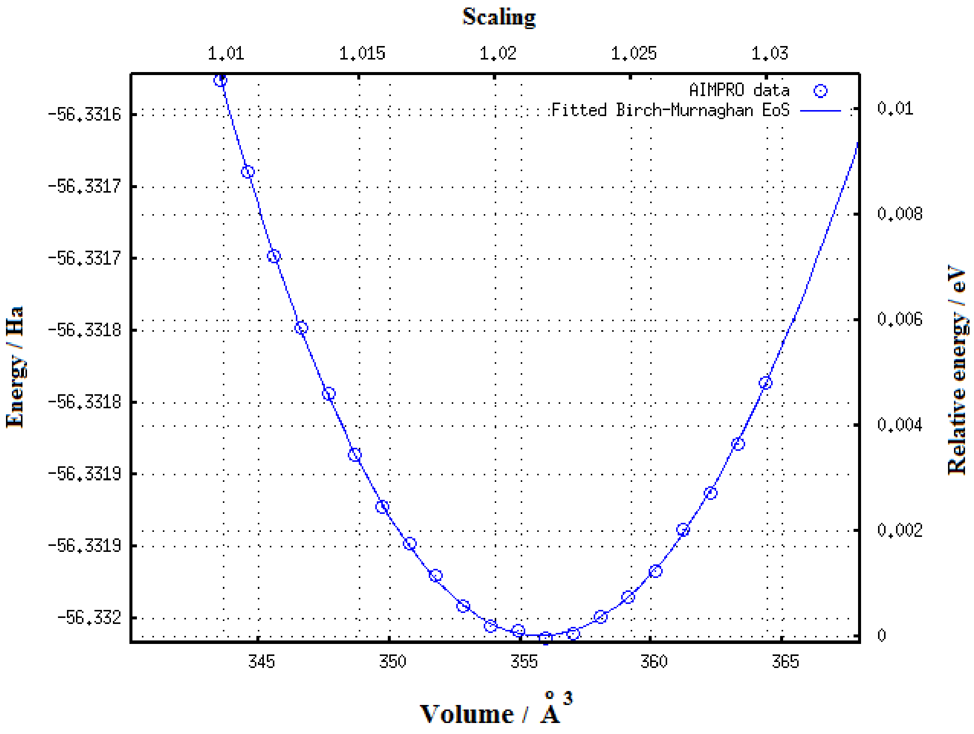

Figure 3. 1: Energy as a function of the unit cell volume for cubic CdS structure; the AIMPRO energy data are fitted to the Birch-Murnaghan equation of state to find the lattice constant.

3.4 Electronic Structure

DFT has been used to calculate the band structure; the theoretical band structure of intrinsic kesterite CZTS is shown in Fig. 3.2. The calculated band energy is plotted in *k*-space (wave vector) along high-symmetry branches (*Z-Γ-X-P-N*) (see Section 1.6.1) in the Brillouin zone (BZ) as illustrated in Fig. 2.1b; the VBM is set to 0 eV of the band structure. For pure CZTS, the VBM and CBM of CZTS are situated at the Γ point, where the CBM (red lines) and the VBM (blue lines) are aligned, reflecting the direct band gap of CZTS around the centre of the BZ at the Γ point, with a theoretical band gap of approximately 0.017 eV between VBM and CBM. This result is in good agreement with DFT calculations for the previous theoretical work by Maeda (0eV) [143] and Paier (0.096eV) [115]. It differs from the experimental band gap value for CZTS which is 1.45eV [144].

In general, the approximations of DFT reflect underestimation of the unoccupied states' energies in the system which is a well-known shortcoming of the systematic band gap width problem in this theory. However, band gap curvatures are matched well with the experimental results. In addition, DFT gives accurate values of other elastic properties such as the lattice constant that can be obtained without knowledge of the band gaps and it is agreed with the experimental data.

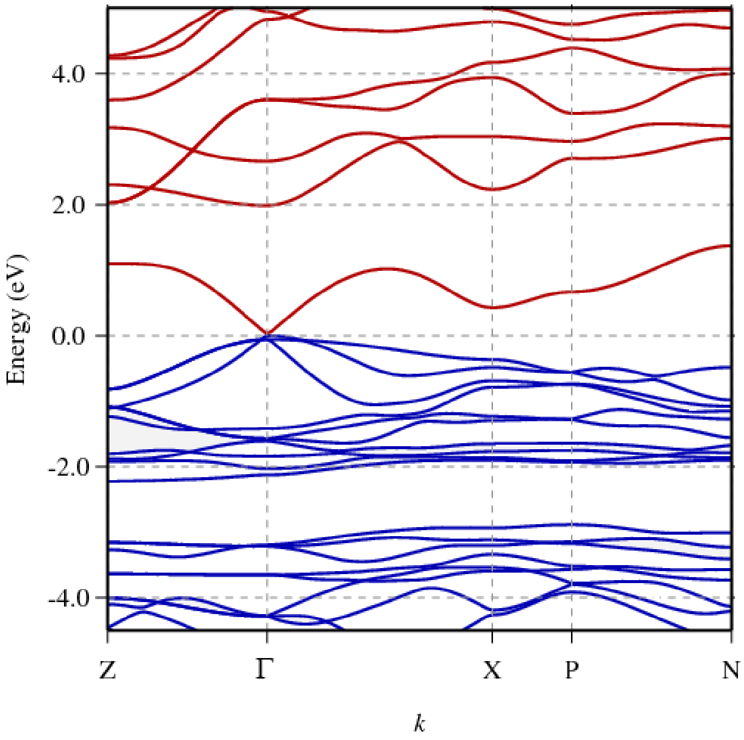

Figure 3. 2: The calculated band structure of primitive bulk CZTS. The occupied and unoccupied electronic states corresponding to the VBS and CBS are blue and red, respectively. *k* is the wave vector. *Z*, *Γ*, *X*, *P* and *N* represent high-symmetry points in the Brillouin zone [134].

3.5 Formation Energy

An important property to investigate dopants and intrinsic defects is the formation energy. The difference in energy between the configuration of atoms and the sum of their free energies in the reference state (their elemental state) is known as the formation energy and this is given by Eq. 3.2.

$$E^f(x,q) = E^{\mathrm{tot}}(x,q) - \sum_i n_i\mu_i + q\mu_e + \xi(x,q) \tag{3.2}$$

where $E^{tot}(x,q)$ is the total energy of the system with a defect x in the charge state q, n_i is the number of atoms i of species and μ_i is the chemical potential of the component element i, respectively. μ_e is the electron chemical potential and defined as zero at the valence band maximum. $\xi(x,q)$ is a correction term which refers to the correction in the periodic boundary conditions of the system, particularly to deal with the electrostatic interactions between charged supercells [145]. The correction is given by [146]:

$$\xi(x,q) = \alpha_M \frac{q^2}{L\epsilon} \tag{3.3}$$

where α_M is the Madelung constant which depends upon the lattice. q^2 is the unbalanced charge and this introduces error in electrical levels that involve higher charge states [145]. L is the lattice parameter, ϵ the permittivity of the material (dielectric constant).

For the defect system, the formation energy is defined as a function of the chemical potentials of the atomic species of the material and electrons. The concentration and stability of defects have been calculated by using the formation energy method with respect to the chemical potentials of the atoms. The formation energy of defects in the neutral charge state strongly relies on the atomic chemical potential of the species in the system.

The formation energy can be calculated as a difference in adjacent defect and pure systems according to the difference in the number of particles. For example, in the case of vacancy, one fewer of species i, Eq. (3.2) can be written as:

$$E^f(x,q) = E^{\text{tot}}(x,q) - E^{\text{tot}}(\text{pure}) + \mu_i + q\mu_e \tag{3.4}$$

For example, in the neutral charge state, the formation energy of Cu vacancy inside CZTS with 16-atom ($Cu_4Zn_2Sn_2S_8$) is equal to:

$$E^f(\text{V}_{\text{Cu}}) = E^{\text{tot}}(\text{V}_{\text{Cu}}) - 3\mu_{Cu} - 2\mu_{Zn} - 2\mu_{Sn} - 8\mu_S \tag{3.5}$$

$$= E^{\text{tot}}(\text{V}_{\text{Cu}}) - (4\mu_{Cu} + \mu_{Cu}) - 2\mu_{Zn} - 2\mu_{Sn} - 8\mu_S$$

$$= E^{\text{tot}}(\text{V}_{\text{Cu}}) - (4\mu_{Cu} + 2\mu_{Zn} + 2\mu_{Sn} + 8\mu_S) + \mu_{Cu}$$

$$E^f(\text{V}_{\text{Cu}}) = E^{tot}(\text{V}_{\text{Cu}}) - E^{\text{tot}}(\text{pure}) + \mu_{Cu} \tag{3.6}$$

Eq. (3.2) has been used to find the defect formation energy as a linear function of μ_e, and this equation could estimate the electrical levels of the defect (Section 3.6). Furthermore, this equation is used to calculate the heats of formations associated with the formation of defects. In this thesis, Eq. (3.2) has been used to find the equations of the vacancies and anti-site defects in CZTS without and with charges.

3.6 Electrical Levels

Impurities or intrinsic defects inside the crystal structure often introduce electrical energy levels that represent the potential for a defect to adopt different charge depending upon μ_e. A significant characteristic of defects in semiconductors and insulators is the electrical level of defects generated by doping.

The electrical and optical properties of materials are highly affected by the specific position of the defect levels, since electrons could transfer from one band to another by processes of carrier generation and recombination. In general, carrier generation occurs when an electron gains enough energy to move from the VB to CB leaving a hole in the VB, whilst carrier recombination occurs when the electron in CB loses energy and reoccupies the hole in the VB. In thermal equilibrium conditions, generation and recombination processes are balanced and the net charge carrier density is constant.

Formation energy is a computational method used to identify the defect level location relative to the band edges. In this method, the electrical level is calculated by comparing the formation energies of two optimised systems having different charged states. For example, the donor level involving occupied states located close to the CBM is known as shallow donor, whereas the acceptor level involving unoccupied states located close to the VBM is known as shallow acceptor, as shown in Fig. 3.3. The deep ionization levels of acceptor and donor defects are located far from the VBM and CBM, respectively. Material conductivity relies on the donor and acceptor level depth of the dominant dopant since carrier traps deep in the band gap will limit conductivity due to their impact in reducing free carrier concentration and reduce carrier mobility.

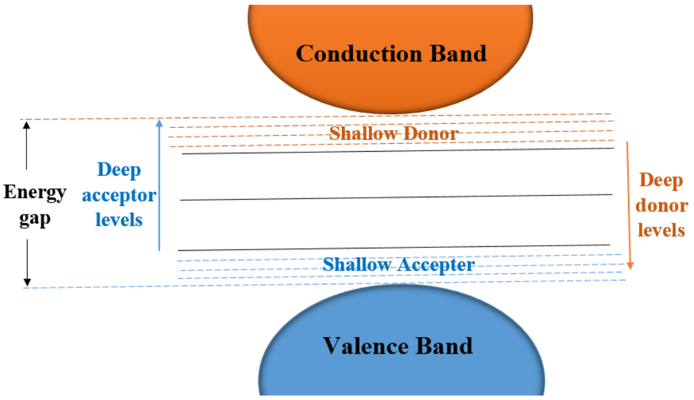

Figure 3. 3: Schematic diagram showing the shallow and deep levels of material

The transition between two different charged states is the electron chemical potential when the two different charge states are in equilibrium with each other, as shown in Fig. 3.4. When the formation energies of positive and neutral charge states are equal, $E^f(0) = E^f(+1)$ and this can be written as (0/+). Similarly, the position of a single ionized acceptor level represented by μ_e when the formation energy of negative and neutral charge states are equal, $E^f(0) = E^f(-1)$ and this can be written as (−/0). Similarly, (++/+) and (− −/−) represent the double-donor and double-acceptor level, respectively. The slashes in the notations point to the change in the defect charge, whereas the defect charge state is represented by the symbols to the left and right of the slash when the Fermi level is above and below the transition energy, respectively. For instance, in (0/+) the defect becomes stable in neutral charge when μ_e is higher than a specific value, whereas the +1 charge state will be stable when μ_e is smaller than the same specific value.

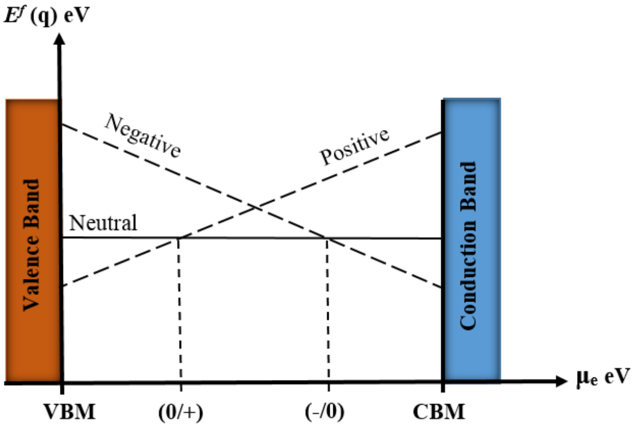

Figure 3. 4: Schematic diagram showing the formation energy E^f(q) for three charge states q of a structure as a function of the electron chemical potential μ_e. VBM and CBM represent the valence band maximum and the conduction band minimum. (0/+) and (−/0) are the single donor and acceptor level, respectively.

3.7 Electrostatic Potential

DFT calculations provide a good description of the band offset [147-150]. The electrostatic potential approach has been adopted to estimate the band offset in this thesis. This approach includes the calculation of the electrostatic potential as a function of position through the super-lattice in the interface.

For example, in order to calculate the VBO of (100)-oriented CZTS/ZnS, the band structure calculations of both bulk CZTS and ZnS should be calculated to get the energies of the VBM in each material. In the heterojunction, ZnS is slightly strained; therefore, the

VBM of the bulk ZnS layer is calculated under the same strain conditions as exist in the interface. The calculated VBM energies of these two bulk materials are different.

The band offset alignment provides the link between the energy scales of the two independent bulk calculations, and this allows the average potentials in each layer of the interface to be matched.

The VBO of the CZTS/ZnS is 0.95eV, and it represents the deference between the VBM of bulk CZTS which is set at zero in the energy scale and the VBM of strained ZnS which represents the horizontal line on the energy scale below the VBM of CZTS, as shown in Fig. 3.5. Fig. 3.6 illustrates the difference in the VBO of the interface before and after matching the average potentials of the two bulk materials with the interface average potential. It is noticed in the interface region that the lineups do not match perfectly because the periodic boundary depends on the electrostatic potential. At bulk, the electrostatic potential does not match that at the interface precisely because there are detailed chemical differences between the bulk and the interface.

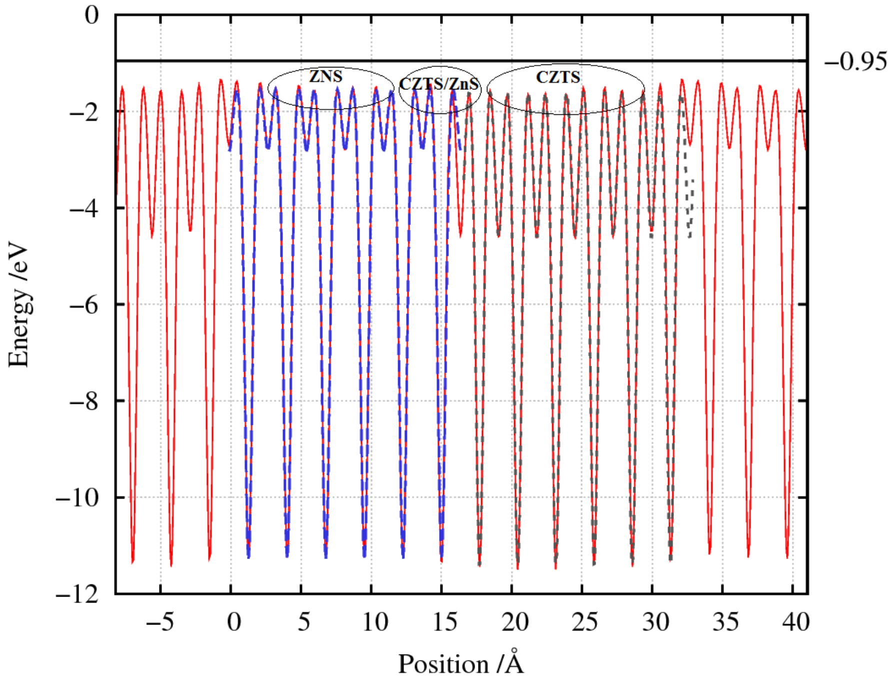

Figure 3. 5: The plot illustrates the electrostatic potential calculation which is used to calculate the VBO for the (001)-oriented CZTS/ZnS. The average bulk potential of bulk CZTS (blue) and bulk strained ZnS (grey) have been aligned with the electrostatic potentials of the CZTS/ZnS (red). The valence band maximum of bulk CZTS is set at zero, and the horizontal lines describe the valence band maximum positions of bulk ZnS.

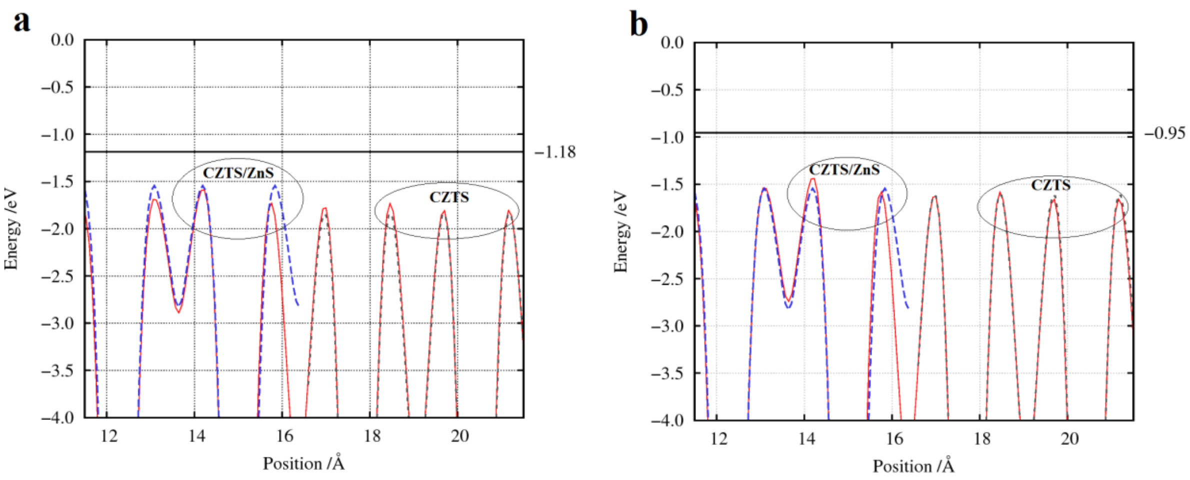

Figure 3. 6: The plot illustrates the band offset alignment for the (001)-oriented CZTS/CdS: (a) the valence band alignment before matching the electrostatic potential of bulk CZTS and bulk ZnS with CZTS/ZnS; (b) the valence band alignment after matching the electrostatic potential of bulk CZTS and bulk ZnS with CZTS/ZnS.

On the other hand, to calculate the CBO of CZTS/ZnS or CZTS/CdS, the calculated VBM of the two bulk CZTS and strained ZnS (or CdS) is used to estimate the CBO. In DFT, the unoccupied states' energies are underestimated. Therefore, for best agreement with experiment results the unoccupied states have been shifted by a constant amount [151, 152]. Adding the experimental value of the energy gap to the VBM gives the correct scaling energy of CBM, as has been performed in other work [147-150]. This approach has been used successfully in the Si/Ge band offset calculation [153].

3.8 Diffusion Barrier

In theoretical chemistry and condensed matter physics, there are issues with calculating the transition rates of chemical reactions or diffusion processes in solids. The climbing image nudged elastic band (CL-NEB) [154] [155] is an efficient method used to find a saddle point and to allow the highest energy image to be driven up towards the saddle point whereas the minimum energy path between two known equilibrium structures. The CL-NEB method works by optimising a set of images along the reaction path between the known initial and final structures. Each image is connected to the previous and next images and corresponds to specific positions of the atoms along the reaction path. This path is known as a minimum energy path (MEP). These atomic images are relaxed according to the force acting on them perpendicular to the path, and an artificial spring force keeping the images is spaced equally along the reaction path. Along this reaction path the structure with the highest energy image is called a saddle point and its energy is a significant quantity for studying the transition process. Only the highest energy image is relaxed with the climbing constraint. The climbing image is not affected by the spring forces at all; therefore, the spacing of the images will be different on each side of the climbing image, and the true force at this image along the tangent is inverted.

The procedure to perform a CL-NEB calculation is as follows. The structures of the initial and final structures, with the diffusion occurring between them, are first optimised to find the minimum energy of both structures. The initial pathway is found by linear interpolation and then optimised to obtain the minimum energy path. Then, the MEP of two structures is found by linear interpolation of a number of images along the path and optimising each image. The maximum energy image along the MEP is the saddle point which represents a barrier for migration of the two structures. Once the minimum energy of the saddle point has been obtained, the energy barrier can be easily calculated by subtracting the energy of the initial (or final) structure from that of the saddle point structure. The result of the activation energy barrier gives information about the possibility of the reaction and its type and whether it is symmetrical or not.

In one case, the structure of the initial and the final structures are equivalent. The energy of these two structures will be the same and the diffusion rate in both forward and backward direction is the same (see Fig. 3.7 (a)); therefore, the diffusion process is considered to be symmetrical.

In another case, the structure of the initial and final structures are non-equivalent. Firstly, if the initial structure has lower energy than the final structure, as shown in Fig. 3.7 (b), the activation energy value of the forward reaction (migration from initial to final state) is higher than that of the reverse reaction. Therefore, the forward reaction is endothermic (absorbs energy from the system), while the reverse reaction is exothermic (releases energy from the system). Based on that, the forward reaction is always more stable since the defects in the initial state have higher activation energy than the defects in the final state, and the reverse reaction rate is faster than that of the forward reaction. Secondly, the final structure has lower energy than the initial structure. The activation energy value of the forward reaction is lower than that of the reverse reaction, as shown in Fig. 3.7 (c).

For this thesis, CL-NEB was implemented within AIMPRO to calculate the activation energy barrier. The barrier is optimised until the image forces are less than 10^{-3} atomic units, and the saddle-point energy changes by less than 1meV.

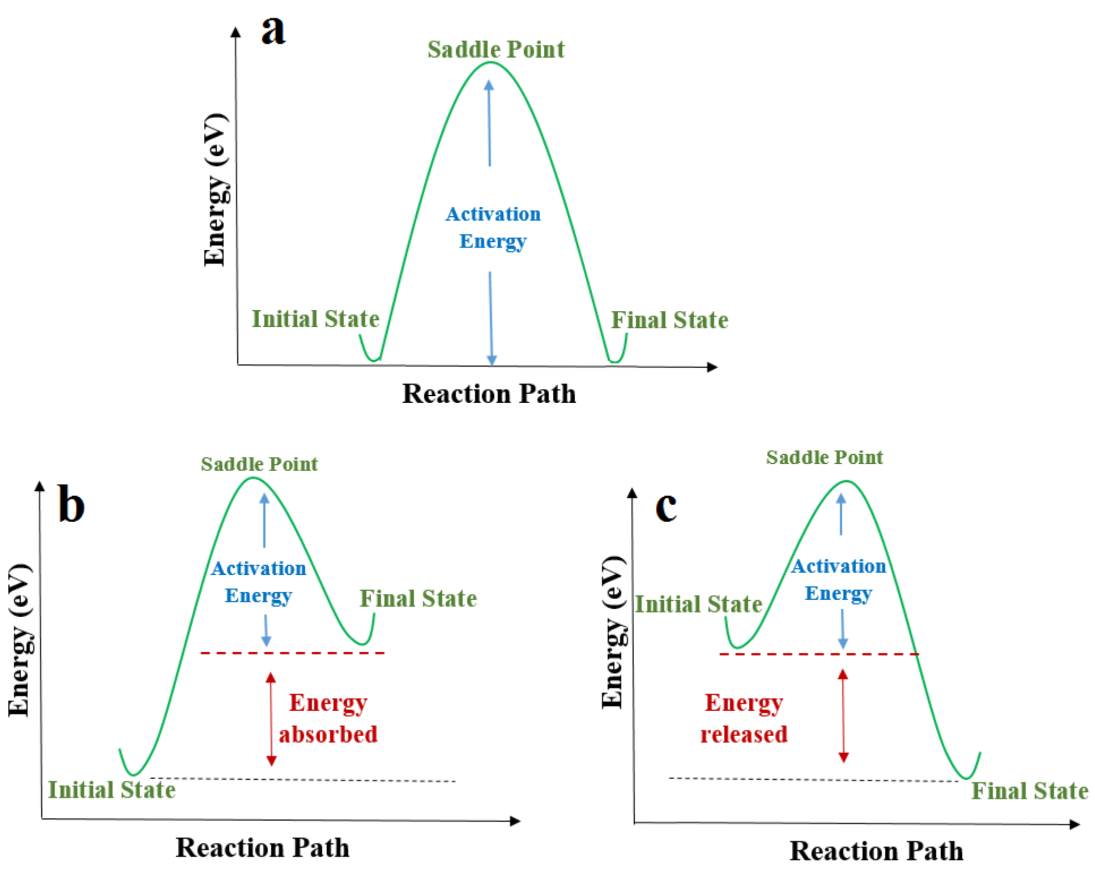

Figure 3. 7: Schematic diagram describing the three types of NEB calculations: (a) the diffusion of the equilibrium reaction: (b) when the diffusion of the forward reaction is endothermic: (c) when the diffusion of the forward reaction is exothermic.

3.9 Binding Energy

Defects can form as point defects or complexes when two defects or more binding energy are bound to each other. Binding energy provides information concerning whether the two defects are likely to be constituted as a complex or two separate point defects during heat treatment growth processing. For a system hosting two defects A and B, the binding energy $E^b(\mathrm{A,B})$ represents the difference in the formation energies between the complex defect (product) and its constituent parts (reactants) as given by:

$$E^b(\mathrm{A,B}) = E^f(\mathrm{A}) + E^f(\mathrm{B}) - E^f(\mathrm{A,B}) \tag{3.7}$$

where $E^f(\mathrm{A})$ and $E^f(\mathrm{B})$ are the formation energies of systems A and B in their isolated forms (reactants). $E^f(\mathrm{A,B})$ refer to the formation energy of the complex (product). For a bound system, the binding energy has a positive value which means that the complex has lower potential energy than the constituent parts.

3.10 Summary

The methods that AIMPRO code uses to calculate different physical quantities is discussed in this chapter. AIMPRO enables a quantitative estimation regarding the calculations of the band structure, formation energy, electronic levels and diffusion barrier based on DFT and supercell method to be given. These quantities can be directly or indirectly compared to the experimental data. Despite the fact that DFT has high accuracy compared with the experimental observations, to study the defects, it is essential to take into account both experimental and theoretical evidence to acquire all the information to identify the defects.

Chapter 4

Bulk CZTS and Secondary Phases

4.1 Introduction

In the perfect crystal structure, each atom has a specific position and deviation from this ideal crystal lattice is referred to as defects. In a semiconductor, defects could be divided into two essential kinds: point defects and extended defects. A point defect is not extended in space in any dimension and this indicates that the lattice disorder is localised about a lattice site and includes a few nearest neighbours. In a semiconductor crystal, there are two main point defect categories: intrinsic (vacancies, antisite or self-interstitial) and extrinsic point defects including impurity atoms that occupy substitutional or interstitial lattice sites. For example, silicon is a semiconductor comprised of silicon atoms, each of which forms four bonds based upon its four valence electrons. Phosphorus has one more valence electrons than Si, so where P substitutes for Si in the semiconductor crystal and forms four bonds, there is an electron which is relatively easy to remove from the impurity and excite to the conduction band. The donation of the electron to the conduction band increases the number density of electrons that are free to move, and such impurities are termed donors. Moving the free electron from the donor level of Si to the CB requires much less energy than that of an intrinsic electron. In general, the defects in the semiconductor are used as dopants and create shallow and deep levels. However, defects in general could be beneficial or unhelpful; for instance, the native defects in CZTS make the compound p-type and in this case, impurities do not need to add, while these native defects become an issue if CZTS is required to be n-type.

The element stoichiometric ratios of Cu, Zn, Sn and S in Cu_2ZnSnS_4 are 2:1:1:4. However, a non-stoichiometry crystal structure indicates a high concentration of intrinsic defects and the coexistence of secondary phases [156]. CZTS is thermodynamically stable in only a narrow range of atomic chemical potentials [40, 82], with practical, efficient devices obtained in relatively Cu-poor and Zn-rich conditions [89, 90]; under these growth conditions ZnS constitutes a significant competing secondary phase. This growth condition works to suppress the major deep trap defects $(Cu_3)_{Sn}$ and Sn_{Zn} of growth in the CZTS which affects the cell efficiency [157]. These two key defects act as a recombination centre. In addition, it is found by using first principles calculations that this growth condition is required to prevent the formation of Cu_{Zn}+Sn_{Zn} and $2Cu_{Zn}$+Sn_{Zn} defect clusters which are deep donors in the CZTS gap [156]. Under this growth condition, the intrinsic defects (Cu_{Zn} and V_{Cu}) are responsible for p-type conductivity [90]. It is critical to understand the defect properties, including the native shallow and deep defects.

As-grown CZTS shows p-type conductivity, most probably due to the shallow acceptor levels of the intrinsic defects, Cu_{Zn} and V_{Cu} [22, 82]. Cu_{Zn} or V_{Cu} might contribute the majority of hole carries. Cu_{Zn} antisite [82, 158] might be a dominant native p-type defect, and it may be less likely to form under Cu-poor/Zn-rich conditions. Cu_{Zn} has lower formation energy and a relatively deeper acceptor level than V_{Cu}. In this system the n-type doping is extremely difficult [82]. The formation energies of self-interstitial point defects including Cu_i, Zn_i and Sn_i inside CZTS are high [40, 82]; therefore, examples of co-existence of these donor defects are extremely few.

The low efficiency of the kesterite-based solar cells is attributed to the limited open circuit voltage. The main factors leading to limits in the open circuit voltage are bulk defects, secondary phase’s formation [159].

In this chapter, based on first principle theory, the native defects and secondary phases in CZTS are investigated. Under specific Cu-poor and Zn-rich growth conditions, the phase stability and the formation energy of the point defects, impurities and secondary phases are explained. In addition, the most favourable diffusion barrier of the defects inside CZTS is identified to find the most stable defects, and the influence of these defects on p-type conductivity.

4.2 Computational Method

In this chapter, the computational approach has been described in Chapters 2 and 3 in terms of Brillouin-zone (Section 2.7.1), pseudo potentials (Section 2.7.3), formation energy (Section 3.5), binding energy (Section 3.9), diffusion (Section 3.8), and basis set with cut-off (Section 2.7.2), lattice constant (Section 3.3), binding energy (Section 3.9) and electronic structure (Section 3.4).

The formation energy of defects in the neutral charge state strongly relies on the atomic chemical potential of the species in the system as shown by Eq. (3.2) (Section 3.5) which has been used to find the linear equations of the vacancies and anti-site defects in CZTS with and without charges. The calculated chemical potential of Cu is -1305.11 eV at point P, Q, M and N, and μ_{Zn} is -1647.10, -1647.23, -1647.27 and -1647.16 eV at point P, Q, M and N, respectively. μ_{Sn} is -95.74, -96.15, -96.11 and -95.76 eV at point P, Q, M and N, respectively, while μ_{S} is -278.45, -278.31, -278.31 and -278.43 eV at point P, Q, M and N, respectively.

The crystal structure, sampling, the number of atoms and the relationship between the lattice of elements and secondary phases are listed in Table 4.1. The number of atoms which are listed in Table 4.1 are either for a primitive unit cell or for convenience when the conventional supercell is used. For example, CZTS is chosen to be 16-atom because the 16-atom block relates more simply to the cubic cell which is used for defect analyses.

Table 4. 1: Computational details for CZTS and its elements and secondary phases which are used in this thesis.

Formula	Crystal structure	Sampling	No. of atoms	Relationship between lattice
CZTS	Tetragonal	8×8×4	16	$a=b\neq c$
Cu	Cubic (Face-centred)	10×10×10	1	$a=b=c$
Zn	Hexagonal-close packed	10×10×10	2	$a=b\neq c$
α-Sn	Cubic (Face-centred)	10×10×10	2	$a=b=c$
S	Orthorhombic	2×2×2	128	$a\neq b\neq c$
ZnS	Cubic (Face-centred)	4×4×4	2	$a=b=c$
CuS	Hexagonal-close packed	6×6×2	2	$a=b\neq c$
Cu_2S	Monoclinic	2×2×2	144	$a\neq b\neq c$
α-SnS	Orthorhombic	6×2×6	12	$a\neq b\neq c$
SnS_2	Hexagonal	8×8×2	8	$a=b\neq c$
CTS	Monoclinic	4×6×4	24	$a\neq b\neq c$

The lower and upper bounds of the chemical potential region of CZTS are defined by [90]:

$$\Delta\mu_i(\mathrm{min}) \leq n_i\Delta\mu_i \leq \Delta\mu_i(\mathrm{max}) \qquad 4.1$$

$\Delta\mu_i(\mathrm{max})$ is usually equal to the zero.

$\Delta\mu_i = 0$ (for *i* in element phase, zero is the most positive value for *i*)

where $\Delta\mu_i$ is a difference in the chemical potential between a given value and its elemental state. The maximum value can have is represented by the relevant stable compound energy. For instance, in order to calculate the boundary of $\Delta\mu_{\mathrm{Zn}}$ (equilibrium inside CZTS) at $\Delta\mu_{\mathrm{Cu}}$=-0.2eV, the maximum value of $\Delta\mu_{\mathrm{Zn}}$ is zero and Eq. 4.2 will be used to find the minimum value of $\Delta\mu_{\mathrm{Zn}}$ by replacing $\Delta\mu_{\mathrm{Sn}}$ and $\Delta\mu_{\mathrm{S}}$ with zero (the deviation from the chemical potential defined by the equilibrium of the element) while $\Delta\mu_{\mathrm{Cu}}$ with -0.2eV. The reference state which defines the zero on the scale of the (Δ) is the element.

Eq. 4.2 will be:

$$2(-0.2) + \Delta\mu_{\mathrm{Zn}} = \Delta H_{\mathrm{CZTS}} = -4.07\mathrm{eV}$$

So $\Delta\mu_{\mathrm{Zn}} = -3.67$eV, this presents the minimum value of the Zn can be optioned under these conditions, and compensates for this value in Eq. 4.1; therefore, the boundary of $\Delta\mu_{\mathrm{Zn}}$ at $\Delta\mu_{\mathrm{Cu}}$=-0.2eV will be:

$$-3.67 \leq \Delta\mu_{\mathrm{Zn}} \leq 0$$

4.3 Results and Discussion

4.3.1 CZTS Crystal Structure

The ground state crystal structure of CZTS is zinc-blend derived kesterite. The crystal structure contains 8-atom primitive unit cells and it is a body-centered tetragonal, with c~2a (pseudocubic). For convenience, the simulation of bulk CZTS has been formed based on the non-primitive simple tetragonal unit cell containing two formula units [160] (*a*=*b*≠*c*, α=β=γ=90). The simulation cell is 16-atom, as illustrated in Fig. 4.1. The basic unit of CZTS is the tetrahedron. Cu and Zn atoms are located in the layer z=0, 1/2 and 1, whereas Cu and Sn atoms are located in the layer z=1/4 and 3/4, as shown in Fig. 4.1. Each metal atom is coordinated to four S atoms, and each S atom is coordinated to four metal atoms (two Cu and one atom of Zn and Sn).

Because of the different interactions between metal cation and sulfur anion, the lengths of every cation-anion bond are not identical. In the kesterite crystal structure, the Cu-S, Zn-S and Sn-S bond lengths are 0.232, 0.236 and 0.247nm, respectively, as illustrated in Fig. 4.1. The distance between the pair of sulphur atoms neighbouring the Cu, Zn or Sn inside bulk CZTS are 0.386, 0.387 and 0.407nm, respectively.

The fundamental property of any crystal structure is the lattice parameter. The calculated lattice constants (Section 3.3) with literature values for comparison are listed in Table 4.2.

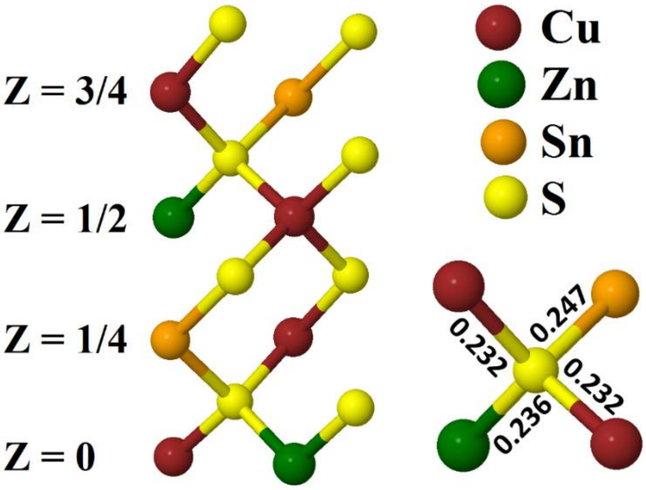

Figure 4. 1: Schematic of CZTS structure. The horizontal and vertical directions are [010] and [001], respectively, with [100] out of the paper. Bond lengths are given in nm.

Table 4. 2: Calculated lattice parameters of kesterite CZTS a, c (all in Å), comparing these parameters with theoretical and experimental results

a	*c*	Method	Ref.
5.426	10.81	Experimental	[144]
5.465	10.944	Theoretical	[143, 161]
5.466	10.929	Theoretical	[115]
5.466	10.932	Theoretical	Present work

The calculated theoretical band structure of kesterite CZTS between high-symmetry points (*Z*-*Γ*-*X*-*P*-*N*) in the Brillouin zone (BZ) has a direct energy band gap around the centre of the BZ at the Γ point and it has an underestimated value as explained in Section 3.4. The calculated energy band structure agrees with the results of a previous study [134].

4.3.2 Bulk Crystal Structure of Elements and Secondary Phases in CZTS

To examine the CZTS compound, the structure of its elements and secondary phases are investigated. The majority of these elements and phases have more than one structure; therefore, the most important step is to choose the right structures that have the minimum energy and are suitable for forming CZTS. AIMPRO was used to calculate the energy of elements (Cu, Zn, Sn, and S) and secondary phases (ZnS, CuS, SnS, SnS_2, and Cu_2SnS_3). In this simulation, a significant computational task is finding the stable equilibrium structure of elements and secondary phases. The resulting lattice constant elements and secondary phases in CZTS are listed in Table 4.3, which are consistent with the findings of previous studies. The crystal structures of elements or secondary phases in CZTS, that found more stability compared with the rest of the other compounds belonging to the same elements or secondary phase's structures, are explained below.

Table 4. 3: Calculated lattice parameters (a, b and c in Å, and β in °) of CZTS compound and its elements and secondary phases, comparing these parameters with previous work.

Formula		Lattice Constant		
		Present work	Previous work	Ref.
Cu	*a*	3.53827	3.597	[162]
Zn	*a*	2.6647	2.6648	[163]
	c	4.9467	4.9470	
α-Sn	*a*	6.40826	6.40	[164]
S	*a*	10.46395	10.4646	[165]
	b	12.86588	12.866	
	c	24.48608	24.486	
ZnS	*a*	5.471929	5.45	[166]
CuS	*a*	3.830689	3.788	[167]
	b	16.57474	16.333	
Cu_2S	*a*	14.94868	15.246	[168]
	b	12.23348	11.884	
	c	13.49049	13.494	
	β	115.9686	116.35	
α-SnS	*a*	4.41	4.333	[169]
	b	11.47	11.20	
	c	4.05	3.987	
SnS_2	*a*	3.638	3.64	[170, 171]
	c	5.879	5.89	
CTS	*a*	6.740	6.654	[172]
	b	11.691	11.534	
	c	6.780	6.659	
	β	109.67	109.4	

The quantitative accuracy of the lattice parameter across a wide range of materials is good and provide confidence that all these materials have been modelled accurately.

4.3.3 Formation Enthalpy of Secondary Phases

Any slight change in the stoichiometric ratio of elements in CZTS leads to the formation of secondary phases. Under Cu-poor/Zn-rich growth conditions, the possible secondary phases existing under this condition are listed in Table 4.4, and ZnS is the main secondary phase under this growth condition. The most stable structure of secondary phases in CZTS should require less formation energy than other phases. Therefore, the formation energy of secondary phases as a function of the chemical potential should be calculated to identify the stable region in CZTS.

The formation energy of defects in the neutral charge state strongly relies on the atomic chemical potential of the species in the system (Section 3.5).

Table 4. 4: Calculated formation enthalpies ΔH_f (in eV per formula) of CZTS compound, comparing them with the various theoretical (Theo.) and experimental (Exp.) calculations.

$\Delta H_f(ZnS)$	$\Delta H_f(CuS)$	$\Delta H_f(Cu_2S)$	$\Delta H_f(SnS)$	$\Delta H_f(SnS_2)$	$\Delta H_f(CTS)$	$\Delta H_f(CZTS)$	Method	Ref.
−2.14	−0.55	−0.82	−1.04	−1.45	_	_	Exp.	[157]
−1.63	−0.41	−0.41	−0.92	−1.16	−2.04	−3.77	Theo.	[157]
−1.99	−0.51	−0.86	−0.87	−1.29	−2.61	−4.69	Theo.	[157]
−1.90	−0.51	−0.81	−1.05	−1.33	−2.58	−4.59	Theo.	[90]
−1.75	−0.49	_	−1.01	_	−2.36	−4.21	Theo.	[158]
−1.74	−0.56	−0.69	−0.93	−1.06	−2.29	−4.07	Theo.	Present work

4.3.4 Stable Chemical Potential Range

For high-quality PV, the single phase produced should not contain secondary phases because these phases will generally affect the electrical and optical properties. For example, ZnS secondary phases have a wide band gap; therefore, if this phase exists in the absorber layer, they will potentially add traps for carriers. The population of diverse native defects depends on the conditions of the growth environment. These defects may have an effect when their concentrations are high. The single-phase stability of CZTS requires avoiding the secondary phases, but a series of competitive binary and ternary compounds in CZTS include ZnS, CuS, and CTS, among others. In practice, the elimination of secondary phases in CZTS plays an important role in improving the efficiency of the solar cell. This section focuses on the stability of bulk CZTS.

To produce single-phase CZTS, the native defects should be controlled by making the ratio of elements Cu:Zn:Sn:S nearly equal to the stoichiometric ratio 2:1:1:4 in CZTS. Two reasons may explain the dramatic non-stoichiometry:

(i) coexistence of native defects in CZTS and

(ii) high concentrations of these defects.

The single-phase stability of CZTS requires knowledge of the formation energy of each secondary phase. Usually, the single-phase stability has the lowest formation energy compared with the other secondary phases. Under several thermodynamic conditions, CZTS has stable stoichiometry with its elemental components.

Firstly, the sum of chemical potentials of the component elements should be in equilibrium with the formation energy of the compound [40]. Therefore, the chemical potentials of Cu, Zn, Sn, and S must satisfy the following equation:

$$2\Delta\mu_{\mathrm{Cu}} + \Delta\mu_{\mathrm{Zn}} + \Delta\mu_{\mathrm{Sn}} + 4\Delta\mu_{\mathrm{S}} = \Delta H_f(\mathrm{Cu_2ZnSnS_4}) = -4.07\ \mathrm{eV} \qquad (4.2)$$

where $\Delta H_f(\mathrm{Cu_2ZnSnS_4})$ is the heat of formation of CZTS.

Secondly, the phase of pure elements should be avoided in the samples with the limit of $\Delta\mu_i$=0, which means that *i* is rich enough to form the pure element and is in equilibrium with its standard state (solid, liquid, or gas) [22, 158, 173]. For instance, if $\Delta\mu_{\mathrm{Cu}} \geq 0$ in CZTS, Cu is formed instead of the single-phase CZTS. Therefore, the chemical potential in CZTS should be negative related to elements: $\Delta\mu_{\mathrm{Cu}} < 0$, $\Delta\mu_{\mathrm{Zn}} < 0$, $\Delta\mu_{\mathrm{Sn}} < 0$, and $\Delta\mu_{\mathrm{S}} < 0$.

Thirdly, the secondary sulphide phases formed by Cu, Zn, and Sn cations, which are binary or ternary compounds, should not exist in the equilibrium CZTS phase; these phases include CuS, Cu_2S, ZnS, SnS, SnS_2, Cu_2SnS_3, among others. Furthermore, any state that deviates from the stoichiometry (2:1:1:4) of the CZTS compound should be avoided in accordance with the following relationships [82]:

$$\Delta\mu_{\mathrm{Cu}} + \Delta\mu_{\mathrm{S}} < \Delta H_f(\mathrm{CuS}) = -0.56\ \mathrm{eV} \qquad (4.3a)$$

$$\Delta\mu_{\mathrm{Cu}} + \Delta\mu_{\mathrm{S}} < \Delta H_f(\mathrm{CuS_2}) = -0.69\ \mathrm{eV} \qquad (4.3b)$$

$$\Delta\mu_{\mathrm{Zn}} + \Delta\mu_{\mathrm{S}} < \Delta H_f(\mathrm{ZnS}) = -1.74\ \mathrm{eV} \qquad (4.3c)$$

$$\Delta\mu_{\mathrm{Sn}} + \Delta\mu_{\mathrm{S}} < \Delta H_f(\mathrm{SnS}) = -0.93\ \mathrm{eV} \qquad (4.3d)$$

$$\Delta\mu_{\mathrm{Sn}} + 2\,\Delta\mu_{\mathrm{S}} < \Delta H_f(\mathrm{SnS_2}) = -1.06\ \mathrm{eV} \qquad (4.3e)$$

$$2\Delta\mu_{\mathrm{Cu}} + \Delta\mu_{\mathrm{Sn}} + 3\Delta\mu_{\mathrm{S}} < \Delta H_f(\mathrm{Cu_2SnS_3}) = -2.29\ \mathrm{eV} \qquad (4.3f)$$

The value of the formation energy of secondary phases in Eq. (4.3) is derived from our results, which are listed in Table 4.4. The presence of the secondary phases is always possible in any area that does not satisfy Eq. (4.3). Each region of secondary phases represents the boundary of phases that could coexist throughout the growth process of CZTS. For instance, the co-existence of the CTS secondary phase is in the region which does not satisfy Eq. (4.3f).

The chemical potential diagram calculated by varying $\Delta\mu_{\mathrm{Zn}}$ and $\Delta\mu_{\mathrm{Sn}}$ and fixing $\Delta\mu_{\mathrm{Cu}}$ shows CZTS phase stability and secondary phases around the CZTS phase. The chemical potential range that stabilises CZTS against secondary phases, including: CuS, Cu_2S, ZnS, SnS, SnS_2 and CTS, is plotted in Figs. 4.2, 4.3, 4.4, 4.5 and 4.6 based on Eq. (3.2) (Section 3.5), which was used to find the linear equation of the secondary phases. The area labelled CZTS in Fig. 4.2 represents the chemical potential region that stabilises the single-phase CZTS, which is surrounded by different regions of secondary phases. The values of $\Delta\mu_{\mathrm{Zn}}$ and $\Delta\mu_{\mathrm{Sn}}$ are limited and linked to the value of μ_{Cu}. The slices in Figs. 4.2, 4.3, 4.4, 4.5, 4.6 and 4.7 represent a plane cut at a different value of μ_{Cu} (0, −0.06, −0.2, −0.564, −0.634, and −1.33eV) to show how the secondary phases limit the formation of the single-phase CZTS. When $\mu_{\mathrm{Cu}} = 0$eV (Fig 4.2) represents a Cu-rich case. At $\Delta\mu_{\mathrm{Cu}} = -0.06$ (Fig. 4.3) and −0.2eV (Fig. 4.4) there is a stable region of CZTS. CuS secondary phases are no longer possible at $\Delta\mu_{\mathrm{Cu}} = -0.564$eV (Fig. 4.5). The stable region of CZTS vanishes to nearly a point at $\Delta\mu_{\mathrm{Cu}} = -0.634$eV (Fig. 4.6), and below this value such as at the value of $\mu_{\mathrm{Cu}} =-1.33$eV (Fig. 4.7), there is no stable region of CZTS. These values are chosen because of physical conditions and also to allow a direct comparison with the literature.

The boundaries of the chemical potential region calculated by using Eq. 4.1 for each species based on Eq. 4.2 are:

$$-2.035 \leq \Delta\mu_{\mathrm{Cu}} \leq 0\mathrm{eV} \qquad 4.4\ (a)$$

$$-4.07 \leq \Delta\mu_{\mathrm{Zn}} \leq 0\mathrm{eV} \qquad 4.4\ (b)$$

$$-4.07 \leq \Delta\mu_{\mathrm{Sn}} \leq 0\mathrm{eV} \qquad 4.4\ (c)$$

$$-1.0175 \leq \Delta\mu_{\mathrm{S}} \leq 0\mathrm{eV} \qquad 4.4\ (d)$$

As a result of Eq. (4.2), the chemical potential ranges of Cu, Zn, and Sn can be independent variables in the four compound system and the chemical potential of S is fixed. The stable narrow region limited by the inequalities in Eq. (4.3) is in the three-dimensional ($\Delta\mu_{Cu}$, $\Delta\mu_{Zn}$, $\Delta\mu_{Sn}$) space, while the chemical potential of S relates to Cu, Zn, and Sn.

Under equilibrium conditions, the Cu-rich/Zn-poor conditions generally mean a higher numerical value of $\Delta\mu_{Cu}$ than $\Delta\mu_{Zn}$, which are required for the growth of single-phase CZTS. Conversely, the Cu-poor/Zn-rich conditions correspond to high efficiency devices, which probably produce secondary phases, mainly ZnS. In other words, Zn-rich and Zn-poor conditions usually lead to the formation of ZnS and CTS, respectively [22].

Under Cu-poor/Zn-rich conditions, at $\Delta\mu_{\mathrm{Cu}} = 0\mathrm{eV}$ the single-phase CZTS formation is extremely small (nearly a point) as shown in Fig.4.2. The calculated results of the stable region of chemical potential in CZTS at $\Delta\mu_{\mathrm{Cu}} = 0\mathrm{eV}$ agree with the findings of a previous study Ref. [90].

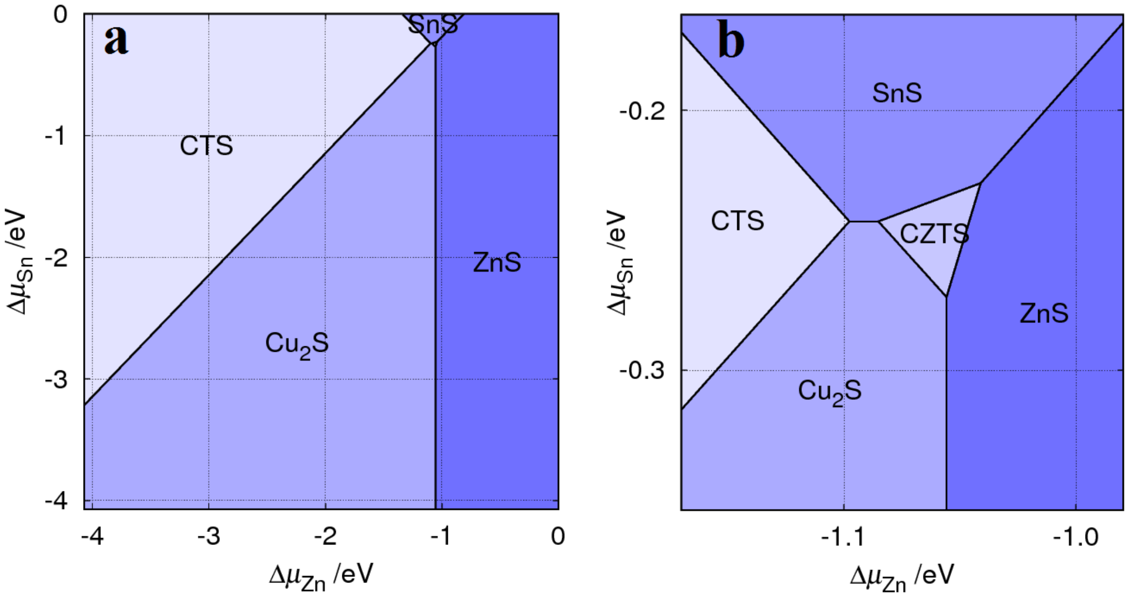

Figure 4. 2: The calculated stable phase diagram for μ_{Cu}=0: (a) the plots of these ranges are as defined by Eq. 4.2; (b) shows the plot over a smaller range of energies highlighting the CZTS stable region.

When μ_{Cu} become more negative at $\Delta\mu_{\mathrm{Cu}} = -0.06, -0.2$ and $-0.564\mathrm{eV}$, the single-phase CZTS becomes a region as shown in Figs. 4.3, 4.4 and 4.5. The areas of the single-phase CZTS regions in Figs. 4.3, 4.4, 4.5 are not constant and change with the more Cu poor. The calculated results of the stable region of chemical potential in CZTS at $\Delta\mu_{\mathrm{Cu}} = -0.06, -0.2$ and $-0.564\mathrm{eV}$ agree with previous findings [90]. In this thesis, all the calculations are under the condition Cu-poor-Zn-rich at $\Delta\mu_{\mathrm{Cu}} = -0.2\mathrm{eV}$, and the single phase stability of CZTS is labelled by P, Q, M and N, as illustrated in Fig. 4.4. These conditions will therefore form this point which is referred to as ‘standard growth conditions’.

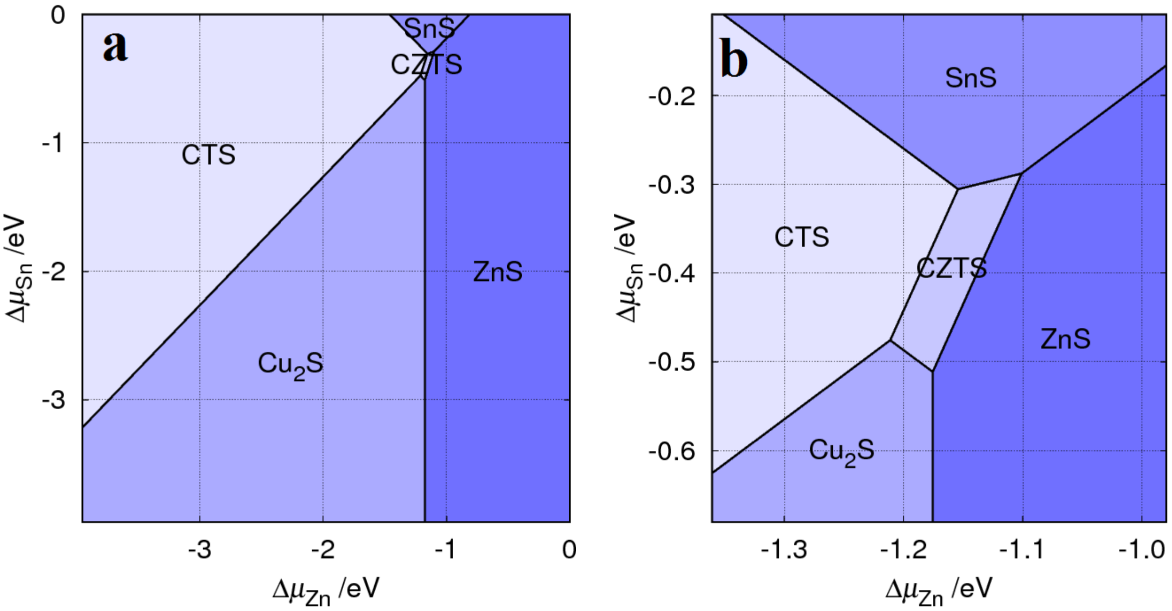

Figure 4. 3: The calculated stable phase diagram for $\mu_{\mathrm{Cu}} = -0.06\mathrm{eV}$; ranges for (a) and (b) are as defined in Eq. 4.2.

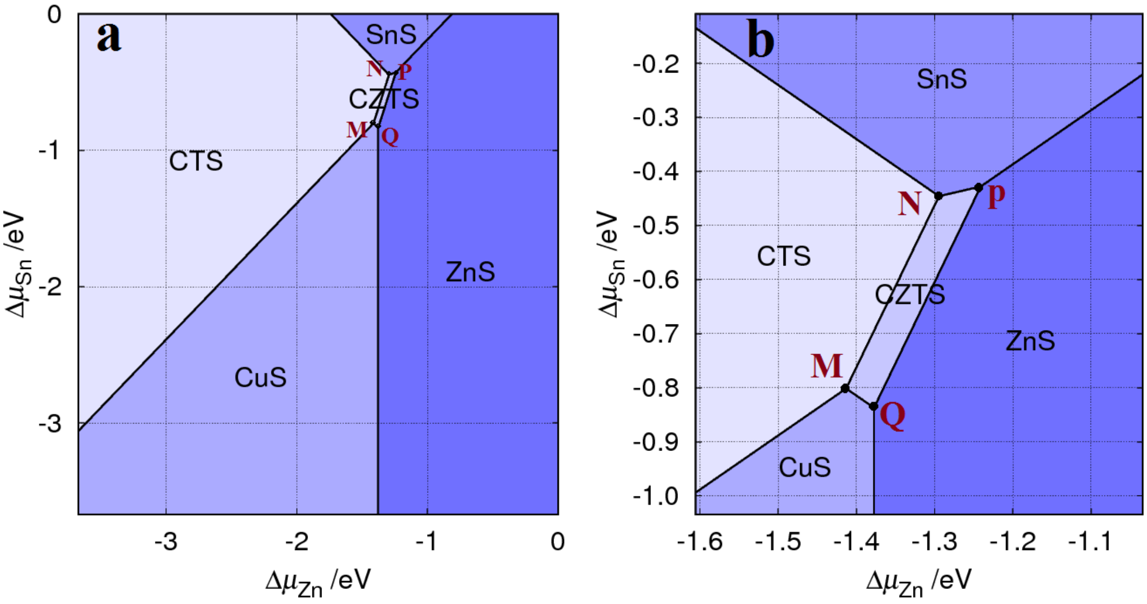

Figure 4. 4: The calculated stable phase diagram for $\mu_{\mathrm{Cu}} = -0.2\mathrm{eV}$; ranges for (a) and (b) are as defined in Eq. 4. The marked points are at the corners of the CZTS stability region.

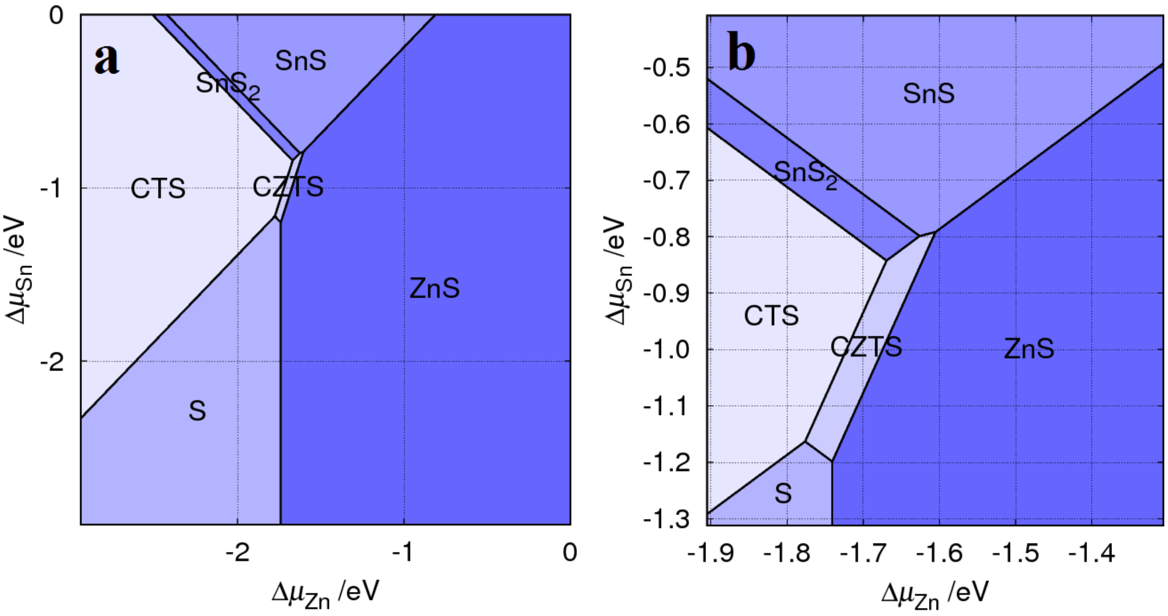

Figure 4. 5: The calculated stable phase diagram for $\mu_{Cu} = -0.564$eV; ranges for (a) and (b) are as defined in Eq. 4.2.

The single-phase CZTS finally vanishes to nearly a point when $\Delta\mu_{Cu} = -0.634$eV as shown in Fig. 4.6. The calculated results of the stable region of chemical potential in CZTS at $\Delta\mu_{Cu} = -0.634$eV agree with the findings of a previous study [90].

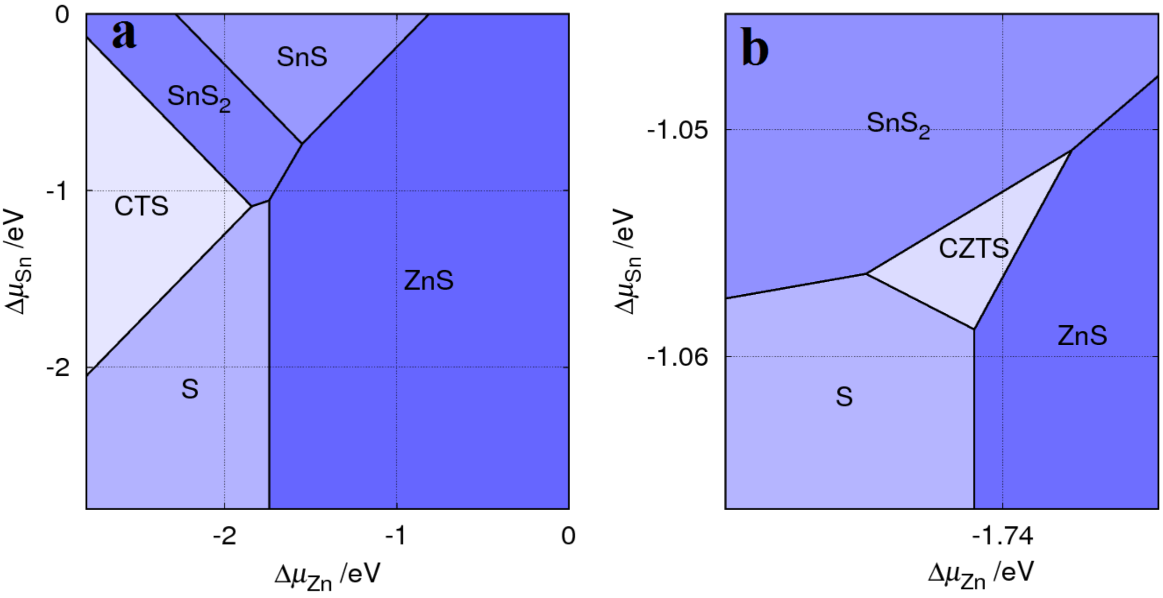

Figure 4. 6: The calculated stable phase diagram for $\mu_{Cu} = -0.634$eV; ranges for (a) and (b) are as defined in Eq. 4.2.

The formation of single-phase CZTS is in equilibrium when conditions are Cu-poor, such as when $\Delta\mu_{\mathrm{Cu}} = -1.33\mathrm{eV}$ as shown in Fig. 4.7. The calculated results of the stable region of chemical potential in CZTS at $\Delta\mu_{\mathrm{Cu}} = -1.33\mathrm{eV}$ agree with the findings of a previous study [90].

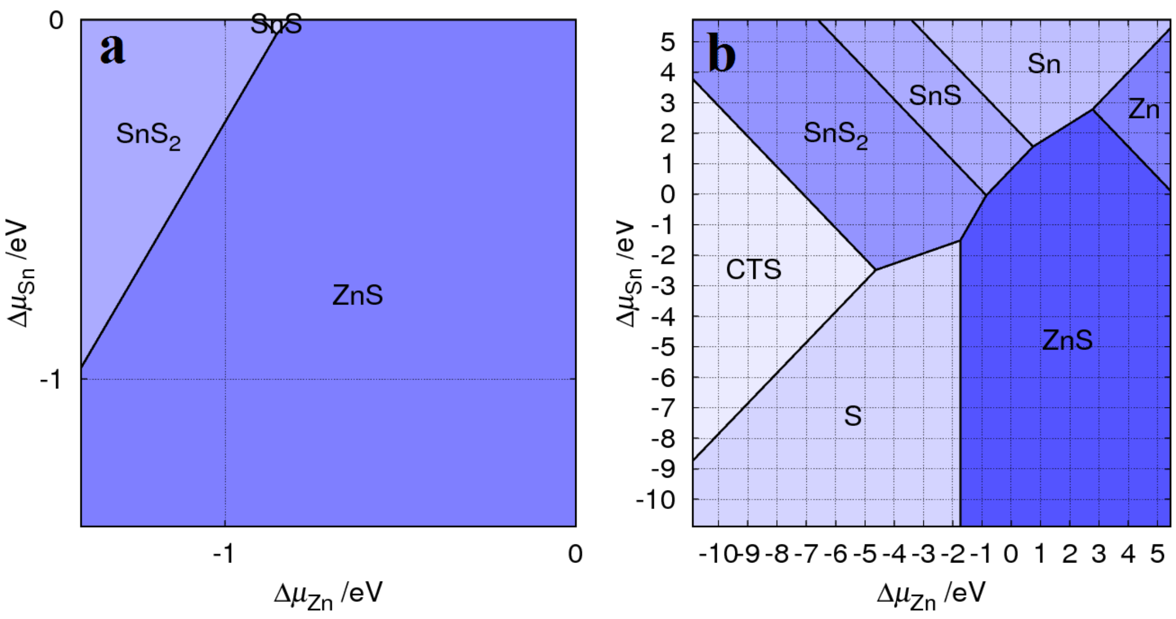

Figure 4. 7: The calculated stable phase diagram for $\mu_{\mathrm{Cu}} = -1.33\mathrm{eV}$; ranges for (a) and (b) are as defined in Eq. 4.2.

Controlling the chemical potential at the different $\Delta\mu_{\mathrm{Zn}}$ and $\Delta\mu_{\mathrm{Sn}}$ planes is crucial. In particular, the chemical potential of Zn is bound to an extremely narrow region; consequently, the stable region is very narrow along the $\Delta\mu_{\mathrm{Zn}}$ axis [40], as shown in Figs. 4.3, 4.4 and 4.5. Therefore, the chemical potential control of Zn is critical for the growth of stoichiometric high-quality single crystals and should be accurately measured. Meanwhile, the ranges of stable $\Delta\mu_{\mathrm{Cu}}$, $\Delta\mu_{\mathrm{Sn}}$ and $\Delta\mu_{\mathrm{S}}$ are wider than $\Delta\mu_{\mathrm{Zn}}$. As can be seen in Figs. 4.4 and 4.5, for CZTS, the stable range on the Sn axis is about 0.4eV whereas on the Zn, it is around 0.2eV.

According to Eq. 4.3 (a, b) the secondary phases of CuS cannot provide at $\Delta\mu_{\mathrm{Cu}} \leq -0.564\mathrm{eV}$, as shown in Figs. 4.5 and 5.6, because Cu is insufficient to form these phases according to Eqs. (4.3a) - (4.3b). In addition, the available chemical potential of S ($-0.735\mathrm{eV} \leq \Delta\mu_{\mathrm{S}} \leq 0\mathrm{eV}$) according to Eq. 4.1 at $\Delta\mu_{\mathrm{Cu}} \leq -0.564\mathrm{eV}$ cannot achieve the value of $\Delta H_f(\mathrm{CuS}) = -0.56$ eV to provide CuS. The calculated results of the stable region of chemical potential in CZTS agree with the findings of a previous study [90].

4.3.5 Intrinsic Point Defect Formation and Ionization in Kesterite

In the compound semiconductor, cation and anion vacancies as well as antisite defects can be formed. CZTS have significant native lattice defects including vacancies (V_{Cu}, V_{Zn}, V_{Sn} and V_S) as shown in Fig. 4.8 and antisites (Cu_{Zn}, Cu_{Sn}, Zn_{Cu}, Zn_{Sn}, Sn_{Cu} and Sn_{Zn}), as illustrated in Fig. 4.9. These defects form by non-stoichiometry or growth annealing [174]. The intrinsic defects can be divided into electron acceptors and donors based on the valences of the elements. For example, the valence of Zn is 2 and the valence of Cu is one so if Zn replaces Cu there is an excess of Cu valence whereas if Cu replaces Zn there is a deficit of Cu. Therefore, Zn in a Cu site will be a donor and Cu in a Zn site will be an acceptor.

For the optimised cation vacancies, the distances between the pair of sulphur atoms neighbouring the Cu, Zn or Sn vacancy inside bulk CZTS are listed in Table 4.5. For the antisites, the bond length of a single acceptor defect Cu_{Zn}-S, a double acceptor defect Cu_{Sn}-S, a single donor defect Zn_{Cu}-S, a double acceptor defect Zn_{Sn}-S, Sn_{Cu}-S and Sn_{Zn}-S are listed in Table 4.5. The strains in CZTS when there are cation vacancies or antisite defects are listed in Table 4.5. The bond length of Zn-S (Fig.4.1) is slightly longer within 0.2% than that of Cu_{Zn}-S (Fig. 4.4), whilst the bond length of Zn_{Cu}-S is 0.5% larger than that of Cu-S, and the bond length of Zn_{Sn}-S is 0.9% shorter than that of Sn-S.

Table 4. 5: Calculated bond-length (nm) and strain (%) for cation vacancies and antisite defects inside CZTS

Formula	Bond-length (nm)	Strain (%)
S-V_{Cu}-S	0.387	+0.2
S-V_{Zn}-S	0.384	−0.8
S-V_{Sn}-S	0.405	−0.5
Cu_{Zn}-S	0.234	−0.8
Cu_{Sn}-S	0.233	−5.0
Zn_{Cu}-S	0.237	+3.0
Zn_{Sn}-S	0.238	−4.0
Sn_{Cu}-S	0.274	+18
Sn_{Zn}-S	0.273	+11

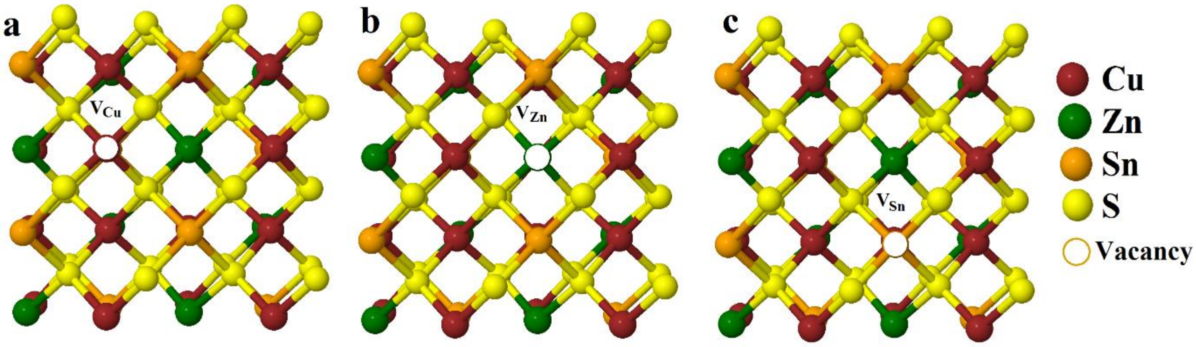

Figure 4. 8: Cation vacancies inside CZTS: (a) V_{Cu}, (b) V_{Zn} and (c) V_{Sn}.

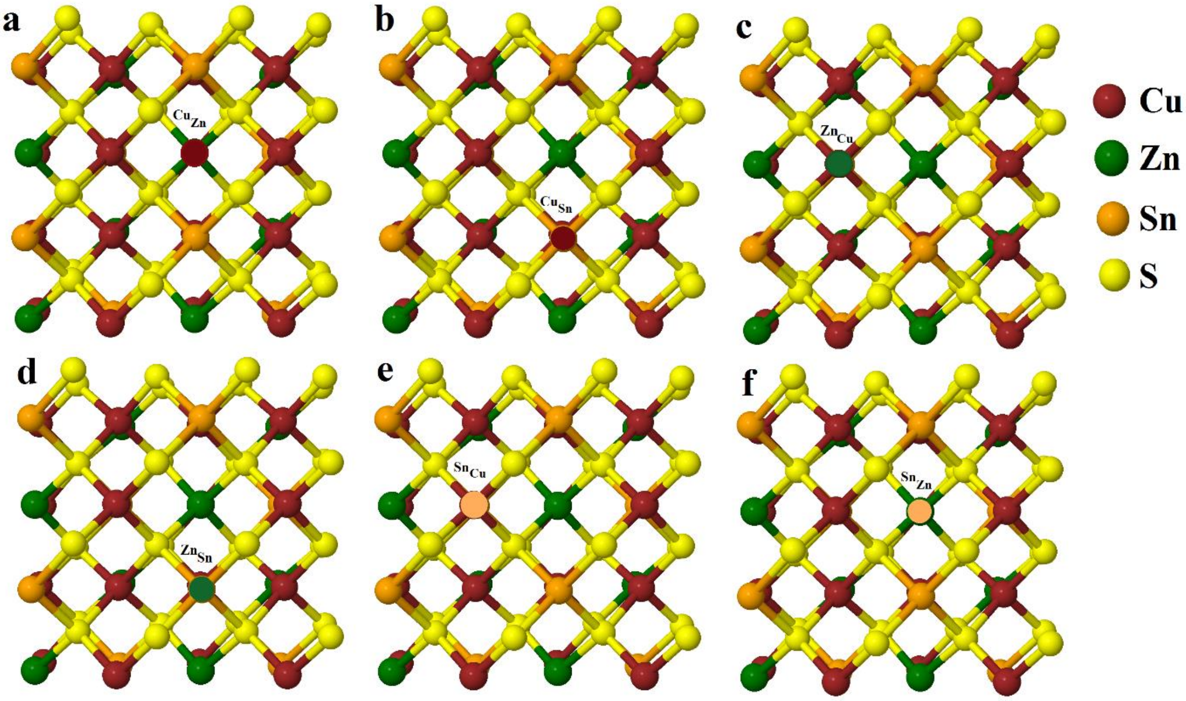

Figure 4. 9: Cation antisites defects inside CZTS: (a) Cu_{Zn}, (b) Cu_{Sn}, (c) Zn_{Cu}, (d) Zn_{Sn}, (e) Sn_{Cu} and (f) Sn_{Zn}.

The formation energy of charged defects depends on the level of μ_e according to Eq. (3.2) (Section 3.5). For instance, as shown in Fig. 4.10, the shift of the Fermi energy from the VBM to the CBM increases (decreases E^f) the probability of formation of the negatively charged acceptors, whereas positively charged donors increase when the Fermi energy shifts toward the VBM (see Section 3.6) [82].

The formation energy of point defects is calculated under standard growth conditions at points P, Q, M and N at different chemical potentials $\mu_{Cu} = -0.2$ and 0 eV (neutral charge states), as listed in Table 4.6. The features of the intrinsic defects of the kesterite CZTS are illustrated in Fig. 4.10, which represents the defect formation energy as a function of μ_e.

The most stable charge state was plotted under the conditions of point P. Point P was chosen to compare our findings with previous results.

Table 4. 6: Calculated defect formation energy ΔH_f (eV) of different points (P, Q, M, N) in CZTS supercell with 512 atoms at different chemical potential (μ_{Cu} =−0.2, 0 eV), comparing them with the previous calculations for a supercell containing 64 atoms [82] and 512 atoms [175].

μ_{Cu} = −0.2 eV (present work)										
Def.	**V_{Cu}**	**V_{Zn}**	**V_{Sn}**	**V_S**	**Cu_{zn}**	**Cu_{sn}**	**Zn_{cu}**	**Zn_{sn}**	**Sn_{cu}**	**Sn_{zn}**
P	0.71	1.07	2.83	1.08	−0.03	0.77	0.97	0.65	2.13	1.14
P(64-atom)	(0.74)	(1.06)	(2.79)		(−0.1)	(0.83)	(0.84)	(0.64)	(2.16)	(1.23)
Q	0.71	0.93	2.42	1.22	−0.17	0.36	1.10	0.37	2.53	1.41
M	0.71	0.89	2.46	1.22	−0.21	0.40	1.14	0.45	2.50	1.34
N	0.71	1.01	2.81	1.10	−0.09	0.75	1.02	0.69	2.14	1.10
μ_{Cu} = 0 eV (present work)										
P	0.91	1.27	3.03	0.88	−0.03	0.77	0.78	0.65	2.13	1.14
Q	0.91	1.13	2.62	1.02	−0.17	0.36	0.92	0.37	2.53	1.41
M	0.91	1.09	2.66	1.02	−0.21	0.40	0.96	0.45	2.50	1.34
N	0.91	1.21	3.01	0.90	−0.09	0.75	0.84	0.69	2.14	1.10
μ_{Cu} = 0 eV Ref [82]										
P	0.77	1.12	2.82	0.99	0.01	0.87	2.42	0.69	6.54	4.11
Q	0.77	0.88	2.11	1.23	−0.23	0.16	2.66	0.22	7.25	4.58
M	0.77	0.79	2.21	1.23	−0.32	0.26	2.76	0.4	7.16	4.39
N	0.77	0.98	2.78	1.04	−0.13	0.83	2.57	0.79	6.59	4.01
μ_{Cu} = 0 eV Ref [175]										
P	0.59	0.89	_	_	−0.06	0.73	_	0.53	_	_
Q	0.59	0.7	_	_	−0.25	0.17	_	0.16	_	_
M	0.59	0.63	_	_	−0.32	0.23	_	0.29	_	_
N	0.59	0.79	_	_	−0.16	0.7	_	0.59	_	_

Shallow acceptor levels in CZTS are V_{Cu} and Cu_{Zn}. These defects act as a single acceptor and can have charge states (1−). V_{Cu} has a more shallow transition energy level compared with other defects as shown in Fig. 4.10. The acceptor antisite Cu_{Zn} has a lower formation energy than the other defects as shown in Fig. 4.10. This trend indicates that the most likely dominant defect in CZTS is always Cu_{Zn} in the stable region of chemical potential.

The ionization and high population of the dominant Cu_{Zn} can produce a considerable number of hole carriers. This trend shows that CZTS always has p-type conductivity and it is difficult to transform it to the n-type [82], since the stability of CZTS is narrow.

Under Cu-poor conditions, the remaining acceptor defects are deep, such as Zn_{Sn}, V_{Zn}, Cu_{Sn} and V_{Sn}. These deep defects act as a double acceptor for Zn_{Sn} and V_{Zn} and can have the charge states 2− whereas Cu_{Sn} and V_{Sn} act as triple and quadruple acceptors and can have the charge states 3− and 4−, respectively. These defects have much deeper levels and higher formation energies as shown in Table 4.6. Therefore, their effect on the p-type conductivity can be ignored in the single-phase CZTS. However, these deeper defects could act as recombination centres.

The shallow donor level of CZTS is Zn_{Cu} acts as a single donor and can have the charge states (1+). This shallow donor defect represents the lowest energy donor [40, 82].

The deep donor levels of CZTS are Sn_{Cu}, Sn_{Zn} and V_S. These deep defects act as a triple, double and double donor and can have the charge states 3+, 2+ and 2+, respectively. The ionization of donor defects produces electrons; the high population of these defects forms high carrier concentrations that affect electrical conductivity. Therefore, the deep levels of the charged donor defects can work as centres for electron–hole recombination.

In a case where the Fermi energy is close to VBM, the formation energy of the positively charged donors, including Zn_{Cu}^{+}, Sn_{Zn}^{2+} and V_S^{2+}, is significantly lower than their neutral states as shown in Fig. 4.10. The reason for that is that when Sn ($5s^2 5p^2$) replaces Cu ($3d^{10} s^1$), the Cu ion should be +1 so Sn loses one electron and three extra electrons (i.e. two 5s and one 5p) occupy the donor levels. The ionization of the single 5p electron is easy because the 5p orbital has high energy; thus, Sn_{Cu} (0/+) is relatively shallow. By contrast, the ionization of the 5s orbital has considerably lower energy than that of the 5p orbital; thus, the two 5s electrons can be ionized with difficulty [40]. Subsequently, the ionization of the electrons for the (+/3+) level is more difficult and occurs deep in the band gap structure. Similarly, two 5s electrons occupy the donor levels when Sn replaces Zn. Whenever Sn becomes less negative while Cu and Zn become more negative, the formation energy of donor defects Sn_{Cu} and Sn_{Zn} is reduced, and that is not suitable for p-type solar cell efficiency. The deep donor levels in the CZTS are V_S anion vacancies as shown in Fig. 4.10. In neutral or charged states, the formation energy of V_S is dramatically high so it cannot be formed easily compared to other cation vacancy defects.

In general, donor defects in the neutral state have higher formation energies than acceptor defects, as shown in Fig. 4.10 and Table 4.6. Therefore, these energies are consistent with the observations, and kesterite samples as grown have p-type conductivity, with Fermi energy close to VBM.

The transitions energies relative to one of the native defects are listed in Table 4.7, and these values can be compared with the relevant data in publications such as Ref. [40]. Noting that the calculated data for the electrical levels are agreed with the literature such as Ref. [40] which including different approaches to correct the periodic boundary conditions.

Table 4. 7: Calculated relative transition energy for the CZTS native defects explored in this study. All energies in (eV).

X (acceptor)	$\boldsymbol{E(-/0)_{\mathrm{x}} - E(-/0)_{\mathrm{V_{Cu}}}}$	$\boldsymbol{E(2-/-)_{\mathrm{x}} - E(2-/-)_{\mathrm{V_{Zn}}}}$
V_{Zn}	0.01	-
V_{Sn}	0.08	0.09
Cu_{Zn}	0.09	-
Cu_{Sn}	0.14	0.17
Zn_{Sn}	0.04	0.04
X (donor)	$E(0/+)_{\mathrm{x}} - E(0/+)_{\mathrm{Sn_{Cu}}}$	$E(+/+2)_{\mathrm{x}} - E(+/+2)_{\mathrm{Sn_{Zn}}}$
V_S	−0.65	−0.21
Zn_{Cu}	−0.03	
Sn_{Zn}	−0.45	

According to Eq. 4.3, when the chemical potential exceeds the boundaries of the stable chemical potential region, such as the secondary or non-stoichiometric phases, the dominant defects in the CZTS can be changed according to the significant change of the formation energies and the population of different defects.

The p-type conductivity of quaternary CZTS can be attributed to the Cu_{Zn} anti-site which differs from the situation in ternary compounds, including CIS. In CIS, the p-type conductivity can be attributed to the V_{Cu}. This trend is attributed to Cu_{Zn} , which has the lowest formation energy in CZTS; by contrast, V_{Cu} has the lowest formation energy in CIS [82].

Actually, under the conditions of point P, our calculations reveal that the formation energy of the neutrally charged V_{Cu} is 0.77eV, whereas the formation energy of neutrally charged Cu_{Zn} is –0.03 eV, which is less than that of V_{Cu}, as plotted in Fig. 4.10. This trend is consistent with the fact that the chemical difference between copper and a vacancy is larger than that between copper and zinc. However, in the quaternary CZTS compound, the difference between Cu(I) and Zn(II) in electrical valence is equivalent to one in the Cu_{Zn} anti-site, which is the same for V_{Cu}. By contrast, in ternary CIS, a significant difference exists between the formation energy of Cu and In, which makes the formation energy of V_{Cu} lower than that of Cu_{In}.

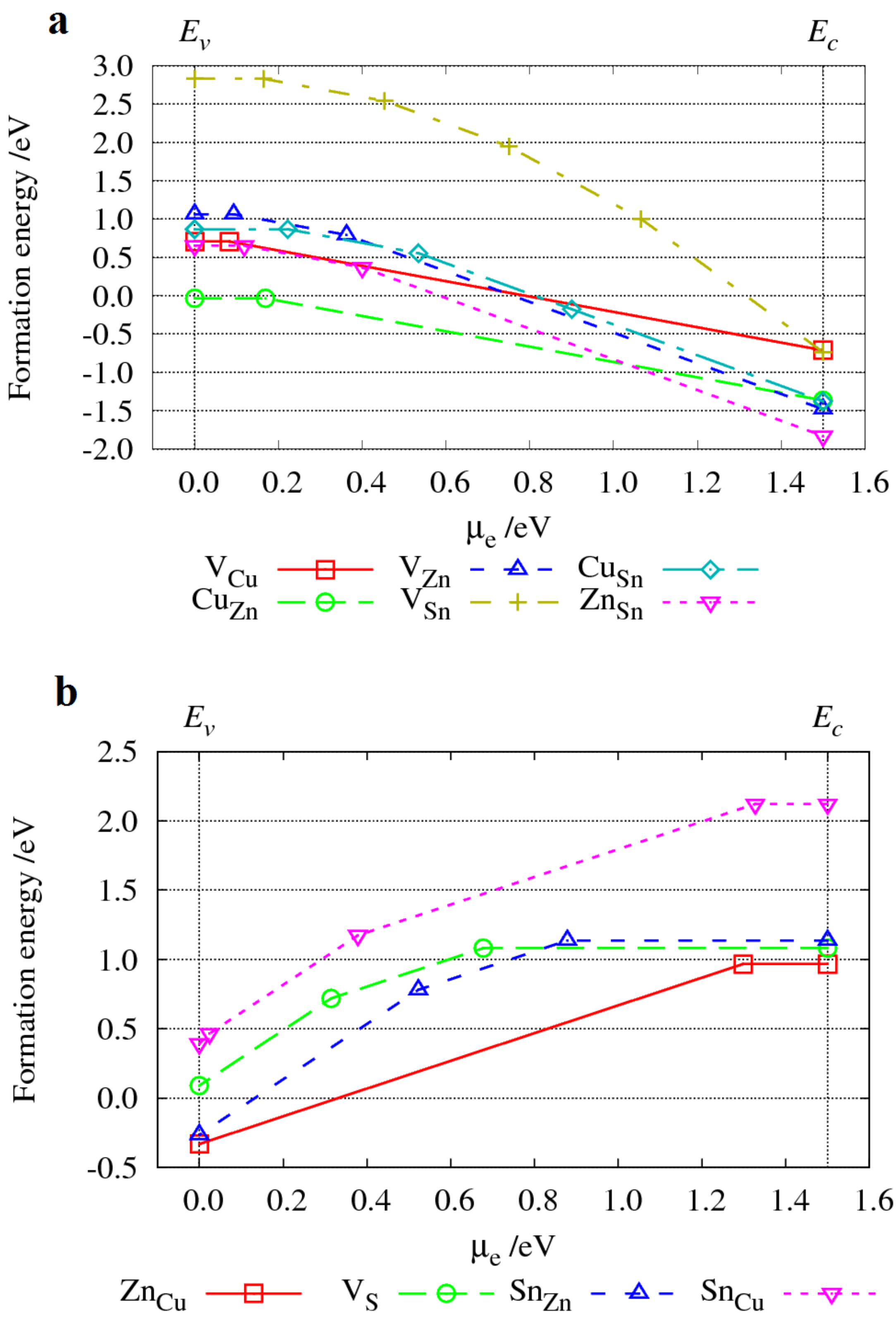

Figure 4. 10: The change of the defect formation energy as a function of the electron chemical potential (μ_e) in CZTS with a 512-atom supercell under the conditions of point P (Fig. 4.4). The most stable charge state for each value of μ_e is only plotted: (a) plots show acceptor defects, (b) plots show donor defects.

It has been found, under equilibrium growth conditions (Cu-rich/Zn-poor) for high-efficient CZTS samples, that Cu_{Zn} and V_{Cu} are the dominant defects. However, given the relatively deep acceptor level of Cu_{Zn}, the performance of the solar cells may not be optimum. Indeed, Cu-poor/Zn-rich conditions are widely used to improve the PV efficiency, which supports the formation of V_{Cu} and restricts the formation of Cu_{Zn}. In addition, Fig 4.10 shows that the formation energy lines of acceptor defects in general are less than those of donor defects. Even when the Fermi level is at the VBM, the formation energies of the neutral donors are dramatically higher than the formation energies of the charged donors Zn_{Cu}^{+} and Sn_{Zn}^{2+}. The low acceptor formation energy illustrates that grown CZTS samples always show p-type conductivity; this trend supports the experimental observations reported by several research groups [176-179].

4.3.6 Cd in Bulk CZTS

CdS is commonly used as the buffer layer for CZTS cells (Chapter 7, Chapter 8). Cd can diffuse across the junction from CdS to CZTS and become an impurity inside CZTS and form substitutional defects in CZTS at the CZTS/CdS interface (Section 8.3.5.2). The impact of Cd inside bulk CZTS has been investigated.

In CZTS, the four bond lengths between Cd_{Cu}, Cd_{Zn} and Cd_{Sn} and sulphur are the same within three decimal places, 0.254nm. The Cd_{Cu}-S is 0.022 longer than that of Cu-S in CZTS, and Cd_{Zn}-S is 0.018 longer than that of Zn-S inside CZTS, while Cd_{Sn}-S is 0.007 shorter than that of Sn-S inside CZTS. Therefore, the strains which arise in CZTS because of Cd_{Cu}, Cd_{Zn} and Cd_{Sn} substitutional defects are +9%, +8% and −3%, respectively.

4.3.7 Formation Energy of Impurities

The formation energy of the impurity defects are calculated including Cd inside bulk CZTS, as shown in Table 4.8 for standard growth conditions at μ_{Cu}=−0.2 eV [40] for the four boundary points P, Q, M and N of the CZTS stable region (see Fig. 4.4), as shown in Table 4.8.

Perhaps unsurprisingly, it is found that the iso-electronic defect Cd_{Zn} has the lowest formation energy compared with the formation energies of the other sites. Therefore, the co-existence of the iso-electronic defect Cd_{Zn} inside CZTS could be easily understood in CZTS compared with other Cd substitution defects under equilibrium growth conditions. In addition, Cd_{Sn} has lower formation energy under the above growth conditions in comparison with the formation energy of the donor substitution defects Cd_{Cu} inside CZTS. Therefore, the acceptor substitution defect for Cd impurity in CZTS can form more easily than donor substitution defects. Maeda et al. [180] obtained that when carrying out CZTS doping with Cd in a supercell containing 64 atoms, the formation energy of Cd_{Zn} (0.53eV) is lower than that of Cd_{Cu} and Cd_{Sn}, and this agrees with the results for 512-atom cells.

Table 4. 8: Calculated formation energies of neutral substitutional defects inside bulk CZTS with 512 atoms for points P, Q, M and N (Fig. 4.4). All energies are in eV.

Defects	$E^f_{\mathrm{P}}(64)$	$E^f_{\mathrm{P}}(512)$	E^f_{Q}	E^f_{M}	E^f_{N}
Cd_{Cu}	1.08	1.06	1.20	1.20	1.08
Cd_{Zn}	0.15	0.10	0.10	0.06	0.06
Cd_{Sn}	0.75	0.75	0.48	0.52	0.75

4.3.8 Binding Energy of Antisite and Substitutional Defects

The process of Cd diffusing to CZTS is via a vacancy. The mechanisms for the diffusion of Cd substituting for Cu, Zn and Sn are likely to involve a Cu, Zn and Sn vacancy; therefore, part of the analyses of energies involves whether or not there is binding of such vacancy to the impurity.

Binding energy refers to the difference in the formation energies between product and reactants. For a bound system, the binding energy is positive (Section 3.9). The binding energies of both antisite and substitutional defects with vacancy inside bulk CZTS are calculated, as listed in Table 4.9. The negative values of the binding energies for Cu_{Zn}+V_{Zn}, Zn_{Sn}+V_{Sn} and Cd_{Sn} +V_{Sn} means that these defects are not bound. However, the positive values of a single donor antisite with vacancy Zn_{Cu}+V_{Cu} and a single donor substitutional with vacancy Cd_{Cu}+V_{Cu} refer to the fact that the defects are bound.

Table 4. 9: Calculated binding energies of both antisite and substitutional defects with vacancy inside bulk CZTS with 64 atoms. All energies are in eV.

Defects	E^b
Cu_{Zn} +V_{Zn}	−0.15
Zn_{Cu} +V_{Cu}	0.56
Zn_{Sn} +V_{Sn}	−0.30
Cd_{Cu} +V_{Cu}	0.77
Cd_{Zn} +V_{Zn}	0.00
Cd_{Sn} +V_{Sn}	−0.05

4.3.9 Inter-diffusion Inside Bulk CZTS

Intrinsic defects such as cation vacancy and antisite defects including Cu_{Zn}, Zn_{Cu} and Zn_{Sn} (Figs. 4.8 and 4.9) inside bulk CZTS in addition to the substitutional defect in CZTS are studied under standard growth conditions. The impurity defects come from the buffer layer CdS.

4.3.9.1 Diffusion of Intrinsic Cation Vacancy Inside CZTS

The diffusion may occur inside CZTS when V_{Cu}, V_{Zn} or V_{Sn} move through the lattice and the Cu, Zn and Sn ion moves to the nearest cation site, respectively. In this process, Cu, Zn or Sn hop to the nearest cation vacancy inside CZTS and leave V_{Cu}, V_{Zn} or V_{Sn}, respectively in the initial place. The calculated diffusion barrier for the absolute energy scale and with reference formation energy at point P are illustrated in Fig. 4.7. Reference formation energy includes the formation energy of the cation vacancy. For Cu diffusing in CZTS, the formation energy of V_{Cu} will add to the activation energy to give the barrier height. The calculated activation energy value of the cation vacancy inside bulk CZTS at point P of the saddle point with formation energies under equilibrium growth conditions are listed in Table 4.6. For points Q, M and N, the differences between the activation energy relative to P are also listed in Table 4.10.

V_{Cu} has the lowest diffusion barrier compared with other cation vacancy defects, and when the formation energy of cation vacancy in the CZTS is included, the lowest barrier is also for V_{Cu}. V_{Sn} has a higher diffusion barrier than the double acceptor defect V_{Zn}. Therefore, V_{Cu} can move more easily inside CZTS than other cation vacancy defects. The formation energy of V_{Cu} (see Table 4.6) is lower than that of the V_{Zn} and V_{Sn}; therefore, it can form more easily inside CZTS than other vacancy defects. According to this, a V_{Cu} acceptor defect can be the dominant defect inside CZTS under equilibrium growth conditions.

It is noticed that there is an intermediate minimum structure in the diffusion barrier reaction with an Sn vacancy, and this could be attributed to the fact that Sn is more relaxed at image four and can make more bonds at that image since Sn atoms are bigger than Cu and Zn. The barrier for all forward and reverse reactions depends on the differences between the saddle point and both the initial and final state.

In CZTS, Cu-S bonds can be considered as weakly covalent, with Zn-S bonds being more ionic, and a little stronger, and Sn-S ionic bonds being stronger still [143]. The bonding and the Cu-poor conditions account for the low formation energy of V_{Cu} and the relatively high formation energy of V_{Sn}, so that it is expected that the Cu vacancy is the dominant cation vacancy in CZTS [143].

For points P, Q, M and N (see Fig. 4.4), the formation energies are calculated, as shown in Table 4.6. The activation energy barriers for point P are listed in Table 4.10, and it is lowest than the activation energy than that of points Q, M and N in the stable region of CZTS. Although the outcome is favourable at point P, there is no substantial difference between the outcome of points P, Q, M and N in the stable region of CZTS (Fig. 4.4), so a similar outcome is expected.

Table 4. 10: Calculated activation energies including the reference formation energy of the native cation vacancies in the bulk CZTS with 512 atoms for point P (Fig. 4.4, Table 4.6) E_{P}^{a}. E^{for} are the forward migration barriers. For points Q, M and N (Fig. 4.4), the relative positions of the activation energies are lower by $\Delta E_{\mathrm{Q}}^{a}$, $\Delta E_{\mathrm{M}}^{a}$ and $\Delta E_{\mathrm{N}}^{a}$, respectively. All energies are in eV.

Defects	E_{P}^{a}	E^{for}	$\Delta E_{\mathrm{Q}}^{a}$	$\Delta E_{\mathrm{M}}^{a}$	$\Delta E_{\mathrm{N}}^{a}$
V_{Cu}	1.87	1.16	0.00	0.00	0.00
V_{Zn}	3.03	1.97	0.14	0.18	0.06
V_{Sn}	5.29	2.46	0.41	0.37	0.02

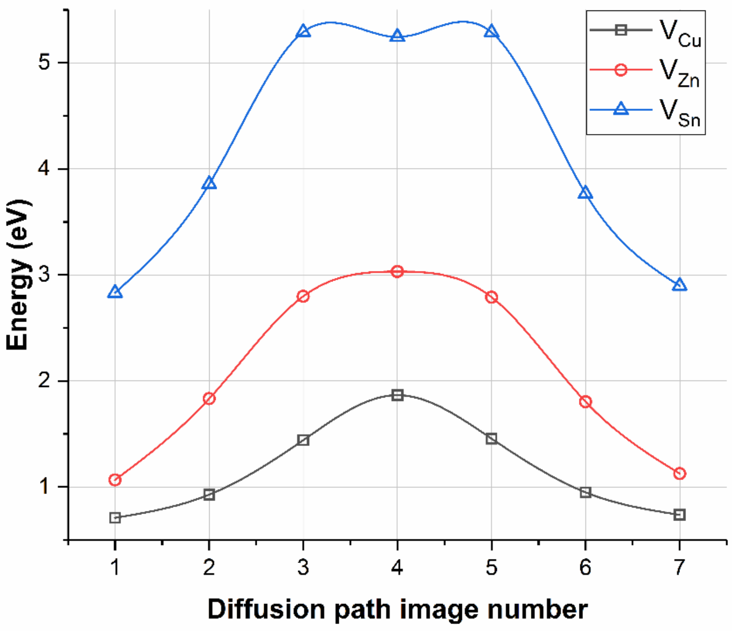

Figure 4. 11: Diffusion barriers calculated for the cation vacancy inside bulk CZTS. The energy scale includes the reference formation energy of the cation vacancies in the bulk CZTS for point P in Fig. 4.4.

4.3.9.2 Diffusion of Antisite Defect Inside Bulk CZTS

The diffusion barrier for Cu_{Zn}, Zn_{Cu} and Zn_{Sn} antisite defects that have low formation energies compared with other antisite defects inside CZTS have been investigated. For example, in a single acceptor antisite defect Cu_{Zn}, Cu can replace the Zn when there is a V_{Zn} vacancy inside CZTS and form Cu_{Zn}, while in a single donor antisite defect Zn_{Cu}, Zn can replace the Cu when there is a V_{Cu} vacancy inside CZTS and form Zn_{Cu}. In this process, the antisite defect can diffuse inside CZTS via a vacancy mechanism.

The calculated diffusion barrier of the cation antisite defects inside CZTS at point P for the absolute energy scale and with reference formation energies are illustrated in Fig. 4.8. Reference formation energy includes the formation energy of the antisite defect with cation vacancy. In this case, Cu_{Zn} diffusing in CZTS via V_{Zn} mechanisms, the formation energies of Cu_{Zn} and V_{Zn} will add to the activation energy to give the barrier height. The calculated activation energy values at point P of the saddle point with the formation energies are listed in Table 4.6. For points Q, M and N, the differences between the activation energy relative to P are also listed in Table 4.11.

Zn_{Cu} is found to have the lowest migration energy compared with Cu_{Zn} and Zn_{Sn} but this barrier becomes higher (3.27eV) when the formation energy of Zn_{Cu} and V_{Cu} is included since the cost of forming Zn_{Cu} in CZTS is relatively high (Table 4.6). Therefore, the most significant minimum activation energy path (migration energy with the formation energy of defects) is observed for the activation diffusion path of a Cu_{Zn} acceptor defect and this could be attributed to the bond strength. The strain in the bond length of Cu_{Zn} (Fig. 4.9) is −0.8 and it is shorter than that of the Zn_{Cu} (+3%) and Zn_{Sn} (−4%) (Section 4.3.5). Therefore, a Cu_{Zn} substitution defect can move more easily inside CZTS than Zn_{Cu} and Zn_{Sn}, under equilibrium conditions.

Cu_{Zn} has the lowest formation energy (Table 4.6). According to this, Cu_{Zn} single acceptor antisite defects can form and diffuse through a Zn vacancy mechanism more easily than Zn_{Cu} and Zn_{Sn} under equilibrium growth conditions.

For points P, Q, M and N (see Fig. 4.4), the formation energies are calculated, as shown in Table 4.6. The activation energy barriers for point P are listed in Table 4.11. The activation energy of Cu_{Zn} is less for point P in the stable region of CZTS than that of points Q, M and N. For Zn_{Cu}, the activation energy for point P is higher than that of points Q, M and N in the stable region of CZTS. For Zn_{Sn} the activation energy for point N is less than that of points P, Q and M in the stable region of CZTS. There is no substantial difference between the outcome of points P, Q, M and N in the stable region of CZTS (Fig. 4.4), so a similar outcome is expected.

Table 4. 11: Calculated activation energies including the reference formation energy of the cation antisite defects in the bulk CZTS with 512 atoms for point P (Fig. 4.4, Table 4.6) E_{P}^{a}. E^{for} is the forward migration barriers. For points Q, M and N (Fig. 4.4), the relative positions of the activation energies are $\Delta E_{\mathrm{Q}}^{a}$, $\Delta E_{\mathrm{M}}^{a}$ and $\Delta E_{\mathrm{N}}^{a}$, respectively. All energies are in eV.

Defects	E_{P}^{a}	E^{for}	$\Delta E_{\mathrm{Q}}^{a}$	$\Delta E_{\mathrm{M}}^{a}$	$\Delta E_{\mathrm{N}}^{a}$
$\mathrm{Cu_{Zn}}$	2.40	1.53	0.27	0.35	0.12
$\mathrm{Zn_{Cu}}$	2.82	1.35	−0.14	−0.18	−0.06
$\mathrm{Zn_{Sn}}$	5.13	1.81	0.60	0.57	−0.02

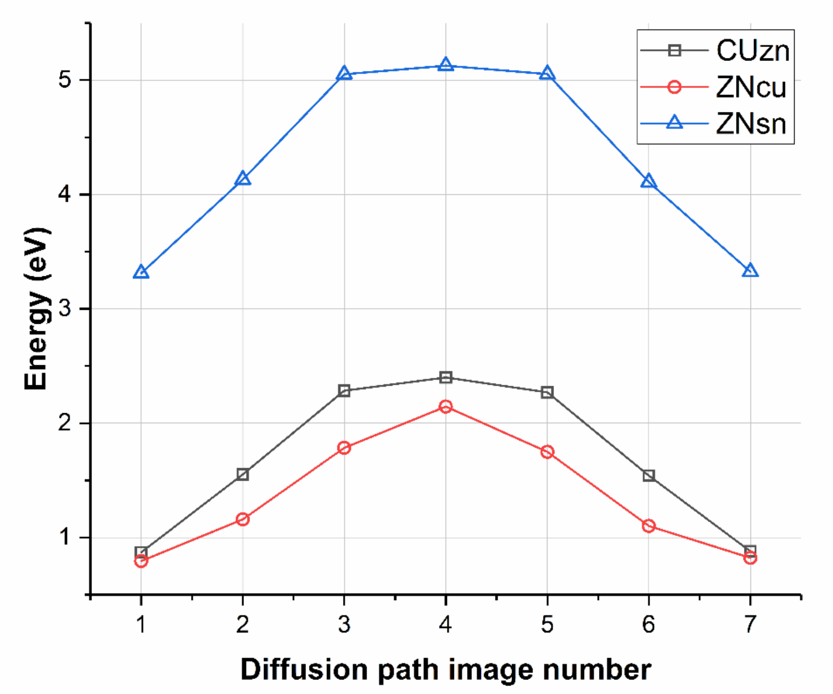

Figure 4. 12: Diffusion barriers calculated for the cation antisite defects inside bulk CZTS. The energy scale includes the reference formation energy of the cation antisite defects in the bulk CZTS for point P in Fig. 4.4.

4.3.9.3 Diffusion of Cd Impurity Inside Bulk CZTS

In a case where there is Cd coming from CdS (buffer layer) into CZTS, these impurities can replace the Cu, Zn and Sn in CZTS and form $\mathrm{Cd_{Cu}}$, $\mathrm{Cd_{Zn}}$ and $\mathrm{Cd_{Sn}}$, respectively. In this process, a substitutional defect can diffuse inside CZTS via a vacancy mechanism. The calculated diffusion barriers of the cation substitutional defects inside CZTS at point P for the absolute energy scale and with reference formation energies are illustrated in Fig. 4.9. Reference formation energy includes the formation energy of the substitutional defect with cation vacancy. In this case, with Cd_{Cu} diffusing in CZTS via V_{Cu} mechanisms, the formation energies of Cd_{Cu} and V_{Cu} will add to the activation energy to give the barrier height. The calculated activation energy values at point P of the saddle point with the formation energies are listed in Table 4.8. For points Q, M and N, the differences between the activation energy relative to P are also listed in Table 4.12.

Cd_{Cu} has the lowest diffusion barrier compared with other substitutional Cd defects, and when the formation energy of V_{Cu} in the CZTS is included, the lowest barrier is also for the Cd_{Cu}. A double acceptor defect Cd_{Sn} has higher diffusion barrier than iso-electronic Cd_{Zn}. Therefore, a Cd_{Cu} substitutional defect can move more easily inside CZTS than other substitutional defects via a V_{Cu} mechanism, and this can be attributed to the bond length. The strain in the bond length of Cd_{Cu}, Cd_{Zn} and Cd_{Sn} with sulfer are +9%, +8% and −3%, respectively (Section 4.3.7).

However, the formation energy of Cd_{Cu} is higher than that of the Cd_{Zn} and Cd_{Sn}; therefore, it cannot form more easily inside CZTS than other substitutional defects. The formation energy of Cd_{Zn} is less than other Cd substitutional defects inside CZTS and the diffusion barrier of this defect is relatively higher than the lowest diffusion barrier of Cd_{Cu}. In addition, Cd_{Cu} has the lowest starting and ending points; therefore, it is more stable than other defects. According to this the donor Cd_{Cu} substitutional defect could be the dominant Cd substitutional defect inside CZTS.

For points P, Q, M and N (see Fig. 4.4), the formation energies are calculated, as shown in Table 4.8. The activation energy barriers for point P are listed in Table 4.12. The activation energy values of Cd_{Cu} are less for points Q, M and N in the stable region of CZTS than that of point P. For Cd_{Zn} and Cd_{Sn}, the activation energy for point P is less than that of points Q, M and N in the stable region of CZTS. As is mentioned in Section 4.3.9.2, a similar outcome between points P, Q, M and N in the stable region of CZTS (Fig. 4.4) is expected.

Table 4. 12: Calculated activation energies including the reference formation energy of the cation substitutional defects in the bulk CZTS with 512 atoms for point P (Fig. 4.4, Table 4.8) E_{P}^{a}. E^{for} represents the forward migration barriers. For points Q, M and N (Fig. 4.4), the relative position of the activation energies are $\Delta E_{\mathrm{Q}}^{a}$, $\Delta E_{\mathrm{M}}^{a}$ and $\Delta E_{\mathrm{N}}^{a}$, respectively. All energies are in eV.

Defects	E_{P}^{a}	E^{for}	$\Delta E_{\mathrm{Q}}^{a}$	$\Delta E_{\mathrm{M}}^{a}$	$\Delta E_{\mathrm{N}}^{a}$
Cd_{Cu}	1.82	0.96	−0.14	−0.14	−0.02
Cd_{Zn}	3.41	2.26	0.14	0.21	0.10
Cd_{Sn}	7.12	3.64	0.68	0.60	0.02

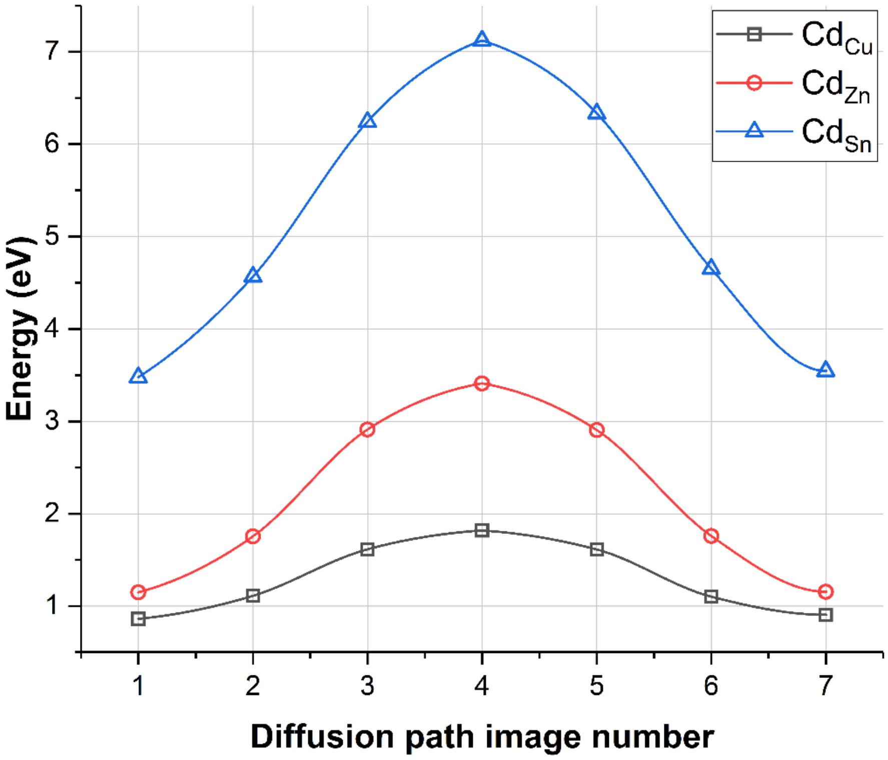

Figure 4. 13: Diffusion barriers calculated for the cation substitutional defects inside bulk CZTS. The energy scale includes the reference formation energy of the cation antisite defects in the bulk CZTS for point P in Fig. 4.4.

4.4 Conclusion

By exploiting the properties of CZTS phase space stability, density functional theory has been used to calculate the formation energies and electronic properties of bulk CZTS, in addition to the secondary phases and intrinsic defects that are almost presented in this material, such as vacancies and anti-sites. These intrinsic defects might have a significant electrical effect on the material-based solar cell.

CZTS phase stability is formed in quite a narrow area under Cu-poor/Zn-rich growth condition and the boundaries of the CZTS phase are shared with other secondary phases. The narrow area of single phase CZTS is variable based on Cu chemical atomic potential value and shrinks to approximately a point as the chemical atomic potential of Cu decreases until it disappears.

Under this growth condition, Cu_{Zn} antisite and V_{Cu} native defects are responsible for p-type conductivity, where Cu_{Zn} has the lowest formation energy compared to the other defects and V_{Cu} has a shallower accepter level than other defects. The low acceptor formation energy illustrates that grown CZTS compound always shows p-type conductivity. However, impurity defects inside CZTS generally come from the buffer layer including CdS. It has been found that the formation energy for a substitutional defect Cd_{Zn} is lower than that of the other Cd substitutional defects.

The dominant native cation vacancy defect inside bulk CZTS is Cu vacancy because it has the lowest activation diffusion barrier and formation energy compared with other native cation vacancy defects. For antisite defects, it has been found that a single acceptor Zn_{Cu} is the dominant antisite defect inside bulk CZTS compared with other antisite defects, since Zn_{Cu} has the lowest activation diffusion barrier via V_{Zn} mechanisms and the lowest formation energy compared with other antisite defects. For Cd impurity defects, it is concluded that the iso-electronic defect Cd_{Zn} is the dominant defect inside bulk CZTS compared with other cd substitutional cation defects.

Energies, electrical levels and diffusion processes in bulk CZTS have been simulated in this chapter, and these analyses are part of the control calculations of the inter-diffusion in the interfaces CZTS/ZnS and CZTS/CdS which are explained in Chapters 6 and 8, respectively.

Chapter 5

Bulk and Strained ZnS

5.1 Introduction

CZTS is thermodynamically stable in a relatively narrow region of atomic chemical potentials [40, 82], and secondary phases such as ZnS, $CuSnS_3$ and Cu_2S might become significant contaminants under some growth conditions. However, efficient devices are obtained for Cu-poor/Zn-rich compositions [89, 90], where intrinsic defects (Cu_{Zn} and V_{Cu}) are responsible for the p-type conductivity [89, 90], and then ZnS, a semiconductor with a band gap of 3.6eV [181], is the main competing secondary phase. Secondary phases [66] affect the performance of photovoltaic devices by reducing the volume of the absorber layer and decreasing the short circuit current.

Typical p-type CZTS solar cells are consecutively deposited layers [182], such as a Mo/CZTS/CdS/ZnO, with ZnS forming as a secondary phase precipitates within a CZTS absorber layer. The ZnS is generally most commonly found as a secondary phase close to the interfaces with the contacts and buffer layers [89, 183], but it is also used as an alternative buffer layer to replace CdS [114, 184, 185] due to the toxicity of cadmium. Therefore, the hetero-structure interface between CZTS and the ZnS is of great interest for CZTS cell performance. In this chapter, ZnS secondary phases are modelled to identify the most stable defects inside bulk cubic and strained ZnS, and the energetics by which metal vacancies move inside the ZnS phase.

5.2 Computational Details

The computational methods in this chapter are illustrated in Chapters 2 and 3 in terms of pseudopotentials (Section 2.7.3), diffusion barrier (Section 3.8), basis set with cut-off (Section 2.7.2), binding energy (Section 3.9) and the formation energy of defects in the neutral charge state which strongly relies on the atomic chemical potential of the species in the system as shown in Section 3.5.

A buffer layer ZnS has been modelled based on a conventional zinc-blende supercell containing a 64-atom and 512-atom supercell. Strained ZnS are modelled using orthorhombic, with a 64-atom and 512-atom supercell, The Brillouin zone of both cubic and strained ZnS is sampled using a 4×4×4 mesh for the 64-atom cell and a 2×2×2 mesh for the 512-atom cell.

A 512-atom supercell is used to calculate the formation energy of intrinsic and substitutional defects. A diffusion barrier for cation vacancy inside bulk cubic ZnS has been calculated by using 512-atom and 64-atom supercells. The differences in the results for both different barrier size cells are less than 0.3eV. Based on this, the 64-atom supercell has been used to calculate the diffusion barrier for substitutional defects by Zn vacancy mechanisms inside bulk cubic and strained ZnS in order to reduce the computational cost. Substitution defect is cost energy to diffuse; therefore, the diffusion process for these defects has been studied by cation vacancy mechanisms, and it is more likely to occur [186-188].

5.3 Results and Discussion

5.3.1 Bulk Crystal Models

In order to build an epitaxial interface between the buffer layer ZnS and the absorber layer CZTS as explained in Chapter 6, strained ZnS should be modelled. In the epitaxial interface, the buffer layer is adjacent and in contact with the absorber layer, and as the strain in the interface is based on the lattice constant of CZTS (see Section 6.3.1), the bulk ZnS have be strained to match CZTS. Cubic and strained ZnS are modelled in the [100] direction (see Fig. 5.1) which is the same orientation as the CZTS/ZnS interface modelled for this study (Section 6.3.1). The calculated lattice constants are listed in Table 5.1. The bond length of cubic and strained ZnS are the same within three decimal places, as shown in Fig 5.1 and this refers to the fact that the strain in ZnS (Table 5.1) is very small compared with CdS

(Section 7.3.1). The strain in the lattice constant of ZnS in [100] is compressive, while in [010] and [001], it is tensile.

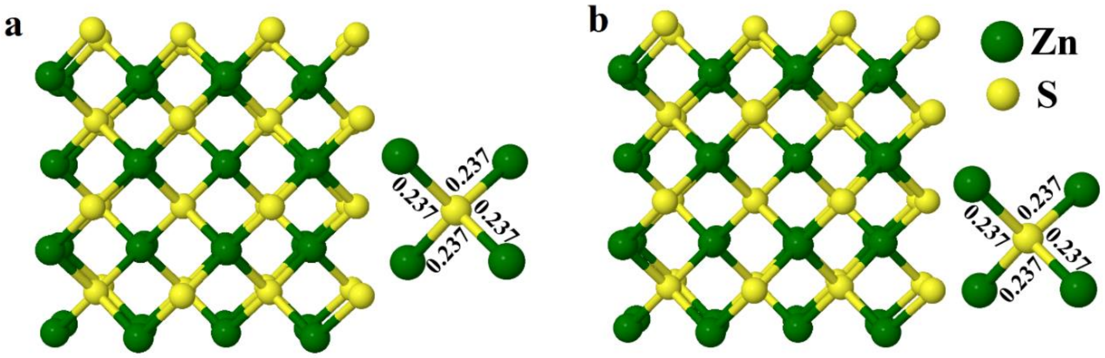

Figure 5. 1: Schematic of ZnS structure simulation supercell: (a) cubic ZnS; (b) strained ZnS. Bond lengths given in nm. The horizontal and vertical directions are [100] and [010], respectively, with [001] out of the paper.

Table 5. 1: Calculated lattice parameters of the bulk and strained ZnS phases. The numbers between the brackets represent the strain in ZnS. The experimental lattice constants is $a_{\mathrm{ZnS}} = 5.45$Å [166]. The lattice constants of strained ZnS are fixed to a_{CZTS} in the [010] direction and $c_{\mathrm{CZTS}}/2$ in the [001] direction, while in the [100] direction, the lattice constant is optimised.

	Lattice constant (Å)		
Material	[100]	[010]	[001]
ZnS	5.472	5.472	5.472
Strained ZnS	5.435 (−0.7%)	5.497 (+0.5%)	5.500 (+0.5%)

5.3.2 Defects in Bulk ZnS

Intrinsic defects such as cation vacancy and substitution defects including Cu$_{\mathrm{Zn}}$ and Sn$_{\mathrm{Zn}}$ inside bulk cubic and strained ZnS are studied under Cu-poor/Zn-rich growth conditions and μ_{Cu}=−0.2eV) [40] (Fig. 4.4). The impurity defects come from CZTS absorber layer. In cubic and strained ZnS, the four equilibrist bond lengths between Cu$_{\mathrm{Zn}}$ and Sn$_{\mathrm{Zn}}$ and sulphur, in addition to the strain between the antisite defects and the nearest sulphur, are listed in Table 5.2. The bond length of Cu impurity defects inside bulk cubic and strained ZnS is shorter than that of Sn impurity defects (Fig. 5.2). The bond length of Cu$_{\mathrm{Zn}}$-S in cubic and strained ZnS is shorter within 0.3% than that of Zn-S, whilst the bond length of Sn$_{\mathrm{Zn}}$-S is longer within 3.5% and 3.6% for cubic and strained ZnS, respectively, than that of Zn-S; therefore, the strain in cubic and strained ZnS for Cu$_{\mathrm{Zn}}$-S is compression and for Sn$_{\mathrm{Zn}}$-S, it is tension.

Table 5. 2: Calculated bond-length (nm) and strain (%) for substitutional defects inside cubic and strained ZnS

Structure	Defects	Bond-length (nm)	Strain (%)
Cubic	Cu_{Zn}-S	0.234	−1%
	Sn_{Zn} -S	0.272	+15%
Strained	Cu_{Zn}-S	0.234	−1%
	Sn_{Zn} -S	0.273	+15%

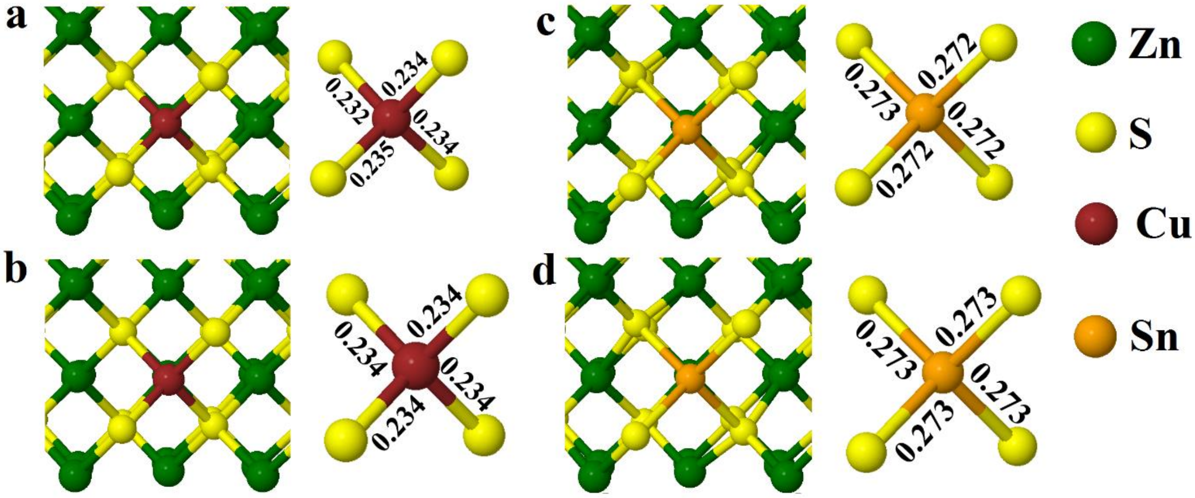

Figure 5. 2: Schematic of substitutional defects in ZnS: (a) CuZn in cubic ZnS; (b) CuZn in strained ZnS; (c) SnZn in cubic ZnS; (d) SnZn in strained ZnS. Bond lengths given in nm. The horizontal and vertical directions are [100] and [010], respectively, with [001] out of the paper.

5.3.3 Formation Energies

The formation energy of the intrinsic defect V_{Zn} and substitution defects Cu_{Zn} and Sn_{Zn} inside bulk cubic and strained ZnS are calculated. The formation energies of all calculated defects are in the stable atomic chemical potential region of CZTS under Cu-poor/Zn-rich equilibrium growth conditions and μ_{Cu}=−0.2eV [40] for the four boundary points P, Q, M and N of the CZTS stable region (Fig. 4.4), as shown in Table 5.3.

The formation energy for the intrinsic and substitutional defects inside strained ZnS are slightly lower than that for the unstrained ZnS. It has been found that acceptor cation intrinsic defects V_{Zn} inside bulk cubic and strained ZnS have higher formation energy than that of acceptor and donor substitutional defects. Acceptor substitutional defects Cu_{Zn} have lower formation energy in comparison with the formation energy of the donor defects Sn_{Zn} for bulk cubic and strained ZnS, and that could be attributed to the bond length.

In cubic and strained ZnS, according to Fig. 5.2, Table 5.3, the strain in the bond length in the case of Cu_{Zn} is smaller than that in the Sn_{Zn}. Therefore, the acceptor substitution defect can form inside ZnS more easily than that of both the neutral donor substitution defect and intrinsic cation defects under equilibrium growth conditions.

Table 5. 3: Calculated formation energies of the vacancies and substitutional defects inside bulk cubic and strained ZnS for points P, Q, M and N (Fig. 4.4). All energies are in eV.

Structure	**Defects**	$\boldsymbol{E_{\mathrm{P}}^{f}(64)}$	$\boldsymbol{E_{\mathrm{P}}^{f}}$	$\boldsymbol{E_{\mathrm{Q}}^{f}}$	$\boldsymbol{E_{\mathrm{M}}^{f}}$	$\boldsymbol{E_{\mathrm{N}}^{f}}$
Cubic	V_{Zn}	3.03	3.10	2.96	2.92	3.04
	Cu_{Zn}	0.78	0.81	0.67	0.63	0.75
	Sn_{Zn}	1.47	1.38	1.65	1.58	1.34
Strained	V_{Zn}	3.02	3.03	2.89	2.85	2.97
	Cu_{Zn}	0.77	0.73	0.60	0.56	0.67
	Sn_{Zn}	1.44	1.27	1.54	1.46	1.23

5.3.4 Binding Energy of Cu and Sn Substitutions to Vacancy

The process of Cu and Sn diffusing to ZnS is via a vacancy. The mechanisms for the diffusion of Cu and Sn substituting for Zn are likely to involve a Zn vacancy; therefore, part of the analyses of energies involves whether or not there is binding of such vacancy to the impurity.

The calculated binding energies of Cu_{Zn} +V_{Zn} and Sn_{Zn} +V_{Zn} inside bulk strained ZnS are 0.41 and 1.6eV, respectively. The positive binding energy refers to the fact that the defects are bound.

5.3.5 Inter-diffusion Inside Bulk Cubic ZnS

The diffusion barrier of intrinsic and substitutional defects for cubic ZnS is studied under equilibrium growth conditions for the four boundary points P, Q, M and N of the CZTS stable region (Fig. 4.4). For the cation vacancy, the reference formation energy will include the formation energy of the cation vacancy. In the case of Zn diffusing in ZnS, the formation energies of V_{Zn} will add to the activation energy to give the barrier height. For the substitutional defects, the reference formation energy includes the formation energy of the substitutional defect with cation vacancy. In the case of Cu_{Zn} diffusing in ZnS via V_{Zn}

mechanisms, the formation energies of Cu_{Zn} and V_{Zn} will add to the activation energy to give the barrier height.

5.3.5.1 Diffusion of Zn Vacancy Inside Cubic ZnS

Diffusion may occur inside ZnS when V_{Zn} moves through the lattice and the Zn ion moves to the nearest cation site. In this process, Zn hops to the nearest cation vacancy inside ZnS and leaves V_{Zn} in the initial place, as shown schematically in Fig. 5.3. The calculated diffusion barriers of the Zn cation vacancy inside bulk cubic ZnS at point P are illustrated in Fig. 5.4. The calculated activation energy values at point P of the saddle point with the formation energies under equilibrium growth conditions (Fig. 4.4) are 4.28 and 4.30eV for 512-atom and 64-atom cells, respectively. For points Q, M and N (Fig. 4.4), the differences between the activation energy relative to P are 0.14, 0.14 and 0.02eV, respectively, and the differences are the same for both cell sizes for the reactions. Although the outcome is favourable at point P, there is no substantial difference between points P, Q, M and N in the stable region of CZTS (Fig. 4.4), so a similar outcome is expected.

A 64-atom supercell has a slightly bigger diffusion barrier within 0.3eV of a 512-atom supercell; this could be attributed to the interaction between defect-defect which is big in a small cell size compared with the large cell size (Section 2.5).

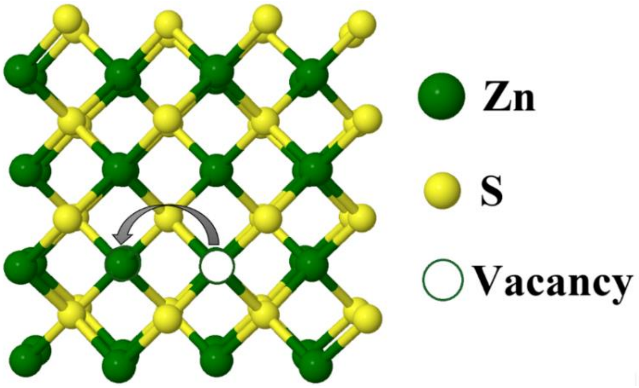

Figure 5. 3: Schematics of Zn diffusing into the nearest metal vacancies in cub ZnS. The horizontal and vertical directions are [100] and [010], respectively, with [001] out of the paper.

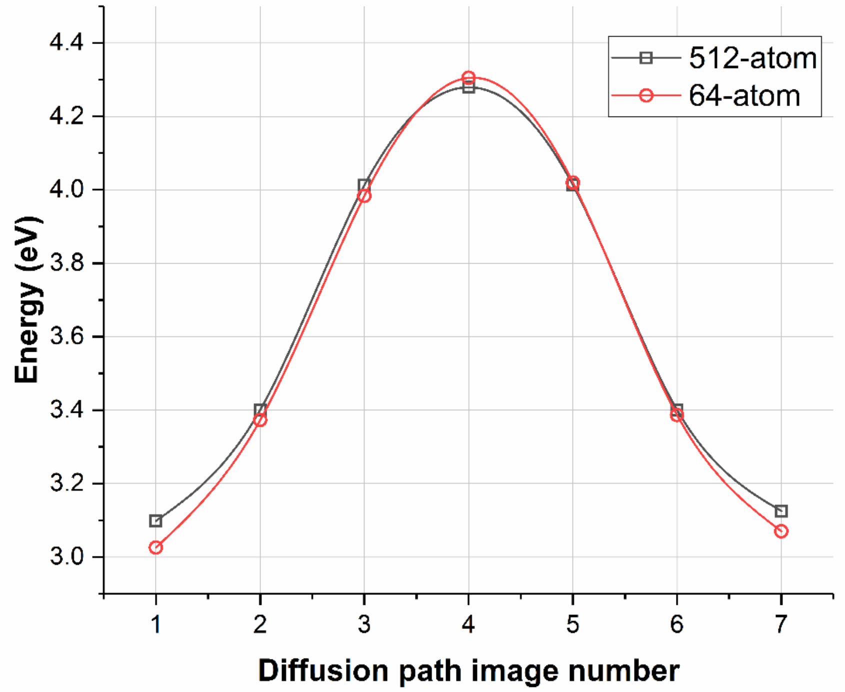

Figure 5. 4: Diffusion barriers calculated for the Zn cation vacancy inside bulk cubic ZnS, with 64-atom and 512-atom cells. The energy scale includes the reference formation energy of the Zn cation vacancies in the bulk ZnS at point P (Fig. 4.4).

5.3.5.2 Diffusion of Cu and Sn Impurities Inside Cubic ZnS

In a case where there is a Cu or Sn impurity coming from CZTS into cubic ZnS, these impurities can replace the Zn inside ZnS and form Cu_{Zn} and Sn_{Zn}, respectively. The calculated diffusion barriers of Cu_{Zn} and Sn_{Zn} substitutional defects in cubic ZnS at point P are illustrated in Fig. 5.5. The calculated activation energy values at point P of the saddle point with the formation energies are listed in Table 5.4. For points Q, M and N, the differences between the activation energy relative to point P are also listed in Table 5.4. There is no substantial difference between the outcome of points P, Q, M and N in the stable region of CZTS (Fig. 4.4), so a similar outcome is expected.

A Cu_{Zn} acceptor defect has the lowest diffusion barrier compared with a Sn_{Zn} donor defect, and this could be attributed to the fact that the strain in Cu_{Zn}-S is lower than that of Sn_{Zn} (Section 5.3.2). Therefore, a Cu_{Zn} substitution defect can move more easily inside cubic ZnS than Sn_{Zn}, under equilibrium conditions via V_{Zn} mechanisms. There is an intermediate minimum structure in the diffusion barrier reaction with an Sn impurity, and this could be attributed to the fact that Sn is more relaxed at image four and can make more bonds at that image since the Sn atom is bigger than Cu and Zn. This intermediate minimum structure also occurs when there is V_{Sn} in bulk CZTS (Section 4.3.9.1). The barrier for all forward and reverse reactions depends on the differences between the saddle point and both the initial and final states.

In bulk cubic ZnS, the formation energy of Cu_{Zn} is less than that of the Sn_{Zn} as shown in Table 5.3. According to this, Cu_{Zn} acceptor substitution defects can be formed and diffused by Zn vacancy mechanisms more easily than Sn_{Zn} inside bulk cubic ZnS under equilibrium conditions.

Table 5. 4: Calculated activation energies including the reference formation energy (eV) of the impurity antisites in the bulk cubic ZnS with a 64-atom cell at point P (Fig. 4.4, Table 5.3) E_{P}^{a}. For points Q, M and N (Fig. 4.4), the relative positions of the activation energies are $\Delta E_{\mathrm{Q}}^{a}$, $\Delta E_{\mathrm{M}}^{a}$ and $\Delta E_{\mathrm{N}}^{a}$, respectively. E^{for} is the forward migration barrier. All energies are in eV.

Reaction	E_{P}^{a}	E^{for}	$\Delta E_{\mathrm{Q}}^{a}$	$\Delta E_{\mathrm{M}}^{a}$	$\Delta E_{\mathrm{N}}^{a}$
Cu_{Zn}	5.12	1.22	0.14	0.18	0.06
Sn_{Zn}	5.74	1.26	-0.27	-0.19	0.04

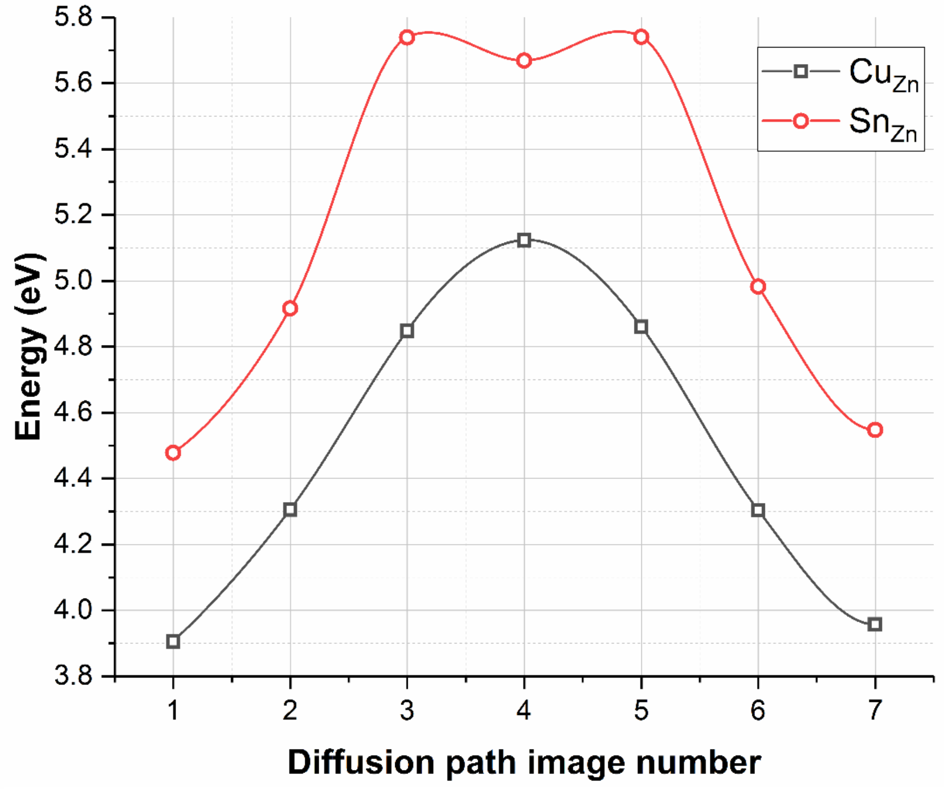

Figure 5. 5: Diffusion barriers calculated for the diffusion of Cu_{Zn} and Sn_{Zn} substitutional defects inside bulk cubic ZnS via a Zn vacancy, with a 64-atom cell. The energy scale includes the reference formation energy of the substitutional defects with Zn cation vacancy in the ZnS at point P (Fig. 4.4).

5.3.6 Inter-diffusion Inside Strained ZnS

The diffusion barrier of cation intrinsic and substitutional defects for strained ZnS are studied in the [110] and [011] directions under equilibrium growth conditions. Based on the interface model condition of CZTS/ZnS (Section 6.3.1), the diffusion barrier in the [010] and [001] directions are approximately the same and they differ in terms of strain (Table 5.1) from the [100] direction. [110] is away from the interface and [011] is in a parallel direction to the interface.

5.3.6.1 Diffusion of Zn Vacancy Inside Strained ZnS

In the case of strain, Zn moves to the nearest cation vacancy in the [110] and [011] directions inside strained ZnS and leaves V_{Zn} in the initial place as shown schematically in Fig. 5.6. Calculated diffusion barriers for a Zn cation vacancy inside bulk strained ZnS at point P are illustrated in Fig. 5.7. The calculated activation energy values of the saddle point at point P with the formation energies under equilibrium growth conditions are listed in Table 5.5. For points Q, M and N (Fig. 4.4), the differences between the activation energy relative to point P are 0.14, 0.14 and 0.02eV, respectively, and the differences are the same for both directions with different cell sizes. As mentioned in Section 5.3.5.1, a similar outcome between points P, Q, M and N in the stable region of CZTS (Fig. 4.4 is expected).

The differences in the diffusion barrier in the [110] direction away from the interface and [011] parallel direction to the interface are small within 0.07eV because the strain in ZnS is small (Table 5.1).

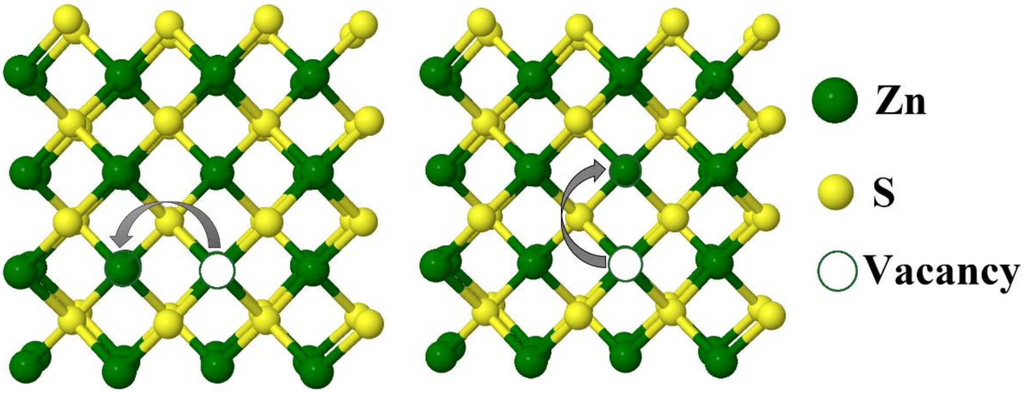

Figure 5. 6: Schematics of Zn diffusing into nearest metal vacancies in strained ZnS: (a) at [110] direction; (b) at [011] direction. The horizontal and vertical directions are [100] and [010], respectively, with [001] out of the paper.

Table 5. 5: Calculated activation energies including the reference formation energy of the intrinsic cation Zn vacancy in the bulk strained ZnS with 512 atoms at the [110] direction away from the interface and the [011] parallel direction to the interface at point P (Fig. 4.4, Table 5.3) $E^{\mathrm{a}}_{\mathrm{P2}}$ for strain and $E^{\mathrm{a}}_{\mathrm{P1}}$ for cubic. E^{for} is the forward migration barrier. All energies are in eV.

Direction	E^{a}_{P1}	E^{a}_{P2}	E^{for}
[110]	4.28	4.22	1.19
[011]	4.28	4.15	1.12

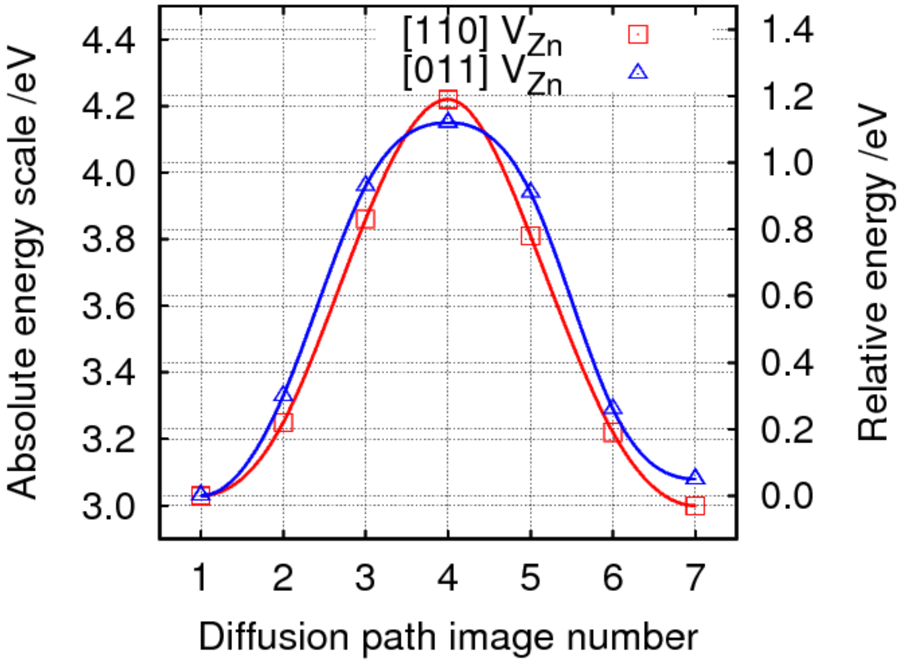

Figure 5. 7: Diffusion barriers calculated for the absolute energy scale and the relative energy including the reference formation energy of Zn cation vacancy inside bulk strained ZnS at point P (Fig. 4.4): (a) at [110] direction; (b) at [011] direction.

5.3.6.2 Diffusion of Cu and Sn Inside Strained ZnS

In a case where there is a Cu or Sn impurity coming from CZTS into strained ZnS, these impurities can replace the Zn inside strained ZnS and form $\mathrm{Cu_{Zn}}$ or $\mathrm{Sn_{Zn}}$, respectively. In this process Cu or Sn impurities can diffuse inside strained ZnS by Zn vacancy. The calculated diffusion barriers of the $\mathrm{Cu_{Zn}}$ and $\mathrm{Sn_{Zn}}$ substitutional defects inside bulk strained ZnS at point P for the absolute energy scale and with reference formation energy in the [110] direction away from the interface and the [011] parallel direction to the interface are illustrated in Fig. 5.8. The calculated activation energy values of the saddle point with the formation energies at point P under equilibrium growth conditions are listed in Table 5.6.

For points Q, M and N, the differences between the activation energy relative to point P are also listed in Table 5.6. There is no substantial difference between the outcome of points P, Q, M and N in the stable region of CZTS (Fig. 4.4), so a similar outcome is expected.

The diffusion barrier of Cu_{Zn} and Sn_{Zn} inside strained ZnS in [011] the parallel direction to the interface is lower than that of the [110] direction away from the interface based on the interface model where the bond length of Zn-S in the [110] direction is longer than that of the cubic; therefore, the strain in the [110] direction is tensile (Table 5.1), while the bond length of Zn-S in the [011] direction is shorter than that of the cubic; therefore, the strain in the [011] direction is compressive. Therefore, the most significant migration path is in the [110] direction.

A Cu_{Zn} single acceptor defect has the lowest diffusion barrier compared with a double donor Sn_{Zn} in both directions. Therefore, a Cu_{Zn} substitution defect can move more easily inside bulk strained ZnS by a V_{Zn} mechanism than Sn_{Zn} substitutional defects in both the [110] direction away from the interface and the [011] parallel direction to the interface. There is an intermediate minimum structure in the diffusion barrier reaction with an Sn impurity, as explained in Section 5.3.5.2.

In the bulk strained ZnS, the formation energy of a Cu_{Zn} acceptor substitutional defect is lower than that of the Sn_{Zn}. According to this, Cu_{Zn} acceptor substitutional defects can form and diffuse by a Zn vacancy mechanism more easily than Sn_{Zn} under equilibrium growth conditions.

Table 5. 6: Calculated activation energies including the reference formation energy of the impurity antisites and cation vacancy in bulk strained ZnS with a 64-atom cell in the [110] direction away from the interface and the [011] parallel direction to the interface at point P (Fig. 4.4, Table 5.3) E_{P2}^{a} for strain and $E_{\mathrm{P1}}^{\mathrm{a}}$ for cubic. For points Q, M and N (Fig. 4.4), the relative positions of the activation energies are $\Delta E_{\mathrm{Q}}^{a}$, $\Delta E_{\mathrm{M}}^{a}$ and $\Delta E_{\mathrm{N}}^{a}$, respectively. E^{for} is the forward migration barrier. All energies are in eV.

Direction	Reaction	E_{P1}^{a}	E_{P2}^{a}	E^{for}	$\Delta E_{\mathrm{Q}}^{a}$	$\Delta E_{\mathrm{M}}^{a}$	$\Delta E_{\mathrm{N}}^{a}$
[110]	Cu_{Zn}	5.12	4.97	1.21	0.14	0.18	0.06
	Sn_{Zn}	5.74	5.56	1.27	-0.27	-0.19	0.04
[011]	Cu_{Zn}	5.12	5.03	1.27	0.14	0.18	0.06
	Sn_{Zn}	5.74	5.64	1.35	-0.27	-0.19	0.04

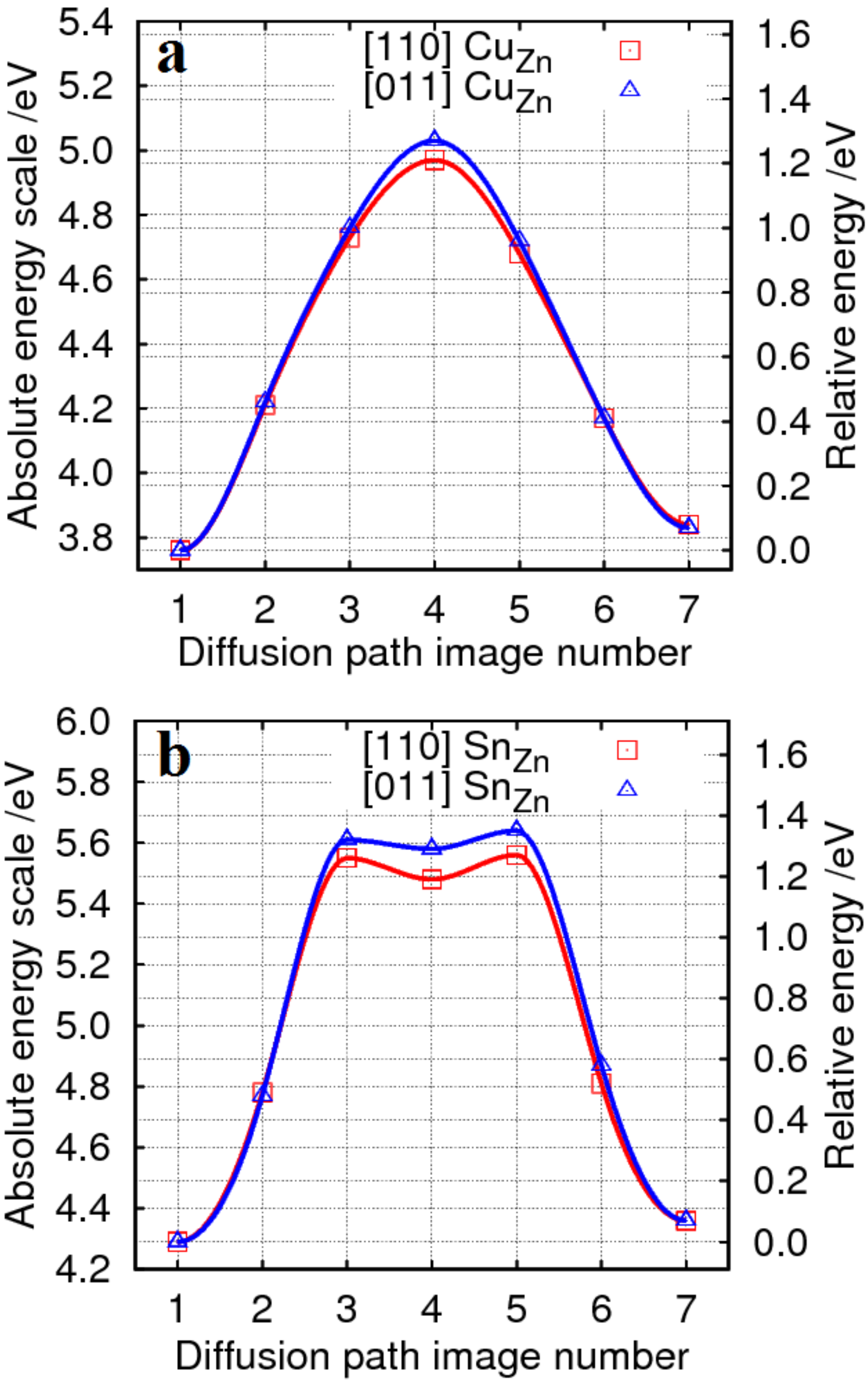

Figure 5. 8: Diffusion barriers calculated for the absolute energy scale and with a reference formation energy of Cu$_{Zn}$ and Sn$_{Zn}$ substitutional defects inside bulk strained ZnS at point P (Fig. 4.4): (a) Cu$_{Zn}$ at [110] and [011]; (b) Sn$_{Zn}$ at [110] away from the interface and [011] parallel direction to the interface.

5.4 Conclusion

A ZnS thin buffer layer is strained to match the thick absorber layer CZTS at the interface. Based on the interface module of CZTS/ZnS, the strain in the lattice constant of ZnS in the [100] direction is compressive, while in the [010] and [001] directions, it is tensile. The strain in the lattice constant of bulk ZnS is quite small. Therefore, the diffusion barriers of defects inside strained ZnS in the [010] direction is approximately the same as in the [001] direction.

Under equilibrium Cu-poor and Zn-rich growth conditions, it is obtained that the formation energies for intrinsic cation vacancy and substitutional defects in strained ZnS are lower than that of the cubic. In addition, the formation energy for Cu_{Zn} substitutional defects in cubic and strained ZnS is lower than that for other intrinsic cation vacancy and substitutional defects.

Under the given conditions, the diffusion barrier of cation vacancy and substitutional defects inside strained ZnS in the [110] direction away from the interface is lower than that of the [011] parallel direction to the interface depending on the interface model where the strain in the [011] direction is tensile, while the strain in the [110] direction is compressive. Therefore, the most significant migration path is in the [110] direction. Furthermore, Cu_{Zn} has the lowest diffusion barrier via V_{Zn} mechanisms compared with Sn_{Zn} defects. The dominant defects in bulk cubic and strained ZnS in both the [110] direction away from the interface and the [011] parallel direction to the interface are Cu_{Zn} single acceptor substitutional defects.

It is informative to compare the processes in ZnS with those derived for CZTS and presented in chapter 4. The diffusion barrier of V_{Zn} inside bulk CZTS is 3.03eV (Section 4.3.9.1), while the diffusion barrier of V_{Zn} inside bulk ZnS is significantly higher at 4.28eV for unstrained (Section 5.3.5.1) and (4.22 - 4.15) eV for biaxially strained ZnS commensurate with a (100) CZTS interface (Section 5.3.6.1). Therefore, V_{Zn} can diffuse inside CZTS more easily than in ZnS, and this will impact the p-type conductivity of CZTS cells.

Chapter 6

CZTS/ZnS (100) Interface Processes

6.1 Introduction

Under Cu-poor and Zn-rich growth conditions for efficient CZTS devices [90], ZnS constitutes a significant competing secondary phase. Lattice misfit between CZTS and the secondary phase has an impact on the PV performance, but the lattice mismatch with ZnS is small of about 0.5%, so the minority carrier recombination at the interface is low [65].

The band offset between CZTS and either ZnS as a precipitation phase or a buffer layer is critical for conversion efficiency [64, 66]. The band alignment in CZTS/ZnS is almost independent of the interface orientation, since the small lattice mismatch at the interface is hardly affected by the chemical bonds. For example, in CZTS/ZnS, the VBO in (111), (101) and (100) is 0.92, 0.95 and 0.92eV, respectively, and the CBO is 1.32, 1.29 and 1.36eV for (111), (101) and (100), respectively [65]. The valence-band offset is affected by the composition and abruptness of the interface, which is, in turn, affected by diffusion processes between materials [189]. For example, the diffusion of Cd and In from the buffer layer is thought to readily diffuse into CZTS, whereas of Zn from a ZnS or ZnO based buffer, it does not [190]. Conversely, Cu does not seem to diffuse out of CZTS into MoS_2 [191].

Electronic properties are affected by the intrinsic lattice defect concentration and this will affect the device efficiency [192]. However, Zn vacancy is a deep acceptor defect in the ZnS [193, 194] while, in CZTS, the Zn vacancy is considered a shallow acceptor [195]. The charge transfer of the deep defect levels might act as recombination centres, while the transformation from one charge state to another is easily for the shallow defect levels and that enhances the carrier concentration in the photovoltaic devices. It has been found that the shallow charge transition levels within the band gap of the CZTS are Cu and Zn vacancies and they are delocalised, whilst the deep charge transition level is the Sn vacancy and it is localised [195].

If V_{Cu} and Cu_{Zn} are responsible for p-type conductivity in CZTS, such defects formed as a result of the intermixing between the buffer layer (or the secondary phase) and the absorber layer are critical for the efficiency of the device. In this chapter, the CZTS/ZnS interface is modelled to identify the most stable defects adjacent to the interface. In addition, the defect diffusion barrier across the interface is investigated along with the impact of cation inter-diffusion across the interface on p-type conductivity. Furthermore, the role of the charge transfer across the interface is discussed.

6.2 Computational Details

For this chapter, the computational methods have been explained in Chapters 2 and 3 in terms of pseudo potentials (Section 2.7.3), formation energy (Section 3.5) and diffusion (Section 3.8), basis set and cut-off (Section 2.7.2). The VBO for the (100) interface has been calculated as explained in Section 3.7.

Kesterite CZTS is modelled using a tetragonal, 16-atom cell with the tetragonal axis along [001], and strained ZnS is modelled using a conventional zinc-blende unit cell. All bulk crystals have their Brillouin zones sampled to converge the energy to better than 10meV/atom. The epitaxial ZnS (100)/CZTS (100) interface is modelled using an orthorhombic ($a \neq b \neq c$), 192-atom supercell made up from three lattice constants each of CZTS and strained ZnS in the [100] direction, so there are 12 layers of each material, as illustrated in Fig. 6.1. The Brillouin zone is sampled using a 1×4×4 mesh. Cubic and strained ZnS in the [100] direction (see Fig. 5.1) are modelled using cubic and orthorhombic (see Section 5.2).

Although there are different orientation types to model the interface, (100)-CZTS/ZnS has been chosen to model the interface in this study, since this direction is a non-polar surface including two Cu, one Zn and one Sn, and computationally it does not cost. However, (001)-CZTS/ZnS and (110)-CZTS/ZnS interface orientation are polarised surfaces and that leads to an electrostatic field and shows relatively high interface energies so they might be computationally complex [65].

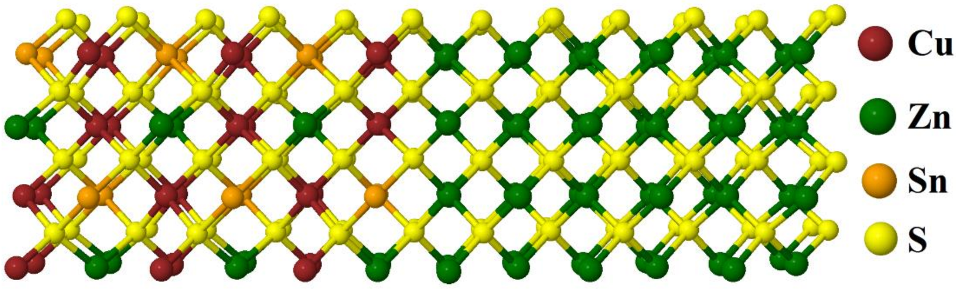

Figure 6. 1: Schematic of the structure of the CZTS/ZnS interface simulation supercell. The horizontal and vertical directions are [100] and [010], respectively, with [001] out of the paper.

6.3 Results and Discussion

6.3.1 Bulk Crystal and Interface Models

It is assumed that the ZnS is a minor component of the composite, and therefore, the lattice constants of CZTS are taken to be equilibrium and the ZnS is strained to match. The calculated lattice constants are listed in Table 6.1. In the supercell, ZnS is strained since the lattice constants parallel to the interface [010] and [001] are fixed to that of the bulk CZTS while a lattice constant in the perpendicular direction [100] to the interface is assumed to be relaxed for all the calculations along the hetero-interface.

Table 6. 1: Calculated lattice parameters of the bulk and strained phases, and the interface supercell. The numbers between the brackets represent the strain in ZnS. The experimental lattice constants are $a_{\mathrm{CZTS}} = 5.426$Å, $c_{\mathrm{CZTS}} = 10.81$Å and $a_{\mathrm{ZnS}} = 5.45$Å [144, 166].

Material	Lattice constant (Å)		
	[100]	[010]	[001]
CZTS	5.497	5.497	11.000
ZnS	5.472	5.472	5.472
Strained ZnS	5.435 (−0.7%)	5.497 (+0.5%)	5.500 (+0.5%)
CZTS/ZnS interface	32.832	5.497	11.000

Strained ZnS has the lattice constants fixed to be a_{CZTS} in the [010] direction and $c_{\mathrm{CZTS}}/2$ in the [001] direction, both representing a +0.5% strain (Table 6.1). The lattice constant (Table 6.1) in the [100] direction was obtained by minimising the energy with the [001] and [010] lattice constants fixed, and represents a −0.7% strain. The supercell [100] lattice constant differs from $3a_{\mathrm{CZTS}} + 3a_{\mathrm{ZnS}}^{\mathrm{strained}}$ only very slightly, the difference arising principally from the detailed differences where the two materials meet.

The estimation of the lattice mismatch is in good agreement with previous work [65] which also obtained a lattice mismatch of 0.5%.

6.3.2 Band Offset Alignment

The valence band offset plays a key role in the conversion efficiency of photovoltaic devices. The calculated results (Section 3.7) of VBO and CBO for CZTS/ZnS in [100] indicate that the band offset is of type one with values of 0.95 and 1. 15eV for VBO and CBO, respectively. The calculated band offset for CBO and VBO is in good agreement with the theoretical finding that obtained that VBO and CBO are 0.92 and 1.36eV, respectively, in the [100] direction [65].

However, the band offset alignment of ZnS/CZTS hetero-structure shows that there is a large spike. Such a large spike (Section 1.3.1) indicates [64, 89] that the ZnS secondary phase in p-type CZTS could be regarded as a resistive barrier to the minority carrier electrons. Therefore, the ZnS could hinder the flow of electrons. Thus, reducing the photo-current (electrons) and blocking the majority carriers' (holes) flow will increase the series resistance. The precipitated ZnS phase [66] is considered an active insulator phase within CZTS but it does not act as a recombination centre or carrier trap.

6.3.3 Inter-diffusion Mechanisms of a CZTS/ZnS Interface Supercell

Inter-diffusion of the metal species across the interface impacts p-type conductivity, and is therefore of importance for device efficiency. A key mode of diffusion occurs when vacant metal sites move through the lattices and across the interface, each diffusion hop being the result of a metal ion moving between nearest sites on the cation sub-lattice.

Where there is a vacancy inside CZTS located adjacent to the interface, a Zn ion from the ZnS may migrate from the ZnS into the CZTS, possibly forming misplaced metal ions in the CZTS, i.e. $\mathrm{Zn_{Cu}}$ or $\mathrm{Zn_{Sn}}$. Similarly, where the vacancy is initially in the ZnS, metal ions may diffuse out of the CZTS, with the potential for the formation of $\mathrm{Cu_{Zn}}$ or $\mathrm{Sn_{Zn}}$ substitutions in ZnS.

To understand the mechanisms underpinning the inter-diffusion between CZTS and ZnS across a [100] interface, the two types of inter-diffusion process at the heterojunction interface are described in the next sections.

6.3.3.1 Diffusion Mechanism 1: CZTS Cation Vacancy

In this mechanism, Zn diffuses from ZnS into a metal vacancy in CZTS, leaving V_{Zn} in ZnS, as shown schematically in Fig. 6.2. The final product of the reaction is Zn_{Cu}, Zn_{Zn} or Zn_{Sn}, in the CZTS, and V_{Zn} inside ZnS. Each case has its own implications regarding the creation and movement of acceptors and donors, and charge transfer across the interface.

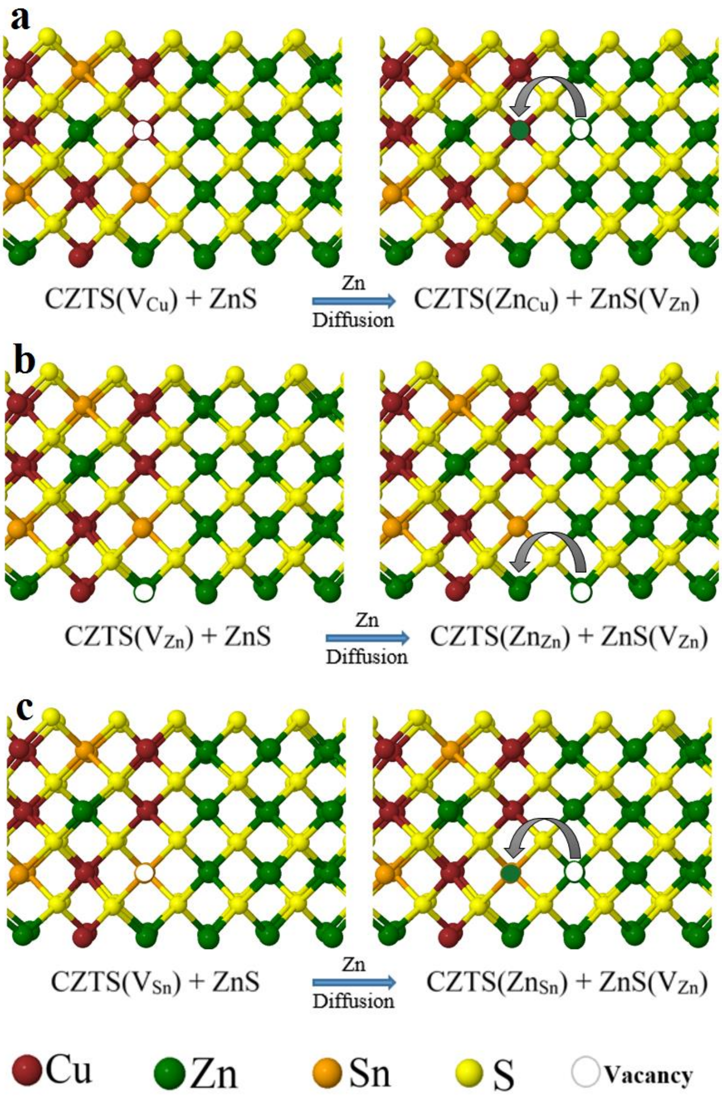

Figure 6. 2: Schematics of Zn diffusing out of ZnS into metal vacancies in CZTS: (a), (b) and (c) show Zn replacing Cu, Zn and Sn, respectively.

Firstly, V_{Cu} in CZTS converts to V_{Zn} in ZnS and Zn_{Cu} in CZTS (Fig. 6.2(a)), which is initially a single acceptor, ending as a donor—double-acceptor complex. There is an electrostatic cost for separating the charges across the interface, which might be offset due to a combination of the difference in the donor and acceptor levels and the VBO, in addition to the fact that there is also energy gain because of the relaxation of defects in those charge states.

Secondly, moving V_{Zn} from CZTS to ZnS (Fig. 6.2(b)) superficially might be expected to result in a double-acceptor in both cases. However, the VBO means the double-acceptor level of V_{Zn} in ZnS is placed below the valence band maximum in the neighbouring CZTS, and that charge transfer between the point defect in ZnS and the valence band in CZTS might take place.

Thirdly, diffusion of V_{Sn}, ostensibly a quadruple acceptor, results in Zn_{Sn} in CZTS and V_{Zn} in ZnS (Fig. 6.2(c)). Both Zn_{Sn} in CZTS and V_{Zn} in ZnS are double acceptors, so one would not expect any compensation between them, but as with the previous case, one may anticipate charge transfer from the CZTS valence band into the V_{Zn} acceptor levels.

6.3.3.2 Diffusion Mechanism 2: ZnS Cation Vacancy

In the second mechanism, V_{Zn} initially lies inside ZnS, and Cu, Zn, or Sn ions then diffuses out of CZTS across the junction, leaving a cation vacancy behind, as shown in Fig. 6.3. As with the mechanisms indicated in Section 6.3.3.1, there are nominally three basic diffusion pathways depending upon which of the three metal elements in CZTS are involved, but removal of a Zn atom from CZTS is, in practice, the reverse of process b in Fig. 6.2(b). In all cases, the initial state (V_{Zn} in ZnS) is a double acceptor with the possibility of charge transfer from the CZTS valence band.

Firstly, Cu can diffuse out of the CZTS to substitute for Zn in ZnS (Fig. 6.3(a)). The products are both expected to be single acceptors, but Cu_{Zn} in ZnS may capture a valence-band electron from CZTS. Secondly, it is noted that the process involving Zn shown in Fig. 6.3(b) is the reverse of Fig. 6.2(b). Thirdly, the other distinct process involves the movement of Sn into ZnS. The products are the double donor Sn_{Zn} in ZnS and the quadruple acceptor V_{Sn} in CZTS (Fig. 6.3(c)). Here, in contrast to all other cases, it is expected that there will be a net flow of electrons from ZnS to CZTS.

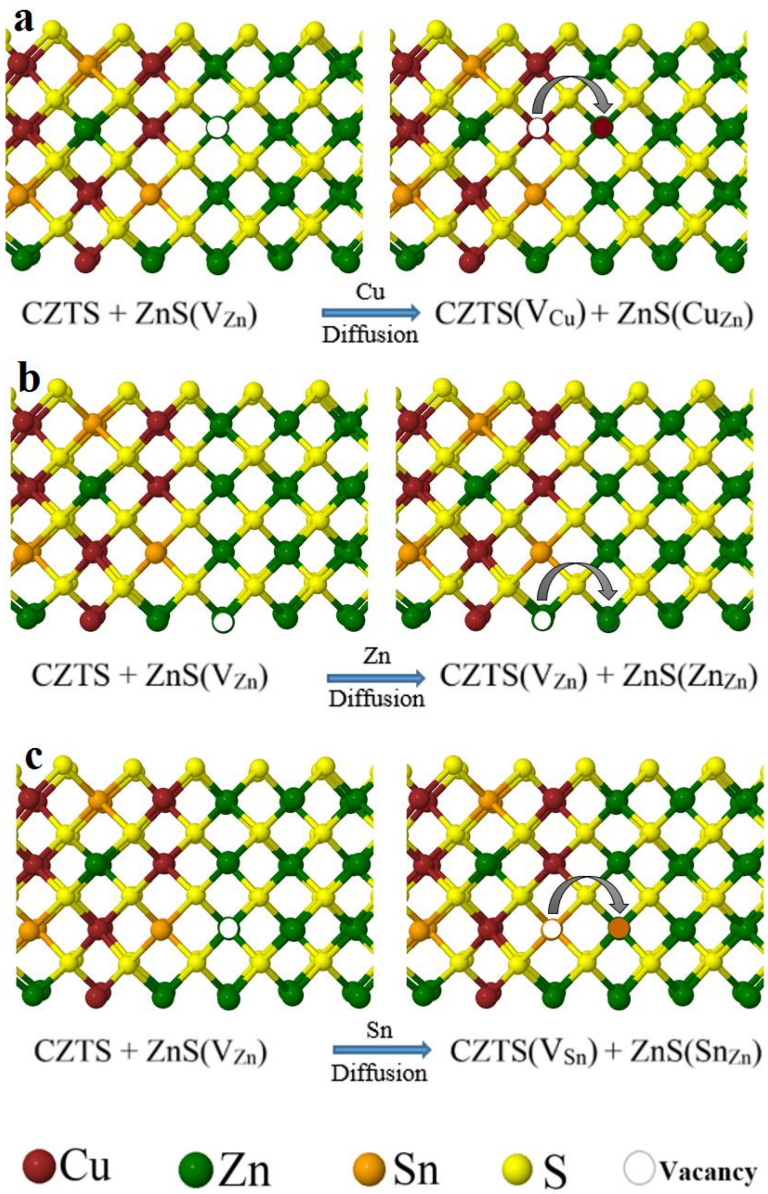

Figure 6. 3: Schematics of V_{Zn} diffusing out of ZnS forming metal vacancies in CZTS: (a), (b) and (c) show Zn being replaced by Cu, Zn and Sn, respectively.

6.3.4 Formation Energies

To identify the most stable defect form and inter-diffusion processes at the hetero-epitaxial interface, both diffusion barriers and the formation energies are required. The formation energies depend upon the atomic chemical potentials (Section 3.5); the atomic chemical potentials are linked through the requirement that CZTS is the equilibrium phase, and for this study we have constrained the analysis to Cu-poor/Zn-rich conditions, with $\mu_{\mathrm{Cu}} = -0.2\mathrm{eV}$ [40] (Fig. 4.4).

Table 6. 2: The calculated reference formation energy of the cation vacancies in the CZTS or ZnS adjacent to the interface for points P, Q, M, and N (Fig. 4.4). All energies are in eV.

Reactions	E_{P}^{f}	E_{Q}^{f}	E_{M}^{f}	E_{N}^{f}
$\mathrm{V}_{\mathrm{Cu}}^{\mathrm{CZTS}}$	1.08	1.08	1.08	1.08
$\mathrm{V}_{\mathrm{Zn}}^{\mathrm{CZTS}}$	1.09	0.95	0.91	1.03
$\mathrm{V}_{\mathrm{Sn}}^{\mathrm{CZTS}}$	2.41	2.00	2.04	2.39
$\mathrm{V}_{\mathrm{Zn}}^{\mathrm{ZnS}}$	1.64	1.51	1.47	1.59

Based on the data in Table 6.2, the formation energy to extract the Cu or Zn cation from CZTS is lower than that to extract the Zn from strained ZnS. Cu or Zn cation vacancy inside CZTS except Sn vacancy can form more easily than that of V_{Zn} in strained ZnS. Therefore, in the CZTS/ZnS heterojunction cell, Zn extraction of CZTS is easier than extracting it from strained ZnS. It is concluded that the single acceptor V_{Cu} and double acceptor V_{Zn} have the lowest formation energy compared to other defects. This could be attributed to the fact that in CZTS, Cu-S bonds are weak covalent bonds and Zn-S has slightly stronger bonds than Cu-S, while Sn-S has strong bonds [143]; in addition, there is an electrostatic cost to removing the atom and it will differ for different bonds. The bonding and the Cu-poor conditions account for the low formation energy of V_{Cu} and the relatively high formation energy of V_{Sn}, so that it is expected that the Cu vacancy is the dominant cation vacancy in CZTS [143].

6.3.5 Diffusion Barriers of CZTS/ZnS

The diffusion of cation vacancies across the interface plays an important role in determining the efficiency of the cell through their impact upon conductivity via both doping and deep carrier traps. Although the diffusion barrier of defects is very dependent on the electron chemical potential (Fermi level at 0K), in this study Fermi level has been assumed to be located at the valence band top of the CZTS for the interface. For some processes, the valence-band offset results drive charge transfer across the interface; for example, a Zn vacancy in ZnS extracts electrons from the CZTS valence band (see Section 6.3.6).

Under this Fermi level assumption, the diffusion barrier of the reactions in neutral charge states and within charge transfer across the interface has been estimated. For each process, the barrier has been estimated, and the processes aligned to a common energy scale based upon the formation energies of the defects at the interface.

For the cation vacancy in CZTS or ZnS at the interface, the reference formation energy will include the formation energy of the cation vacancy. In a case where there is V_{Cu} inside CZTS adjacent to the interface, the formation energy of V_{Cu} in CZTS at the interface will add to the activation energy to give the barrier height.

6.3.5.1 CZTS Cation Vacancy Mechanisms

6.3.5.1.1 CZTS Cation Vacancy Mechanisms in Neutral Charge State

In the first mechanism, as described in Section 6.3.3.1, initially a cation vacancy lies inside the CZTS and a Zn ion diffuses from the ZnS. The calculated barriers are illustrated in Fig. 6.4, where the initial energy is based upon the reference formation energy of the cation vacancies in CZTS adjacent to the interface for point P (Fig. 4.4). A summary of the barriers is provided in Table 6.3 for the point labelled P (Fig. 4.4) for the CZTS stable region.

For example, at the point labelled P (Fig. 4.4), the lowest diffusion barrier is for V_{Cu} in the initial state of the CZTS and when the formation energy of cation vacancy in the initial state of the CZTS for reactions is included, the lowest barrier is also for the V_{Cu} in the initial state of the CZTS. The activation energy values of the saddle points with the formation energy of reference defects, when there is V_{Cu}, V_{Zn} and V_{Sn} in the initial state of the CZTS, are 2.22, 2.47 and 3.66eV, respectively. However, in all cases, the energy is lower for the cation vacancy lying in CZTS than in ZnS, as can be seen in the lower value for all reverse reactions. This is consistent with the inference that in all cases, there is a propensity to transfer charge across the interface when the cation vacancy lies in ZnS, which has an associated electrostatic energy cost. In addition, there is a chemical term in the energy difference, associated with the differences in bond strengths between the metal ions and sulphur.

For the Q, M and N boundary points in the CZTS stable region (Fig. 4.4), the differences between the activation energy relative to point P are also listed in Table 6.3. A similar outcome between the outcome of points P, Q, M and N in the stable region of CZTS (Fig. 4.4) is expected. Under these conditions, it is clear in equilibrium conditions that the most significant migration path involves the copper vacancy, although the zinc vacancy is close by in terms of energy.

Under equilibrium conditions, Cu vacancy in bulk CZTS has the lowest formation energy compared with Zn and Sn vacancies (see Table 3.4). This is based on the fact that Cu vacancy can form and diffuse through the interface more easily than other cation vacancy intrinsic defects. Therefore, Cu vacancy can be the dominant defect inside the interface in this mechanism under equilibrium conditions.

Table 6. 3: Calculated activation energies including the reference formation energy of the cation vacancies in the CZTS adjacent to the interface for point P (Fig. 4.4, Table 6.2), E_{P}^{a}. E^{for} and E^{rev} are the forward and reverse migration barriers. For points Q, M and N (Fig. 4.4), the relative positions of the activation energies are lower by $\Delta E_{\mathrm{Q}}^{a}$, $\Delta E_{\mathrm{M}}^{a}$ and $\Delta E_{\mathrm{N}}^{a}$, respectively. All energies are in eV.

Reaction	E_{P}^{a}	E^{for}	E^{rev}	$\Delta E_{\mathrm{Q}}^{a}$	$\Delta E_{\mathrm{M}}^{a}$	$\Delta E_{\mathrm{N}}^{a}$
$\mathrm{V}_{\mathrm{Cu}}^{\mathrm{CZTS}}$	2.22	1.14 (endothermic)	0.72	0.00	0.00	0.00
$\mathrm{V}_{\mathrm{Zn}}^{\mathrm{CZTS}}$	2.47	1.38 (endothermic)	0.88	0.14	0.18	0.06
$\mathrm{V}_{\mathrm{Sn}}^{\mathrm{CZTS}}$	3.66	1.25 (endothermic)	1.06	0.41	0.37	0.02

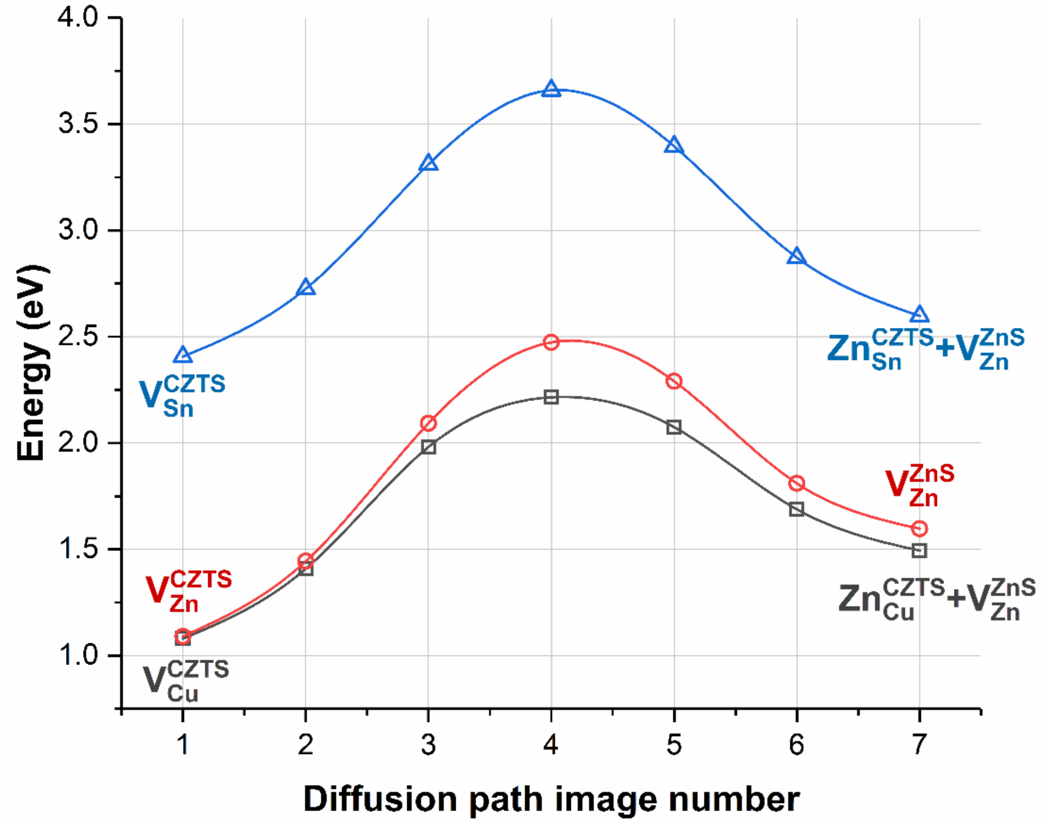

Figure 6. 4: Diffusion barriers calculated for the diffusion of Zn out of ZnS into cation vacancies in CZTS. The energy scale includes the reference formation energy of the cation vacancies in the CZTS adjacent to the interface for point P (Fig. 4.4).

6.3.5.1.2 CZTS Cation Vacancy Mechanisms in Different Charge States

The diffusion barrier of defects with different charge states inside CZTS adjacent to the CZTS/ZnS interface are investigated under equilibrium growth conditions and when the Fermi level located at the VBM of the CZTS (μ_e=E_V) due to the absorber layer CZTS is a p-type material. If the value of μ_e is changed to be higher than E_V, the formation energy of the negative charge state will come down as μ_e goes up.

6.3.5.1.2.1 $\mathbf{V_{Cu}^{CZTS} \rightleftarrows Zn_{Cu}^{CZTS} + V_{Zn}^{ZnS}}$ Reactions

Under equilibrium growth conditions and μ_e=E_V of CZTS, the diffusion barrier of Cu vacancy with different charge states inside CZTS adjacent to the interface are calculated. The lowest diffusion barrier for V_{Cu} in the initial state of the CZTS is for the charge -1 and when the formation energy of cation vacancy in the initial state of the CZTS for reactions is included, the lowest barrier is also for the same charge -1.

The equilibrium reaction for the diffusion barrier with different charge states begins and ends with the same charge (-1) across the interface; therefore, in this case there is not a charge state change as it moved across the interface. For charge 0, -1 and -2 the forward reaction (V_{Cu}^{CZTS}) is endothermic whilst the reverse reaction ($Zn_{Cu}^{CZTS} + V_{Zn}^{ZnS}$) is exothermic and the reaction is more favourable to occur in this direction (see Section 3.8). In the system with and without charge, the initial state of V_{Cu} in CZTS has lower energy than that of the final state V_{Zn} in ZnS and Zn_{Cu} in CZTS so the initial state is more stable than the product and that enhances the holes in CZTS.

The formation energies for point P are calculated, as shown in Table 6.4, and it is the same for the other boundary points Q, M and N of the CZTS stable region (Fig. 4.4). Calculated diffusion barriers at point P are illustrated in Fig. 6.5. The activation energy barriers for point P are listed in Table 6.4 and the activation energy barriers for points Q, M and N are the same for point P for all the reactions; therefore, the outcomes for each point in the stable region of CZTS (Fig. 4.4) are the same.

Table 6. 4: Calculated reference formation energies E_{P}^{f} of $\mathrm{V_{Cu}}$ in the initial state of the CZTS and activation energies E_{P}^{a} including the reference formation energy of the Cu vacancy inside CZTS adjacent to the CZTS/ZnS interface for point P (Fig. 4.4), with differed charge states. E^{for} and $E^{\mathrm{rev}}$are the forward and reverse migration barriers. All energies are in eV.

Charge	$\mathrm{E_P^f}$	E_{P}^{a}	E^{for}	E^{rev}
0	1.08	2.22	1.13 (endothermic)	0.72
−1	1.01	2.11	1.10 (endothermic)	0.79
−2	1.54	2.62	1.08 (endothermic)	0.84

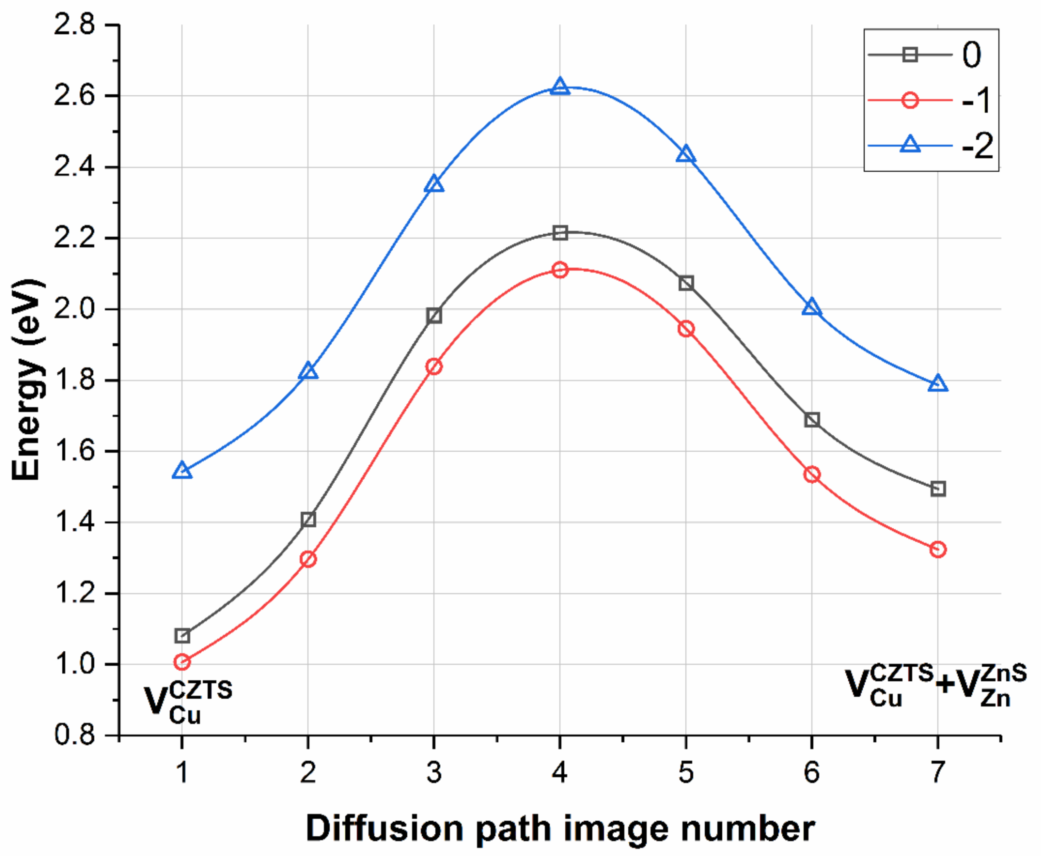

Figure 6. 5: Diffusion barriers calculated with different charge states (0, −1 and −2) for the diffusion of Zn out of ZnS into Cu cation vacancies in CZTS. The energy scale includes the reference formation energy of the cation vacancies in the CZTS adjacent to the interface for point P (Fig. 4.4) at $\mu_e = E_V$.

6.3.5.1.2.2 $V_{Zn}^{CZTS} \rightleftarrows V_{Zn}^{ZnS}$ Reactions

Under equilibrium growth conditions and μ_e=E_V of CZTS, the diffusion barrier of a Zn vacancy with different charge states inside CZTS adjacent to the interface are calculated. The lowest diffusion barrier for V_{Zn} in the initial state of the CZTS with different charge states is for the charge −1 or zero; when the formation energy of cation vacancy in the initial state of the CZTS for reactions is included, the barrier (1.09eV) will become higher (2.24eV), meaning that the cost of forming these defects is high. The lowest activation diffusion barrier including the formation energy is the same for the charge −1.

The equilibrium reaction for the diffusion barrier with different charge states begins with charge −1 and ends with the charge −1 or −2 across the interface; therefore, in this case, there is probably a charge state change as it moved across the interface. This might lead to the absorption of an electron that can come from the Fermi level to the defect state. For charges 0, −1 and −2, the reverse reaction (V_{Zn}^{ZnS}) is exothermic and the reaction is more favourable to occur in this direction (see Section 3.8). In the system with and without charge, the initial state of V_{Zn} in CZTS has lower energy than that of the final state so the initial state is more stable than the product and that enhances the holes in CZTS.

For points P, Q, M and N (Fig. 4.4), the formation energies are calculated, as shown in Table 6.5. The calculated diffusion barriers at point P are illustrated in Fig. 6.6. The activation energy barriers for point P are listed in Table 6.5. For the Q, M and N boundary points in the CZTS stable region (Fig. 4.4), the differences between the activation energy relative to point P are 0.41, 0.18 and 0.06eV, respectively, and the differences are the same for all the reactions. Although the outcome is favourable in point P, there is no substantial difference between the outcome of points P, Q, M and N in the stable region of CZTS (Fig. 4.4), so a similar outcome is expected.

Table 6. 5: Calculated reference formation energies (E_P^f, E_Q^f, E_M^f and E_N^f) of V_{Zn} in the initial state of the CZTS and activation energies E_P^a including the reference formation energy of the Zn vacancy inside CZTS adjacent to the CZTS/ZnS interface for point P (Fig. 4.4), with differing charge states. E^{for} and E^{rev} are the forward and reverse migration barriers. All energies are in eV.

Charge	E_P^f	E_Q^f	E_M^f	E_N^f	E_P^a	E^{for}	E^{rev}
0	1.09	0.95	0.91	1.03	2.47	1.38 (endothermic)	0.88
−1	1.00	0.87	0.83	0.95	2.24	1.24 (endothermic)	0.87
−2	1.17	1.03	0.99	1.11	2.25	1.08 (endothermic)	0.86

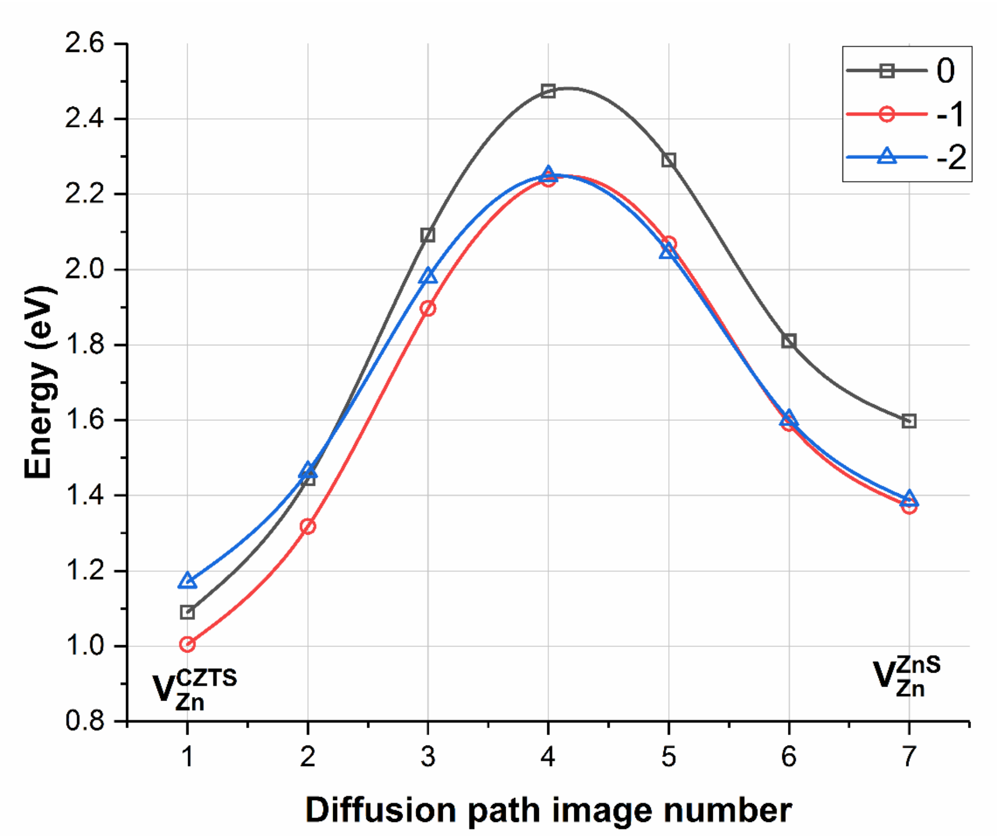

Figure 6. 6: Diffusion barriers calculated with different charge states (0, −1, and −2) for the diffusion of Zn out of ZnS into Zn cation vacancies in CZTS. The energy scale includes the reference formation energy of the cation vacancies in the CZTS adjacent to the interface for point P (Fig. 4.4) at μ_e=E_V.

6.3.5.1.2.3 $V_{Sn}^{CZTS} \rightleftarrows Zn_{Sn}^{CZTS} + V_{Zn}^{ZnS}$ Reactions

Under equilibrium growth conditions and μ_e=E_V of CZTS, the diffusion barrier of an Sn vacancy with different charge states inside CZTS adjacent to the interface are calculated. The lowest diffusion barrier for V_{Sn} in the initial state of the CZTS with different charge states is for the charge −1, but when the formation energy of cation vacancy in the initial state of the CZTS for reactions is included, the barrier (2.21eV) will become higher (3.35eV). The lowest activation diffusion barrier including the formation energy is for the charge −2.

The equilibrium reaction for the diffusion barrier with different charge states begins with the charge −1 or −2 and ends with the charge −2 across the interface; therefore, in this case probably there is a charge state change as it moved across the interface, and this is the same as the case of Zn out of ZnS into Zn cation vacancies in CZTS (Section 6.3.5.1.2.2). As the defect V_{Sn} moves from the CZTS side adjacent to the interface to the ZnS side adjacent to the interface, the lowest energy of the charge state in CZTS is −1 and it will change to −2 when the defect move across the interface to ZnS. This leads to the production of an electron that can come from the valence band top of the CZTS and leave a hole in CZTS. For the charges 0 and -1, the reverse reaction ($\mathrm{Zn}_{\mathrm{Sn}}^{\mathrm{CZTS}} + \mathrm{V}_{\mathrm{Zn}}^{\mathrm{ZnS}}$) is exothermic, whilst for the charges -2, -3 and -4, the forward reaction ($\mathrm{V}_{\mathrm{Sn}}^{\mathrm{CZTS}}$) is exothermic and the reaction is more favourable to occur in this direction (see Section 3.8). In the system, for charges 0 and -1, the initial state of V_{Sn} in CZTS has lower energy than that of the final state V_{Zn} in ZnS and $\mathrm{Zn}_{\mathrm{Sn}}$ in CZTS so the initial state is more stable than the product and that enhances the holes in CZTS; however, the other charges are the opposite.

For points P, Q, M and N (Fig. 4.4), the formation energies are calculated, as shown in Table 6.6. Calculated diffusion barriers at point P are illustrated in Fig. 6.7. The activation energy barriers for point P are listed in Table 6.6. For the Q, M and N boundary points in the CZTS stable region (Fig. 4.4), the differences between the activation energy relative to point P are 0.41, 0.37 and 0.02eV, respectively, and the differences are the same for all the reactions. A similar outcome between the points P, Q, M and N in the stable region of CZTS (Fig. 4.4) is expected, as is the case in Section 6.3.5.1.2.2.

Table 6. 6: Calculated reference formation energies ($\mathrm{E}_{P}^{\mathrm{f}}$, $\mathrm{E}_{Q}^{\mathrm{f}}$, $\mathrm{E}_{M}^{\mathrm{f}}$ and $\mathrm{E}_{N}^{\mathrm{f}}$) of V_{Sn} in the initial state of the CZTS and activation energies E_{P}^{a} including the reference formation energy of the Sn vacancy inside CZTS adjacent to the CZTS/ZnS interface for point P (Fig. 4.4), with differing charge states. E^{for} and E^{rev} are the forward and reverse migration barriers. All energies are in eV.

Charge	E_{P}^{f}	E_{Q}^{f}	E_{M}^{f}	E_{N}^{f}	E_{P}^{a}	E^{for}	E^{rev}
0	2.41	2.00	2.04	2.39	3.66	1.25 (endothermic)	1.06
−1	2.21	1.80	1.84	2.19	3.35	1.14 (endothermic)	1.04
−2	2.24	1.84	1.87	2.22	3.30	1.06 (exothermic)	1.08
−3	2.47	2.06	2.10	2.45	3.50	1.03 (exothermic)	1.17
−4	2.76	2.35	2.39	2.74	3.71	0.95 (exothermic)	1.17

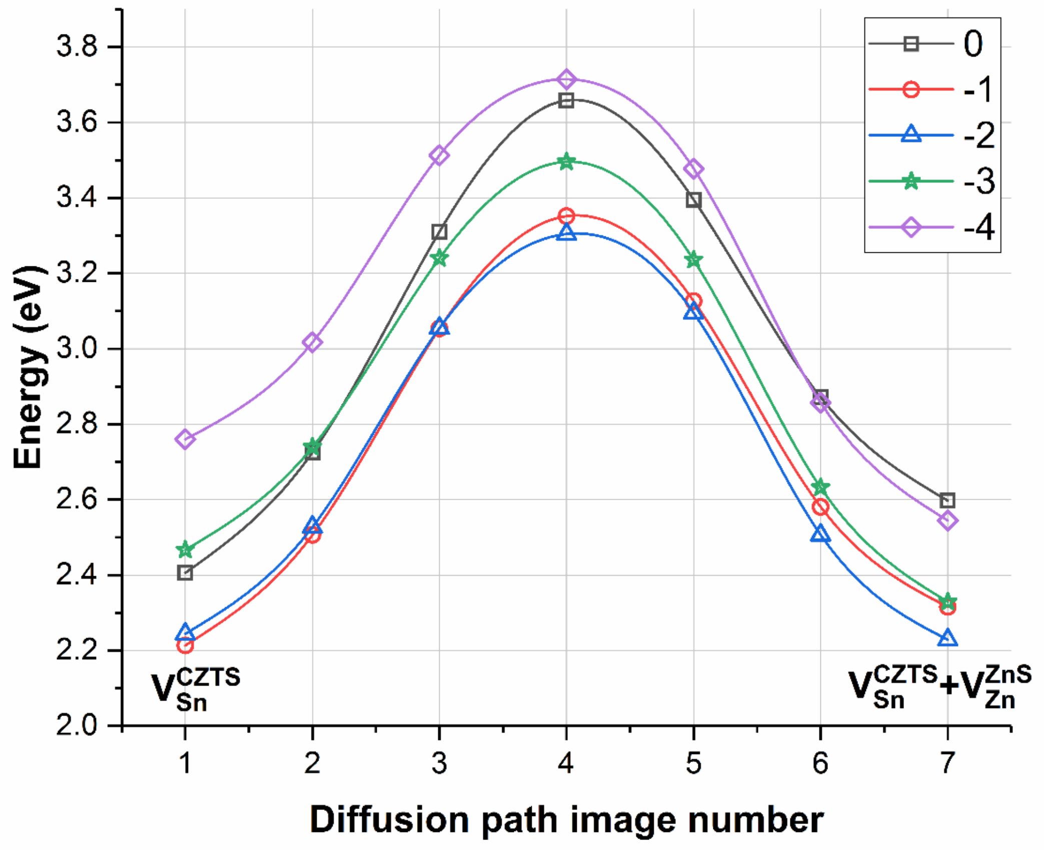

Figure 6. 7: Diffusion barriers calculated with different charge states (0, −1, −2, −3 and −4) for the diffusion of Zn out of ZnS into Sn cation vacancies in CZTS. The energy scale includes the reference formation energy of the cation vacancies in the CZTS adjacent to the interface for point P (Fig. 4.4) at μ_e=E_V.

6.3.5.2 ZnS Cation Vacancy Mechanisms

6.3.5.2.1 ZnS Cation Vacancy Mechanisms in Neutral Charge State

In the second mechanism, as described in Section 6.3.3.2, V_{Zn} diffuses out of ZnS. As with the CZTS cation vacancy mechanisms, the energies are listed in Table 6.2. The barriers calculated for the reference point P (Fig. 4.4) are shown in Fig. 6.8. A summary of the barriers is provided in Table 6.7 for the four boundary points (Fig. 4.4) for the CZTS stable region.

Mirroring the previous cases (Section 6.3.5.1.1), the reverse reaction barriers are lower than forward for two of the three reactions that result in impurities (Cu or Sn) being incorporated into the ZnS lattice, with the energy cost including an electrostatic term from charge transferred across the interface, as well as a bond-strength term. It is noticed that there is an intermediate minimum structure in the diffusion barrier reaction with an Sn impurity, and this could be attributed to the fact that Sn is more relaxed at image four and can make more bonds at that image since the Sn atoms are bigger than Cu and Zn. This intermediate minimum structure also occurs when there is V_{Sn} in bulk CZTS (Section 4.3.9.1), and also when there is an Sn impurity inside cubic and strained ZnS (Section 5.3.5.2 and Section 5.3.6.2). The barrier for all forward and reverse reactions depends on the differences between the saddle point and both the initial and final state.

However, under given equilibrium conditions, moving V_{Zn} to form V_{Zn} in CZTS is exothermic, meaning that pre-existing V_{Zn} in ZnS are highly likely to diffuse into the CZTS. The isoelectronic process has the most significant migration path compared with other diffusion barriers in this mechanism under equilibrium conditions, and when the formation energy of V_{Zn} in the initial state of the ZnS is included, the lowest activation diffusion barrier is also for V_{Zn} out of ZnS onto Zn cation sites in CZTS.

For the Q, M and N boundary points in the CZTS stable region (Fig. 4.4), the differences between the activation energy relative to point P are 0.14, 0.18 and 0.06eV, respectively and the differences are the same for all three reactions. A similar outcome between points P, Q, M and N in the stable region of CZTS (Fig. 4.4) is expected, as for the case in Section 6.3.5.1.2.2 and Section 6.3.5.1.2.3.

Table 6. 7: Calculated activation energies including the reference formation energy of the cation vacancies in the ZnS adjacent to the interface for point P (Fig. 4.4, Table 6.2), E_{P}^{a}. E^{for} and E^{rev} are the forward and reverse migration barriers. All energies are in eV.

Reaction	E_{P}^{a}	E^{for}	E^{rev}
$\mathrm{V}_{\mathrm{Zn}}^{\mathrm{ZnS}} \leftrightarrow \mathrm{Cu}_{\mathrm{Zn}}^{\mathrm{ZnS}} + \mathrm{V}_{\mathrm{Cu}}^{\mathrm{CZTS}}$	2.55	0.90 (endothermic)	0.64
$\mathrm{V}_{\mathrm{Zn}}^{\mathrm{ZnS}} \leftrightarrow \mathrm{V}_{\mathrm{Zn}}^{\mathrm{CZTS}}$	2.47	0.88 (exothermic)	1.38
$\mathrm{V}_{\mathrm{Zn}}^{\mathrm{ZnS}} \leftrightarrow \mathrm{Sn}_{\mathrm{Zn}}^{\mathrm{ZnS}} + \mathrm{V}_{\mathrm{Sn}}^{\mathrm{CZTS}}$	2.93	1.29 (endothermic)	1.02

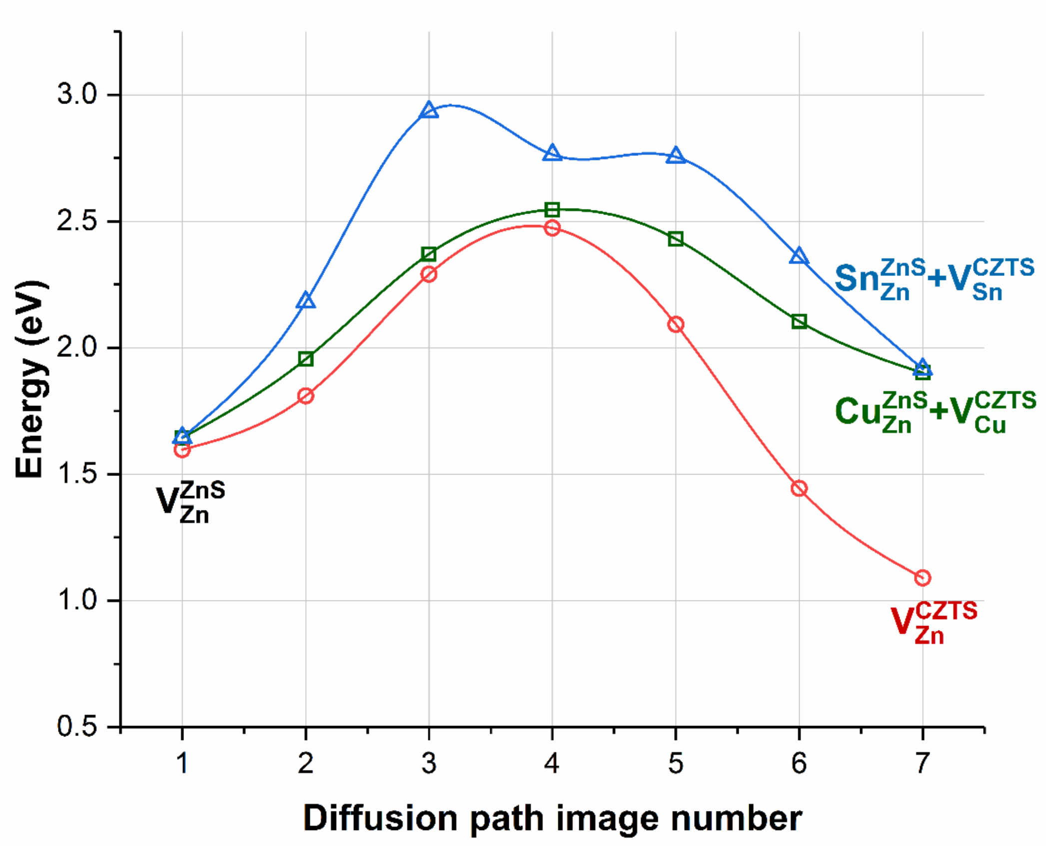

Figure 6. 8: Diffusion barriers calculated for the diffusion of either Cu, Zn or Sn out of CZTS into cation sites in ZnS adjacent to the interface. The energy scale includes the reference formation energy of the cation vacancies in the ZnS adjacent to the interface for point P (Fig. 4.4).

6.3.5.2.2 ZnS Cation Vacancy Mechanisms in Different Charge States

6.3.5.2.2.1 $V_{Zn}^{ZnS} \rightleftarrows Cu_{Zn}^{ZnS} + V_{Cu}^{CZTS}$ Reactions

Under equilibrium growth conditions μ_e=E_V of CZTS, the diffusion barriers of Cu out of CZTS into cation sites in ZnS adjacent to the interface are calculated. The lowest diffusion barrier for V_{Zn} in ZnS and Cu diffusing out of CZTS to replace the V_{Zn} in ZnS is for the charges −1, while when the formation energy of V_{Zn} in the initial state of the ZnS is included, the lowest activation diffusion barrier is also for the charge −1. The equilibrium reaction for the diffusion barrier with different charge states begins and ends with the same charge (−1) across the interface; therefore, in this case there is no change in charge state as it moved across the interface.

For the charges 0, −1 and −2, the forward reaction (V_{Zn}^{ZnS}) is endothermic whilst the reverse reaction ($Cu_{Zn}^{ZnS} + V_{Cu}^{CZTS}$) is exothermic and the reaction is more favourable to occur in this direction (see Section 3.8). In the system with and without charge, the initial state of V_{Zn} in ZnS has lower energy than that of the final state so the initial state is more stable than the product and that enhances the holes in ZnS so the cation elements in CZTS can move across the interface and replace the V_{Zn}.

For points P, Q, M and N (Fig. 4.4), the formation energies are calculated, as shown in Table 6.8. Calculated diffusion barriers at point P are illustrated in Fig. 6.9. The activation energy barriers for point P are listed in Table 6.12. For the Q, M and N boundary points in the CZTS stable region (Fig. 4.4), the differences between the activation energy relative to point P are 0.14, 0.18 and 0.06eV, respectively, and the differences are the same for all three reactions, and as is mentioned in Section 6.3.5.2.1, a similar outcome between points P, Q, M and N in the stable region of CZTS (Fig. 4.4) is expected.

Table 6. 8: Calculated reference formation energies (E_P^{f}, E_Q^{f}, E_M^{f} and E_N^{f}) of V_{Zn} in the initial state of the ZnS and activation energies including the reference formation energy E_{P}^{a} of the Zn vacancy inside ZnS and Cu diffusing out of CZTS to replace the V_{Zn} for point P (Fig. 4.4), with differing charge states. E^{for} and E^{rev} are the forward and reverse migration barriers. All energies are in eV.

Charge	E_{P}^{f}	E_{Q}^{f}	E_{M}^{f}	E_{N}^{f}	E_{P}^{a}	E^{for}	E^{rev}
0	1.64	1.51	1.47	1.59	2.55	0.90 (endothermic)	0.64
−1	1.47	1.33	1.29	1.41	2.36	0.89 (endothermic)	0.69
−2	1.62	1.49	1.45	1.56	2.51	0.89 (endothermic)	0.75

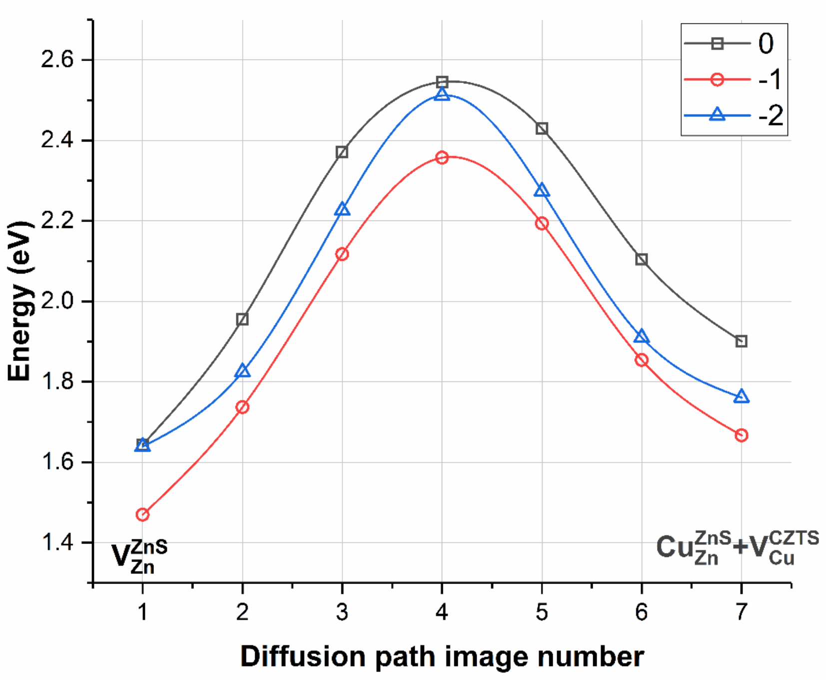

Figure 6. 9: Diffusion barriers calculated with different charge states (0, −1 and −2) for the diffusion of Cu out of CZTS into cation sites in ZnS adjacent to the interface. The energy scale includes the reference formation energy of the cation vacancies in the ZnS adjacent to the interface for point P (Fig. 4.4) at μ_e=E_V.

6.3.5.2.2.2 $V_{Zn}^{ZnS} \rightleftarrows V_{Zn}^{CZTS}$ Reactions

This mechanism is opposite to the Zn metal vacancy inside CZTS adjacent to the CZTS/ZnS interface (see Section 6.3.1.2.2), since it is an isoelectronic process. Under equilibrium growth conditions and μ_e=E_V of CZTS, the diffusion barrier of Zn out of CZTS into cation sites in ZnS adjacent to the interface are calculated. The lowest diffusion barrier of V_{Zn} in ZnS and Zn diffusing out of CZTS to replace the V_{Zn} in ZnS is for the charge −2 and when the formation energy of V_{Zn} in the initial state of the ZnS is included, the lowest activation diffusion barrier is for both charge −1. The equilibrium reaction for the diffusion barrier with different charge states begins with the charges −1 or −2 and ends with the same charge (−1) across the interface; therefore, in this case, probably there is a charge state change as it moved across the interface. This might lead to the absorption of an electron that can come from the Fermi level to the defect state.

For the charges 0, −1 and −2, the forward reaction (V_{Zn}^{ZnS}) is exothermic and the reaction is more favourable to occur in this direction (see Section 3.8). The charge −2 is less exothermic than that of the charges 0 and −1. In the system with and without charge, the initial state of V_{Zn} in ZnS has higher energy than that of the final state so the final state is more stable than the initial state and that enhances the holes in CZTS. In contrast, the diffusion of V_{Zn} out of ZnS onto Cu cation sites in CZTS is endothermic.

For points P, Q, M and N (Fig. 4.4), the formation energies are calculated, as shown in Table 6.5. Calculated diffusion barriers at point P are illustrated in Fig. 6.10. The activation energy barriers for point P are listed in Table 6.9. For the Q, M and N boundary points in the CZTS stable region (Fig. 4.4), the differences between the activation energy relative to point P are 0.14, 0.18 and 0.06eV, respectively, and the differences are the same for all three reactions, and as is mentioned in Section 6.3.5.2.1, a similar outcome between points P, Q, M and N in the stable region of CZTS (Fig. 4.4) is expected.

Table 6. 9: Calculated activation energies including the reference formation energy of the Zn vacancy inside CZTS adjacent to the CZTS/ZnS interface for point P (Fig. 4.4, Table 6.5) E_{P}^{a}. E^{for} and $E^{\mathrm{rev}}$are the forward and reverse migration barriers. All energies are in eV.

Charge	E_{P}^{a}	E^{for}	E^{rev}
0	2.47	0.88 (exothermic)	1.38
−1	2.24	0.87 (exothermic)	1.24
−2	2.25	0.86 (exothermic)	1.08

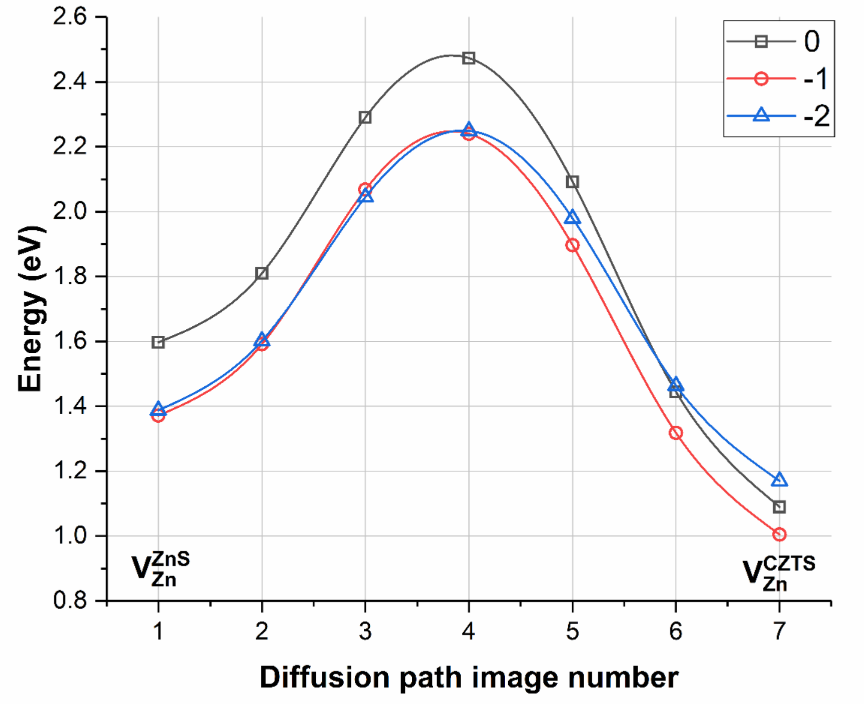

Figure 6. 10: Diffusion barriers calculated with different charge states (0, −1 and −2) for the diffusion of Zn out of CZTS into cation sites in ZnS adjacent to the interface. The energy scale includes the reference formation energy of the cation vacancies in the ZnS adjacent to the interface for point P (Fig. 4.4) at $\mu_e = E_V$.

6.3.5.2.2.3 $\mathbf{V_{Zn}^{ZnS} \rightleftarrows Sn_{Zn}^{ZnS} + V_{Sn}^{CZTS}}$ Reactions

Under equilibrium growth conditions and μ_e=E_V of CZTS, the diffusion barriers of V_{Zn} in ZnS and Sn diffusing out of CZTS to replace the V_{Zn} in ZnS are calculated. The lowest diffusion barrier of Sn out of CZTS into cation sites in ZnS is for the charge -1 and when the formation energy of V_{Zn} in the initial state of the ZnS is included, the lowest activation diffusion barrier is for the charge -2.

The equilibrium reaction for the diffusion barrier with different charge states begins with the charge -1 and ends with the charges -1 or -2 across the interface; therefore, in this case there is a charge state change as it moved across the interface, and this is same as the case of Sn out of CZTS into cation sites in ZnS (Section 6.3.5.2.2.2). As the defect (V_{Zn}) moves from the ZnS side adjacent to the interface to the CZTS side adjacent to the interface, the lowest energy of the charge state in ZnS is -1 and it will change to -2 when the defect move across the interface to CZTS. This leads to the production of an electron that can come from the valence band top of the CZTS and leave a hole in CZTS.

For the charges 0, 1 and 2, the reverse reaction ($Sn_{Zn}^{ZnS} + V_{Sn}^{CZTS}$) is exothermic, whilst for the charges -1, -2, -3 and -4, the forward reaction (V_{Zn}^{ZnS}) is exothermic and the reaction is more favourable to occur in this direction (see Section 3.8). In the system for charges -1, -2, -3 and -4, the final have lower energy than that of the initial state so the final state is more stable than the initial state and that enhances the holes in CZTS. The diffusion barrier reactions have an intermediate minimum structure in the diffusion barrier reaction with an Sn impurity, as explained in Section 6.3.5.2.1.

For points P, Q, M and N (Fig. 4.4), the formation energies are calculated, as shown in Table 6.14. Calculated diffusion barriers at point P are illustrated in Fig. 6.11. The activation energy barriers for point P are listed in Table 6.15. For the Q, M and N boundary points in the CZTS stable region (Fig. 4.4), the differences between the activation energy relative to point P are 0.14, 0.18 and 0.06eV, respectively, and the differences are the same for all the reactions, and as is mentioned in Section 6.3.5.2.1, a similar outcome between points P, Q, M and N in the stable region of CZTS (Fig. 4.4) is expected.

Table 6. 10: Calculated reference formation energies (E_P^{f}, E_Q^{f}, E_M^{f} and E_N^{f}) of $\mathrm{V_{Zn}}$ in the initial state of the ZnS and activation energies including the reference formation energy E_{P}^{a} of the Zn vacancy inside ZnS and Sn diffusing out of CZTS to replace the $\mathrm{V_{Zn}}$ for point P (Fig. 4.4), with differing charge states. E^{for} and E^{rev} are the forward and reverse migration barriers. All energies are in eV.

Charge	E_{P}^{f}	E_{Q}^{f}	E_{M}^{f}	E_{N}^{f}	E_{P}^{a}	E^{for}	E^{rev}
2	2.40	2.26	2.22	2.34	3.76	1.36 (endothermic)	1.15
1	1.99	1.85	1.81	1.93	3.19	1.20 (endothermic)	1.17
0	1.64	1.51	1.47	1.59	2.93	1.29 (endothermic)	1.02
−1	1.47	1.33	1.29	1.41	2.16	0.69 (exothermic)	1.15
−2	1.62	1.49	1.45	1.56	2.13	0.51 (exothermic)	1.17
−3	2.01	1.87	1.83	1.95	2.43	0.42 (exothermic)	1.19
−4	2.47	2.33	2.29	2.41	2.76	0.30 (exothermic)	1.16

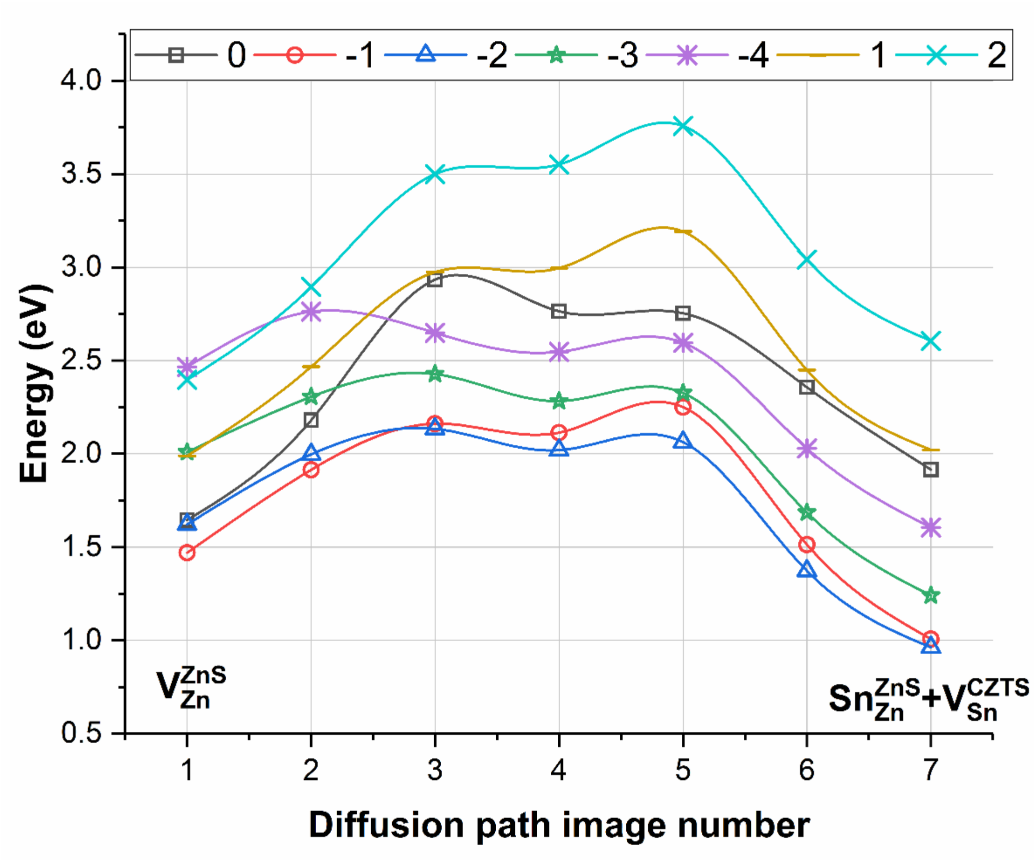

Figure 6. 11: Diffusion barriers calculated with different charge states (0, −1, −2, −3, −4, 1 and 2) for the diffusion of Sn out of CZTS into cation sites in ZnS adjacent to the interface. The energy scale includes the reference formation energy of the cation vacancies in the ZnS adjacent to the interface for point P (Fig. 4.4) at $\mu_{\mathrm{e}}=E_{\mathrm{V}}$.

6.3.5.3 Zn Diffusion Inside the ZnS Part Adjacent to the Interface

The diffusion process inside the ZnS part mirrors the bulk strained ZnS (Section 5.3.6.1). Considering that there is strain in the ZnS layer (Section 5.3.1), the diffusion of Zn inside ZnS in the parallel direction or away from the CZTS/ZnS interface will be different and that will affect cell conductivity; the concentration of the cation vacancy in CZTS which is formed by moving the elements from CZTS to ZnS depends on the concentration of the Zn vacancy in ZnS, and that affects the p-type CZTS conductivity.

In this case, a Zn atom moves to the nearest cation vacancy inside the ZnS part adjusted to the interface and leaves V_{Zn} in the initial place (Section 5.3.6.1**)**, as shown schematically in Fig. 6.12. There is a cation vacancy lying inside the ZnS part in this process. The diffusion barrier of Zn metal inside the ZnS part depends on the interface direction, since the ZnS lattice lengths in the [010] and [001] directions differ from the [100] direction due to the interface strain (see Section 6.3.1). Due to the interface model conditions, the diffusion barriers in the away direction from the interface [1 1 0], [1 $\bar{1}$ 0], [1 0 1] and [1 0 $\bar{1}$] differ from the parallel direction to the interface [0 1 1], [0 1 $\bar{1}$], [0 $\bar{1}$ 1] and [0 $\bar{1}$ $\bar{1}$].

The calculated diffusion barriers at point P for the absolute energy scale and with reference formation energy in the [110] direction away from the interface and the [011] parallel direction to the interface are illustrated in Fig. 6.13. The diffusion barrier in the [110] and [011] directions are closed and this is attributed to the strain in ZnS being very small (see Section 6.3.1). The diffusion barrier of the [110] direction away from the interface and the [011] direction parallel to the interface begin with the same point and end with different points where the end point in the [110] direction away from the interface is higher than that of the [011] direction parallel to the interface.

The diffusion barrier in the [110] direction away from the interface and the [011] direction parallel direction to the interface are different and this is attributed to the fact that the strain in ZnS is relatively small (see Section 7.3.1), in addition to the electrostatic effect. The lowest diffusion barrier for Zn diffusion inside the ZnS part adjacent to the interface is for the [011] parallel direction to the interface. This result agrees with the result for bulk strained ZnS (Section 5.3.6.1**)**.

The diffusion barrier of the [110] direction away from the interface and the [011] parallel direction begins with the same point and ends with different points where the end point in the [110] direction away from the interface is higher than that of the [011] parallel directions. For the [110] direction away from the interface, the difference between the starting and ending points is attributed to moving the charge transferred from the CZTS valence band further from the interface which costs energy to work against the electrostatic field. In the [011] parallel direction to the interface, the difference between the starting and ending points is attributed to the local environment where the starting point for the Zn atom in ZnS is located next to the Zn atom in CZTS, while at the end point, the Zn atom in ZnS is located next to the Sn atom in CZTS.

For both the [110] direction away from the interface and the [011] direction parallel to the interface, the reverse reactions are exothermic and the reaction is more favourable to occur in this reverse direction (see Section 3.8). As a result, in the [110] direction away from the interface, the Zn vacancy can move more easily towards the interface than in the opposite direction. Therefore, the probability of finding a Zn vacancy inside the ZnS part adjacent to the interface is greater closed to the interface than that away from the interface. This enhances transfer of the cation from CZTS adjacent to the interface to ZnS and leaves cation vacancy inside CZTS, and that enhances the p-type conductivity of the cell.

For the P, Q, M and N points (Fig. 4.4), the formation energies are calculated, as shown in Table 6.2. The activation energy barriers for point P are listed in Table 6.11. For the Q, M and N boundary points in the CZTS stable region (Fig. 4.4), the differences between the activation energy relative to point P are 0.14, 0.18 and 0.06eV, respectively, and the differences are the same for both reactions; a similar outcome between points P, Q, M and N in the stable region of CZTS (Fig. 4.4) is expected.

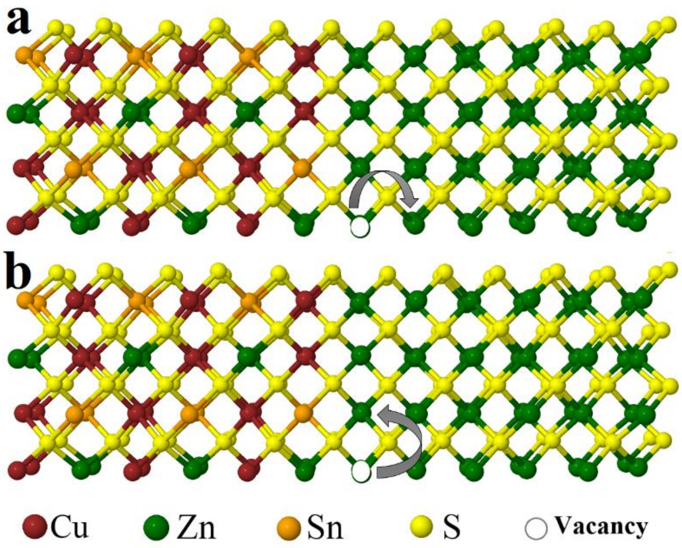

Figure 6. 12: Schematics of diffusion barriers for Zn diffusing into metal vacancies in strained ZnS part adjacent to the CZTS/ZnS interface in (a) [110] direction away from the interface, (b) [011] parallel direction to the interface.

Table 6. 11: Calculated activation energies including the reference formation energy of the Zn vacancy for Zn diffusing inside the ZnS part adjacent to the interface at the [110] direction away from the interface and the [011] parallel direction to the interface for point P (see Section 4.3.4, Table 6.2) E_{P}^{a}. E^{for} and E^{rev} are the forward and reverse migration barriers. All energies are in eV.

Direction	E_{P}^{a}	E^{for}	E^{rev}
[110] away from the interface	4.64	1.61 (endothermic)	0.65
[011] parallel to the interface	4.57	1.54 (endothermic)	1.12

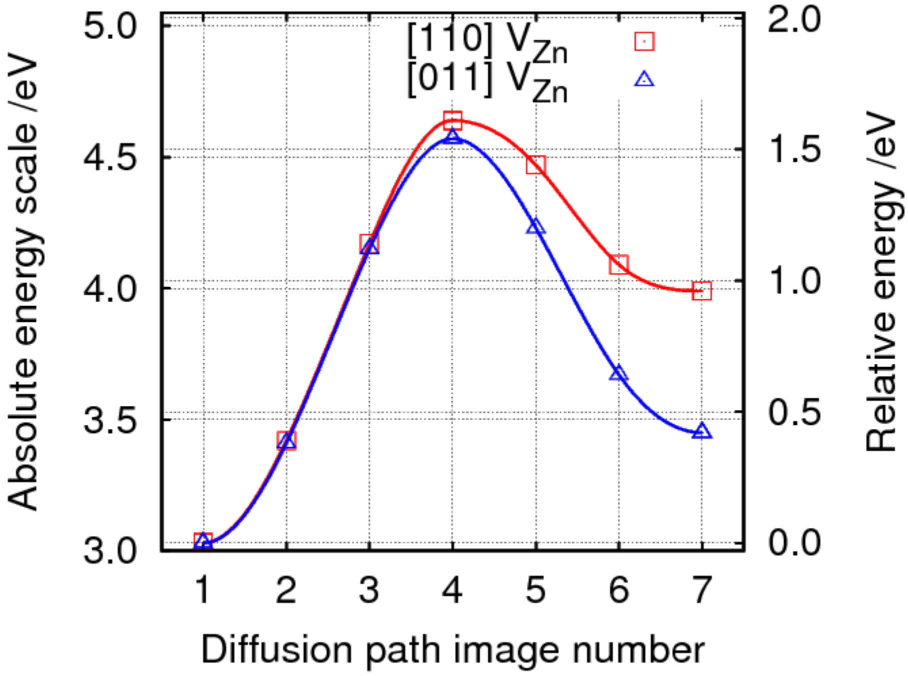

Figure 6. 13: Diffusion barriers calculated for the absolute energy scale and with reference formation energy of Zn diffusing into metal vacancies in the strained ZnS part adjacent to the CZTS/ZnS interface in the [110] direction away from the interface and the [011] parallel direction to the interface at point P (Fig. 4.4).

6.3.6 Charge Density

Charge density describes the amount of electric charge per unit volume. By calculating the value of the charge density for the mesh points throughout the periodic boundary of the CZTS/ZnS interface a numerical integral can be performed to investigate how much charge there is between two limit points along the [100] direction in the simulated cell. From the calculated charge density the total amount of electrons in that region can be determined and then the nuclear charge can be subtracted to get the total charge.

In the slab, the [100] direction is divided into slices (see Fig. 6.14) and then the average charge density in the number of slices is calculated in each slice; therefore, the amount of charge between two limit points in all those slices can be determined by summing the calculated average charge density across the across section area through the interface direction.

The boundary of the sulphur plane at the interface has to be chosen (see Fig. 6.15) and depending on the side where the vacancy is located. The sulphur layer associated with the defect is common, and the boundary of the common sulphur plane could be on one side or the other depending on the defect (away from the defect to avoid the interaction between the vacancy and the neighbouring S). The area under these curves between two limits is integrated and this area represents the total charge. Two planes are defined, and the sum of the charge between them is found. The boundary planes are chosen to be minima in the average charge densities subject to the choice of which side is a S layer.

In this analysis the number of electrons has been accounted in the CZTS and ZnS parts of both slabs free of defects and when there is a Zn vacancy located in the first and second nearest neighbour to the interface, and the electron charge is expected to be equal to the nuclear charge in each part of the slab. The total charges of the CZTS and ZnS within and without a Zn vacancy and net charge are listed in Table 6.12. It is found that there is no significant charge transfer between the ZnS secondary phase and the CZTS absorber layer if the Zn vacancy is inside CZTS, whereas there is when one Zn vacancy is inside the ZnS in the first and second layer adjacent to the [100] interface direction.

When there is no net charge and the vacancy is in one side or other, either have a neutral double acceptor in the absorber layer or an ionised double acceptor and two holes in the secondary phases. If the Zn vacancy is in the ZnS side, and there is extra electrons adding to the system (net charge), the adding electrons is cancelled the holes which are being in the valence band of CZTS, while in case the vacancy is in the CZTS side, the adding extra electrons will end with ionised double acceptor in the CZTS side. Therefore, a Zn vacancy inside ZnS with and without the net charge can produce two more electrons in the ZnS side than the pure case.

The analysis illustrates that in the slab with a Zn vacancy inside the ZnS, there is a net charge flow from the CZTS into the secondary phase (see Fig. 6.16), and the number of electrons in the secondary phases is significantly greater than the corresponding number of protons. The total amount of charge in the slab with a Zn vacancy inside ZnS is around two electrons more in the ZnS with the vacancy present and two fewer in the CZTS.

Table 6. 12: The total charge within and without vacancy and net charge is calculated based on the charge density after subtracting the amount of nuclear charge.

Slab	The total charge	
	CZTS	ZnS
(CZTS-ZnS) bulk	0.00e	-0.05e
CZTS(V_{Zn})-ZnS	0.00e	-0.02e
CZTS(V_{Zn})-ZnS (sec. neighbour)	0.01e	-0.04e
CZTS(V_{Zn})-ZnS (q_{total}=-2e)	-2.00e	0.00e
CZTS(V_{Zn})-ZnS(q_{total}=-2e)(sec. neighbour)	-2.00e	0.00e
CZTS-ZnS(V_{Zn})	2.00e	-1.98e
CZTS-ZnS(V_{Zn}) (sec. neighbour)	1.99e	-1.98e
CZTS-ZnSV_{Zn} (q_{total}=-2e)	0.00e	-2.00e
CZTS-ZnSV_{Zn}(q_{total}=-2e)(sec. neighbour)	0.00e	-2.00e

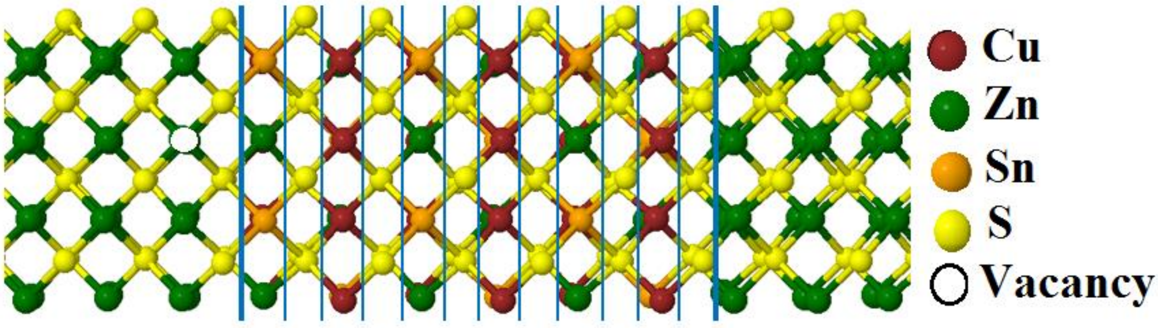

Figure 6. 14: Schematic of the structure of the CZTS/ZnS interface show the slices between two limit points when there is a vacancy in ZnS at the interface.

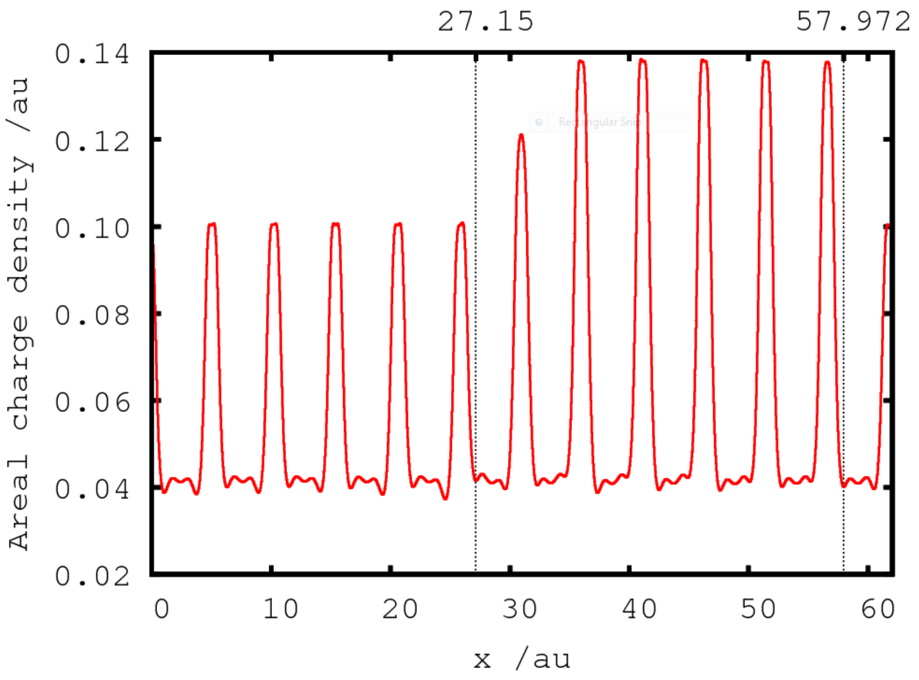

Figure 6. 15: Calculated charge density between two points across the CZTS/ZnS slab when there is a Zn vacancy inside ZnS adjacent to the interface.

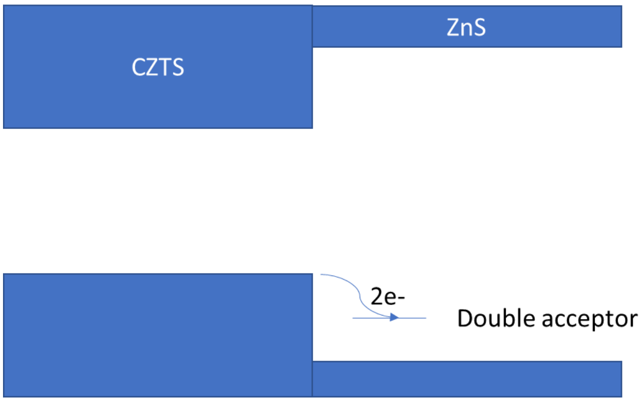

Figure 6. 16: Schematic of the CZTS/ZnS interface model illustrating charge transfer from VBM of CZTS to ZnS when there is a Zn vacancy inside ZnS adjacent to the interface.

6.3.7 Wave Function

The analysis of the wave function illustrates that the highest energy occupied state (VBM) for the slab free of defects is mainly made up of 3*p* orbital of the S atom in CZTS and the lowest empty state (CBM) of the slab with a Zn vacancy inside ZnS is also 3*p* orbital of the S atom in CZTS, as shown in Fig. 6.17. Wave function analysis indicates that for both slabs free of defects and with a Zn vacancy inside ZnS, the highest occupied electronic state in the pure case is the VBM of CZTS, and it is the same for the lowest empty state in the defect case. Therefore, the lowest empty state of the slab when there is V_{Zn} inside ZnS is the valence band top of the CZTS.

The shape of the lowest empty state is based on the anti-bonding contribution of the S atom. The lowest empty state of the ZnS with V_{Zn} looks the same as the 3*p*-orbital of the S atom in the CZTS when there are holes in the top of the valence band (see Fig. 6.17 (b)). The state in the vicinity of Fermi energy when the vacancy is on the ZnS side are shown in (Fig. 6.17 (b)), and the localization of the empty states is characteristically similar to the valence band of the perfect CZTS layer.

V_{Zn} inside ZnS is quite localised because a Zn vacancy is considered quite a deep defect in ZnS. The shallow level arises below the valence band top of the CZTS; therefore, it is filled. The holes in the CZTS are delocalised, because they are in the valence band top (shallow state level). The empty states of a Zn vacancy inside ZnS are filled by the electrons that come from the valence band top of CZTS. Therefore, in the slab, the lowest energy empty state is not the conduction band state, it is the VBM of CZTS. There is a charge transfer through the slab from the CZTS to ZnS when there is a Zn vacancy inside ZnS.

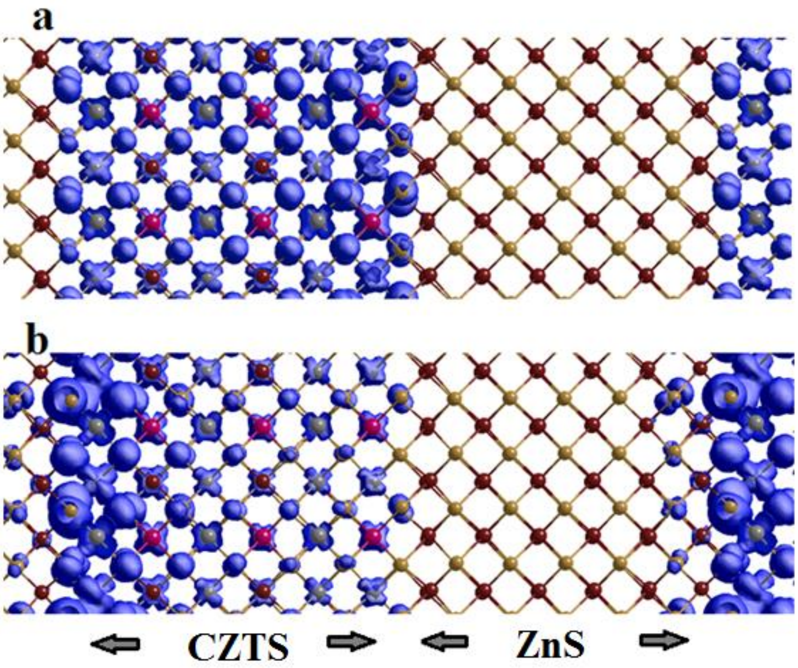

Figure 6. 17: The valence band maximum wave function of the CZTS/ZnS interface: (a) the wave function of the bulk interface; (b) the wave function of the interface with a Zn vacancy in the ZnS side.

6.4 Conclusions

The results show that at for a (100)-CZTS/ZnS heterojunction under the equilibrium growth conditions considered for this study, the formation energy for a Cu or Zn vacancy in CZTS adjacent to the interface in the first mechanisms is lower than for a Zn vacancy in ZnS adjacent to the interface in the second mechanisms. This is in line with the p-type doping in as-grown CZTS under these conditions.

It is observed that, under the given conditions, V_{Cu} in CZTS adjacent to the interface has the lowest activation diffusion barrier compared with other defects; however, the energetics of this process are unfavourable for of migration into the ZnS, meaning that the buffer layer will act as an effective diffusion barrier to these p-type doping centres.

The equilibrium reaction for the diffusion barrier with different charge states refers to the fact that there is no changing charge state as moved across the interface in case there is V_{Cu} inside CZTS adjacent to the interface in the first mechanisms, and when there is V_{Zn} in ZnS adjacent to the interface and Cu diffusing out of CZTS to replace the V_{Zn} in ZnS in the second mechanisms. However, there is a changing charge state as moved across the interface in a case where there is V_{Zn} or V_{Sn} inside CZTS adjacent to the interface in the first mechanisms, and when there is V_{Zn} in ZnS adjacent to the interface and Zn or Sn diffusing out of CZTS to replace the V_{Zn} in ZnS in the second mechanisms.

The diffusion barrier in the equilibrium charge states of all cation vacancies within CZTS in the first mechanisms is exothermic. In equilibrium charge states, the diffusion of V_{Zn} in ZnS adjacent to the interface and Cu or Sn diffusing out of CZTS to replace the V_{Zn} in ZnS in the second mechanisms is endothermic, while the diffusion of Zn out of CZTS into cation sites in ZnS adjacent to the interface in the second mechanisms is exothermic.

In the first mechanisms, the lowest activation diffusion barrier with a different charge state for V_{Cu} and V_{Zn} inside CZTS adjacent to the interface is for the charge -1, while the lowest activation diffusion barrier with a different charge state for V_{Sn} inside CZTS adjacent to the interface is for the charge -2. In the second mechanisms, the lowest activation diffusion barrier with a different charge state for V_{Zn} in ZnS adjacent to the interface and Cu or Zn diffusing out of CZTS to replace the V_{Zn} in ZnS, respectively, is for the charge -1, while the lowest activation diffusion barrier with a different charge state for V_{Zn} in ZnS adjacent to the interface and Sn diffusing out of CZTS to replace the V_{Zn} in ZnS is for the charge -2.

The lowest activation diffusion barrier for a Zn atom moving to the nearest cation vacancy inside the ZnS part at the CZTS/ZnS is for the [011] parallel direction to the interface, and this is agreed with the result for bulk strained ZnS.

The role of charge transfer across the interface is of great significance. In all cases, processes proceed more easily in the direction that reduces or eliminates the transfer of electrons between point defects on either side of the interface, or between a point defect on the ZnS side and the CZTS valence band. However, additionally, cation vacancies trapped within the ZnS secondary phase will generate holes in the near-by CZTS, enhancing the p-type doping of the absorber layer.

It is noted that under the given conditions, the relatively low formation energy of V_{Cu}, and the energetic unfavourability of the migration into the ZnS, means that the secondary phase or capping layer will act as an effective diffusion barrier to these p-type doping centres. This, in turn, means that the presence of ZnS secondary phases within the absorber layer will affect the diffusivity of copper vacancies, and therefore, the operation of PV devices.

Analyses reveal that if there is a Zn vacancy inside the ZnS secondary phase adjacent to the interface, there is a charge transfer at the interface from the valence band top of the CZTS to the ZnS and this leaves holes in the CZTS adjacent to the interface, which enhances the p-type conductivity of the CZTS. It is found that the highest occupied electronic state in the slab free and the lowest empty state in the slab with a Zn vacancy inside ZnS are the same which is the valence band top of bulk CZTS. In addition, the shape of the lowest empty state of the slab when there is a Zn vacancy in the ZnS is mainly 3p-orbital of the S atom in the CZTS.

Overall, the lattice mismatch in CZTS /ZnS [65] is relatively small (Section 6.3.1), because the strain in CZTS is small, of about 0.5%, and this will lead to a low dislocation at the interface. This is in line with the p-type doping in as-grown CZTS. However, the band offset (Section 3.7) has a big spike [65] (Section 6.3.2). This large spike [64, 89] act as a resistive barrier to the minority carrier electrons and increases R_s (Section 1.2.3) by reducing J_{SC} [62] and this affects the η (Section 1.2.3). Therefore, this big spike is not optimal for solar cell efficiency (Section 1.3.1). In the inter-diffusion processes for the CZTS/ZnS interface, in the first mechanisms (Section 6.3.5.1.1), the diffusion barrier in the equilibrium charge states of all cation vacancies within CZTS is endothermic, and this does not enhance the p-type conductivity of CZTS.

Chapter 7

Bulk and Strained CdS

7.1 Introduction

CdS has been commonly used as a partner in the heterojunction for $CuInSe_2$, CdTe, and CZTS [119, 196, 197]. Good quality crystal materials at the interface are obtained when the lattice constant of the epitaxial layer (thin layer) is identical or close to that of the substrate (thick layer) to avoid the lattice mismatch. When the lattice constant of the epitaxial layer is not precisely equal to that of the substrate, then the epitaxial layer stretches (if the lattice constant of the epitaxial layer is less than that of the substrate) or compresses (if the lattice constant of the epitaxial layer is bigger than that of the substrate). In general, the lattice misfit at the interface causes lattice strain and deformation of the interface structure, which may modify the valence band maximum and conduction band minimum as well as the band gap.

The lattice mismatch between the CZTS/CdS heterojunction is about 7%, leading to dislocations and defects in the interface and potentially causing recombination for the minority carrier at the heterojunction interface [65]. Tajima et al. [113] found that the recombination at the CdS/CZTS interface decreases when the junction is epitaxial and that improves the solar cell performance. Nagoya et al. [65] found that the band gap of ZB-CdS is reduced by the strain to fit the CZTS lattice. In this chapter, CdS buffer layers are investigated as alternative layers to ZnS which has been investigated as a secondary phase or buffer layer (Chapter 5) to get a highly efficient device and to know the impact of the strain.

7.2 Computational Details

The computational methods in this chapter are illustrated in Chapters 2 and 3 in terms of pseudo potentials (Section 2.7.3), diffusion barrier (Section 3.8), basis set with cut-off (Section 2.7.2), binding energy (Section 3.9) and the formation energy of defects in the neutral charge state which strongly relies on the atomic chemical potential of the species in the system as shown in Section 3.5.

The chemical potential of Cd is obtained from $\mu_{\mathrm{Cd}} = E(\mathrm{CdS}) - \mu_{\mathrm{S}}$, where $E(\mathrm{CdS})$ is the total energy per formula unit of bulk CdS. For cubic CdS, the chemical potential of Cd is -1254.423178, -1254.559553, -1254.559553 and -1254.442635 eV at point P, Q, M and N, respectively. For strained CdS μ_{Cd} is -1254.32019, -1254.456564, -1254.456564 and -1254.339646 eV at point P, Q, M and N, respectively.

Bulk cubic and strained CdS models are mirrored to bulk cubic and strained ZnS (Section 5.3.1). Buffer layer CdS has been modelled based on a conventional zinc-blende supercell containing a 64-atom and 512-atom supercell. Strained CdS are modelled using orthorhombic, with a 64-atom and 512-atom supercell, The Brillouin zone of both cubic and strained CdS is sampling using a 4×4×4 mesh for a 64-atom supercell and a 2×2×2 mesh for a 512-atom supercell.

7.3 Results and Discussion

7.3.1 Bulk Crystal Models

Bulk cubic and strained CdS models are mirrored to the bulk cubic and strained ZnS phase (Section 5.3.1). In order to build an epitaxial interface between the buffer layer CdS and the absorber layer CZTS as explained in Chapter 8, strained CdS should be modelled. In the epitaxial interface, the buffer layer is adjacent and in contact with the absorber layer, and as the strain in the interface is based on the lattice constant of CZTS (see Section 8.3.1), therefore, the bulk CdS have be strained to match CZTS. Cubic and strained CdS are modelled in the [100] direction (see Fig. 7.1) which is the same orientation as the CZTS/CdS interface modelled for this study (Section 8.3.1). The calculated lattice constants are listed in Table 7.1. The bond length of cubic and strained CdS are not the same, as shown in Fig 7.1 and this refers to the fact that the strain in CdS (Table 7.1) is not small compared with ZnS (Section 5.3.1). CdS have a larger lattice constant than ZnS (Section 5.3.1), therefore the strain in the lattice constant of CdS is much higher than ZnS. The strain in the lattice constant of CdS in [100] is tensile, while in the [010] and [001], it is compressive, and this is in contrast with bulk strained ZnS.

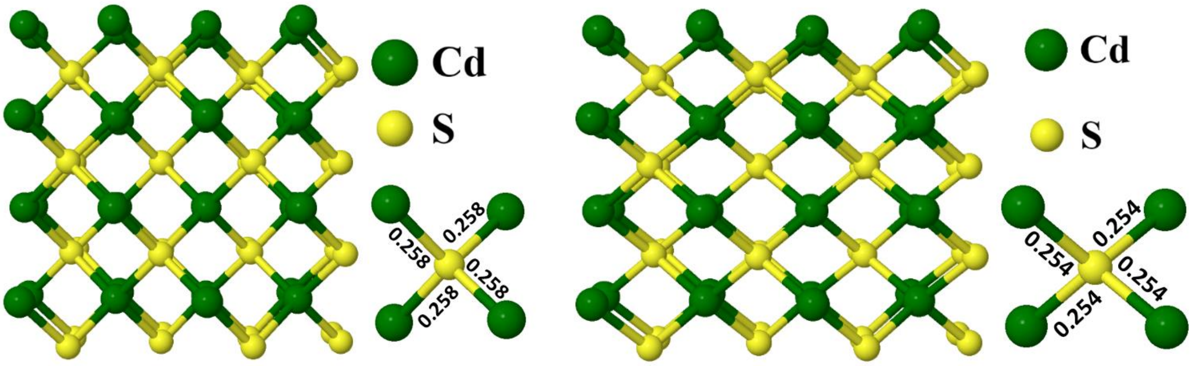

Figure 7. 1: Schematic of CdS structure simulation supercell: (a) cubic CdS, (b) strained CdS. The horizontal and vertical directions are [100] and [010], respectively, with [001] out of the paper. Bond lengths given in nm.

Table 7. 1: Calculated lattice parameters of the bulk and strained phases. The numbers between the brackets represent the strain in CdS. The experimental lattice constants is $a_{\mathrm{CdS}} = 5.81$Å [198]. The lattice constants of strained CdS are fixed to a_{CZTS} in the [010] direction and $c_{\mathrm{CZTS}}/2$ in the [001], while in the [100] direction the lattice constant is optimised.

	Lattice constant (Å)		
Material	[100]	[010]	[001]
CdS	5.952	5.952	5.952
Strained CdS	6.548 (+11%)	5.497 (−7%)	5.500 (−7%)

7.3.2 Defects in Bulk CdS

Intrinsic defects such as cation vacancy and substitution defects including $\mathrm{Cu_{Cd}}$, $\mathrm{Zn_{Cd}}$ and $\mathrm{Sn_{Cd}}$ (Fig. 7.2) inside bulk cubic and strained CdS are studied under the growth conditions of (Cu-poor/Zn-rich and $\mu_{\mathrm{Cu}}=-0.2$eV) [40] (Fig. 4.4). The impurity defects come from the CZTS absorber layer. In cubic and strained CdS, the four equilibrist bond lengths between $\mathrm{Cu_{Cd}}$, $\mathrm{Zn_{Cd}}$ and $\mathrm{Sn_{Cd}}$ and sulphur in addition to the strain between the substitution defects and the nearest sulphur are listed in Table 7.2. For cubic and strained CdS, the bond length of $\mathrm{Cu_{Cd}}$-S and $\mathrm{Zn_{Cd}}$-S is shorter within 2.1% and 1.7% than that of Cd-S, whilst the bond length of $\mathrm{Sn_{Cd}}$-S is longer within 1.7% than that of Cd-S; therefore, the strain in cubic and strained CdS for $\mathrm{Cu_{Cd}}$-S and $\mathrm{Zn_{Cd}}$-S is compression and for $\mathrm{Sn_{Cd}}$-S, it is tension.

Table 7. 2: Calculated bond-length (nm) and strain (%) for substitutional defects inside cubic and strained CdS.

Structure	Defects	Bond-length (nm)	Strain (%)
Cubic	Cu_{Cd}-S	0.237	−8%
	Zn_{Cd}-S	0.241	−6.6%
	Sn_{Cd} -S	0.275	+6.6%
Strained	Cu_{Cd}-S	0.233	−8%
	Zn_{Cd}-S	0.237	−7%
	Sn_{Cd} -S	0.271	+7%

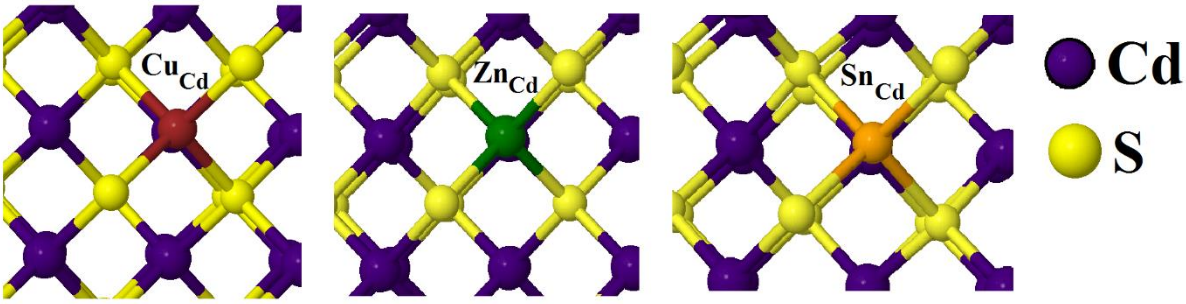

Figure 7. 2: Schematic of substitutional defects in CdS: (a) Cu_{Cd} in CdS, (b) Zn_{Cd} in CdS, (c) Sn_{Cd} in ZnS. Bond lengths given in nm. The horizontal and vertical directions are [100] and [010], respectively, with [001] out of the paper.

7.3.3 Formation Energies

The formation energy of intrinsic defect V_{Cd} and substitution defects Cu_{Cd}, Zn_{Cd} and Sn_{Cd} inside bulk cubic and strained CdS are calculated. The formation energies of all calculated defects are in the stable atomic chemical potential region of CZTS under the equilibrium growth conditions of (Cu-poor/Zn-rich and μ_{Cu}=−0.2eV) [40] for the four boundary points P, Q, M and N of the CZTS stable region (Fig. 4.4), as shown in Table 7.3.

It is found that the formation energies of cation vacancy and substitutional defects in cubic CdS are higher than that of the strained CdS except for the Sn_{Cd} and that can be attributed to the strain where the strain of the Sn_{Cd} is tensile whereas the strain for the other defects are compressive. Acceptor cation intrinsic defects V_{Cd} inside bulk cubic and strained CdS have higher formation energy than that of acceptor and donor substitutional defects. Iso-electronic defects Zn_{Cd} have the lowest formation energy in comparison with the formation energy of acceptor Cu_{Cd}, donor Sn_{Zn} and cation vacancy defects for bulk cubic and strained CdS. Therefore, the iso-electronic defect can form more easily inside CdS than that of both the neutral donor substitution defect and acceptor cation defects under the equilibrium growth condition. Therefore, the co-existence of Cd at a Zn site Cd_{Zn} could be easily presented in the CZTS/CdS heterojunction.

Table 7. 3: Calculated formation energies of the vacancies and substitutional defects inside bulk cubic and strained CdS for points P, Q, M and N (Fig. 4). All energies are in eV.

Structure	**Defects**	$E_P^f(64)$	E_P^f	E_Q^f	E_M^f	E_N^f
Cubic	V_{Cd}	3.36	3.41	3.28	3.28	3.39
	Cu_{Cd}	0.99	0.99	0.85	0.85	0.97
	Zn_{Cd}	0.13	0.11	0.11	0.15	0.15
	Sn_{Cd}	0.80	0.79	1.07	1.03	0.79
Strained	V_{Cd}	2.61	2.52	2.39	2.39	2.50
	Cu_{Cd}	0.61	0.60	0.47	0.47	0.59
	Zn_{Cd}	0.04	0.02	0.02	0.06	0.06
	Sn_{Cd}	1.09	1.08	1.35	1.31	1.08

7.3.4 Binding Energy of Cu, Zn and Sn Substitutions to Vacancy

The process of Cu, Zn and Sn diffusing to CdS is via a V_{Cd} vacancy; therefore, part of the analyses of energies involves whether or not there is binding of such vacancy to the impurity. The binding energies of substitutional defects with vacancy inside bulk strained CdS are calculated, as listed in Table 7.4. The binding energy of Zn_{Cd} +V_{Cd} is not significant; therefore it might be not bound specially in the high temperature.

Table 7. 4: Calculated binding energies of substitutional defects with vacancy inside strained CdS with 64 atoms. All energies are in eV.

Defects	E^b
Cu_{Cd} +V_{Cd}	0.40
Zn_{Cd} +V_{Cd}	0.12
Sn_{Cd} +V_{Cd}	1.58

7.3.5 Inter-diffusion Inside Bulk Cubic CdS

The diffusion processes for CdS mirror ZnS processes (Chapter 5). The diffusion barrier of intrinsic and substitutional defects for cubic CdS is studied under the equilibrium growth conditions for the four boundary points P, Q, M and N of the CZTS stable region (Fig. 4.4). For the cation vacancy, the reference formation energy will include the formation energy of the cation vacancy. In the case of Cd diffusing in CdS, the formation energies of V_{Cd} will add to the activation energy to find the barrier height. For the substitutional defects, the reference formation energy includes the formation energy of the substitutional defect with cation vacancy. In the case of Cu_{Cd} diffusing in CdS via V_{Cd} mechanisms, the formation energies of Cu_{Cd} and V_{Cd} will add to the activation energy to find the barrier height.

7.3.5.1 Diffusion of Cd Vacancy in Cubic CdS

This process has already been modelled in bulk cubic ZnS (Section 5.3.4.1). Diffusion may occur inside CdS when V_{Cd} moves through the lattices and the Cd ion moves to the nearest cation site. In this process, Cd hop to the nearest cation vacancy inside CdS and leaving V_{Cd} in the initial place, as shown schematically in Fig.7.3. The diffusion of the cation vacancy lies CdS supercell affect the conductivity of the CdS/CZTS cell, since the diffusion barrier might be variable in the different directions of the cell based on the strained. This is depending on CdS lattice length in the different orientations which is based on the strain in CdS. Therefore, the defect might diffuse in a specific direction more than in other directions.

The calculated diffusion barrier of the Cd cation vacancy inside bulk cubic CdS for the absolute energy scale and with reference formation energy at point P are illustrated in Fig. 7.4. The calculated activation energy value of the intrinsic cation vacancy at point P of the saddle point with the formation energies under the equilibrium growth (Fig. 4.4) are 4.40eV. For the Q, M and N points (Fig. 4.4), the difference between the activation energy relative to P are 0.14, 0.14 and 0.02eV, respectively. Although the outcome is favourable in point P, there is no substantial difference between the outcome of points P, Q, M and N in the stable region of CZTS (Fig. 4.4), so it is expected to have a similar outcome.

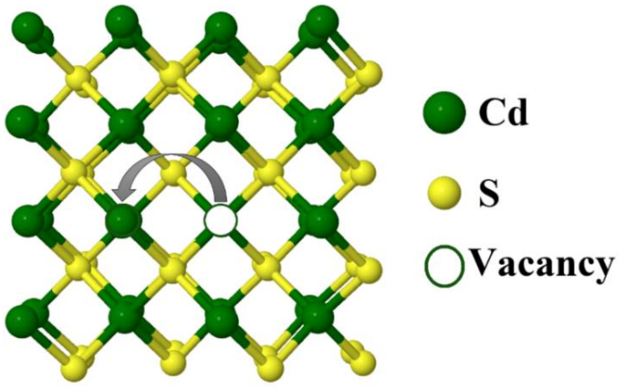

Figure 7. 3: Schematics of Cd diffusing into the nearest metal vacancies in cub CdS. The horizontal and vertical directions are [100] and [010], respectively, with [001] out of the paper.

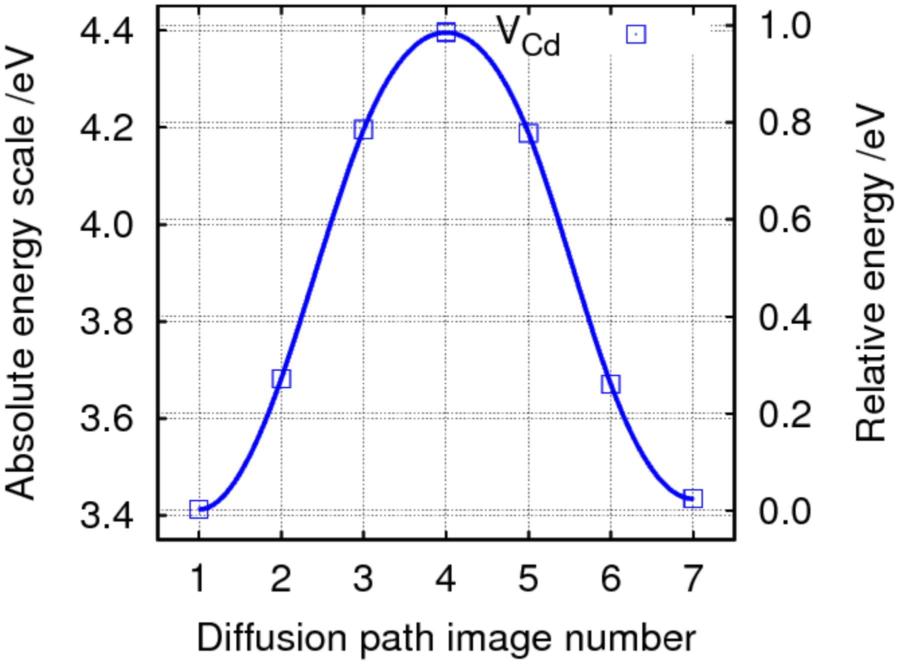

Figure 7. 4: Diffusion barrier calculated in the absolute energy scale and with reference formation energy of the Cd cation vacancy inside bulk cubic CdS with a 512-atom supercell at point P (Fig. 4.4).

7.3.5.2 Diffusion of Cu, Zn and Sn Impurities Inside Cubic CdS

A diffusion process with impurity has already been modelled in bulk cubic ZnS (Section 5.3.4.2). In the case where there is Cu, Zn or Sn impurity coming from the CZTS absorber layer into cubic CdS, these impurities can replace the Cd inside CdS and form Cu_{Cd}, Zn_{Cd} or Sn_{Cd}, respectively. The calculated diffusion barrier of the Cu_{Cd}, Zn_{Cd} and Sn_{Cd} substitutional defects inside cubic CdS at point P are illustrated in Fig. 7.5. The calculated activation energy value at point P of the saddle point with the formation energies are listed in Table 7.5. For the Q, M and N points, the difference between the activation energy relative to P are also listed in Table 7.5. There is no substantial difference between the outcome of points P, Q, M and N in the stable region of CZTS (Fig. 4.4), so it is expected to have a similar outcome.

Zn_{Cd} neutral charge defect has the lowest diffusion barrier compared with other substitution defects, and Cu_{Cd} has a higher diffusion barrier than Sn_{Cd}. Therefore, Zn_{Cd} defect can move more easily inside cubic CdS than other substitutional defects, under equilibrium conditions. There is intermediate minimum structure in the diffusion barrier reaction with Sn impurity, and this could be attributed to the fact that Sn is more relaxed at image four and can make more bonds at that image since the Sn atoms have a bigger size than Cu, Zn and Cd. This intermediate minimum structure also occurs when there is V_{Sn} in bulk CZTS (Section 4.3.9.1). The barrier for all forward and reverse reactions depends on the differences between the saddle point and both the initial and final state.

In bulk cubic CdS, the formation energy of Zn_{Cd} is less than that of the Cu_{Cd} and Sn_{Cd} as shown in Table 7.3. According to this, Zn_{Cd} iso-electronic substitution defects can be formed and diffused by a Zn vacancy mechanism more easily than Cu_{Cd} and Sn_{Cd} inside bulk cubic CdS under equilibrium growth conditions.

Table 7. 5: Calculated activation energies including the reference formation energy (eV) of the impurities antisites and cation vacancy in the bulk cubic CdS with a 512-atom supercell at point P (Fig. 4.4, Table 7.3) E_{P}^{a}. For points Q, M and N (Fig. 4.4), the relative positions of the activation energies are $\Delta E_{\mathrm{Q}}^{a}$, $\Delta E_{\mathrm{M}}^{a}$ and $\Delta E_{\mathrm{N}}^{a}$, respectively. E^{for} is the forward migration barrier. All energies are in eV.

Reaction	E_{P}^{a}	E^{for}	$\Delta E_{\mathrm{Q}}^{a}$	$\Delta E_{\mathrm{M}}^{a}$	$\Delta E_{\mathrm{N}}^{a}$
Cu_{Cd}	5.77	1.42	0.27	0.27	0.04
Zn_{Cd}	4.96	1.47	0.14	0.10	-0.02
Sn_{Cd}	5.63	1.47	-0.14	-0.10	0.02

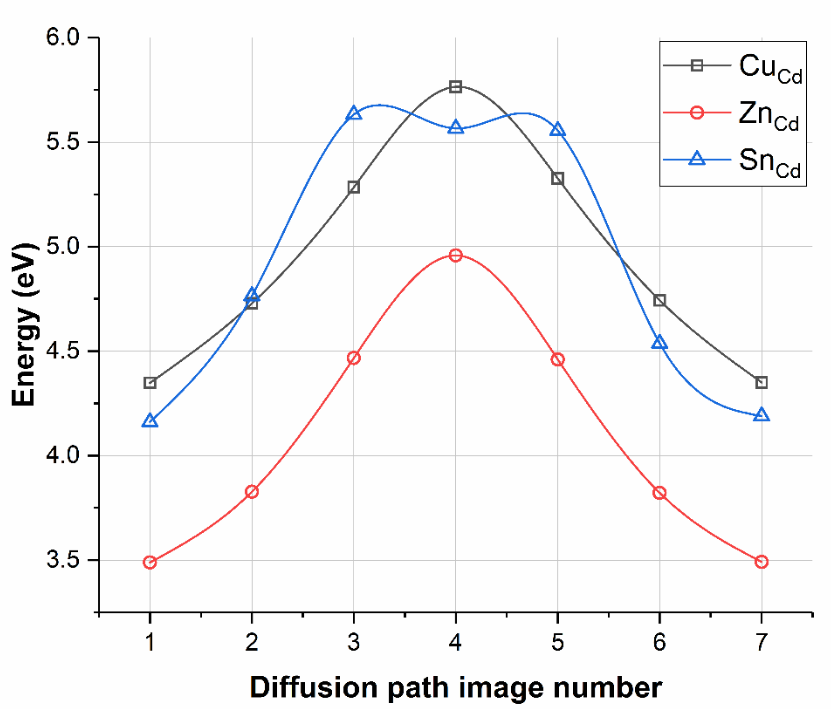

Figure 7. 5: Diffusion barriers calculated for the diffusion of Cu_{Cd}, Zn_{Cd} and Sn_{Cd} substitutional defects inside bulk cubic CdS via a Cd vacancy, with a 64-atom supercell. The energy scale includes the reference formation energy of the substitutional defects with Cd cation vacancies in the CdS at the point P (Fig. 4.4).

7.3.6 Inter-diffusion Inside Strained CdS

The diffusion barrier of cation intrinsic and substitutional defects for strained CdS are studied in the [110] and [011] directions under equilibrium growth conditions. Based on the interface model condition of CZTS/CdS (Section 6.3.1), the diffusion barrier in the [010] and [001] directions are approximately the same and they differ significantly in terms of strain (Table 7.1) from the [100] direction. [110] is away from the interface and [011] is a parallel direction to the interface. Due to the fact that the strain in CdS is not small (Section 8.3.1), the diffusion barrier inside CdS in the different orientations will affect by strain.

7.3.6.1 Diffusion of Cd Vacancy in Strained CdS

This process has already been modelled in bulk strained ZnS (Section 5.3.5.1). In the case of strain, Cd move to the nearest cation vacancy in the [110] and [011] directions inside strained CdS, leaving V_{Cd} in the initial place as shown schematically in Fig.7.6. Calculated diffusion barriers of the Cd cation vacancy inside bulk strained CdS at point P are illustrated in Fig. 7.7. The calculated activation energy value of the saddle point at point P with the formation energies under equilibrium growth conditions are listed in Table 7.5. For the Q, M and N points (Fig. 4.4), the differences between the activation energies relative to P are 0.14, 0.14 and 0.02eV, respectively and the differences are the same for both directions. As is mentioned in Section 7.3.5.1, a similar outcome between the points P, Q, M and N in the stable region of CZTS (Fig. 4.4) is expected.

The differences in the diffusion barrier in [110] away from the interface and [011] in a parallel direction to the interface are 0.75eV because the strain in CdS is big (Table 7.1). The diffusion barrier of intrinsic cation vacancy inside strained CdS is lower for the [011] parallel direction than that of [110] away from the interface. Therefore, the most significant migration path is in the [011] direction which is parallel to the (100)-CZTS/CdS interface.

The diffusion barrier of cubic CdS is higher than that of the strained CdS because of the strain. Therefore, the Cd can move more easily inside strained CdS and particularly in the [011] direction than that of cubic CdS.

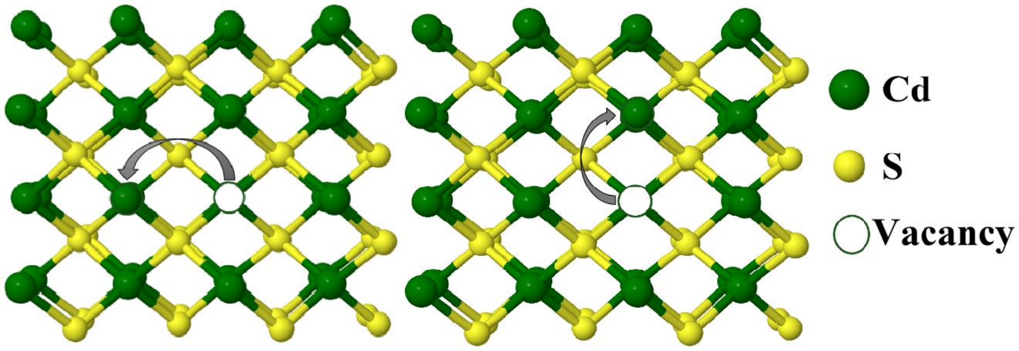

Figure 7. 6: Schematics of Cd diffusing into nearest metal vacancies in strained CdS: (a) at [110] direction. (b) at [011] direction. The horizontal and vertical directions are [100] and [010], respectively, with [001] out of the paper.

Table 7. 6: Calculated activation energies including the reference formation energy (eV) of the intrinsic cation Zn vacancy in the bulk strained CdS with a 512-atom supercell at [110] away from the interface and the [011] parallel direction to the interface at point P (Fig. 4.4, Table 7.3) E_{P2}^{a} for strain whereas $E_{\mathrm{P1}}^{\mathrm{a}}$ for cubic. E^{for} is the forward migration barrier. All energies are in eV.

Direction	E_{P1}^{a}	E_{P2}^{a}	E^{for}
[110]	4.40	3.65	1.13
[011]	4.40	2.90	0.37

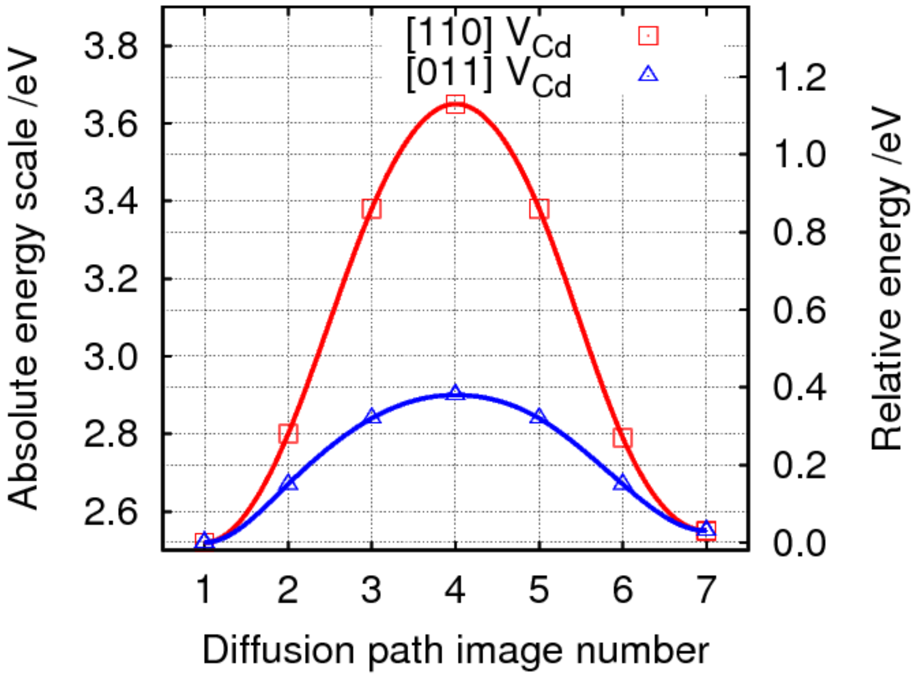

Figure 7. 7: Diffusion barriers calculated for the absolute energy scale and with reference formation energy of the Cd cation vacancy inside bulk strained CdS with a 512-atom supercell at [110] away from the interface and the [011] parallel direction at point P (Fig. 4.4).

7.3.6.2 Diffusion of Cu, Zn and Sn Inside Strained CdS

The diffusion process with impurity has already been modelled in bulk strained ZnS (Section 5.3.5.2). In the case where there is Cu, Zn or Sn impurities coming from CZTS into strained CdS, these impurities can replace the Cd inside strained CdS and form Cu_{Cd}, Zn_{Cd} or Sn_{Cd}, respectively. In this process Cu, Zn or Sn impurities can diffuse inside strained CdS by a Cd vacancy. The calculated diffusion barrier of the Cu_{Cd}, Zn_{Cd} and Sn_{Cd} substitutional defects inside bulk strained CdS at point P for the absolute energy scale and with reference formation energy in the [110] direction away from the interface and the [011] parallel direction to the interface are illustrated in Fig. 7.8. The calculated activation energy value of the saddle point with the formation energies at point P under equilibrium growth conditions are listed in Table 7.6. For the Q, M and N points, the differences between the activation energy relative to point P are also listed in Table 7.7. There is no substantial difference between the outcome of points P, Q, M and N in the stable region of CZTS (Fig. 4.4), so it is expected to have a similar outcome.

The Zn_{Cd} iso-electronic defect has the lowest diffusion barrier compared with the Cu_{Cd} acceptor defect and the Sn_{Cd} donor defect in both directions. Therefore, the Zn_{Cd} substitution defect can move more easily inside bulk strained CdS via a V_{Cd} mechanism than Cu_{Cd} acceptor substitutional and Sn_{Zn} donor substitutional defects in both the [110] direction away from the interface and the [011] parallel direction to the interface. There is an intermediate minimum structure in the diffusion barrier reaction with an Sn impurity, as explained in Section 7.3.5.2.

In the bulk strained CdS, the formation energy of Zn_{Cd} is lower than that of the Cu_{Cd} and Sn_{Zn}. According to this, Zn_{Cd} neutral charge substitutional defects can form and diffuse by a Cd vacancy mechanism more easily than Cu_{Cd} and Sn_{Cd} under equilibrium growth conditions.

The diffusion barrier of Cu_{Cd}, Zn_{Cd} and Sn_{Cd} inside strained CdS in the [011] parallel direction to the interface is lower than that of the [110] direction away from the interface based on the interface model where the bond length of Cd-S in the [110] direction is shorter than that of cubic; therefore, the strain in the [110] direction is compressive (Table 7.1), while the bond length of Cd-S in the [011] direction is longer than that of the cubic; therefore, the strain in the [011] direction is tensile. Therefore, the most significant migration path is in the [011] direction. In contrast, Cu_{Zn} and Sn_{Zn} inside strained ZnS have tensile strain in the [110] direction (Table 5.1), while in the [011] direction they have compressive strain based on the interface module.

Table 7. 7: Calculated activation energies including the reference formation energy (eV) of the impurities antisites in the bulk strained CdS with a 512-atom supercell in the [110] direction away from the interface and the [011] parallel direction to the interface at point P (Fig. 4.4, Table 7.3) E^{a}_{P2} for strain, whereas E^{a}_{P1} for cubic. For points Q, M and N (Fig. 4.4), the relative positions of the activation energies are $\Delta E^{a}_{\mathrm{Q}}$, $\Delta E^{a}_{\mathrm{M}}$ and $\Delta E^{a}_{\mathrm{N}}$, respectively. E^{for} is the forward migration barrier. All energies are in eV.

Direction	Reaction	E^{a}_{P1}	E^{a}_{P2}	E^{for}	$\Delta E^{a}_{\mathrm{Q}}$	$\Delta E^{a}_{\mathrm{M}}$	$\Delta E^{a}_{\mathrm{N}}$
[110]	$\mathrm{Cu_{cd}}$	5.77	4.34	1.11	0.27	0.27	0.04
	$\mathrm{Zn_{Cd}}$	4.96	3.88	1.23	0.14	0.10	-0.02
	$\mathrm{Sn_{Cd}}$	5.63	5.10	1.40	-0.14	-0.10	0.02
[011]	$\mathrm{Cu_{cd}}$	5.77	3.91	0.68	0.27	0.27	0.04
	$\mathrm{Zn_{Cd}}$	4.96	3.40	0.74	0.14	0.10	-0.02
	$\mathrm{Sn_{Cd}}$	5.63	4.53	0.83	-0.14	-0.10	0.02

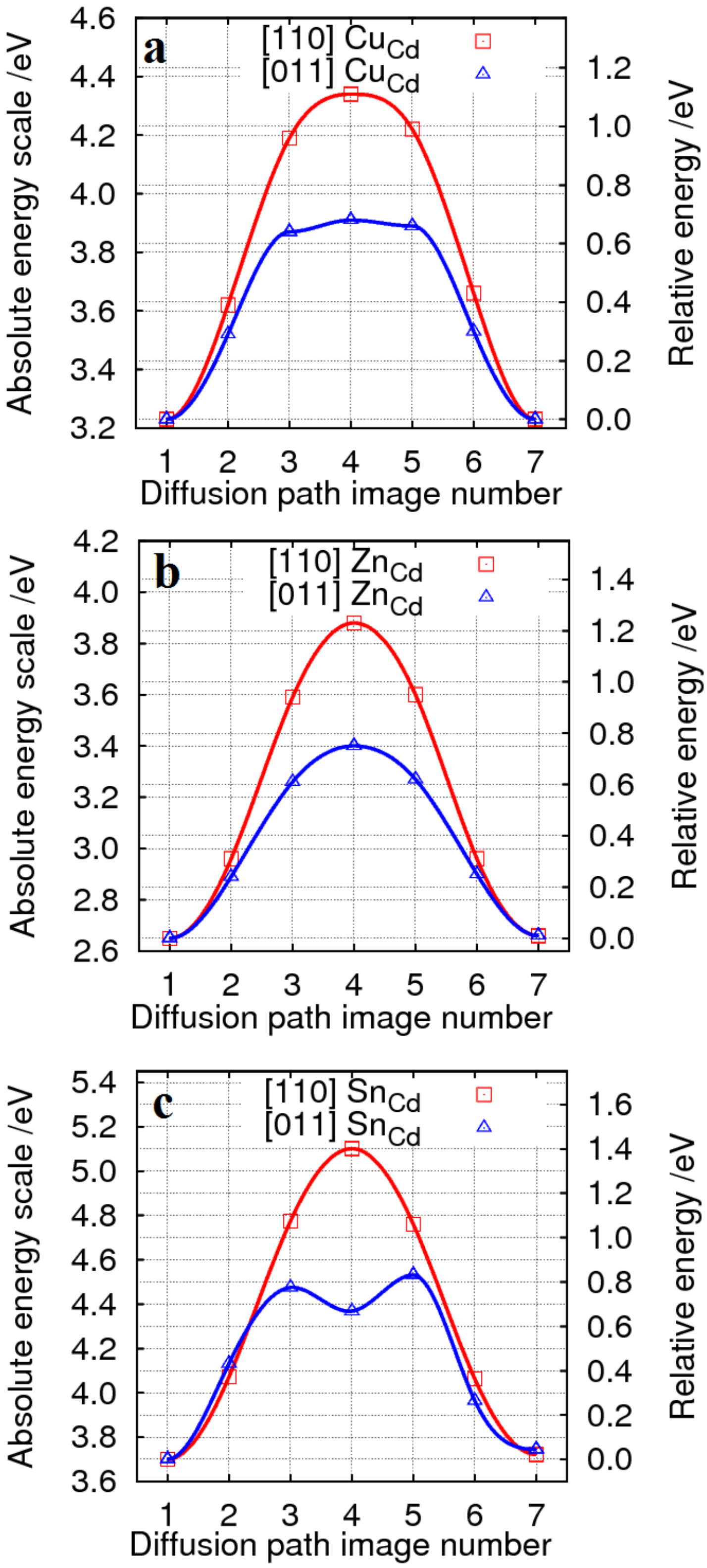

Figure 7. 8: Diffusion barriers calculated for the absolute energy scale and with reference formation energy of the Cu_{Cd}, Zn_{Cd} and Sn_{Cd} substitutional defects inside bulk strained CdS with a 64-atom supercell at point P (Fig. 4.4): (a) in the [110] direction away from the interface; (b) in the [011] parallel direction to the interface.

7.4 Conclusion

The CdS thin buffer layer is strained to match the thick absorber layer CZTS at the interface. Based on the interface module of CZTS/CdS, the strain in the lattice constant of CdS in [100] is tensile, while in the [010] and [001] directions, it is compressive, and this is in contrast with bulk strained ZnS. Therefore, the diffusion barriers of defects inside strained CdS in [010] are approximately the same as in the [001] direction. The strain in the lattice constant of CdS in [100] and [001] is much higher than ZnS, since the lattice constant of CdS is larger than that of CZTS.

Under equilibrium growth conditions which are Cu-poor and Zn-rich, it is found that the formation energies for intrinsic cation vacancy and substitutional defects in strained CdS are lower than that of the cubic except for the Sn_{Cd} since the strain of the Sn_{Cd} substitutional defect is tensile whereas the strain for the other substitutional defects are compressive. In addition, the formation energy for Zn_{Cd} substitutional defects in cubic and strained CdS is lower than that of other substitutional defects.

Under the given conditions, the diffusion barrier of cation vacancy and substitutional defects inside strained CdS in the [011] parallel direction to the interface are lower than that of the [110] direction away from the interface based on the fact that the interface model of the strain in the [110] direction is tensile, while the strain in the [011] direction is compressive. Therefore, the most significant migration path is in the [011] direction. Furthermore, Zn_{Cd} has the lowest diffusion barrier via V_{Cd} mechanisms compared with other substitutional defects. The dominant defects in bulk cubic and strained CdS in the [110] direction away from the interface and the [011] parallel direction to the interface are Zn_{Cd} iso-electronic substitutional defects.

Chapter **8**

CZTS/CdS (100) Interface Processes

8.1 Introduction

The process between CZTS and secondary phases ZnS which has been investigated (Chapter 6) mirrors the process at the CZTS/CdS interface in terms of modelling and diffusion across the boundary. CZTS is attractive material for low cost thin film photovoltaic applications [199]. The interface between the CZTS absorber layer and the CdS buffer layer is one of the most important issues affecting CZTS/CdS cell performance [65]. Cd can diffuse from the CdS buffer layer to CZTS as an impurity and Cu, Zn and Sn can diffuse to the CdS as impurities and this differs from ZnS/CZTS (Section 6.3.3). This diffusion can affect the lattice mismatch, band offset alignment and the inter-diffusion of the cell. CdS has been commonly used as a partner in the heterojunction for $CuInSe_2$, CdTe, and CZTS [119, 196, 197].

The band offset alignments at the hetero-interface could dramatically influence the current and both of the electrical and electronic properties of heterojunction solar cells (Section 1.3). Based on the experimental and theoretical results, it has been concluded that the band alignments at the CdS/CZTS interface are two types (see Fig. 8.1) [200, 201] depending on the interface orientation [202], such as [110], [001] or [112]. The difference between these two types is substantial, since transport properties are expected to be drastically different between them; therefore, the carriers' lifetime, traps, recombination, diffusion length and collection efficiency will be affected at the interface.

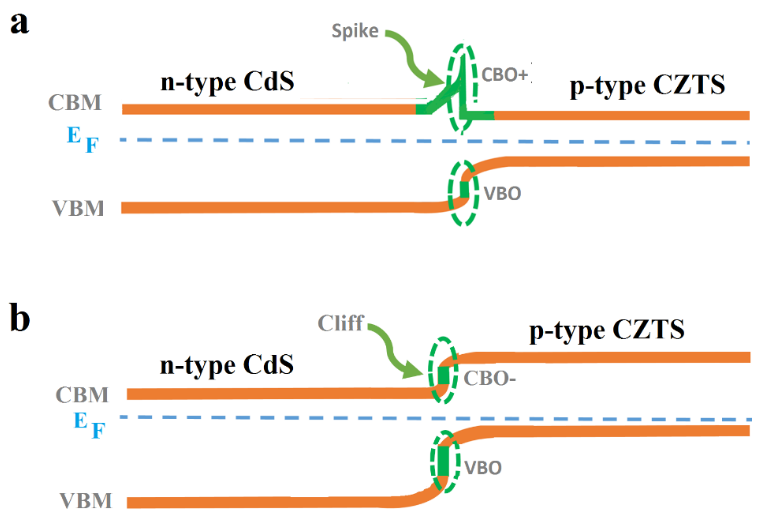

Figure 8. 1: Schematic electronic structure for heterojunctions band offset lineups between p-type CZTS (absorber layer) and n-type CdS (buffer layer). CBM: conduction band minimum; VBM: the valence band maximum; VBO: valence band offset; CBO: conduction band offset and E_F: Fermi level: (a) type one (spike), (b) type two (cliff).

In type one, CBO is positive and called a spike (Section 1.3.1), and the conduction band minimum of CZTS is lower than that of CdS. In type two, CBO is negative and called a cliff (Section 1.3.2), and the conduction band minimum of CZTS is higher than that of CdS. The relatively low V_{OC} of the CZTS solar cells could be due to improved probability for interface recombination of majority carriers induced by a cliff-like conduction band offset at the CdS/CZTS interface because the VBM of CZTS is close to the CBM of CdS. CZTS/CdS heterojunction has a higher efficiency when spike-like than that when cliff-like, since the low performance of CZTS cells is attributed to the V_{OC} limited by the cliff-like [118].

A wide range of experimental and theoretical studies have been done to determine band offset between different orientations [65, 118]. It has been found by using first principle calculations that the valence band offset of CdS/CZTS in the (001) and (010) directions oriented are 1.2eV and 1.0eV, respectively, and the band offset in any case is of type two [203]. Dong et al., obtained results showing that the band alignment for CZTS[001]/CdS[111] is of type two, the valence band and conduction offset are 0.98eV and 0.05eV, respectively and they found that these results support their experimental findings which are 1.06±0.1eV for the valence band offset and 0.13±0.1 eV for the conduction band offset [121]. Bon et al. [200] found that, on the basis of first principle band structure, the band alignment of CdS/CZTS is of type two for the interface between CdS and CZTS along (001) [204]. However, based on the first principles calculation, the conduction band offset of CZTS/ZB-CdS in (100) orientation is 0.18eV and for the CZTS(112)/ZB-CdS(111), CZTS(102)/ZB-CdS(101), and for CZTS(112)/W-CdS (0001) orientation the values are 0.20, 0.22 and 0.28eV, respectively [65]. These values show that the band offset alignment could be type one or two, and that depends on the orientation.

Tajima et al. [113] observed that the efficiency of the solar cell became better and improved the photovoltaic properties when they chose the (100) direction CdS(100)/CZTS(100) and annealing at 573K. Kto et al. [201] reported that there is a significant diffusion of Zn and Se at the CdS/CZTSe interface, though Zn slightly diffuses at the CdS/CZTS interface. Aizawa et al. [205] obtained an efficiency decrease when increasing the internal diffusion of Cd into CZTS by increasing the temperature since R_{Sh} and FF decrease when increasing the time of heating. These processes are very important for device operation, and inter-diffusion is likely to have been understood as being mediated by the motion of vacancies on the metal side between various materials.

It is believed that in the p-type CZTS, the native defects V_{Cu} and Cu_{Zn} are responsible for p-type conductivity [40, 90]. Therefore, the defect types formed as a result of the intermixing between the buffer layer and the absorber layer are critical for a high efficiency device. In this chapter, the CZTS/CdS interface is modeled to identify the most stable defects adjacent to the interface. In addition, the defects diffusion barrier across the interface and the impact of cation inter-diffusion across the interface for p-type conductivity are investigated. Furthermore, the role of the charge transfer across the interface is discussed.

8.2 Computational Details

For this chapter, the computational methods have been explained in Chapters 2 and 3 in terms of pseudopotentials (Section 2.7.3), formation energy (Section 3.5) and diffusion (Section 3.8), basis set and cut-off (Section 2.7.2). The VBO for the (100) interface has been calculated as explained in Section 3.7.

The model of bulk cubic and strained CdS in addition to CdS/CZTS interface mirror the bulk ZnS phase (Section 5.3.1, Section 7.3.1) and ZnS/CZTS (Section 6.2). Kesterite CZTS is modeled using a tetragonal, 16-atom cell with the tetragonal axis along [001], and strained CdS is modeled using a conventional zinc-blende unit cell as with the CZTS/ZnS interface (Section 6.2). (100)-CZTS/CdS has been chosen to model the interface in this study, since this direction is a non-polar surface. All bulk crystals have their Brillouin-zones sampled to converge the energy to better than 10meV/atom. The epitaxial (100)-CdS/CZTS interface is modelled using an orthorhombic ($a \neq b \neq c$), 192-atom supercell made up from three lattice constants each of CZTS and strained CdS in the [100] direction, so there are 12 layers of each material, as illustrated in Fig. 8.2. The Brillouin-zone is sampled using a 1×4×4 mesh. Cubic and strained CdS in the [100] direction (see Fig. 7.1) are modelled using cubic and orthorhombic (see Section 7.2).

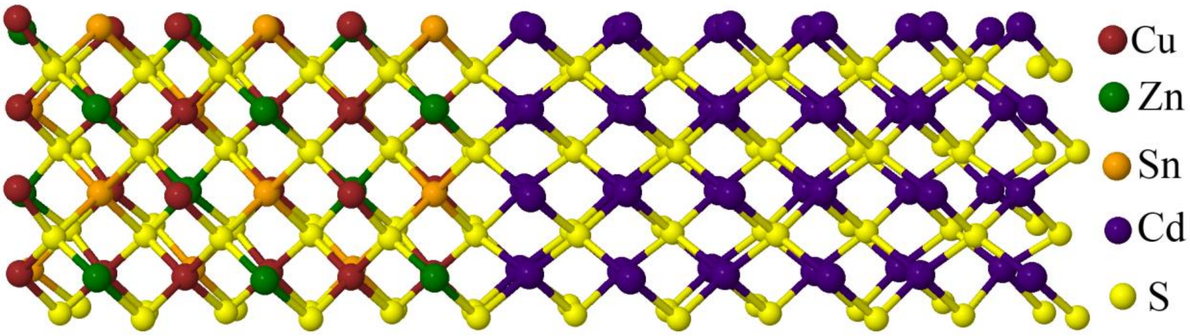

Figure 8. 2: Schematic of the structure of the CZTS/CdS interface simulation supercell. The horizontal and vertical directions are [100] and [010], respectively, with [001] out of the paper.

8.3 Results and Discussion

8.3.1 Bulk Crystal and Interface Models

CZTS/CdS interface models mirror the CZTS/ZnS interface (Section 6.3.1). In the actual CZTS solar cell, the CdS buffer layer is much thinner than CZTS. It is assumed that a thin buffer layer of CdS is deposited epitaxially on CZTS, and therefore the lattice constants of CZTS are taken to be in equilibrium and the CdS is strained to match. The calculated lattice constants are listed in Table 8.1.

Table 8. 1: Calculated lattice parameters of the bulk and strained phases, and the interface supercell. The numbers between the brackets represent the strain in CdS. The experimental lattice constants are $a_{\text{CZTS}} = 5.426$Å, $c_{\text{CZTS}} = 10.81$Å and $a_{\text{CdS}} = 5.81$Å [198].

	Lattice constant (Å)		
Material	[100]	[010]	[001]
CZTS	5.497	5.497	11.000
CdS	5.952	5.952	5.952
Strained CdS	6.548 (+10%)	5.497 (−8%)	5.500 (−8%)
CZTS/CdS interface	36.250	5.497	11.000

Strained CdS has the lattice constants fixed to be a_{CZTS} in the [010] direction and $c_{\mathrm{CZTS}}/2$ in the [001] direction, both representing a −8% strain (Table 8.1). The lattice constant (Table 8.1) in the [100] direction was obtained by minimising the energy with the [001] and [010] lattice constants fixed, and represents a +10% strain. The supercell [100] lattice constant differs from $3a_{\mathrm{CZTS}} + 3a_{\mathrm{CdS}}^{\mathrm{strained}}$ only very slightly, the difference arising principally from the detailed differences where the two materials meet.

Calculated lattice mismatch of a CZTS/CdS heterojunction is about 8% agreed with Ref. [65]. This value leads to the production of dislocations and defects in the interface and would cause minority carrier recombination at the heterojunction interface [65]. Although there is a very large strain, thick layers of materials are typically relieved by the misfit of dislocation. The computational model for such a problem is beyond the scope of this work, but will be of interest for future evaluation. In general, modelling the epitaxial interface and diffusion process across the boundary are relevant even with the dislocation present in addition to that at the device level including when the intermixing is significant beyond that of the dislocation effect. In contrast, the lattice misfit for CZTS/ZnS is 0.5% (Section 6.3.1).

8.3.2 Band Offset Alignment

The band offset calculation (Section 3.7) is critical for solar cell performance. The calculated results of VBO and CBO for CZTS/CdS in [100] revealed that band alignment is of type one with a value of 0.69 and 0.21eV for VBO and CBO, respectively. The calculated band alignment of CBO and VBO is in good agreement with the previous theoretical work that obtained that VBO and CBO are 0.57 and 0.18eV, respectively, in the [100] direction [65]. The band offset alignment of the CZTS/CdS hetero-interface illustrates that there is a spike (Section 1.3.1). CdS/CZTS has a relatively small positive spike and the band offset is attributed to the interface strain induced by the lattice mismatch and it is generally optimal for the solar cell performance.

In contrast, the band offset of CZTS/ZnS has a large spike (Section 6.3.2) compared with that of the CZTS/CdS, since the strain in the CdS buffer layer is larger than that of the ZnS layer (Section 6.3.1) based on the lattice constant.

8.3.3 Inter-diffusion Mechanisms of CZTS/CdS Interface Supercell

Inter-diffusion process across the boundary of CZTS/ZnS (Chapter 6) mirrors CZTS/CdS. Understanding the effects of the intermixing at the buffer/absorber layer should identify the diffusion process. In general, the diffusion process happens by moving the vacancy to the nearest element. In the case where there is a metal vacancy inside CZTS (Fig. 8.3), the Cd inside CdS migrates into CZTS replacing the metal vacancy and forming Cd_{Cu}, Cd_{Zn} or Cd_{Sn} inside CZTS, leave V_{Cd} in CdS, or cation elements migrate from CZTS to replace Cd in CdS, leaving V_{Cu}, V_{Zn} and V_{Sn} in CZTS (Fig. 8.4). Cd coming from the CdS buffer layer is an impurity inside CZTS, while Zn coming from the ZnS buffer layer is not an impurity inside CZTS (Section 6.3.3). The process of the diffusion paths is illustrated in the two mechanisms below:

8.3.3.1 Diffusion Mechanism 1: CZTS Cation Vacancy

This process has already been modelled for the CZTS/ZnS interface (Section 6.3.3.1). In this mechanism, Cd diffuses out from CdS into a metal vacancy inside CZTS and substitutes this metal to form Cd_{Cu}, Cd_{Zn} and Cd_{Sn}, respectively inside the CZTS and leaves V_{Cd} inside CdS, as shown schematically in Fig. 8.3. Each case has its own implications regarding the creation and movement of acceptors and donors, and charge transfer across the interface.

Firstly, Cd diffuses out of the CdS substituting for Cu when there is a vacancy of Cu inside CZTS as shown in Fig. 8.3(a). In this reaction the initial state is a single acceptor while the end state represents both the single donor Cd_{Cu} form inside CZTS and the double acceptor V_{Cd} form inside CdS. There is energy cost and gain, and that is the same as seen in the case of CZTS/ZnS (Section 6.3.3.1). CZTS hetero-structure would show a single charge acceptor.

Secondly, Cd diffuses out of the CdS substituting for Zn when there is a vacancy of Zn inside CZTS as shown in Fig. 8.3(b). In this reaction, the initial state is a double acceptor while the end state represents both the iso-electronic defect Cd_{Zn} forming inside CZTS and the double acceptor V_{Cd} forming inside CdS. The CZTS heterojunction would show a double charges acceptor.

Thirdly, if there is V_{Sn} inside CZTS, Cd diffuses out of the CdS substituting for Sn (Fig. 8.3(c)). In this reaction the initial state is a quadruple acceptor while the end state represents both the double acceptor Cd_{Sn} forming inside CZTS and the double acceptor V_{Cd} forming inside CdS. Therefore, the CZTS junction shows a quadruple charge acceptor. The quadruple acceptor V_{Sn} has a deep acceptor level (Fig. 4.10,) and higher formation energy than other cation vacancy defects (Table 4.6) inside CZTS; the property of this formation is much lower than the other vacancies.

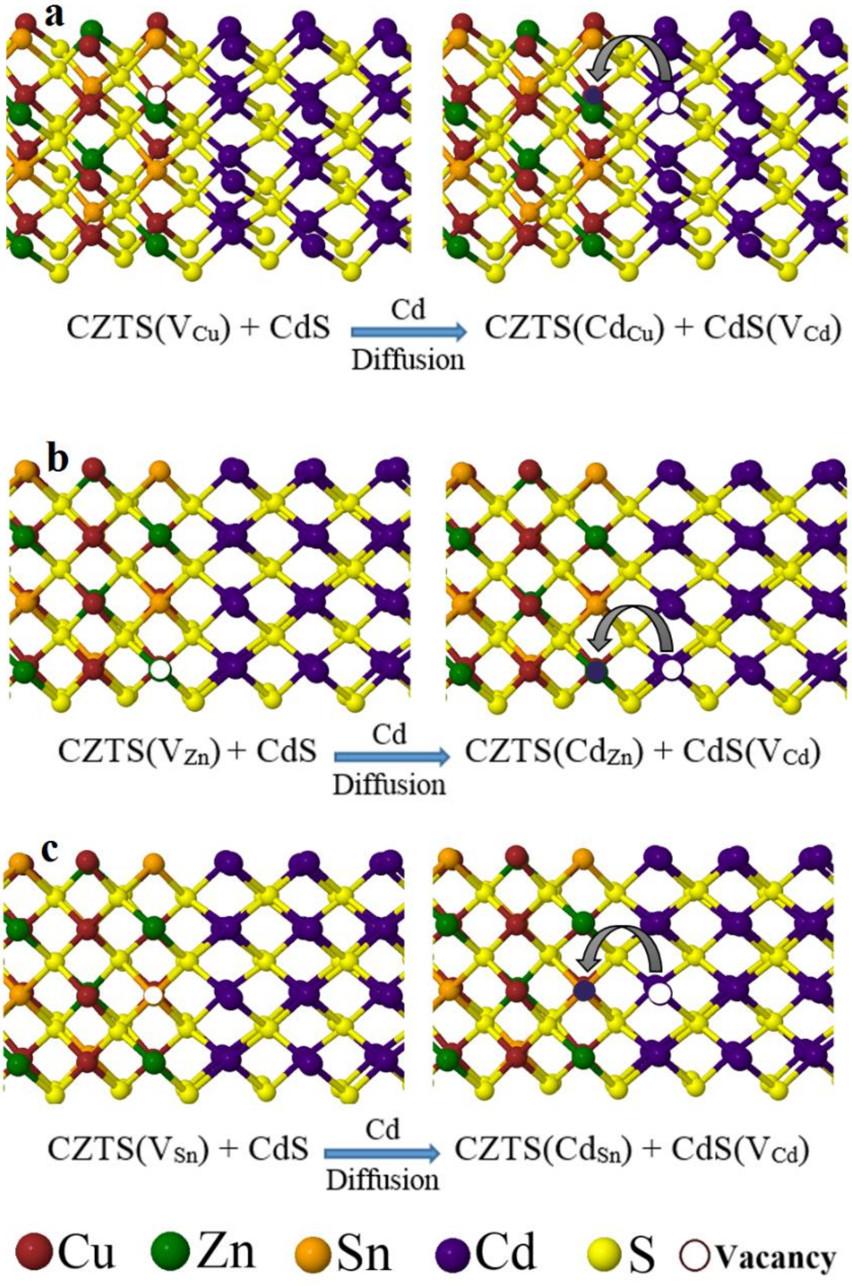

Figure 8. 3: Schematics of Cd diffusing out of CdS into metal vacancies in CZTS: (a), (b) and (c) show Cd replacing Cu, Zn and Sn, respectively.

8.3.3.2 Diffusion Mechanism 2: CdS Cation Vacancy

This process has already been modelled for the CZTS/ZnS interface (Section 6.3.3.2). In the second mechanism, there is Cd vacancy inside CdS, the Cu, Zn or Sn diffusing out of CZTS across the junction to the CdS to replace Cd. Any element in CZTS diffusing into the CdS will leave a vacancy in the CZTS.

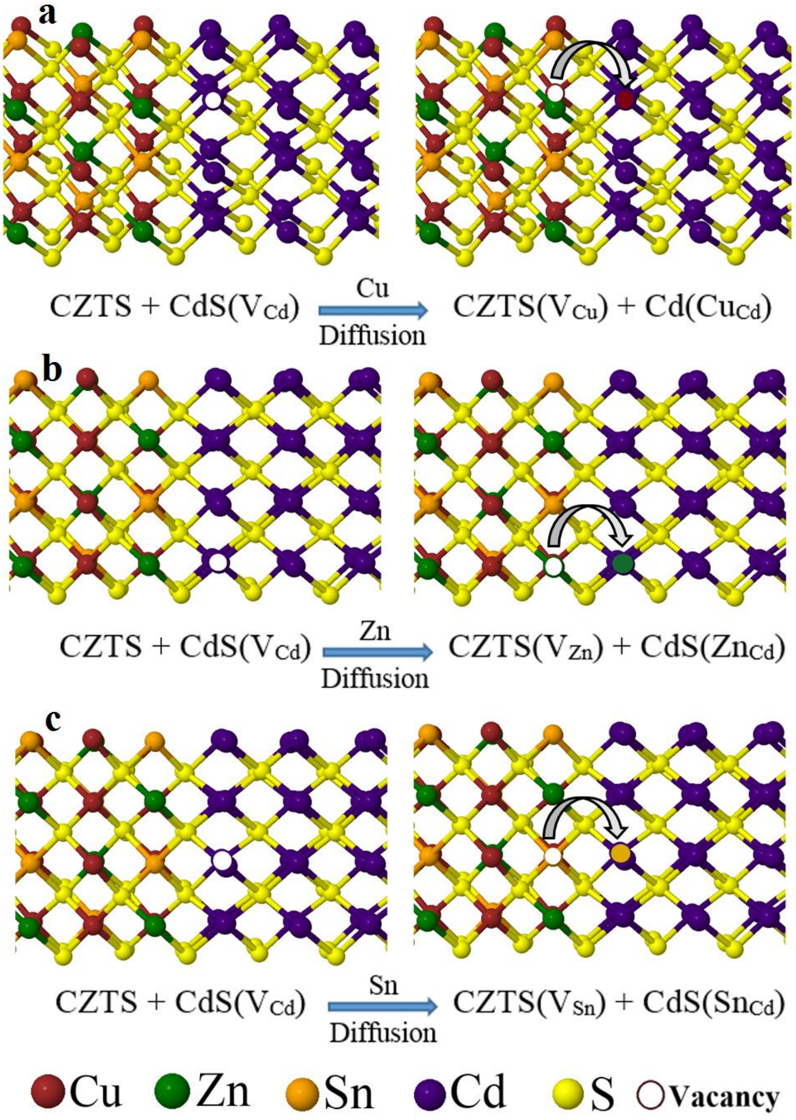

Figure 8. 4: Schematics of V_{Cd} diffusing out of CdS forming metal vacancies in CZTS: (a), (b) and (c) show Cd being replaced by Cu, Zn and Sn, respectively.

Firstly, Cu diffuses out of the CZTS to CdS (Fig. 8.4(a)), when there is Cd vacancy in CdS. In this reaction, the initial state is a double acceptor while the end state represents both the single accepter V_{Cu} and Cu_{Cd} forming inside CZTS and CdS, respectively. The CZTS hetero-structure surface shows a double acceptor. Secondly, there is a case where the Zn jumps from CZTS to the CdS when there is Cd vacancy in CdS, as shown in Fig. 8.4(b). In this reaction, the initial state is a double acceptor while the end state represents both an iso-electronic defect Zn_{Cd} forming in CdS and the double acceptor V_{Zn} forming in CZTS. The total charge via the surface of the CZTS junction is a double acceptor charge. Thirdly, there is a case where the Sn jumps from CZTS to CdS when there is Cd vacancy in CdS, see Fig. 8.4(c). In this reaction, the initial state is a double acceptor in CdS while the end state represents both the double donor Sn_{Cd} forming in CdS and the quadruple acceptor V_{Sn} forming in CZTS. The CZTS surface would show a double donor charge across the junction, and it is detrimental to the performance of the p-type CZTS cell.

8.3.4 Interface Formation Energies

In order to determine the most stable defect arising and inter-diffusion processes at the hetero-epitaxial interface, both the diffusion barriers and the formation energies are required. The formation energies depend upon the atomic chemical potentials (Section 3.5); the atomic chemical potentials are linked through the requirement that CZTS is the equilibrium phase, and for this study the analysis ise constrained to Cu-poor/Zn-rich conditions, with $\mu_{\mathrm{Cu}} = -0.2\mathrm{eV}$ [40].

The calculated formation energies for cation vacancy inside CZTS or CdS adjacent to the interface are listed in Table 8.2. In second mechanisms, the formation energy of V_{Cd} in CdS adjacent to the interface which listed in Table 8.2 represents the lowest energy site found at the interface.

Based on the data in Table 8.2, it is concluded that the single acceptor V_{Cu} in CZTS adjacent to the interface has the lowest formation energy compared to other defects, and it can form more easily than other defects, because the Cu-S bonds are weak covalent bonds compared with Zn-S bonds and Sn-S inside CZTS [143]; in addition, there is electrostatic cost for removing the atom and it will differ for different bonds.

Table 8. 2**:** The calculated reference formation energy of the cation vacancies in the CZTS or CdS adjacent to the interface for points P, Q, M, and N (Fig. 4.4). All energies are in eV.

Reactions	E^f_{P}	E^f_{Q}	E^f_{M}	E^f_{N}
$\mathrm{V}^{\mathrm{CZTS}}_{\mathrm{Cu}}$	0.90	0.90	0.90	0.90
$\mathrm{V}^{\mathrm{CZTS}}_{\mathrm{Zn}}$	1.10	0.96	0.92	1.04
$\mathrm{V}^{\mathrm{CZTS}}_{\mathrm{Sn}}$	2.43	2.02	2.06	2.41
$\mathrm{V}^{\mathrm{CdS}}_{\mathrm{Cd}}$	1.11	0.97	0.97	1.09

8.3.5 Diffusion Barriers of CZTS/CdS

The electron chemical potential (Fermi level at 0K) in this study has been assumed to be that located at the valence band top of the CZTS for the interface. In some processes, the valence-band offset results drive charge transfer across the interface (see Section 6.3.6). Under this Fermi level assumption, the diffusion barrier of the reactions in neutral charge states and within charge transfer across the interface has been estimated. For each process, the barrier has been estimated and the processes aligned to a common energy scale based upon the formation energies of the defects at the interface.

For the cation vacancy in CZTS or CdS at the interface, the reference formation energy will include the formation energy of the cation vacancy in the initial state, and this process is also used in the CZTS/ZnS interface (Section 6.3.5). In a case where there is V_{Zn} in the initial state inside CZTS adjacent to the interface, the formation energy of V_{Zn} in the initial state of CZTS at the interface will add to the activation energy to find the barrier height.

8.3.5.1 CZTS Cation Vacancy Mechanisms

8.3.5.1.1 CZTS Cation Vacancy Mechanisms in Neutral Charge State

This mechanism has already been modelled in the CZTS/ZnS interface (Section 6.3.1.1). In the first mechanism, as described in Section 8.3.3.1, there is a metal vacancy which lies inside CZTS in the initial state, and both of the substitutional defects and V_{Cd} are present as part of the final state inside CZTS and CdS, respectively. The calculated barriers are illustrated in Fig. 8.5, where the initial energy is based upon the reference formation energy of the cation vacancies in CZTS adjacent to the interface for point P (Fig. 4.4). A summary of the barriers is provided in Table 8.3 for the point labelled P (Fig. 4.4) of the CZTS stable region.

At the point labelled P (Fig. 4.4), the lowest diffusion barrier is for V_{Cu} in the initial state of the CZTS and when the formation energy of the cation vacancy in the initial state of the CZTS for reactions is included, the lowest barrier is also for the V_{Cu} in the initial state of the CZTS, this is the same as for the case of CZTS/ZnS (Section 6.3.5.1.1). The activation energy value of the saddle points with the formation energy of reference defects when there is a V_{Cu}, V_{Zn} and V_{Sn} in the initial state of the CZTS is 1.86, 2.16 and 3.27eV, respectively. However, the end point of all reactions (V_{Cd} in CdS and substitutional defects in CZTS) has lower energy than the initial state (cation vacancy in CZTS). Pre-existing metal vacancies in CZTS are most likely to diffuse into the CdS, since moving a metal vacancy to form substitutional defects in CZTS is exothermic (Section 3.8), and this is in contrast with the case for CZTS/ZnS (Section 6.3.5.1.1).

For the Q, M and N boundary points in the CZTS stable region (Fig. 4.4), the differences between the activation energy relative to point P are also listed in Table 8.3. A similar outcome between the outcome of points P, Q, M and N in the stable region of CZTS (Fig. 4.4) is expected. In this mechanism, V_{Sn} in CZTS have the lowest migration energy compared with V_{Cu} and V_{Zn} but this barrier will be the highest (3.27eV) when the formation energy of V_{Sn} is included since the cost of forming V_{Sn} in CZTS is so high (Table 8.2). Therefore, the most significant minimum activation energy path (migration energy with the formation energy of defects) is observed for the activation diffusion path of V_{Cu} in CZTS; in addition, the path of V_{Zn} also has lower activation diffusion barriers in comparison with other paths of diffusion.

Cu vacancy inside bulk CZTS has the lowest formation energy compared with Zn and Sn vacancies. According to this, Cu vacancy can be formed and diffused more easily than other defects. Therefore, Cu vacancy can be the dominant defect inside the CZTS/CdS interface in this mechanism under equilibrium growth conditions.

Table 8. 3: Calculated activation energies including the reference formation energy of the cation vacancies in the CZTS adjacent to the interface for the point P (Fig. 4.4, Table 8.2), E_{P}^{a}. E^{for} and E^{rev} are the forward and reverse migration barriers. For points Q, M and N (Fig. 4.4), the relative positions of the activation energies are lower by $\Delta E_{\mathrm{Q}}^{a}$, $\Delta E_{\mathrm{M}}^{a}$ and $\Delta E_{\mathrm{N}}^{a}$, respectively. All energies are in eV.

Reactions	E_{P}^{a}	E^{for}	E^{rev}	$\Delta E_{\mathrm{Q}}^{a}$	$\Delta E_{\mathrm{M}}^{a}$	$\Delta E_{\mathrm{N}}^{a}$
$V_{\mathrm{Cu}}^{\mathrm{CZTS}}$	1.86	0.97 (exothermic)	1.01	0.00	0.00	0.00
$V_{\mathrm{Zn}}^{\mathrm{CZTS}}$	2.16	1.06 (exothermic)	1.10	0.14	0.18	0.06
$V_{\mathrm{Sn}}^{\mathrm{CZTS}}$	3.27	0.84 (exothermic)	1.17	0.41	0.37	0.02

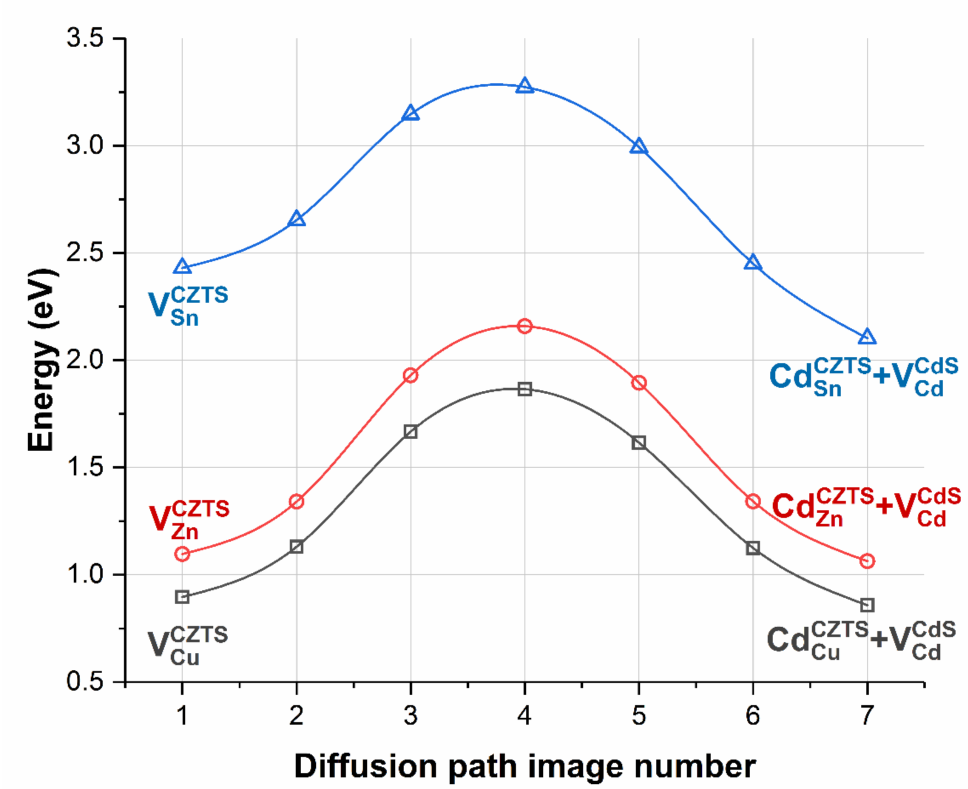

Figure 8. 5: Diffusion barriers calculated for the diffusion of Cd out of CdS into cation vacancies in CZTS. The energy scale includes the reference formation energy of the cation vacancies in the CZTS adjacent to the interface for the point P (Fig. 4.4).

8.3.5.1.2 CZTS Cation Vacancy Mechanisms in Different Charge States

Under equilibrium growth conditions, the diffusion barrier of defects with different charge states inside CZTS adjacent to the CZTS/CdS interface are investigated (Figs. 8.6, 8.7 and 8.8) when the Fermi level located at the VBM of the CZTS (μ_e=E_V) due to the absorber layer CZTS is a p-type material. If the value of μ_e is changed to be relatively higher than E_V, then the negative charge state will come down as μ_e goes up.

8.3.5.1.2.1 $V_{Cu}^{CZTS} \rightleftarrows Cd_{Cu}^{CZTS} + V_{Cd}^{CdS}$ Reactions

This mechanism has already been modelled in the CZTS/ZnS interface (Section 6.3.5.1.2.1). Under equilibrium growth conditions and μ_e=E_V of CZTS, the diffusion barrier of V_{Cu} with different charge states inside CZTS adjacent to the interface is calculated. The lowest diffusion barrier for V_{Cu} in the initial state of the CZTS is for charge −2 and when the formation energy of cation vacancy in the initial state of the CZTS for reactions is included, the lowest barrier is for the charge −1. This is the same as the case for CZTS/ZnS (Section 6.3.5.1.2.1)

The equilibrium reaction for the diffusion barrier including the formation energy to form the defects with different charge states begins and ends with the same charge (−1) across the interface; therefore, in this case there is no charge state changing as it moved across the interface. For the charges 0, −1 and −2 the forward reaction (V_{Cu} in CZTS) is exothermic and the reaction is more favourable to occur in this direction. In the system, for charges 0, −1 and −2 the reverse states of V_{Cd} in CdS and Cd_{Cu} in CZTS have the lowest energy compared to that of the initial state (V_{Cu} in CZTS), so the final state is more stable than the initial state and that enhances the holes in CZTS; however, the other charges are the opposite.

The formation energies for point P are calculated, as shown in Table 8.4, and the formation energies for the other boundary points Q, M and N of the CZTS stable region (Fig. 4.4) are the same as for point P. The calculated diffusion barriers at point P are illustrated in Fig. 8.6. The activation energy barriers for point P are listed in Table 8.4 and the activation energy barriers for Q, M and N points are the same as for point P for all the reactions; therefore, the outcomes for each point in the stable region of CZTS (Fig. 4.4) are the same.

Table 8. 4: Calculated reference formation energies E_{P}^{f} of V_{Cu} in the initial state of the CZTS and activation energies E_{P}^{a} including the reference formation energy of the Cu vacancy inside CZTS adjacent to the CZTS/CdS interface for the point P (Fig. 4.4), with differing charge states. E^{for} and E^{rev} are the forward and reverse migration barriers. All energies are in eV.

Charge	$\mathrm{E}_{\mathrm{P}}^{\mathrm{f}}$	E_{P}^{a}	E^{for}	E^{rev}
0	0.90	1.86	0.97 (exothermic)	1.01
−1	0.82	1.71	0.89 (exothermic)	1.09
−2	1.31	2.11	0.80 (exothermic)	1.08

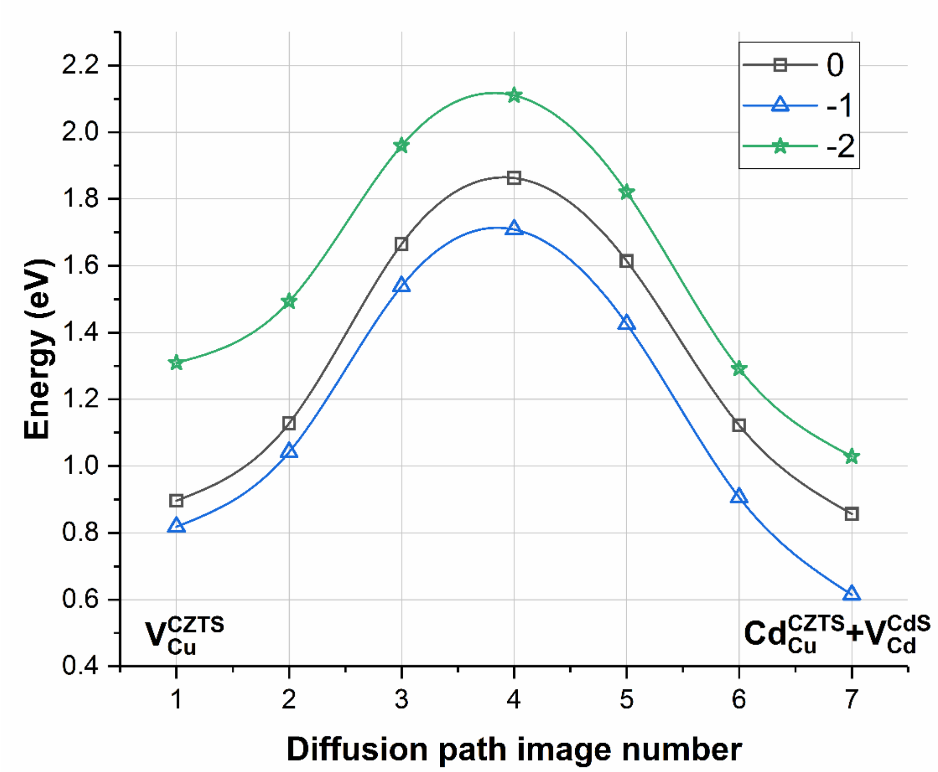

Figure 8. 6: Diffusion barriers calculated with different charge states (0, −1 and −2) for the diffusion of Cd out of CdS into Cu cation vacancies in CZTS. The energy scale includes the reference formation energy of the cation vacancies in the CZTS adjacent to the interface for the point P (Fig. 4.4) at μ_e=E_V.

8.3.5.1.2.2 $V_{Zn}^{CZTS} \rightleftarrows Cd_{Zn}^{CZTS} + V_{Cd}^{CdS}$ Reactions

This mechanism has already been modelled in the CZTS/ZnS interface (Section 6.3.5.1.2.2). Under equilibrium growth conditions and μ_e=E_V of CZTS, the diffusion barrier of V_{Zn} with different charge states inside CZTS adjacent to the interface are calculated. The lowest diffusion barrier for V_{Zn} in the initial state of the CZTS is for charge −1 and when the formation energy of cation vacancy in the initial state of the CZTS for reactions is included, the lowest barrier is also for the same charge −1.

The equilibrium reaction for the diffusion barrier with different charge states begins with charge −1 and ends with charge −2 across the interface; therefore, in this case there is a charge state changing as it moved across the interface. This leads to the absorption of an electron that can come from the Fermi level to the defect state. For charges 0, −1, and −2, the forward reaction (V_{Zn} in CZTS) is exothermic and the reaction is more favourable to occur in this direction (see Section 3.8). In the system, with and without charge, the initial state of V_{Zn} in CZTS has higher energy than that of the final state (V_{Cd} in CdS and Cd_{Zn} in CZTS) so the final state is more stable than the initial state.

For the P, Q, M and N points (Fig. 4.4), the formation energies are calculated, as shown in Table 8.5. Calculated diffusion barriers at point P are illustrated in Fig. 8.7. The activation energy barriers for point P are listed in Table 8.5. For the Q, M and N boundary points in the CZTS stable region (Fig. 4.4), the differences between the activation energy relative to point P are 0.14, 0.18 and 0.06eV, respectively and the differences are the same for all the reactions. Although the outcome is favourable in point P, there is no substantial difference between the outcome of points P, Q, M and N in the stable region of CZTS (Fig. 4.4), so it is expected to have a similar outcome.

Table 8. 5: Calculated reference formation energies (E_{P}^{f}, E_{Q}^{f}, E_{M}^{f} and E_{N}^{f}) of $\mathrm{V_{Zn}}$ in the initial state of the CZTS and activation energies E_{P}^{a} including the reference formation energy of the Zn vacancy inside CZTS adjacent to the CZTS/CdS interface for the point P (Fig. 4.4), with differing charge states. E^{for} and $E^{\mathrm{rev}}$are the forward and reverse migration barriers. All energies are in eV.

Charge	E_{P}^{f}	E_{Q}^{f}	E_{M}^{f}	E_{N}^{f}	E_{P}^{a}	E^{for}	E^{rev}
0	1.10	0.96	0.92	1.04	2.16	2.02 (exothermic)	1.98
−1	0.99	0.85	0.81	0.93	1.89	1.75 (exothermic)	1.72
−2	1.14	1.00	0.97	1.08	1.90	1.77 (exothermic)	1.73

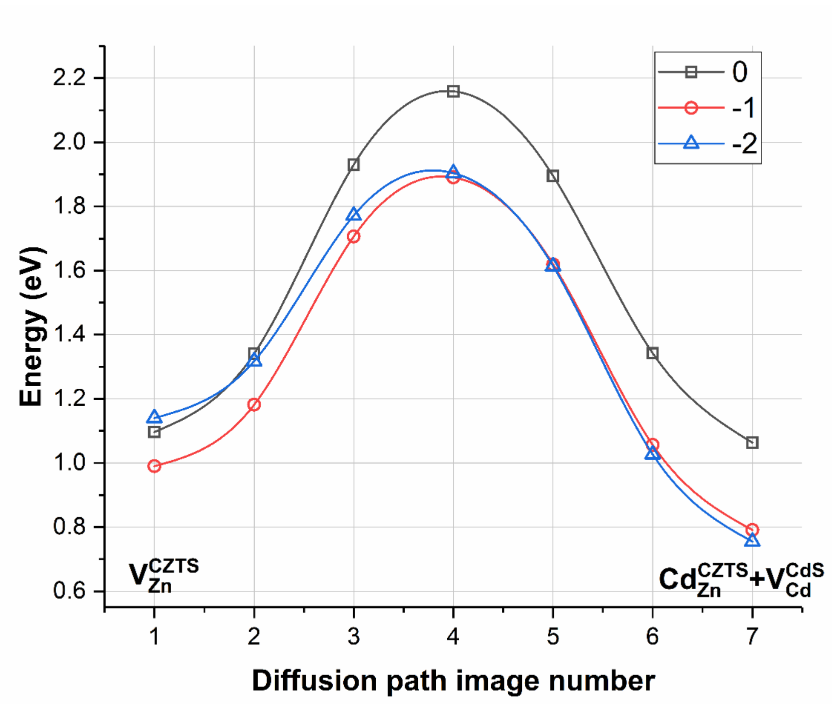

Figure 8. 7: Diffusion barriers calculated with different charge states (0, −1, and −2) for the diffusion of Cd out of CdS into Zn cation vacancies in CZTS. The energy scale includes the reference formation energy of the cation vacancies in the CZTS adjacent to the interface for the point P (Fig. 4.4) at μ_e=E_V.

8.3.5.1.2.3 $\mathbf{V_{Sn}^{CZTS} \rightleftarrows Cd_{Sn}^{CZTS} + V_{Cd}^{CdS}}$ Reactions

This mechanism has already been modelled in the CZTS/ZnS interface (Section 6.3.5.1.2.3). Under equilibrium growth conditions and μ_e=E_V of CZTS, the diffusion barriers of V_{Sn} with different charge states inside CZTS adjacent to the interface are calculated. The lowest diffusion barrier for V_{Sn} in the initial state of the CZTS with different charge states is for charge −4 but when the formation energy of cation vacancy in the initial state of the CZTS for reactions is included, the barrier (0.42eV) will become higher (3.22eV). The lowest activation diffusion barrier including the formation energy is for the charge −2. This is the same as in the case for CZTS/ZnS (Section 6.3.5.1.2.3).

The equilibrium reaction for the diffusion barrier with different charge states begins with charge −1 and ends with charge −2 across the interface; therefore, in this case there is a charge state changing as it moved across the interface, and this is same as the case for Cd out of CdS into Zn cation vacancies in CZTS (Section 8.3.5.1.2.2). For charges 0, −1, −2, −3 and −4 the reverse reaction (V_{Cd} in CdS and Cd_{Sn} in CZTS) is exothermic and the reaction is more favourable to occur in this direction (see Section 3.8). In the system, with and without charge, the initial state of V_{Sn} in CZTS has higher energy than that of the final state (V_{Cd} in CdS and Cd_{Sn} in CZTS) so the final state is more stable than the initial state.

For the P, Q, M and N points (Fig. 4.4), the formation energies are calculated, as shown in Table 8.6. Calculated diffusion barriers at point P are illustrated in Fig. 8.8. The activation energy barriers for point P are listed in Table 8.6. For the Q, M and N boundary points in the CZTS stable region (Fig. 4.4), the differences between the activation energy relative to point P are 0.41, 0.37 and 0.02eV, respectively and the differences are the same for all the reactions. A similar outcome between the outcome of points P, Q, M and N in the stable region of CZTS (Fig. 4.4) is expected, as is the case in Section 8.3.5.1.2.2.

Table 8. 6: Calculated reference formation energies (E_{P}^{f}, E_{Q}^{f}, E_{M}^{f} and E_{N}^{f}) of $\mathrm{V_{Sn}}$ in the initial state of the CZTS and activation energies E_{P}^{a} including the reference formation energy of the Sn vacancy inside CZTS adjacent to the CZTS/CdS interface for the point P (Fig. 4.4), with differing charge states. E^{for} and E^{rev} are the forward and reverse migration barriers. All energies are in eV.

Charge	E_{P}^{f}	E_{Q}^{f}	E_{M}^{f}	E_{N}^{f}	E_{P}^{a}	E^{for}	E^{rev}
0	2.43	2.02	2.06	2.41	3.27	0.84 (exothermic)	1.17
−1	2.22	1.81	1.85	2.20	2.89	0.67 (exothermic)	1.16
−2	2.26	1.85	1.89	2.24	2.79	0.53 (exothermic)	1.24
−3	2.49	2.08	2.12	2.47	2.94	0.45 (exothermic)	1.35
−4	2.79	2.38	2.42	2.77	3.22	0.42 (exothermic)	1.46

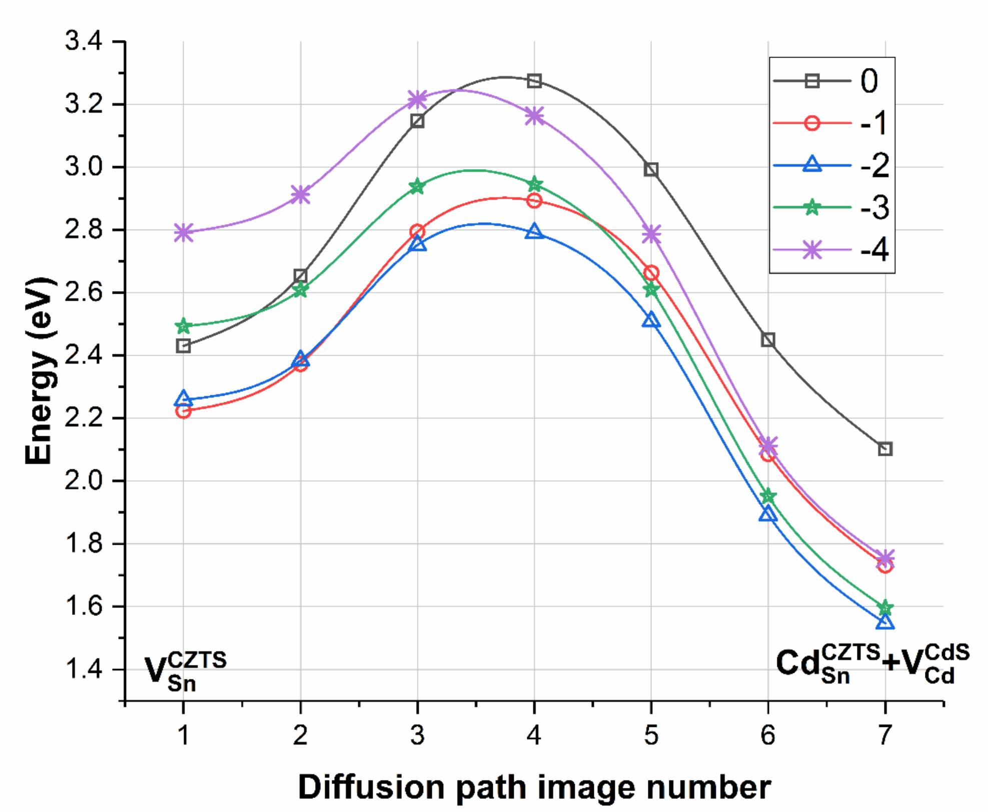

Figure 8. 8: Diffusion barriers calculated with different charge states (0, −1, −2, −3 and −4) for the diffusion of Cd out of CdS into Sn cation vacancies in CZTS. The energy scale includes the reference formation energy of the cation vacancies in the CZTS adjacent to the interface for the point P at $\mu_{\mathrm{e}}=E_{\mathrm{V}}$.

8.3.5.2 CdS Cation Vacancy Mechanisms

8.3.5.2.1 CdS Cation Vacancy Mechanisms in Neutral Charge State

This mechanism has already been modelled in the CZTS/ZnS interface (Section 6.3.5.2.1). In the second mechanism, as described in Section 8.3.3.2, V_{Cd} diffuses out of CdS. The calculated reference formation energies of the cation vacancy in the CdS adjacent to the interface for the points P, Q, M, and N (Fig. 4.4) are listed in Table 8.2. Calculated diffusion barriers at point P are illustrated in Fig. 8.9. The activation energy barriers for point P are listed in Table 8.7.

The barriers for the reverse reactions (vacancy in CZTS and substitutional defects in CdS) are lower than that of the forward for two of the three reactions that result in impurities (Zn or Sn) being incorporated into the CdS lattice, with the energy cost including an electrostatic term from charge transferred across the interface, as well as a bond-strength term. It is noticed that there is an intermediate minimum structure in the diffusion barrier reaction with an Sn impurity, and this could be attributed to the fact that Sn is more relaxed at image four and can make more bonds at that image since the Sn atoms are bigger than Cu, Zn and Cd. This intermediate minimum structure also occurs when there is V_{Sn} in bulk CZTS (Section 4.3.9.1), and also when there is an Sn impurity inside cubic and strained CdS (Section 7.3.5.2 and Section 7.3.6.2). The barrier for all forward and reverse reactions depends on the differences between the saddle point and both of the initial and final state. This result agrees with the CZTS/ZnS interface when there is V_{Zn} in ZnS and Sn diffusing out of CZTS to replace the V_{Zn} in ZnS as calculated (Section 6.3.5.2.1).

Moving V_{Cd} to form V_{Cu} in CZTS is exothermic, meaning that pre-existing V_{Cd} in CdS are likely to diffuse into the CZTS replacing Cu under given equilibrium conditions. In this mechanism, the lowest diffusion barrier is for Cu replacing Cd in CdS and when the formation energy includes the lowest diffusion barrier, it is also for Cu replacing Cd in CdS. Therefore, the most significant minimum migration path is observed for the migration path of Cu replacing Cd in CdS. In addition to that Zn_{Cd} substitutional defect has the lowest starting and ending points; therefore, it is more stable than other defects. However, Zn_{Cd} inside strained CdS has a lower formation energy than that of Cu_{Cd} and Sn_{Cd} substitutional defects (Table 7.2). According to this, a Zn_{Cd} substitutional defect might be formed and diffused more easily than other defects. Therefore, it might be the dominant defect inside the CZTS/CdS interface when there is a cation vacancy inside CdS under given conditions.

For the Q, M and N boundary points in the CZTS stable region (Fig. 4.4), the differences between the activation energy for Q, M and N points relative to point P are 0.14, 0.14 and 0.02eV, respectively and the differences are the same for all the reactions. A similar outcome between the outcome of points P, Q, M and N in the stable region of CZTS (Fig. 4.4) is expected, as is the case in Section 8.3.5.1.2.2 and Section 8.3.5.1.2.3.

Table 8. 7: Calculated activation energies (of VCd in CdS with either Cu, Zn or Sn cation diffusing out of CZTS across the junction into the CdS adjacent to the interface) including the reference formation energy of the cation vacancy in the CdS adjacent to the interface for the point P (Fig. 4.4, Table 8.2), E_{P}^{a}. E^{for} and E^{rev} are the forward and reverse migration barriers. All energies are in eV.

Reaction	E_{P}^{a}	E^{for}	E^{rev}
$\mathrm{V_{Cd}^{CdS}} \rightleftarrows \mathrm{Cu_{Cd}^{CdS}} + \mathrm{V_{Cu}^{CZTS}}$	2.19	0.68 (exothermic)	0.89
$\mathrm{V_{Cd}^{CdS}} \rightleftarrows \mathrm{Zn_{Cd}^{CdS}} + \mathrm{V_{Zn}^{CZTS}}$	2.65	1.53 (endothermic)	1.43
$\mathrm{V_{Cd}^{CdS}} \rightleftarrows \mathrm{Sn_{Cd}^{CdS}} + \mathrm{V_{Sn}^{CZTS}}$	3.33	2.22 (endothermic)	0.70

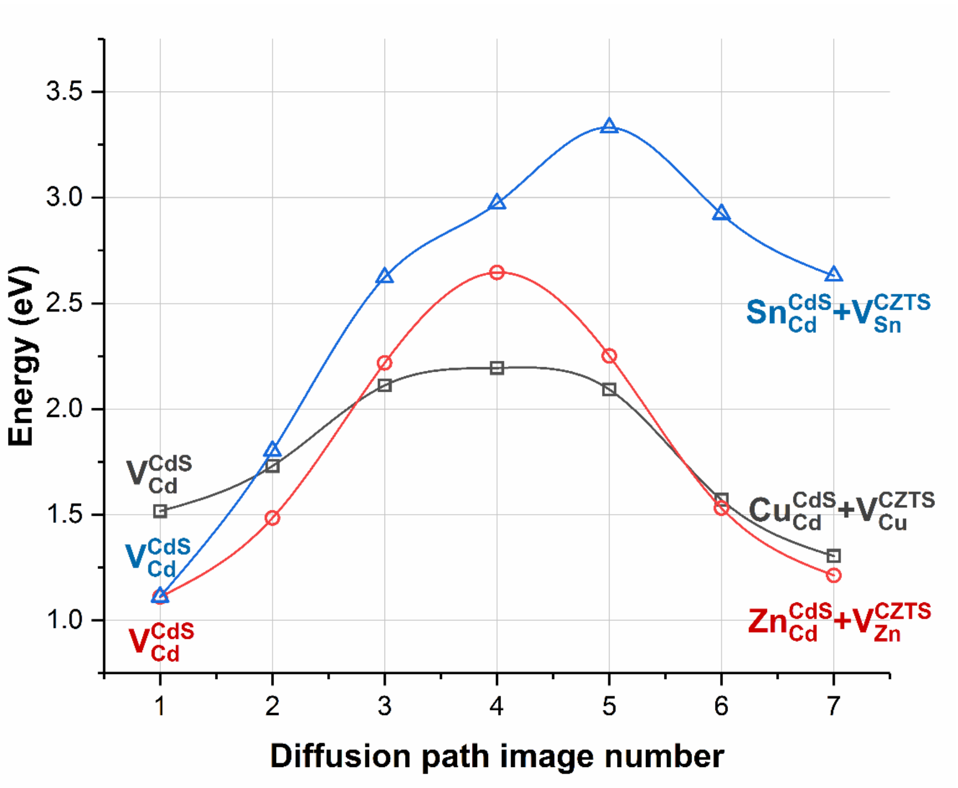

Figure 8. 9: Diffusion barriers calculated for the diffusion of $\mathrm{V_{Cd}}$ in CdS with either Cu, Zn or Sn cation diffusing out of CZTS across the junction into the CdS adjacent to the interface. The energy scale includes the reference formation energy of the cation vacancies in the CdS adjacent to the interface for the point P (Fig. 4.4).

8.3.5.2.2 CdS Cation Vacancy Mechanisms in Different Charge States

8.3.5.2.2.1 $\mathbf{V_{Cd}^{CdS} \rightleftarrows Cu_{Cd}^{CdS} + V_{Cu}^{CZTS}}$ Reactions

This mechanism has already been modelled in the CZTS/ZnS interface (Section 6.3.5.2.2.1). Under equilibrium growth conditions μ_e=E_V of CZTS, the diffusion barriers of V_{Cd} in CdS with Cu diffusing out of CZTS across the junction into the CdS adjacent to the interface are calculated. The lowest diffusion barrier for V_{Cd} in CdS and Cu diffusing out of CZTS to replace the V_{Cd} in CdS is for charge −1 and when the formation energy of V_{Cd} in the initial state of the CdS is included, the lowest activation diffusion barrier is also for charge −1. The equilibrium reaction for the diffusion barrier with different charge states begins and ends with the same charge (−1) across the interface; therefore, in this case there is no charge state changing as moved across the interface.

For charges 0, −1 and −2, the forward reaction of V_{Cd} diffusing out of CdS is exothermic and the reaction is more favourable to occur in this direction (see Section 3.8). In the system with and without charge, the initial state of V_{Cd} in CdS has higher energy than that of the final state (Cd_{Cu} in CdS and V_{Cu} in CZTS) so the final state is more stable than the initial state and that enhances the holes in CZTS.

For the P, Q, M and N points (Fig. 4.4), the formation energies are calculated, as shown in Table 8.8. Calculated diffusion barriers at point P are illustrated in Fig. 8.8. The activation energy barriers for point P are listed in Table 6.8. For the Q, M and N boundary points in the CZTS stable region (Fig. 4.4), the differences between the activation energy relative to point P are 0.14, 0.14 and 0.02eV, respectively and the differences are the same for all three reactions, and as is mentioned in Section 8.3.5.2.1, a similar outcome between the points P, Q, M and N in the stable region of CZTS (Fig. 4.4) is expected.

Table 8. 8: Calculated reference formation energies (E_P^f, E_Q^f, E_M^f and E_N^f) of V_{Cd} in the initial state of the CdS and activation energies E_P^a including the reference formation energy of the Cd vacancy inside CdS and Cu diffusing out of CZTS to replace the V_{Cd} in CdS for point P (Fig. 4.4), with differed charge states. E^{for} and E^{rev} are the forward and reverse migration barriers. All energies are in eV.

Charge	E_P^f	E_Q^f	E_M^f	E_N^f	E_P^a	E^{for}	E^{rev}
0	1.52	1.38	1.38	1.50	2.23	0.71 (exothermic)	0.94
−1	1.28	1.15	1.15	1.27	1.97	0.68 (exothermic)	0.86
−2	1.37	1.24	1.24	1.36	2.07	0.69 (exothermic)	0.83

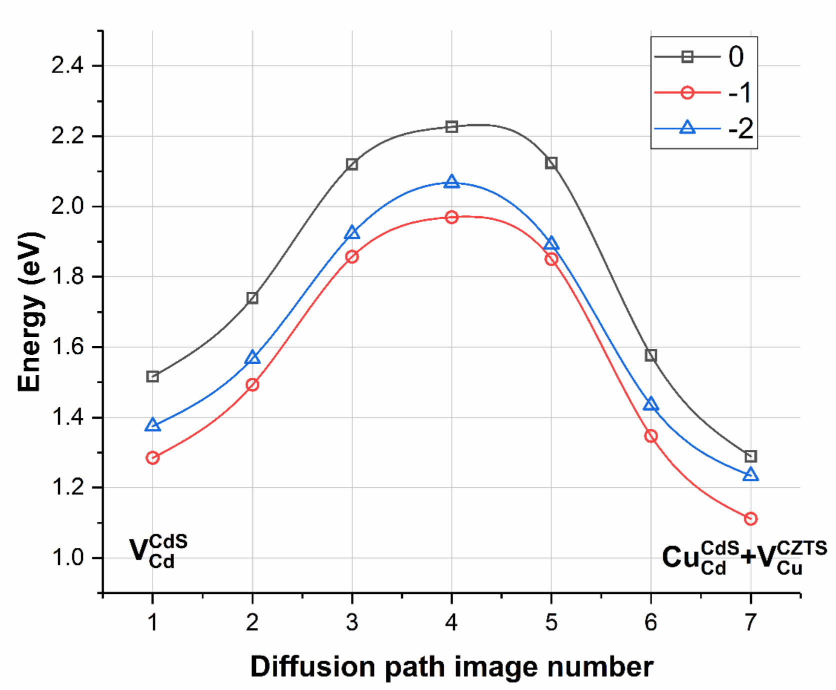

Figure 8. 10: Diffusion barriers calculated with different charge states (0, −1 and −2) for the diffusion of V_{Cd} in CdS with Sn diffusing out of CZTS across the junction into the CdS adjacent to the interface. The energy scale includes the reference formation energy of the cation vacancies in the CdS adjacent to the interface for point P (Fig. 4.4) at μ_e=E_V.

8.3.5.2.2.2 $V_{Cd}^{CdS} \rightleftarrows Zn_{Cd}^{CdS} + V_{Zn}^{CZTS}$ Reactions

This mechanism has already been modelled in the CZTS/ZnS interface (Section 6.3.5.2.2.2). Under equilibrium growth conditions μ_e=E_V of CZTS, the diffusion barriers of V_{Cd} in CdS with Zn diffusing out of CZTS across the junction into the CdS adjacent to the interface are calculated. The lowest diffusion barrier of V_{Cd} inside CdS and Zn diffusing out of CZTS to replace the V_{Cd} in CdS is for charge −1 and when the formation energy of V_{Cd} in the initial state of the CdS is included, the lowest activation diffusion barrier is for both charges −1 and −2.

The equilibrium reaction for the diffusion barrier with different charge states begins with charges −2 and −1 and ends with charge −1 across the interface; therefore, in this case, there is a charge state changing as moved across the interface. This leads to the absorption of an electron that can come from the Fermi level to the defect state.

For charges 0, −1 and −2, the forward reaction of V_{Cd} diffusing out of CdS is endothermic whist the reverse reaction (Zn_{Cd} in CdS and V_{Zn} in CZTS) is exothermic and the reaction is more favourable to occur in this direction (see Section 3.8). In the system with and without charge, the initial state of V_{Cd} in CdS has lower energy than that of the final state so the initial state is more stable than the product and that enhances the holes in

CdS so the Zn cation elements in CZTS can move across the interface and replace the V_{Cd}. In contrast, the diffusion of V_{Cd} out of CdS onto Cu cation sites in CZTS is exothermic (Section 8.5.3.2.2.1).

For the P, Q, M and N points (Fig. 4.4), the formation energies are calculated, as shown in Table 8.9. Calculated diffusion barriers at point P are illustrated in Fig. 8.11. The activation energy barriers for point P are listed in Table 8.9. For the Q, M and N boundary points in the CZTS stable region (Fig. 4.4), the differences between the activation energy relative to point P are 0.14, 0.14 and 0.02eV, respectively, and the differences are the same for all three reactions, and as is mentioned in Section 8.3.5.2.1; a similar outcome between the points P, Q, M and N in the stable region of CZTS (Fig. 4.4) is expected.

Table 8. 9: Calculated reference formation energies (E_{P}^{f}, E_{Q}^{f}, E_{M}^{f} and E_{N}^{f}) of V_{Cd} in the initial state of the CdS and activation energies E_{P}^{a} including the reference formation energy of the Cd vacancy inside CdS and Zn diffusing out of CZTS to replace the V_{Cd} in CdS for the point P (Fig. 4.4), with differing charge states. E^{for} and E^{rev} are the forward and reverse migration barriers. All energies are in eV.

Charge	E_{P}^{f}	E_{Q}^{f}	E_{M}^{f}	E_{N}^{f}	E_{P}^{a}	E^{for}	E^{rev}
0	1.11	0.97	0.97	1.09	2.64	1.53 (endothermic)	1.43
−1	0.81	0.67	0.67	0.79	2.29	1.48 (endothermic)	1.21
−2	0.75	0.61	0.61	0.73	2.29	1.54 (endothermic)	1.07

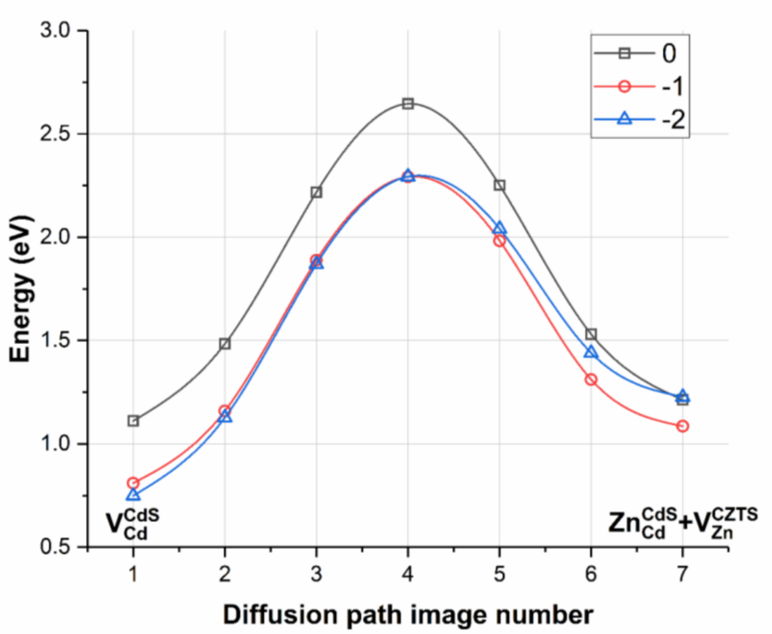

Figure 8. 11: Diffusion barriers calculated with different charge states (0, −1 and −2) for the diffusion of V_{Cd} in CdS with Zn diffusing out of CZTS across the junction into the CdS adjacent to the interface. The energy scale includes the reference formation energy of the cation vacancies in the CdS adjacent to the interface for point P (Fig. 4.4).

8.3.5.2.2.3 $V_{Cd}^{CdS} \rightleftarrows Sn_{Cd}^{CdS} + V_{Sn}^{CZTS}$ Reactions

This mechanism has already been modelled in the CZTS/ZnS interface (Section 6.3.5.2.2.3). Under equilibrium growth conditions μ_e=E_V of CZTS, the diffusion barriers of V_{Cd} in CdS with Sn diffusing out of CZTS across the junction into the CdS adjacent to the interface are calculated. The charges −2, −3 and −4 are unstable under given conditions; these reactions have no maximum barrier, and for this individual process, V_{Sn} should move further in the CZTS probably to have an end point. There is an intermediate minimum structure in the diffusion barrier reaction with an Sn impurity or vacancy, as explained in Section 8.3.5.2.1. This result is in agreement with the CZTS/ZnS interface when there is V_{Zn} in ZnS and Sn diffusing out of CZTS to replace the V_{Zn} in ZnS with different charge states (Section 6.3.5.2.2.3).

The lowest diffusion barrier of V_{Cd} inside CdS and Zn diffusing out of CZTS to replace the V_{Cd} in CdS is for charge −1 and when the formation energy of V_{Cd} in the initial state of the CdS is included, the lowest activation diffusion barrier is also for charge −1. The equilibrium reaction for the diffusion barrier with different charge states begins with charge −1 and ends with charge 0 across the interface; therefore, in this case there is a charge state changing as moved across the interface, and this is same as the case for Zn out of CZTS into cation sites in CdS (Section 8.3.5.2.2.2).

For charge 0, −1, −2, 1 and 2, the forward reaction of V_{Cd} diffusing out of CdS is endothermic whilst the reverse reaction (Sn_{Cd} in CZTS and V_{Sn} in CZTS) is exothermic and the reaction is more favourable to occur in this direction (see Section 3.8). In the system with and without charge, the initial state of V_{Cd} in CdS has lower energy than that of the final state so the initial state is more stable than the product and that enhances the holes in CdS so the Sn cation elements in CZTS can move across the interface and replace the V_{Cd}. Similarly, the diffusion of V_{Cd} out of CdS onto Zn cation sites in CZTS is also endothermic (Section 8.5.3.2.2.1).

For points P, Q, M and N (Fig. 4.4), the formation energies are calculated, as shown in Table 8.10. Calculated diffusion barriers at point P are illustrated in Fig. 8.12. The activation energy barriers for point P are listed in Table 8.10. For the Q, M and N boundary points in the CZTS stable region (Fig. 4.4), the differences between the activation energy relative to point P are 0.14, 0.14 and 0.02eV, respectively, and the differences are the same for all three reactions, as is mentioned in Section 8.3.5.2.1; a similar outcome between the points P, Q, M and N in the stable region of CZTS (Fig. 4.4) is expected.

Table 8. 10: Calculated reference formation energies (E_{P}^{f}, E_{Q}^{f}, E_{M}^{f} and E_{N}^{f}) of $\mathrm{V_{Cd}}$ in the initial state of the CdS and activation energies E_{P}^{a} including the reference formation energy of the Cd vacancy inside CdS and Sn diffusing out of CZTS to replace the $\mathrm{V_{Cd}}$ in CdS for the points P (Fig. 4.4), with differing charge states. E^{for} and E^{rev} are the forward and reverse migration barriers. All energies are in eV.

Charge	E_{P}^{f}	E_{Q}^{f}	E_{M}^{f}	E_{N}^{f}	E_{P}^{a}	E^{for}	E^{rev}
2	2.03	1.89	1.89	2.01	4.02	1.99 (endothermic)	0.98
1	1.53	1.39	1.39	1.51	3.57	2.05 (endothermic)	0.80
0	1.11	0.98	0.98	1.09	3.43	2.32 (endothermic)	0.77
−1	0.81	0.67	0.67	0.79	3.11	2.29 (endothermic)	0.35
−2	0.75	0.61	0.61	0.73	3.10	2.35 (endothermic)	0.04
−3	1.04	0.90	0.90	1.02	3.42	2.38 (endothermic)	0.00
−4	1.47	1.33	1.33	1.45	3.70	2.24 (endothermic)	0.00

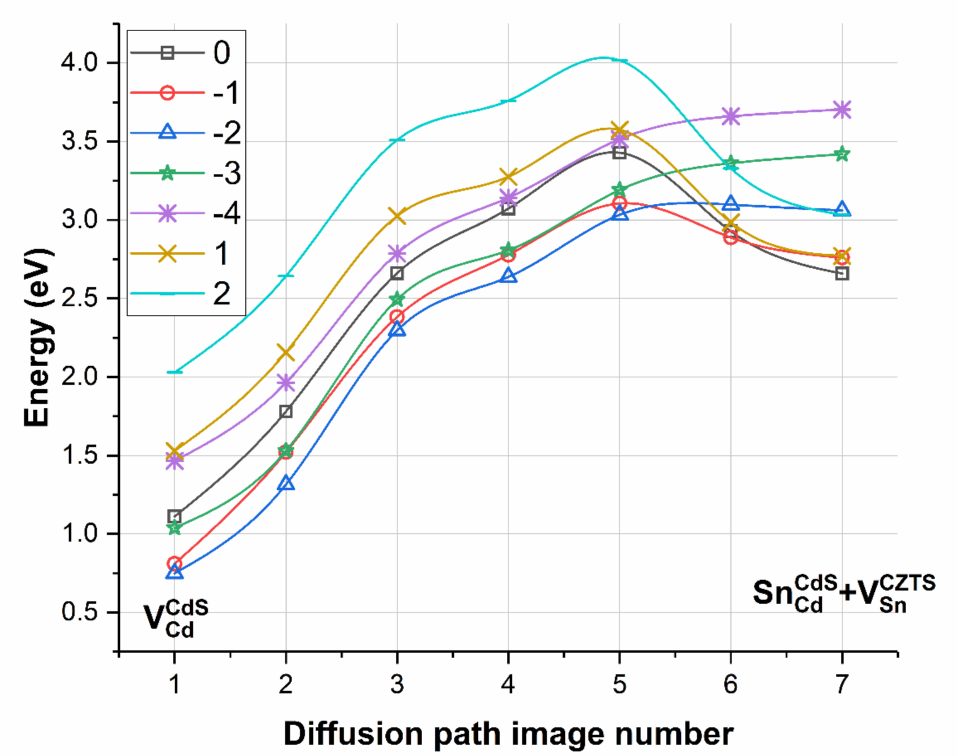

Figure 8. 12: Diffusion barriers calculated with different charge states (0, −1, −2, −3, −4, 1 and 2) for the diffusion of $\mathrm{V_{Cd}}$ in CdS with Sn diffusing out of CZTS across the junction into the CdS adjacent to the interface. The energy scale includes the reference formation energy of the cation vacancies in the CdS adjacent to the interface for the point P (Fig. 4.4).

8.3.5.3 Cd Diffusion Inside the CdS Part of the Interface

This process has already been modelled in the CZTS/ZnS interface (Section 6.3.5.3). The diffusion process inside the CdS part mirrors bulk strained CdS (Section 7.3.6.1). Considering that there is a strain in the CdS buffer layer (Section 7.3.1), the diffusion of Cd inside CdS in the parallel direction and away from the CZTS/CdS interface will be different and that will affect the cell conductivity; The concentration of cation vacancy in CZTS which forms by moving the elements from CZTS to CdS depends on the concentration of the Cd vacancy in CdS, and that affects the p-type CZTS conductivity.

In this case, the Cd atom moves to the nearest cation vacancy inside the CdS part adjusted to the interface and leaving V_{Cd} in the initial place (Section 7.3.6.1**)**, as shown schematically in Fig. 8.13. There is a cation vacancy lying inside the CdS part in this process. The diffusion barrier of Cd metal inside the CdS part depends on the interface direction, since the CdS lattice lengths in the [010] and [001] directions differ from the [100] direction due to the interface strain (see Section 8.3.1). Based on interface model conditions, the diffusion barrier in the away direction from the interface differ from the parallel direction to the interface (Section 6.3.5.3).

The calculated diffusion barrier at point P for the absolute energy scale and with a reference formation energy of V_{Cd} in the [110] direction away from the interface and the [011] parallel direction to the interface are illustrated in Fig. 8.14. The lowest diffusion barrier for the Cd atom moves to the nearest cation vacancy inside the CdS part is for [011] parallel direction to the interface, and this agrees with the result of bulk strained CdS (Section 7.3.6.1**)**. This is in consistent with when a Zn atom moves to the nearest cation vacancy inside the ZnS part at the CZTS/ZnS interface (Section 6.3.5.3). This result also agrees with the result for bulk strained CdS (Section 7.3.6.1).

The diffusion barriers in the [110] direction away from the interface and the [011] parallel direction to the interface are different and this is attributed to the fact that the strain (see Section 7.3.1) in CdS is high compared with the case for ZnS (see Section 5.3.1), in addition to the electrostatic effect.

The diffusion barrier in the [110] direction away from the interface and the [011] parallel direction begins with the same point and ends with different points where the end point in the [110] direction away from the interface is higher than that for the [011] parallel directions. For the [110] direction away from the interface, the difference between the starting and ending points is attributed to moving the charge transferred from CZTS valence band further from the interface which costs energy to work against the electronic field. In the [011] parallel directions to the interface, the difference between the starting and ending points is attributed to the local environment where the starting point for the Cd atom in CdS is located next to the Zn atom in CZTS, while the end point of the Cd atom in CdS is located next to the Sn atom in CZTS.

For both the [110] direction away from the interface and the [011] direction parallel to the interface, the reverse reactions are exothermic and the reactions are more favourable to occur in this reverse direction (Section 3.8). As a result, in the [110] direction away from the interface, the Cd vacancy can move more easily towards the interface than the opposite direction. Therefore, the probability of finding a Cd vacancy inside the CdS part adjacent to the interface is greater closed to the interface than that away from the interface. This enhances the transfer of the cation vacancy from CZTS adjacent to the interface to CdS and leaves a cation vacancy inside CZTS, and that enhances the p-type conductivity of the cell.

For the P, Q, M and N points (Fig. 4.4), the formation energies are calculated, as shown in Table 8.2. The activation energy barriers for point P are listed in Table 8.11. For the Q, M and N boundary points in the CZTS stable region (Fig. 4.4), the differences between the activation energy relative to point P are 0.14, 0.14 and 0.02eV, respectively, and the differences are the same for both reactions; a similar outcome between the points P, Q, M and N in the stable region of CZTS (Fig. 4.4) is expected.

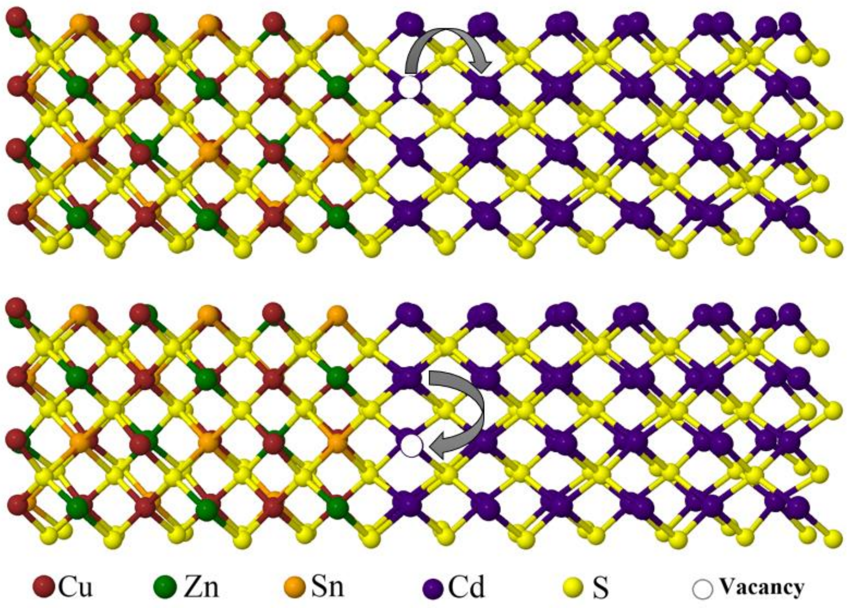

Figure 8. 13: Diffusion barriers for Cd diffusing into metal vacancies in the strained CdS part of the CZTS/CdS interface in (a) the [110] and (b) the [011] directions.

Table 8. 11: Calculated activation energies including the reference formation energy of Cd vacancy for Cd diffusing inside the CdS part adjacent to the interface in the [110] direction away from the interface and the [011] parallel direction to the interface for the point P (see Section 4.3.4, Table 8.2) E_{P}^{a}. E^{for} and $E^{\mathrm{rev}}$are the forward and reverse migration barriers. All energies are in eV.

Direction	E_{P}^{a}	E^{for}	E^{rev}
[110] away from the interface	3.66	1.06 (endothermic)	0.92
[011] parallel to the interface	2.92	0.32 (endothermic)	0.05

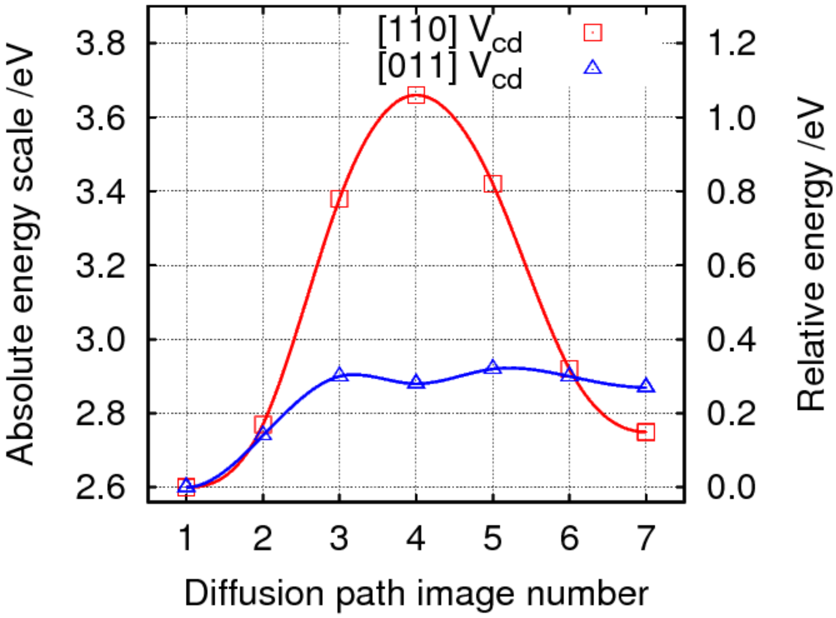

Figure 8. 14: Diffusion barriers calculated for the absolute energy scale and with reference formation energy of Cd diffusing into metal vacancies in the strained CdS part adjacent to the CZTS/CdS interface in the [110] direction away from the interface and the [011] parallel directions at point P (Fig. 4.4).

8.4 Conclusions

It is noted that at a (100)-CZTS/CdS heterojunction and under equilibrium growth conditions, V_{Cu} in the CZTS adjacent to the interface has relatively low formation energy compared to that of other defects. This is in line with the p-type doping in as-grown CZTS under these conditions. This result agrees with the (100)-CZTS/ZnS heterojunction. In addition, it is concluded that the lattice mismatch in CZTS/CdS (8%) is higher than that of CZTS/ZnS (0.5%), since the strain in ZnS is lower than that of CdS.

It is observed that, under the given conditions, V_{Cu} has the lowest activation diffusion barrier compared with other defects; however, the energetic of this process is favourability of the migration into the CdS, meaning that the buffer layer will enhance p-type doping centres.

The equilibrium reaction for the diffusion barrier with different charge states refers to the fact that there is no charge state changing as moved across the interface in case there is V_{Cu} inside CZTS adjacent to the interface in the first mechanisms, and when there is V_{Cd} in CdS adjacent to the interface and Cu diffusing out of CZTS to replace the V_{Cd} in CdS in the second mechanisms. However, there is a changing charge state as moved across the interface in a case where there is V_{Zn} or V_{Sn} inside CZTS adjacent to the interface in the first mechanisms, and when there is V_{Cd} in CdS adjacent to the interface and Zn or Sn diffusing out of CZTS to replace the V_{Cd} in CdS in the second mechanisms.

The diffusion barrier with different charge states of all cation vacancies in CZTS adjacent to the interface is exothermic. In all charge states for the second mechanisms, the diffusion of V_{Cd} in CdS adjacent to the interface and Cu diffusing out of CZTS to replace the V_{Cd} in CdS is exothermic, while the diffusion of Zn or Sn out of CZTS into cation sites in CdS adjacent to the interface is endothermic.

The lowest activation diffusion barrier with a different charge state in the first mechanisms for V_{Cu} and V_{Zn} inside CZTS adjacent to the interface is for charge -1, while for V_{Sn} inside CZTS adjacent to the interface is for charge -2. The lowest activation diffusion barrier with a different charge state in the second mechanisms for V_{Cd} in CdS adjacent to the interface and Cu or Sn diffusing out of CZTS to replace the V_{Cd} in CdS is for charge -1, while for V_{Cd} in CdS adjacent to the interface and Zn diffusing out of CZTS to replace the V_{Cd} in CdS is for charges -1 and -2.

The difference in the diffusion barrier of a Cd atom moving to the nearest cation vacancy inside CdS at CZTS/CdS between the [110] direction away from the interface and the [011] parallel direction to the interface is big compared with the difference in the diffusion barrier of a Zn atom moving to the nearest cation vacancy inside the ZnS part at the CZTS/ZnS interface between the [110] direction away from the interface and the [011] parallel direction to the interface (Section 6.3.5.3), because the strain in ZnS is lower than that of CdS. The lowest activation diffusion barrier for a Cd atom moving to the nearest cation vacancy inside the CdS part is for the [011] parallel direction to the interface; this agrees with the result of the bulk strained CdS. This is in consistent with a Zn atom moving to the nearest cation vacancy inside the ZnS part at the CZTS/ZnS interface (Section 6.3.5.3).

Chapter 9

Summary and Future Work

9.1 Summary

The objectives for the project reported in this thesis are focused on the most common defects in CZTS based solar cells in addition to the impact of defects arising from the intermixing between the buffer layer and CZTS. Two attractive buffer layers have been chosen in this thesis. First, because the single CZTS phase stability is quite narrowly defined by the chemical potentials, with practical efficient devices obtained in relatively Cu-poor and Zn-rich conditions, ZnS is the main secondary phases in CZTS and it has been used as an alternative buffer layer to CdS. Second, CdS is used commonly as a buffer layer to CZTS, since it improves cell efficiency.

Density function theory has been performed. In the CZTS/(ZnS or CdS) heterojunctions are comprised of kesterite CZTS epitaxially connected to cubic ZnS or CdS along the [100] lattice directions of both materials and the strain is entirely accommodated within the ZnS or CdS to simulate the situation of a thin ZnS or CdS layer on a relatively thicker CZTS material, with the [100] lattice direction being optimised to minimise the total energy. All the results have been calculated under the typical Cu-poor/Zn-rich growth condition at $\mu_{\mathrm{Cu}} = -0.2\mathrm{eV}$.

In this chapter, the results have been summarised in three main areas listed here.

9.1.1 CZTS based solar cells

In the initial part, phase stability, electrical level and the diffusion processes of CZTS have been investigated; these analyses are part of the control calculations for the inter-diffusion in the interfaces CZTS/ZnS and CZTS/CdS.

The single-phase stability of CZTS has been investigated among the secondary phases with different values of $\Delta\mu_{\mathrm{Cu}}$ to show how the secondary phases limit the formation of the single-phase CZTS. It has been concluded that at $\Delta\mu_{\mathrm{Cu}}$ = 0eV the stable region of CZTS is nearly a point, and when $\Delta\mu_{\mathrm{Cu}}$ becomes more negative at $\Delta\mu_{\mathrm{Cu}} = -0.06, -0.2$ and $-0.564\mathrm{eV}$, the single-phase CZTS becomes a region and the areas of the single-phase CZTS regions are not constant and change with more Cu poor. At $\Delta\mu_{\mathrm{Cu}}$ = −0.634eV, the CZTS stable region vanishes to approximately a point, and below this value such as at the value of $\Delta\mu_{\mathrm{Cu}}$ =−1.33eV there is no stable region of CZTS.

It has been found that under the standard growth conditions, the intrinsic defects in CZTS $\mathrm{Cu_{Zn}}$ have the lowest formation energy compared to the other defects and $\mathrm{V_{Cu}}$ have a shallower accepter level than other defects consistent with these intrinsic defects being responsible for p-type conductivity of CZTS.

The activation diffusion barrier has been studied for the cation vacancy, antisite and substitutional defects inside CZTS. It has been found that the dominant native cation vacancy defects inside bulk CZTS are Cu vacancies because they have the lowest activation diffusion barrier and formation energy compared with other native cation vacancy defects. For antisite defects, it is concluded that single acceptor $\mathrm{Cu_{Zn}}$ is the dominant antisite defect inside bulk CZTS compared with other antisite defects, since $\mathrm{Cu_{Zn}}$ has the lowest activation diffusion barrier via $\mathrm{V_{Zn}}$ mechanisms and the lowest formation energy compared with other antisite defects. For Cd impurity defects in CZTS, the dominant Cd substitutional cation defects inside bulk CZTS are iso-electronic $\mathrm{Cd_{Zn}}$ defects. It has been found that a substitutional $\mathrm{Cd_{Zn}}$ defect has the lowest formation energy compared with the other substitutional Cd defects.

9.1.2 CZTS/ZnS

Under growth conditions, it is expected that there would be ZnS secondary phases and the interface between those in the bulk materials and absorber layer is of interest. In order to study the CZTS/ZnS hetero-structure, bulk cubic and strained ZnS have been investigated in terms of the most common native and impurity defects and the interdiffusion. In ZnS secondary phases, it has been shown that the strain in the lattice constant of bulk ZnS in the [100] direction is compressive, while in the [010] and [001] directions, it is tensile, and the strain in the lattice constant of bulk ZnS is not significant, since the lattice constant of ZnS is similar to that of CZTS. The formation energies for intrinsic cation vacancy and impurity defects, such as Cu and Sn in strained bulk ZnS are less than that of the cubic ZnS; therefore, these defects can form more easily in strained ZnS than cubic ZnS. Cu and Sn are impurity defects inside ZnS coming from the CZTS absorber layer. The formation energy for Cu_{Zn} single acceptor substitutional defects in cubic and strained ZnS is lower than that of Sn_{Zn} double donor substitutional defects. The diffusion barrier of substitutional defects inside strained ZnS in the [110] direction away from the interface is lower than that of the [011] parallel direction to the interface; this is a consequence resulting from the interface model where the strain in the [011] direction is tensile, while the strain in the [110] direction is compressive. Therefore, the most frequent migration path is in the [110] direction. Furthermore, Cu_{Zn} has the lowest diffusion barrier via V_{Zn} mechanisms compared with Sn_{Zn} defects. There are many processes but, in particular, the Cu_{Zn}, which is thought to contribute p-type conductivity when diffusing via V_{Zn}, has the lowest overall barrier.

For the CZTS/ZnS interface, the calculated results of band offset for CZTS/ZnS in the [100] direction indicate that the band offset is of type one. CZTS/ZnS has a large spike indicating that the ZnS secondary phase in p-type CZTS could be regarded as a resistive barrier to the minority carrier electrons.

For the CZTS/ZnS interface, the formation energy of Cu and Zn cation vacancy in CZTS adjacent to the interface in the first mechanisms is lower than that of Zn vacancy in ZnS adjacent to the interface in the second mechanisms. This is in line with the p-type doping in as-grown CZTS under these conditions.

V_{Cu} in CZTS adjacent to the interface has the lowest activation diffusion barrier compared with other defects; however, the energetic of this process is unfavourability of the migration into the ZnS, means that the buffer layer will act as an effective diffusion barrier to these p-type doping centres.

There are two fundamental groups for diffusion processes, one with the vacancy originating from CZTS and one when the vacancy originates from the other material, and these are described in the thesis as two types. The first mechanism is where a metal vacancy lies within the CZTS, and Zn diffuses from ZnS into the CZTS. Then this Zn atom may occupy any of the Cu, Zn and Sn sites in CZTS, leaving V_{Zn} in the ZnS. Where the Zn moves into a Cu or Sn site, this results in the formation of an anti-site in the CZTS. In the second mechanism, we consider a Zn vacancy inside ZnS, with either Cu, Zn, or Sn diffusing out of CZTS across the junction into the ZnS.

The equilibrium reaction for the diffusion barrier with different charge states refers to the fact that there is no charge state changing as it moves across the interface in the first mechanisms when there is V_{Cu} inside CZTS adjacent to the interface, and in the second mechanisms, when there is V_{Zn} in ZnS adjacent to the interface and Cu diffusing out of CZTS to replace the V_{Zn} in ZnS. However, there is a charge state changing as it moves across the interface in the first mechanisms when there is V_{Zn} or V_{Sn} inside CZTS adjacent to the interface, and in the second mechanisms when there is V_{Zn} in ZnS adjacent to the interface and Zn or Sn diffusing out of CZTS to replace the V_{Zn} in ZnS.

In the first mechanisms, the diffusion barrier in the equilibrium charge states of all cation vacancies within CZTS is endothermic. In the second mechanisms, the diffusion barrier in the equilibrium charge states of V_{Zn} in ZnS adjacent to the interface and Cu or Sn diffusing out of CZTS to replace the V_{Zn} in ZnS is endothermic, while the diffusion of Zn out of CZTS into cation sites in ZnS adjacent to the interface is exothermic.

The lowest activation diffusion barrier with a different charge state in the first mechanisms for V_{Cu} and V_{Zn} inside CZTS adjacent to the interface is for the charge -1, while for V_{Sn} inside CZTS adjacent to the interface, it is for the charge -2. The lowest activation diffusion barrier with a different charge state in the second mechanisms for V_{Zn} in ZnS adjacent to the interface and Cu or Zn diffusing out of CZTS to replace the V_{Zn} in ZnS, respectively, is for the charge -1, while for V_{Zn} in ZnS adjacent to the interface and Sn diffusing out of CZTS to replace the V_{Zn} in ZnS is for the charge -2.

In general, two mechanisms (diffusion and drift) drive the movement of the defects across the junction. The movement of the neutral charged defects through the junction occurs because of the diffusion force (concentration gradient), while the movement of the charged defects through the junction occurs because of the drift force (potential gradient).

For a Zn atom moving to the nearest cation vacancy inside the ZnS part at the CZTS/ZnS, the lowest activation diffusion barrier is for the [011] parallel direction to the interface, and this is agreed with the result for the bulk strained ZnS.

9.1.3 CZTS/CdS

As with the CZTS/ZnS case, to examine the CZTS/CdS hetero-structure, bulk cubic and strained CdS have been investigated. For the CdS buffer layer, it has been found that, based on the interface module of CZTS/CdS, the strain in the lattice constant of bulk CdS in the [100] direction is tensile, while in the [010] and [001] directions, it is compressive, and this is in contrast with bulk strained ZnS. The strain in the lattice constant of CdS in the [100] and [001] directions is much higher than ZnS, since the lattice constant of CdS is larger than that of ZnS.

In strained CdS, the formation energies for intrinsic cation vacancy and substitutional defects Cu_{Cd} and Zn_{Cd} are lower than that of the cubic except for the Sn_{Cd}, because the strain for the Sn_{Cd} substitutional defect is tensile whereas the strains for the other substitutional defects are compressive. In addition, the formation energy for Zn_{Cd} substitutional defects in cubic and strained CdS is lower than that for other substitutional defects.

The diffusion barrier of the cation vacancy and substitutional defects inside strained CdS in the [011] parallel direction to the interface is lower than that of the [110] direction away from the interface based on the fact that the interface model for the strain in the [110] direction is tensile, while the strain in the [011] direction is compressive, and this is in contrast with the CZTS/ZnS interface.

Therefore, the most frequent migration path in bulk strained CdS is in the [011] direction. Furthermore, Zn_{Cd} has the lowest diffusion barrier via V_{Cd} mechanisms compared with other substitutional defects. There are many processes but, in particular, the Zn_{Cd} when diffusing via V_{Cd} has the lowest overall barrier.

For the CZTS/CdS interface, the calculated results of band alignment for CZTS/CdS in the [100] direction revealed that band alignment is of type one and has a relatively small positive spike compared with that of the CZTS/ZnS, since the strain in the CdS buffer layer is larger than that of the ZnS layer based on the lattice constant. Therefore, the lattice mismatch in CZTS/CdS (8%) is higher than that of CZTS/ZnS (0.5%).

It is noted that at a (100)-CZTS/CdS heterojunction and under equilibrium growth conditions, V_{Cu} in the CZTS adjacent to the interface has relatively low formation energy compared to that of other defects. This is in line with the p-type doping. This result is in agreement with the (100)-CZTS/ZnS heterojunction.

It is calculated that under the given conditions, V_{Cu} has the lowest activation diffusion barrier compared with other defects; however, the energetic of this process is favourability of the migration into the CdS, meaning that the buffer layer is expected to enhance p-type doping centres.

The equilibrium reaction for the diffusion barrier with different charge states refers to the fact that there is no charge state changing as it moves across the interface in a case where there is V_{Cu} inside CZTS adjacent to the interface in the first mechanisms, and when there is V_{Cd} in CdS adjacent to the interface and Cu diffusing out of CZTS to replace the V_{Cd} in CdS in the second mechanisms. However, there is a charge state changing as it moves across the interface in a case where there is V_{Zn} or V_{Sn} inside CZTS adjacent to the interface in the first mechanisms, and when there is V_{Cd} in CdS adjacent to the interface and Zn or Sn diffusing out of CZTS to replace the V_{Cd} in CdS in the second mechanisms.

The diffusion barrier with different charge states for all cation vacancies in CZTS adjacent to the interface is exothermic. In all charge states for the second mechanisms, the diffusion of V_{Cd} in CdS adjacent to the interface and Cu diffusing out of CZTS to replace the V_{Cd} in CdS is exothermic, while the diffusion of Zn or Sn out of CZTS into cation sites in CdS adjacent to the interface is endothermic.

The lowest activation diffusion barrier with a different charge state in the first mechanisms for V_{Cu} and V_{Zn} inside CZTS adjacent to the interface is for the charge -1, while for V_{Sn} inside CZTS adjacent to the interface, it is for the charge -2. The lowest activation diffusion barrier with a different charge state in the second mechanisms for V_{Cd} in CdS adjacent to the interface and Cu or Sn diffusing out of CZTS to replace the V_{Cd} in CdS is for the charge -1, while for V_{Cd} in CdS adjacent to the interface and Zn diffusing out of CZTS to replace the V_{Cd} in CdS is for the charges -1 and -2.

The difference in the diffusion barrier when a Cd atom moves to the nearest cation vacancy inside CdS at CZTS/CdS between the [110] direction away from the interface and the [011] parallel direction to the interface is big compared with the difference in the diffusion barrier when a Zn atom moves to the nearest cation vacancy inside the ZnS part at the CZTS/ZnS interface between the [110] direction away from the interface and the [011] parallel direction to the interface, because the strain in ZnS is lower than that for CdS. The lowest activation diffusion barrier when a Cd atom moves to the nearest cation vacancy inside the CdS part is for the [011] parallel direction to the interface, and this agrees with the result for bulk strained CdS. This is agreed with when a Zn atom moves to the nearest cation vacancy inside the ZnS part at the CZTS/ZnS interface.

Overall, each interface has some advantages and disadvantages affecting the solar cell performance wherein the ZnS or CdS is used in the n-type buffer layer. For (100)-CZTS/ZnS, the strain is small; therefore, the lattice mismatch in CZTS/ZnS [65] is relatively small (Section 6.3.1), and this is expected to lead to a low dislocation density at the interface. This is in line with the p-type doping in as-grown CZTS [40]. However, the calculated band offset (Section 3.7) of CZTS/ZnS [65] has a big spike (Section 6.3.2). This large spike is generally not optimal for solar cell performance (Section 1.3.1) because this large spike [64, 89] could act as a resistive barrier to the minority carrier electrons and increase R_S (Section 1.2.3) by reducing J_{SC} [62] and this will affect the η (Section 1.2.3). V_{OC}, generally in the straddled alignment, is nearly stable [62]. Additionally processes in the interface where inter-diffusion might take place will affect the performance of these devices. In the inter-diffusion processes for ZnS/CZTS interface, in the first mechanisms (Section 6.3.5.1.1), the diffusion barrier in the equilibrium charge states for all cation vacancies within CZTS adjacent to the CZTS/ZnS interface is endothermic, and this will not enhance p-type conductivity of CZTS.

For (100)-CdS/CZTS, the lattice mismatch is big (Section 8.3.1), so the strain in CdS is big compared with CZTS/ZnS. This will tend to lead to high dislocation densities' at the interface; furthermore Cd is toxic, whereas Zn is not [114, 185] and the technology sector is being driven to a sustainable and non-toxic future. This is not in line with the p-type doping in as-grown CZTS. However, the band offset of CZTS/CdS has a small spike (Section 8.3.2), and this is optimal for solar cell performance (Section 1.3.1) because, in the small spike, the J_{SC} and FF are nearly constant [62]. Additionally processes in the interface where inter-diffusion might take place will affect the performance of these devices. In the inter-diffusion processes for CdS/CZTS interface, in the first mechanisms (Section 8.3.5.1.1), the diffusion barrier with different charge states for all cation vacancies within CZTS adjacent to the CZTS/CdS interface is exothermic, and this will enhance p-type conductivity of CZTS.

In general, both interfaces have contrasting results for the different factors, including strain, band offset and diffusion processes. However, there are many unanswered questions remaining. The conclusion as for the data presented in this study are specific to a (100) interface, but they would need to be re-examined for different interface orientations, such as (001) and (110). Evaluation of different interfaces might reveal additional factors, for example, a big spike might be present for (100) interface and not for different orientations.

9.2 Future work

This study can be improved by modelling the dislocation at the CZTS/CdS interface which arises from the misfit at the junction. In order to eliminate the strain or the band offset at the interface, it is recommended that a different buffer layer or different orientation is chosen.

CZTS can be replaced with CZTSe to understand the role of Se in the inter-diffusion mechanisms and how that will affect the device operation. Furthermore, study of the diffusion processes between the main secondary phase ZnSe and the absorber layer would be of interest.

In addition, the use of a screened exchange approach is recommended rather than LDA or GGA to get accurate electronic structure results by eliminating the underestimation in the band gap.

Bibliography

1. Tyagi, V.V., S.C. Kaushik, and S.K. Tyagi, *Advancement in solar photovoltaic/thermal (PV/T) hybrid collector technology.* Renewable & Sustainable Energy Reviews, 2012. **16**(3): p. 1383-1398.
2. Urban, O., et al., *Interactive effects of ultraviolet radiation and elevated CO_2 concentration on photosynthetic characteristics of European beech saplings during the vegetation season.* Plant Physiology and Biochemistry, 2019. **134**: p. 20-30.
3. Ying, N., et al., *Long-term link detection in the CO_2 concentration climate network.* Journal of Cleaner Production, 2019. **208**: p. 1403-1408.
4. Bakke, J.R., et al., *Nanoengineering and interfacial engineering of photovoltaics by atomic layer deposition.* Nanoscale, 2011. **3**(9): p. 3482-3508.
5. Lewis, N.S. and D.G. Nocera, *Powering the planet: Chemical challenges in solar energy utilization.* Proceedings of the National Academy of Sciences, 2006. **103**(43): p. 15729-15735.
6. Gong, J.W., J. Liang, and K. Sumathy, *Review on dye-sensitized solar cells (DSSCs): Fundamental concepts and novel materials.* Renewable & Sustainable Energy Reviews, 2012. **16**(8): p. 5848-5860.
7. Cook, T.R., et al., *Solar energy supply and storage for the legacy and nonlegacy worlds.* Chemical reviews, 2010. **110**(11): p. 6474-6502.
8. Grätzel, M., *Photoelectrochemical cells.* Nature, 2001. **414**(6861): p. 338-344.
9. Copeland, A.W., O.D. Black, and A.B. Garrett, *The Photovoltaic Effect.* Chemical reviews, 1942. **31**(1): p. 177-226.
10. Huber, F., *P-N Junction Photovoltaic Effect in Anodically Formed Oxide Films of Titanium.* Journal of The Electrochemical Society, 1963. **110**(7): p. 846-847.
11. Green, M.A., *Photovoltaic principles.* Physica E: Low-dimensional Systems and Nanostructures, 2002. **14**(1): p. 11-17.
12. Ludin, N.A., et al., *Review on the development of natural dye photosensitizer for dye-sensitized solar cells.* Renewable and Sustainable Energy Reviews, 2014. **31**: p. 386-396.

13. Green, M.A., *The path to 25% silicon solar cell efficiency: history of silicon cell evolution.* Progress in Photovoltaics: Research and Applications, 2009. **17**(3): p. 183-189.

14. Ohl, R.S., *Light-sensitive electric device including silicon*. 1948, Google Patents.

15. Martinez-Val, J.M., *Energy for Sustainable Development: A systematic approach for a badly defined challenge.* Energy conversion and management, 2013. **72**: p. 3-11.

16. Rakshit, H., et al., *A Survey on Energy Demand and Solar Photovoltaic Electricity.*

17. Wolden, C.A., et al., *Photovoltaic manufacturing: Present status, future prospects, and research needs.* Journal of Vacuum Science & Technology A: Vacuum, Surfaces, and Films, 2011. **29**(3): p. 030801.

18. Mallouk, T.E., *The emerging technology of solar fuels*. 2010, ACS Publications.

19. Hagfeldt, A., et al., *Dye-sensitized solar cells.* Chemical reviews, 2010. **110**(11): p. 6595-6663.

20. Lund, H., *Renewable energy strategies for sustainable development.* Energy, 2007. **32**(6): p. 912-919.

21. Jäger-Waldau, A., *Snapshot of Photovoltaics—March 2017.* https://www.researchgate.net/publication/316787508, 2017. **9, 783;**(10.3390/su9050783).

22. Walsh, A., et al., *Kesterite Thin-Film Solar Cells: Advances in Materials Modelling of Cu_2ZnSnS_4.* Advanced Energy Materials, 2012. **2**(4): p. 400-409.

23. Pillai, S., et al., *Surface plasmon enhanced silicon solar cells.* Journal of Applied Physics, 2007. **101**(9): p. 093105.

24. Asim, N., et al., *A review on the role of materials science in solar cells.* Renewable and Sustainable Energy Reviews, 2012. **16**(8): p. 5834-5847.

25. Imamzai, M., et al. *A Review on Comparison between Traditional Silicon Solar Cells and Thin-Film CdTe Solar Cells*. in *Proceedings of National Graduate Conference (Nat-Grad)*. 2012.

26. Shockley, W. and H.J. Queisser, *Detailed balance limit of efficiency of p-n junction solar cells.* Journal of applied physics, 1961. **32**(3): p. 510-519.

27. Xu, Y., T. Gong, and J.N. Munday, *The generalized Shockley-Queisser limit for nanostructured solar cells.* Scientific reports, 2015. **5**: p. 13536.

28. Rühle, S., *Tabulated values of the Shockley–Queisser limit for single junction solar cells.* Solar Energy, 2016. **130**: p. 139-147.

29. Shah, A.V., R. Platz, and H. Keppner, *Thin-film silicon solar cells: a review and selected trends.* Solar energy materials and solar cells, 1995. **38**(1-4): p. 501-520.
30. Tyagi, V.V., S.C. Kaushik, and S.K. Tyagi, *Advancement in solar photovoltaic/thermal (PV/T) hybrid collector technology.* Renewable and Sustainable Energy Reviews, 2012. **16**(3): p. 1383-1398.
31. Tarui, H., S. Tsuda, and S. Nakano, *Recent progress of amorphous silicon solar cell applications and systems.* Renewable energy, 1996. **8**(1-4): p. 390-395.
32. Hamakawa, Y., *Recent advances in amorphous silicon technologies and its application to solar cells.* Renewable energy, 1996. **8**(1-4): p. 10-16.
33. Keppner, H., et al., *Microcrystalline silicon and micromorph tandem solar cells.* Applied Physics A: Materials Science & Processing, 1999. **69**(2): p. 169-177.
34. Nakamura, N., et al., *The Influence of the Si-H2 Bond on the Light-Induced Effect in a-Si Films and a-Si Solar Cells.* Japanese Journal of Applied Physics, 1989. **28**(10R): p. 1762.
35. Scharber, M.C. and N.S. Sariciftci, *Efficiency of bulk-heterojunction organic solar cells.* Prog Polym Sci, 2013. **38**(12): p. 1929-1940.
36. Peter, L.M., *Towards sustainable photovoltaics: the search for new materials.* Philosophical Transactions of the Royal Society of London A: Mathematical, Physical and Engineering Sciences, 2011. **369**(1942): p. 1840-1856.
37. Peter, L.M., *Towards sustainable photovoltaics: the search for new materials.* Philos Trans A Math Phys Eng Sci, 2011. **369**(1942): p. 1840-56.
38. Vanalakar, S.A., et al., *A review on pulsed laser deposited CZTS thin films for solar cell applications.* Journal of Alloys and Compounds, 2015. **619**: p. 109-121.
39. Hossain, M.I., *Prospects of Czts Solar Cells from the Perspective of Material Properties, Fabrication Methods and Current Research Challenges.* Chalcogenide Letters, 2012. **9**(6): p. 231-242.
40. Chen, S., et al., *Classification of lattice defects in the kesterite Cu_2ZnSnS_4 and $Cu_2ZnSnSe_4$ earth-abundant solar cell absorbers.* Adv Mater, 2013. **25**(11): p. 1522-39.
41. Hossain, M.I., *Prospects of Czts Solar Cells from the Perspective of Material Properties, Fabrication Methods and Current Research Challenges.* Chalcogenide Letters, 2012. **9**(6): p. 231-242.

42. Das, S., K.C. Mandal, and R.N. Bhattacharya, *Earth-Abundant $Cu_2ZnSn(S, Se)_4$ (CZTSSe) Solar Cells*, in *Semiconductor Materials for Solar Photovoltaic Cells*. 2016, Springer. p. 25-74.
43. Shang, S.L., et al., *Cation Disorder Regulation by Microstate Configurational Entropy in Photovoltaic Absorber Materials $Cu_2ZnSn(S,Se)(_4)$.* Journal of Physical Chemistry C, 2014. **118**(43): p. 24884-24889.
44. Ananthan, M.R. and B. Mahalaksmi, *Review on CZTS based solar cells.* Advances in Natural and applied sciences, 2014. **8**(21): p. 72-76.
45. Richards, B.S. and A. Shalav, *Photovoltaics devices.* The Handbook of Photonics, 2007: p. 8-19.
46. Liu, S., et al., *Heterostructured semiconductor nanowire arrays for artificial photosynthesis.* Materials Horizons, 2016. **3**(4): p. 270-282.
47. Pivrikas, A., H. Neugebauer, and N.S. Sariciftci, *Charge carrier lifetime and recombination in bulk heterojunction solar cells.* IEEE journal of selected topics in quantum electronics, 2010. **16**(6): p. 1746-1758.
48. Nelson, J., *The physics of solar cells*. 2003: World Scientific Publishing Company.
49. Fang, X., et al., *Flexible counter electrodes based on metal sheet and polymer film for dye-sensitized solar cells.* Thin Solid Films, 2005. **472**(1-2): p. 242-245.
50. Theiss, S.D., et al. *Polysilicon thin film transistors fabricated at 100/spl deg/C on a flexible plastic substrate*. in *Electron Devices Meeting, 1998. IEDM'98. Technical Digest., International*. 1998. IEEE.
51. Won, S.H., et al., *Effect of mechanical and electrical stresses on the performance of an a-Si: H TFT on plastic substrate.* Journal of The Electrochemical Society, 2004. **151**(3): p. G167-G170.
52. Okada, Y., et al. *43.4: A 4-inch Reflective Color TFT-LCD Using a Plastic Substrate*. in *SID Symposium Digest of Technical Papers*. 2002. Wiley Online Library.
53. Rhoderick, E.H., *Metal-semiconductor contacts.* IEE Proceedings I-Solid-State and Electron Devices, 1982. **129**(1): p. 1.
54. Romeo, A., *Growth and characterization of high efficiency CdTe/CdS solar cells*. 2002, University of Parma.
55. Mali, S.S., et al., *Novel synthesis of kesterite Cu_2ZnSnS_4 nanoflakes by successive ionic layer adsorption and reaction technique: characterization and application.* Electrochimica Acta, 2012. **66**: p. 216-221.

56. Green, M.A., *General temperature dependence of solar cell performance and implications for device modelling.* Progress in Photovoltaics: Research and Applications, 2003. **11**(5): p. 333-340.
57. Jordan, D.C. and S.R. Kurtz, *Photovoltaic degradation rates—an analytical review.* Progress in photovoltaics: Research and Applications, 2013. **21**(1): p. 12-29.
58. Chauhan, A.K. and P. Kumar, *Degradation in perovskite solar cells stored under different environmental conditions.* Journal of Physics D: Applied Physics, 2017. **50**(32): p. 325105.
59. Kaur, K., N. Kumar, and M. Kumar, *Strategic review of interface carrier recombination in earth abundant Cu-Zn-Sn-S-Se solar cells: Current challenges and future prospective.* Journal of Materials Chemistry A, 2017.
60. Neuschitzer, M., et al., *Towards high performance Cd-free CZTSe solar cells with a ZnS (O, OH) buffer layer: the influence of thiourea concentration on chemical bath deposition.* Journal of Physics D: Applied Physics, 2016. **49**(12): p. 125602.
61. Kroemer, H., *Quasi-Electric Fields and Band Offsets: Teaching Electrons New Tricks (Nobel Lecture).* ChemPhysChem, 2001. **2**(8-9): p. 490-499.
62. Minemoto, T., et al., *Theoretical analysis of the effect of conduction band offset of window/CIS layers on performance of CIS solar cells using device simulation.* Solar Energy Materials and Solar Cells, 2001. **67**(1): p. 83-88.
63. Konovalov, I. and R. Szargan, *Valence band alignment with a small spike at the CuI/$CuInS_2$ interface.* Applied physics letters, 2003. **82**(13): p. 2088-2090.
64. Bao, W. and M. Ichimura, *Influence of Secondary Phases in Kesterite- Cu_2ZnSnS_4 Absorber Material Based on the First Principles Calculation.* International Journal of Photoenergy, 2015. **2015**.
65. Nagoya, A., R. Asahi, and G. Kresse, *First-principles study of Cu_2ZnSnS_4 and the related band offsets for photovoltaic applications.* Journal of Physics: Condensed Matter, 2011. **23**(40): p. 404203.
66. Mendis, B.G., et al., *The role of secondary phase precipitation on grain boundary electrical activity in Cu_2ZnSnS_4 (CZTS) photovoltaic absorber layer material.* Journal of applied physics, 2012. **112**(12): p. 124508.
67. Mikhailova, M.P. and A.N. Titkov, *Type II heterojunctions in the GaInAsSb/GaSb system.* Semiconductor science and technology, 1994. **9**(7): p. 1279.

68. Mikhailova, M.P., K.D. Moiseev, and Y.P. Yakovlev, *Interface-induced optical and transport phenomena in type II broken-gap single heterojunctions.* Semiconductor science and technology, 2004. **19**(10): p. R109.

69. Ekpunobi, A.J., *Curvature of band overlap in InAs/GaSb Type II superlattices.* Materials science in semiconductor processing, 2005. **8**(4): p. 463-466.

70. Cheng, Y.-W., et al., *Bonding and electronic properties of the* Cu_2ZnSnS_4*/WZ–ZnO interface from first-principles calculations.* Journal of Physics D: Applied Physics, 2016. **49**(28): p. 285107.

71. Phaltane, S.A., et al., *Photocatalytic degradation of methylene blue by hydrothermally synthesized CZTS nanoparticles.* Journal of Materials Science: Materials in Electronics, 2017. **28**(11): p. 8186-8191.

72. Katagiri, H., et al., *Development of thin film solar cell based on* Cu_2ZnSnS_4 *thin films.* Solar Energy Materials and Solar Cells, 2001. **65**(1): p. 141-148.

73. Liu, W.C., et al., *Facile hydrothermal synthesis of hydrotropic* Cu_2ZnSnS_4 *nanocrystal quantum dots: band-gap engineering and phonon confinement effect.* Journal of Materials Chemistry A, 2013. **1**(9): p. 3182-3186.

74. Ito, K. and T. Nakazawa, *Electrical and optical properties of stannite-type quaternary semiconductor thin films.* Japanese Journal of Applied Physics, 1988. **27**(11R): p. 2094.

75. Huang, T.J., et al., *CZTS-based materials and interfaces and their effects on the performance of thin film solar cells.* physica status solidi (RRL)-Rapid Research Letters, 2014. **8**(09): p. 735-762.

76. Katagiri, H., et al., *Preparation and evaluation of* Cu_2ZnSnS_4 *thin films by sulfurization of E□ B evaporated precursors.* Solar Energy Materials and Solar Cells, 1997. **49**(1-4): p. 407-414.

77. Katagiri, H. *Survey of development of CZTS-based thin film solar cells*. in *Photonics (ICP), 2012 IEEE 3rd International Conference on*. 2012. IEEE.

78. Katagiri, H. and K. Jimbo. *Development of rare metal-free CZTS-based thin film solar cells*. in *Photovoltaic Specialists Conference (PVSC), 2011 37th IEEE*. 2011. IEEE.

79. Chen, H., et al., *Electrodeposited CZTS solar cells from Reline electrolyte.* Green Chemistry, 2014. **16**(8): p. 3841-3845.

80. Meissner, D., et al. *50 Years of Monograin Solar Cells: Time to Go to Market*. in *Meeting Abstracts*. 2009. The Electrochemical Society.

81. Tinker, L. and R. Jones-Albertus. *Emerging PV technologies: The path to market competitiveness*. in *Photovoltaic Specialists Conference (PVSC), 2016 IEEE 43rd*. 2016. IEEE.

82. Chen, S., et al., *Intrinsic point defects and complexes in the quaternary kesterite semiconductor Cu_2ZnSnS_4.* Physical Review B, 2010. **81**(24): p. 245204.

83. Khalate, S.A., et al., *Effect of deposition temperature on the properties of Cu_2ZnSnS_4 (CZTS) thin films.* Superlattices and Microstructures, 2017. **103**: p. 335-342.

84. Green, M.A., et al., *Solar cell efficiency tables (Version 45).* Progress in photovoltaics: research and applications, 2015. **23**(1): p. 1-9.

85. Pawar, S.M., et al., *Growth of void free Cu_2ZnSnS_4 (CZTS) thin films by sulfurization of stacked metallic precursor films.* Vacuum, 2014. **104**: p. 57-60.

86. Delbos, S., *Kësterite thin films for photovoltaics: a review.* EPJ Photovoltaics, 2012. **3**: p. 35004.

87. Scragg, J.J.S., et al., *A low-temperature order-disorder transition in Cu_2ZnSnS_4 thin films.* Applied Physics Letters, 2014. **104**(4): p. 041911.

88. Tan, J.M.R., et al., *Understanding the synthetic pathway of a single-phase quarternary semiconductor using surface-enhanced Raman scattering: a case of wurtzite Cu_2ZnSnS_4 nanoparticles.* Journal of the American Chemical Society, 2014. **136**(18): p. 6684-6692.

89. Li, W., et al., *The effect of ZnS segregation on Zn-rich CZTS thin film solar cells.* Journal of Alloys and Compounds, 2015. **632**: p. 178-184.

90. Sarker, P., M.M. Al-Jassim, and M.N. Huda, *Theoretical limits on the stability of single-phase kesterite- Cu_2ZnSnS_4.* Journal of Applied Physics, 2015. **117**(3): p. 035702.

91. Scragg, J.J., et al., *New routes to sustainable photovoltaics: evaluation of Cu_2ZnSnS_4 as an alternative absorber material.* physica status solidi (b), 2008. **245**(9): p. 1772-1778.

92. Tang, A., et al., *One step electrodeposition of Cu_2ZnSnS_4 thin films in a novel bath with sulfurization free annealing.* Applied Surface Science, 2017. **402**: p. 70-77.

93. Ziti, A., et al., *Study of kesterite CZTS thin films deposited by spin coating technique for photovoltaic applications.* Superlattices and Microstructures, 2017.

94. Singh, O.P., et al., *Effect of temperature on thermal expansion and anharmonicity in Cu_2ZnSnS_4 thin films grown by co-sputtering and sulfurization.* Materials Chemistry and Physics, 2014. **146**(3): p. 452-455.

95. Daranfed, W., et al., *Synthesis and Characterization of Cu_2ZnSnS_4 Absorber Layers by Ultrasonic Spray Pyrolysis*, in *Properties and Characterization of Modern Materials*. 2017, Springer. p. 325-331.

96. Shin, B., et al., *Thin film solar cell with 8.4% power conversion efficiency using an earth‐abundant Cu_2ZnSnS_4 absorber.* Progress in Photovoltaics: Research and Applications, 2013. **21**(1): p. 72-76.

97. Fan, F.-J., L. Wu, and S.-H. Yu, *Energetic I–III–VI^2 and I^2–II–IV–VI^4 nanocrystals: synthesis, photovoltaic and thermoelectric applications.* Energy & Environmental Science, 2014. **7**(1): p. 190-208.

98. Zongyan, Z. and Z. Xiang, *Electronic, optical, and mechanical properties of Cu_2ZnSnS_4 with four crystal structures.* Journal of Semiconductors, 2015. **36**(8): p. 083004.

99. Chang, J. and E.R. Waclawik, *Colloidal semiconductor nanocrystals: controlled synthesis and surface chemistry in organic media.* RSC Advances, 2014. **4**(45): p. 23505-23527.

100. Chen, S., et al., *Crystal and electronic band structure of Cu_2ZnSnX_4 (X= S and Se) photovoltaic absorbers: First-principles insights.* Applied Physics Letters, 2009. **94**(4): p. 041903.

101. Chen, S., et al., *Wurtzite-derived polytypes of kesterite and stannite quaternary chalcogenide semiconductors.* Physical Review B, 2010. **82**(19): p. 195203.

102. Siebentritt, S. and S. Schorr, *Kesterites - a challenging material for solar cells.* Progress in Photovoltaics, 2012. **20**(5): p. 512-519.

103. Buffiere, M., et al., *Microstructural analysis of 9.7% efficient $Cu_2ZnSnSe_4$ thin film solar cells.* Applied Physics Letters, 2014. **105**(18): p. 183903.

104. López-Marino, S., et al., *Inhibiting the absorber/Mo-back contact decomposition reaction in $Cu_2ZnSnSe_4$ solar cells: the role of a ZnO intermediate nanolayer.* Journal of Materials Chemistry A, 2013. **1**(29): p. 8338-8343.

105. Oueslati, S., et al., *Study of alternative back contacts for thin film $Cu_2ZnSnSe_4$-based solar cells.* Journal of Physics D-Applied Physics, 2015. **48**(3): p. 035103.

106. Patel, M. and A. Ray, *Enhancement of output performance of Cu_2ZnSnS_4 thin film solar cells—a numerical simulation approach and comparison to experiments.* Physica B: Condensed Matter, 2012. **407**(21): p. 4391-4397.

107. Simya, O.K., A. Mahaboobbatcha, and K. Balachander, *A comparative study on the performance of Kesterite based thin film solar cells using SCAPS simulation program.* Superlattices and Microstructures, 2015. **82**: p. 248-261.

108. Scragg, J.J., et al., *A detrimental reaction at the molybdenum back contact in* $Cu_2ZnSn(S, Se)_4$ *thin-film solar cells.* Journal of the American Chemical Society, 2012. **134**(47): p. 19330-19333.

109. Liu, X., et al., *Improving* Cu_2ZnSnS_4 *(CZTS) solar cell performance by an ultrathin ZnO intermediate layer between CZTS absorber and Mo back contact.* physica status solidi (RRL)-Rapid Research Letters, 2014. **8**(12): p. 966-970.

110. Liu, F., et al., *Enhancing the* Cu_2ZnSnS_4 *solar cell efficiency by back contact modification: Inserting a thin TiB2 intermediate layer at* Cu_2ZnSnS_4*/Mo interface.* Applied Physics Letters, 2014. **104**(5): p. 051105.

111. Biccari, F., et al., *Fabrication of* Cu_2ZnSnS_4 *solar cells by sulfurization of evaporated precursors.* Energy Procedia, 2011. **10**: p. 187-191.

112. Опанасюк, A.C., et al., *Properties of the Window Layers for the CZTSe and CZTS Based Solar Cells.* 2012.

113. Tajima, S., et al., *Atom-probe tomographic study of interfaces of* Cu_2ZnSnS_4 *photovoltaic cells.* Applied Physics Letters, 2014. **105**(9): p. 093901.

114. Kim, J., et al., *Optimization of sputtered ZnS buffer for* Cu_2ZnSnS_4 *thin film solar cells.* Thin Solid Films, 2014. **566**: p. 88-92.

115. Paier, J., et al., Cu_2ZnSnS_4 *as a potential photovoltaic material: a hybrid Hartree-Fock density functional theory study.* Physical Review B, 2009. **79**(11): p. 115126.

116. Haight, R., et al., *Band alignment at the* $Cu_2ZnSn(S_xSe_{1-x})_4$*/CdS interface.* Applied Physics Letters, 2011. **98**(25): p. 253502.

117. Li, J., et al., *The band alignment at CdS/*$Cu_2ZnSnSe_4$ *heterojunction interface.* Surface and Interface Analysis, 2013. **45**(2): p. 682-684.

118. Crovetto, A. and O. Hansen, *What is the band alignment of* $Cu_2ZnSn(S, Se)_4$ *solar cells?* Solar Energy Materials and Solar Cells, 2017. **169**: p. 177-194.

119. Chen, H.-J., et al., *Structural and photoelectron spectroscopic studies of band alignment at the* Cu_2ZnSnS_4*/CdS heterojunction with slight Ni doping in* Cu_2ZnSnS_4*.* Journal of Physics D: Applied Physics, 2016. **49**(33): p. 335102.

120. Huang, S., W. Luo, and Z. Zou, *Band positions and photoelectrochemical properties of* Cu_2ZnSnS_4 *thin films by the ultrasonic spray pyrolysis method.* Journal of Physics D: Applied Physics, 2013. **46**(23): p. 235108.

121. Dong, Z.-Y., et al., *An experimental and first-principles study on band alignments at interfaces of Cu_2ZnSnS_4/CdS/ZnO heterojunctions.* Journal of Physics D: Applied Physics, 2014. **47**(7): p. 075304.

122. Kumar, M. and C. Persson, *Cu_2ZnSnS_4 and $Cu_2ZnSnSe_4$ as Potential Earth-Abundant Thin-Film Absorber Materials: A Density Functional Theory Study.* Int. J. Theor. Appl. Sci., 2013. **5**: p. 1.

123. Born, M. and R. Oppenheimer, *On the quantum theory of molecules,* in *Quantum Chemistry: Classic Scientific Papers*. 2000, World Scientific. p. 1-24.

124. Mittendorfer, F. and J. Hafner, *Initial steps in the desulfurization of thiophene/Ni(100) - A DFT study.* Journal of Catalysis, 2003. **214**(2): p. 234-241.

125. Hohenberg, P. and W. Kohn, *Inhomogeneous electron gas.* Physical review, 1964. **136**(3B): p. B864.

126. Kohn, W. and L.J. Sham, *Self-consistent equations including exchange and correlation effects.* Physical review, 1965. **140**(4A): p. A1133.

127. Becke, A.D., *Density‐functional thermochemistry. III. The role of exact exchange.* The Journal of chemical physics, 1993. **98**(7): p. 5648-5652.

128. Perdew, J.P., K. Burke, and M. Ernzerhof, *Generalized gradient approximation made simple.* Physical Review Letters, 1996. **77**(18): p. 3865-3868.

129. Briddon, P.R. and R. Jones, *LDA calculations using a basis of Gaussian orbitals.* physica status solidi (b), 2000. **217**(1): p. 131-171.

130. Jones, R. and P.R. Briddon, *The ab initio cluster method and the dynamics of defects in semiconductors.* Identification of Defects in Semiconductors, 1998. **51**: p. 287-349.

131. Monkhorst, H.J. and J.D. Pack, *Special Points for Brillouin-Zone Integrations.* Physical Review B, 1976. **13**(12): p. 5188-5192.

132. Cohen, M.L. and T.K. Bergstresser, *Band structures and pseudopotential form factors for fourteen semiconductors of the diamond and zinc-blende structures.* Physical Review, 1966. **141**(2): p. 789.

133. Setyawan, W. and S. Curtarolo, *High-throughput electronic band structure calculations: Challenges and tools.* Computational materials science, 2010. **49**(2): p. 299-312.

134. Camps, I., et al., *Elastic and optical properties of $Cu_2ZnSn(SexS_{1-x})_4$ alloys: density functional calculations.* Semiconductor Science and Technology, 2012. **27**(11): p. 115001.

135. Rayson, M.J. and P.R. Briddon, *Highly efficient method for Kohn-Sham density functional calculations of 500–10 000 atom systems.* Physical Review B, 2009. **80**(20): p. 205104.
136. Coutinho, J., et al., *Electrical activity of chalcogen-hydrogen defects in silicon.* Physical Review B, 2003. **67**(3): p. 035205.
137. Troullier, N., *N. Troullier and JL Martins, Phys. Rev. B 43, 1993 (1991).* Phys. Rev. B, 1991. **43**: p. 1993.
138. Hartwigsen, C., S. Goedecker, and J. Hutter, *Relativistic separable dual-space Gaussian pseudopotentials from H to Rn.* Physical Review B, 1998. **58**(7): p. 3641-3662.
139. Gonze, X., *Towards a potential-based conjugate gradient algorithm for order-N self-consistent total energy calculations.* Physical Review B, 1996. **54**(7): p. 4383.
140. Perry, A., *A modified conjugate gradient algorithm.* Operations Research, 1978. **26**(6): p. 1073-1078.
141. Møller, M.F., *A scaled conjugate gradient algorithm for fast supervised learning.* Neural networks, 1993. **6**(4): p. 525-533.
142. Birch, F., *Finite elastic strain of cubic crystals.* Physical review, 1947. **71**(11): p. 809.
143. Maeda, T., S. Nakamura, and T. Wada, *First-Principles Study on Cd Doping in* Cu_2ZnSnS_4 *and* $Cu_2ZnSnSe_4$. Japanese Journal of Applied Physics, 2012. **51**(10): p. 10NC11.
144. Katagiri, H., et al., *Preparation and evaluation of* Cu_2ZnSnS_4 *thin films by sulfurization of E□ B evaporated precursors.* Solar Energy Materials and Solar Cells, 1997. **49**(1): p. 407-414.
145. Torpo, L., T.E.M. Staab, and R.M. Nieminen, *Divacancy in 3 C− and 4 H− SiC: An extremely stable defect.* Physical Review B, 2002. **65**(8): p. 085202.
146. Taylor, S.E. and F. Bruneval, *Understanding and correcting the spurious interactions in charged supercells.* Physical Review B, 2011. **84**(7): p. 075155.
147. Sque, S.J., R. Jones, and P.R. Briddon, *Hydrogenation and oxygenation of the (100) diamond surface and the consequences for transfer doping.* physica status solidi (a), 2005. **202**(11): p. 2091-2097.
148. Sque, S.J., R. Jones, and P.R. Briddon, *Structure, electronics, and interaction of hydrogen and oxygen on diamond surfaces.* Physical review B, 2006. **73**(8): p. 085313.

149. Rutter, M.J. and J. Robertson, *Ab initio calculation of electron affinities of diamond surfaces.* Physical Review B, 1998. **57**(15): p. 9241.

150. Baraff, G.A. and M. Schlüter, *Migration of interstitials in silicon.* Physical Review B, 1984. **30**(6): p. 3460.

151. Baraff, G.A. and M. Schluter, *Defects and Radiation Effects in Semiconductors—1980.* 1981.

152. Godby, R.W., M. Schlüter, and L.J. Sham, *Self-energy operators and exchange-correlation potentials in semiconductors.* Physical Review B, 1988. **37**(17): p. 10159.

153. Van de Walle, C.G. and R.M. Martin, *Theoretical calculations of heterojunction discontinuities in the Si/Ge system.* Physical Review B, 1986. **34**(8): p. 5621.

154. Henkelman, G. and H. Jónsson, *Improved tangent estimate in the nudged elastic band method for finding minimum energy paths and saddle points.* The Journal of chemical physics, 2000. **113**(22): p. 9978-9985.

155. Henkelman, G., B.P. Uberuaga, and H. Jónsson, *A climbing image nudged elastic band method for finding saddle points and minimum energy paths.* The Journal of chemical physics, 2000. **113**(22): p. 9901-9904.

156. Chen, S.Y., et al., *Abundance of Cu-Zn + Sn-Zn and 2Cu(Zn) + Sn-Zn defect clusters in kesterite solar cells.* Applied Physics Letters, 2012. **101**(22): p. 223901.

157. Han, D., et al., *Deep electron traps and origin of p-type conductivity in the earth-abundant solar-cell material* Cu_2ZnSnS_4. Physical Review B, 2013. **87**(15): p. 155206.

158. Chen, S.Y., et al., *Defect physics of the kesterite thin-film solar cell absorber* Cu_2ZnSnS_4. Applied Physics Letters, 2010. **96**(2): p. 021902.

159. Courel, M., J.A. Andrade-Arvizu, and O. Vigil-Galán, *Loss mechanisms influence on* Cu_2ZnSnS_4*/CdS-based thin film solar cell performance.* Solid-State Electronics, 2015. **111**: p. 243-250.

160. Amiri, N.B.M. and A. Postnikov, *Electronic structure and lattice dynamics in kesterite-type* $Cu_2ZnSnSe_4$ *from first-principles calculations.* Physical Review B, 2010. **82**(20): p. 205204.

161. Maeda, T., S. Nakamura, and T. Wada, *First Principles Calculations of Defect Formation in In-Free Photovoltaic Semiconductors* Cu_2ZnSnS_4 *and* $Cu_2ZnSnSe_4$. Japanese Journal of Applied Physics, 2011. **50**(4): p. 04DP07.

162. Davey, W.P., *Precision measurements of the lattice constants of twelve common metals.* Physical Review, 1925. **25**(6): p. 753.

163. Lubarda, V.A., *On the effective lattice parameter of binary alloys.* Mechanics of Materials, 2003. **35**(1-2): p. 53-68.

164. Cheong, B.H. and K.J. Chang, *First-principles study of the structural properties of Sn under pressure.* Phys Rev B Condens Matter, 1991. **44**(9): p. 4103-4108.

165. Rettig, S.J. and J. Trotter, *Refinement of the structure of orthorhombic sulfur, α-S8.* Acta Crystallographica Section C: Crystal Structure Communications, 1987. **43**(12): p. 2260-2262.

166. Wright, K. and J.D. Gale, *Interatomic potentials for the simulation of the zinc-blende and wurtzite forms of ZnS and CdS: Bulk structure, properties, and phase stability.* Physical Review B, 2004. **70**(3): p. 035211.

167. Gotsis, H.J., A.C. Barnes, and P. Strange, *Experimental and Theoretical Investigation of the Crystal-Structure of Cus.* Journal of Physics-Condensed Matter, 1992. **4**(50): p. 10461-10468.

168. Leon, M., N. Terao, and F. Rueda, *On the phase transition of chalcocite Cu_2S thin films.* physica status solidi (a), 1981. **67**(1): p. K11-K14.

169. Wiedemeier, H. and H.G.V. Schnering, *Refinement of the Structures of Ges, Gese, Sns and Snse.* Zeitschrift Fur Kristallographie, 1978. **148**(3-4): p. 295-303.

170. Arora, S.K., D.H. Patel, and M.K. Agarwal, *Microtopographical Characterization of Vapour-grown SnS_2 Single Crystals.* Crystal Research and Technology, 1993. **28**(5): p. 623-627.

171. Burton, L.A. and A. Walsh, *Phase Stability of the Earth-Abundant Tin Sulfides SnS, SnS2, and Sn2S3.* Journal of Physical Chemistry C, 2012. **116**(45): p. 24262-24267.

172. Nomura, T., et al., *Crystal structures and band-gap energies of $Cu_2Sn (S, Se)_3$ (0≤ x≤ 1.0) solid solution.* physica status solidi (c), 2013. **10**(7-8): p. 1093-1097.

173. Xu, P., et al., *Stability and electronic structure of Cu_2ZnSnS_4 surfaces: first-principles study.* Physical Review B, 2013. **88**(4): p. 045427.

174. Meyer, B.K. and W. Stadler, *Native defect identification in II–VI materials.* Journal of Crystal Growth, 1996. **161**(1-4): p. 119-127.

175. Nagoya, A., et al., *Defect formation and phase stability of Cu_2ZnSnS_4 photovoltaic material.* Physical Review B, 2010. **81**(11): p. 113202.

176. Leitao, J.P., et al., *Photoluminescence and electrical study of fluctuating potentials in Cu_2ZnSnS_4-based thin films.* Physical Review B, 2011. **84**(2): p. 024120.

177. Tanaka, T., et al., *Preparation of Cu_2ZnSnS_4 thin films by hybrid sputtering.* Journal of Physics and Chemistry of Solids, 2005. **66**(11): p. 1978-1981.
178. Katagiri, H., et al., *Development of thin film solar cell based on Cu_2ZnSnS_4 thin films.* Solar Energy Materials and Solar Cells, 2001. **65**(1-4): p. 141-148.
179. Tanaka, T., et al., *Influence of composition ratio on properties of Cu_2ZnSnS_4 thin films fabricated by co-evaporation.* Thin Solid Films, 2010. **518**(21): p. S29-S33.
180. Maeda, T., S. Nakamura, and T. Wada, *First-principles study on Cd doping in Cu_2ZnSnS_4 and $Cu_2ZnSnSe_4$.* Japanese Journal of Applied Physics, 2012. **51**(10S): p. 10NC11.
181. Barkhouse, D.A.R., et al., *Cd-free buffer layer materials on $Cu_2ZnSn(SxSe_{1-x})_4$: Band alignments with ZnO, ZnS, and In2S3.* Applied Physics Letters, 2012. **100**(19): p. 193904.
182. Vigil-Galán, O., et al., *Toward a high Cu_2ZnSnS_4 solar cell efficiency processed by spray pyrolysis method.* Journal of Renewable and Sustainable Energy, 2013. **5**(5): p. 053137.
183. Nam, D., et al., *Solar conversion efficiency and distribution of ZnS secondary phase in Cu_2ZnSnS_4 solar cells.* Solar Energy Materials and Solar Cells, 2016. **149**: p. 226-231.
184. Hossain, M.I., et al. *Potential buffer layers for Cu_2ZnSnS_4 (CZTS) solar cells from numerical analysis*. in *Clean Energy and Technology (CEAT), 2013 IEEE Conference on*. 2013. IEEE.
185. Yan, C., et al., *Band alignments of different buffer layers (CdS, Zn (O, S), and In_2S_3) on Cu_2ZnSnS_4.* Applied Physics Letters, 2014. **104**(17): p. 173901.
186. Ghorai, A., *A review on bulk diffusion in metallic solids.* 2014.
187. Kislenko, S.A., M.S. Vlaskin, and A.Z. Zhuk, *Diffusion of cation impurities by vacancy mechanism in α-Al_2O_3: Effect of cation size and valence.* Solid State Ionics, 2016. **293**: p. 1-6.
188. Pichler, P., *Impurity diffusion in silicon*, in *Intrinsic Point Defects, Impurities, and Their Diffusion in Silicon*. 2004, Springer. p. 229-279.
189. Erhart, P. and K. Albe, *First-principles study of migration mechanisms and diffusion of oxygen in zinc oxide.* Physical Review B, 2006. **73**(11): p. 115207.
190. Kato, T., et al. *Characterization of front and back interfaces on Cu_2ZnSnS_4 thin-film solar cells*. in *27th European photovoltaic solar energy conference and exhibition*. 2012.

191. Timo Wätjen, J., et al., *Cu out-diffusion in kesterites—A transmission electron microscopy specimen preparation artifact.* Applied Physics Letters, 2013. **102**(5): p. 051902.

192. Mutter, D. and S.T. Dunham, *Calculation of Defect Concentrations and Phase Stability in Cu_2ZnSnS_4 and $Cu_2ZnSnSe_4$ From Stoichiometry.* IEEE Journal of Photovoltaics, 2015. **5**(4): p. 1188-1196.

193. Varley, J.B. and V. Lordi, *Electrical properties of point defects in CdS and ZnS.* Applied Physics Letters, 2013. **103**(10): p. 102103.

194. Varley, J.B. and V. Lordi, *Intermixing at the absorber-buffer layer interface in thin-film solar cells: The electronic effects of point defects in Cu(In, Ga)(Se, S)$_2$ and Cu_2ZnSn(Se, S)$_4$ devices.* Journal of Applied Physics, 2014. **116**(6): p. 063505.

195. Zhang, X., et al., *The instability of S vacancies in Cu_2ZnSnS_4.* RSC Advances, 2016. **6**(19): p. 15424-15429.

196. Toki, S., et al. *Improvement of Cu(In, Ga)Se_2 photovoltaic performance by adding Cu-poor compounds Cu(In, Ga)$_3Se_5$ at Cu(In, Ga)Se_2/CdS interface*. in *Photovoltaic Specialists Conference (PVSC), 2016 IEEE 43rd*. 2016. IEEE.

197. Thuy, U.T.D., et al., *Comparative photoluminescence properties of type-I and type-II CdTe/CdS core/shell quantum dots.* Optical Materials, 2016. **53**: p. 34-38.

198. Zakharov, O., et al., *Quasiparticle band structures of six II-VI compounds: ZnS, ZnSe, ZnTe, CdS, CdSe, and CdTe.* Physical Review B, 1994. **50**(15): p. 10780.

199. Katagiri, H., et al., *Development of CZTS-based thin film solar cells.* Thin Solid Films, 2009. **517**(7): p. 2455-2460.

200. Bao, W. and M. Ichimura, *Prediction of the band offsets at the CdS/ Cu_2ZnSnS_4 interface based on the first-principles calculation.* Japanese Journal of Applied Physics, 2012. **51**(10S): p. 10NC31.

201. Kato, T., et al. *Buffer/absorber interface study on Cu_2ZnSnS_4 and $Cu_2ZnSnSe_4$ based solar cells: band alignment and its impact on the solar cell performance*. in *Proc. 28th European Photovoltaic Solar Energy Conf. Exhib*. 2013.

202. Chen, S., et al., *Compositional dependence of structural and electronic properties of Cu_2ZnSn(S, Se)$_4$ alloys for thin film solar cells.* Physical Review B, 2011. **83**(12): p. 125201.

203. Bao, W. and M. Ichimura, *First-principles study on influences of crystal structure and orientation on band offsets at the CdS/ Cu_2ZnSnS_4 interface.* International Journal of Photoenergy, 2012. **2012**.

204. Santoni, A., et al., *Valence band offset at the CdS/ Cu_2ZnSnS_4 interface probed by x-ray photoelectron spectroscopy*. Journal of Physics D: Applied Physics, 2013. **46**(17): p. 175101.

205. Aizawa, T., et al., *Investigation of ZnO: Al window layer of Cu_2ZnSnS_4 thin film solar cells prepared by non-vacuum processing*. physica status solidi (c), 2013. **10**(7-8): p. 1050-1054.